Lehrstuhl für Baumechanik der Technischen Universität München

Plastic Shape Functions of Plate Systems –

Reducing Modal DOF for Stochastic Nonlinear Dynamics of Large Scale Plate Systems

Yuh-Luen Lin

Vollständiger Abdruck der von der Fakultät für Bauingenieur- und Vermessungswesen der Technischen Universität München zur Erlangung des akademischen Grades eines

Doktor-Ingenieurs

genehmigten Dissertation.

Vorsitzender:	Univ.-Prof. Dr.-Ing. K.-U. Bletzinger
Prüfer der Dissertation:	
	1. Univ.-Prof. Dr.-Ing. H. Grundmann, em.
	2. Univ.-Prof. Dr.-Ing. Dr.-Ing. habil. G.H. Müller
	3. Univ.-Prof. Dr.-Ing. M.B. Bischoff, Universität Stuttgart

Die Dissertation wurde am 25.09.2006 bei der Technischen Universität München eingereicht und durch die Fakultät für Bauingenieur- und Vermessungswesen am 16.02.2007 angenommen.

Plastic Shape Functions of Plate Systems –

Reducing modal DOF for stochastic nonlinear dynamics
of large scale plate systems

Abstract

Plate systems which excited by stochastic dynamic loadings with the consideration of the material non-linearity is investigated. To describe the arisen plastifications, a 2D hysteretic material model is used. In order to reduce the number of modal degrees of freedom in the numerical analysis within the time domain as by the elastic dynamics, the plastic shape functions are introduced, which are specifically fitted to the plastic parts of curvatures resulted from the yielding and are systematically developed by means of the FEM. Due to the high reduction capability, 10,000 Monte-Carlo-Simulations can be performed for instance on a flat slab with about 30,000 FE-DOF.

Keywords

Plate system, flat slab, 2D hysteretic material model, FEM, BFS/Schäfer plate element, modal extension, Plastic Shape Function, stochastic dynamics, Monte Carlo Simulation

Plastische Formfunktionen der Plattensysteme –

Reduzieren modale DOF für stochastische nichtlineare Dynamik
der großen Plattensysteme

Zusammenfassung

Untersucht werden Platten unter stochastischen dynamischen Anregungen mit Berücksichtigung der Material-Nichtlinearität. Zur Beschreibung der auftretenden Plastizierungen wird ein 2D hysteretisches Materialmodell verwendet. Um die Anzahl der modalen Freiheitsgrade der numerischen Analyse im Zeitbereich ähnlich wie in der elastischen Dynamik reduzieren zu können, werden "Plastische Formfunktionen" eingeführt, die speziell den plastischen Krümmungsanteilen angepasst sind und mittels FEM systematisch entwickelt werden. Das hohe Reduktionspotential ermöglicht z.B. 10.000 Monte-Carlo-Simulationen an einer Flachdecke mit ca. 30.000 FEM-Freiheitsgraden.

Schlüsselwörter

Plattensystem, flache Decke, 2D hysteretische Materialmodell, FEM, BFS/Schäfer Plattenelement, modale Erweiterung, Plastische Formfunktionen, stochastische Dynamik, Monte Carlo Simulation

Vorwort

Die vorliegende Arbeit entstand am Lehrstuhl für Baumechanik der Technischen Universität München während meiner selbständigen Tätigkeit in den Jahren 2002-2006.

Herrn Prof. Dr.-Ing. H. Grundmann danke ich herzlich für die fachliche Unterstützung und die Diskussionsbereitschaft während der Ausarbeitung. Herrn Prof. Dr.-Ing. G. Müller und Herrn Prof. Dr.-Ing. M. Bischoff gilt mein Dank für die zahlreiche Anregungen und die Übernahme des Koreferats. Herrn Prof. Dr.-Ing. K.-U. Bletzinger danke ich für die Übernahme des Vorsitzes des Prüfungsausschusses.

Allen meinen Kollegen am Lehrstuhl danke ich für die freundliche Arbeitsatmosphäre und die Hilfsbereitschaft, insbesondere Herrn Dipl.-Ing. Kai Müller. Ich möchte auch den Leuten danken, die mir hier in Deutschland geholfen haben.

Mein besonderer Dank gilt meinen Eltern für ihren steten Rückhalt und ihr Verständnis für meine lange Abwesenheit in der vergangenen Jahre.

Meiner Frau danke ganz herzlich ich für ihre Begleitung und ihre Unterstützung.

München, im März 2007 Yuh-Luen Lin

Contents

Notation

Abbreviation

2D-HMiPSP	two-dimensional hysteretic model in principal stress plane
DMCS	direct Monte-Carlo simulation
DOF	degrees of freedom
ESL	equivalent statistical linearization
MCS	Monte-Carlo simulation
MDOF	multi degrees of freedom
NSD	nonlinear stochastic dynamics
PSF	plastic shape function
SDOF	single degree of freedom
VYD	value of yielding determinate of the 2D-HMiPSP

Latin Alphabet

$B_{x,i}, B_{y,i}, B_{xy,i}$	interpolation functions of curvatures
$\mathbf{C}_e$	element damping matrix
E	Young's modulus
E^t	tangential stiffness or post-yielding strength
f_B	body force
f_S	surface force
f_T	D'Alembert's inertial force
$F(\sigma_{ij})$	yield function
G	shear modulus
h	thickness of plate
$H(t)$	Heaviside function
$\mathbf{H}_{ex}, \mathbf{H}_{ey}, \mathbf{H}_{exy}$	vectors of accessory hysteretic equations
J_1', J_2', J_3'	invariants of deviatoric stress tensor
K^P	plastic modulus
K_b	bending stiffness of the plate
$\mathbf{K}_e$	element stiffness matrix of elasticity
$\mathbf{K}_{ex}, \mathbf{K}_{ey}, \mathbf{K}_{exy}$	element stiffness matrices of hysteresis
m_x, m_y, m_{xy}	bending and twisting moments per unit length
$\tilde{M}_p$	plastic limit of moment
$\tilde{M}_y$	elastic limit of moment

$\mathbf{M}_e$	element mass matrix
$N(x, y)$	shape function of deflection
$\tilde{N}(x, y)$	interpolation functions of variable Y
$\tilde{\mathbf{p}}(t)$	vector of stochastic loading process
$\bar{p}(x, y, t)$	dynamic area load
$\bar{\mathbf{P}}_e(t)$	equivalent element nodal forces
S_{ij}	deviatoric stress components
$\mathbf{S}$	deviatoric stress tensor
$\mathbf{S}(\omega)$	spectral density function
$u(x, y, z)$	elongations of plate in x-direction
δU	vector of virtual displacement
$v(x, y, z)$	elongations of plate in y-direction
$w(x, y, t)$	deflections of plate
w_i^*	generalized degree of freedom
$\mathbf{w}_e$	vector of the nodal deformations
$\ddot{\mathbf{w}}_e$	vector of nodal accelerations
$\delta W, \delta W_i, \delta W_e$	total, internal and external virtual work
Y	hysteretic variable for moment-curvature correlations
$\mathbf{Y}_{ex}, \mathbf{Y}_{ey}, \mathbf{Y}_{exy}$	vectors of hysteretic variables
z	hysteretic variable of nonlinear restoring forces

Greek Alphabet

α	ratio of post-yielding to preyielding stiffness
$\boldsymbol{\alpha}^h$	hardening parameters
δ_{ij}	Kronecker delta
ϵ_Y	yield strain
ϵ_{ij}	strain components
ϵ'_{ij}	deviatoric strain components
$\boldsymbol{\epsilon}$	strain tensor
$\tilde{\kappa}_p$	plastic limit of curvature
$\tilde{\kappa}_y$	elastic limit of curvature
$\kappa_x, \kappa_y, \kappa_{xy}$	bending and twisting curvatures
ν	Poisson's ratio
μ_G, β_G	coefficients of Gumbel-distribution
μ_S, σ_S	mean and standard deviation of simulation results
ω_i	natural frequency
$\psi(x, y)$	rotation angles of cross-sections of plate
ϕ_i	eigenvector
$\psi_p, \tilde{\psi}_p$	plastic shape function, orthogonalized
Φ	mode-shape matrix
ρ	density of material
$\sigma_1, \sigma_2, \sigma_3$	principal stresses
$\sigma_x, \sigma_y, \tau_{xy}$	plane stresses in Cartesian coordinate
σ_Y, σ_Y^0	yield stress, initial yield stress
σ_{ij}	stress components

θ	principal stress angle
$\tilde{\theta}$	principal strain angle
θ_m	equally distributed random phase angle between $[0..2\pi]$
$\boldsymbol{\sigma}$	stress tensor
τ_Y	yield stress of pure shear
ξ	hysteretic variable for stress-strain correlations
ζ_i	damping ratio
æ	element damping coefficient

Chapter 1

Introduction

1.1 Motivation

From 'Empire State Building' to 'Taipei 101', from 'Golden Gate Bridge' to 'Akashi-Kaikyo Bridge' and from 'Aswan Dam' to 'Three Gorges Dam', the dimension of the civil engineering constructions expands rapidly in the last century. On the other hand, the natural disasters, especially the earthquakes like [18] – 1908 Messina (Italy); 1976 Tangshan (China); 1994 Northridge, California (USA); 1995 Kobe (Japan); 1999 Chi-Chi (Taiwan) [49] and 2004 India Ocean earthquake & tsunamis, have never stopped to attack the havings of the civilization. As a result the risk of our society increases constantly regarding the nature disasters. Therefore there are urgent needs to reduce such risks with all possible efforts. From the aspect of structural engineers the most important thing to do is to ensure that the constructions, no matter whether in existence or in plan, should be able to sustain the trials of nature, such as strong earthquakes mentioned above.

In regard to the extreme seismic excitations, the structures may undergo during the quake the overstepping of the material elastic limit. Therefore it is important for the engineers to be able to realize the seismic behaviors of the constructions through nonlinear dynamic analyses. Furthermore, with the understanding of nonlinear system responses it is also possible to control the critical state of structures near collapse in a planned way by applying the *Capacity Design* concept, so that the seismic resistance of constructions can be ensured on the one hand, and on the other hand constructions can be designed more efficient and more economical than in the past.

For nonlinear dynamic analyses the mathematical nonlinear material model has a very important role. With acceptable accuracy this model should factually rebuild the real stress-strain relations in the material especially beyond the elastic limit. Because closed analytical solutions of complex constructions are generally unavailable even under elastic considerations, this nonlinear material model should also be suitable to be easily introduced into the common numerical solution's algorithms – the FEM for example,

so that it can be applied to the practical uses.

Another nature of the seismic excitations to be considered is its random characteristics. As a result the system responses, which the engineers deal with, are also random and belong to the subjects of nonlinear stochastic dynamics (NSD), which represents an integral part of the reliability analysis of constructions. By the reliability analysis a correct representation of the seismic input, i.e., a sensible generation of pseudo random signals, is indispensable for making a reasonable prognosis about the failure probability of structural systems. Besides the random inputs, the uncertainty of the system parameters, e.g., damping or stiffness, can also have influence on the structural reliability analysis. But if the wind or seismic loading is concerned as the excitation, which has wide-band spectrum density, the system responses are comparatively less sensitive to the uncertain system characteristics, so that these uncertainties can be neglected for simplification of such reliability analysis.

After establishing the mechanical model the most crucial question is how to solve the NSD problems, which require highly theoretical and numerical efforts. Such efforts are especially extreme by the reliability analysis, since an explicit determination of the probability of critical system responses, which lie at the tail of the probability density, is necessary. In the last three decades the NSD has become a significant branch of structural dynamics , and various procedures have been developed to predict the response of nonlinear systems under stochastic non-parametrical external excitations. Progresses of NSD come not only from the earthquake engineering but also from other specific fields, such as the offshore platform engineering, the aeronautical engineering, etc., which can be found in numerous publications [3], [55].

In comparison with the deterministic consideration the computational complexity of nonlinear stochastic dynamic problems is excessively high, therefore most of the procedures suggested for the NDS problems are limited to small systems with fewer degrees of freedom and a direct application of them for the engineering practice is still restricted. In order to diminish the gradually increasing risks of civil constructions facing the natural disasters, there are insistent needs to develop an algorithm, which can significantly reduce the computational complexity, especially for systems with large scale in nonlinear stochastic dynamics.

1.2 Previous Research

As mentioned above three major subjects, which are listed in the following, have to be handled by establishing and solving the NSD problems.

- Proposal of nonlinear material model
- Strategy for stochastic analysis
- Procedure of reducing system DOF

In the coming subsections a brief overview of the developing history and the current stand of these three subjects is given.

1.2.1 Nonlinear Material Model

The first research of the nonlinear material behaviors was done by Tresca (1864), who proposed the yielding condition of metals [41] [16]. The constitutive law of yielding was first postulated by Saint-Venant in 1870 for the two-dimensional stress state, in which the proportionality between the stress and strain in Hook's law was replaced by the relation between the derivative of stress and strain. This constitutive postulate was then extended by Levy in the same year for the three-dimensional stress state. Levy's constitutive equation is only valid for fictive, the so-called rigid-plastic material without elastic strains, since it is an equation of relations between principal stresses and total strains [64].

A further impetus for the development of a general theory in the classical plasticity was given by von Mises with his works in 1913, which are the well known " von Mises yielding criterion " and the " Levy-Mises constitutive postulate " (this name comes from the conformation of the independent works from Levy and from von Mises respectively). The nonlinear stress-strain relation was then extend by Prandtl (1924) and Reuss (1930) for more general uses by means of considering the Hooke's elastic strains. Since then much research was done and various theories were proposed; a detailed developing history of the classical plasticity theory can be found in [41].

Following another independent line the hysteretic material model was developed to give a direct description of the nonlinear force-displacement relationship. Two of the simplest hysteretic models are to note, namely the bilinear model [37] and the smooth Ramberg-Osgood model [38], which have different formulations of the nonlinear force-displacement relationship for loading and unloading states, respectively. Because their incoherence under a circular loading, analytical solutions of these models are difficult to find.

The hysteretic bilinear model with a closed mathematical formulation was suggested by Suzuki and Minai in 1985 [91] through the introduction of the Heaviside function as the mechanism of distinguishing the loading states. Consequently this hysteretic model is directly integrable and can be easily added to the common differential equations. But even earlier Bouc proposed in 1967 the continuous smooth hysteretic model, which can better indicate the nonlinear material behaviors under circular loadings. In 1976 Wen extended the work of Bouc in a general form by including a new power index, so that the hysteretic model is more flexible and is able to describe the macro force-displacement relationship of various materials beyond yielding. Because its applicability and flexibility a lot of attention was given to the so-called Bouc-Wen hysteretic model. Based on this model several developments were made for different needs, such as hysteretic for degrading systems - Baber and Wen (1981), biaxial hysteretic model - Park et al.

(1986), hysteretic in tensor form - Casciati (1989) and Simulescu (1989), etc.. A brief review of the various hysteretic models can be found in [101] and [96].

1.2.2 Algorithms of NSD Problems

The procedures of solving the NSD problems can be roughly classified into the analytical, the approximated and simulation methods. Generally NSD problems can not be solved exactly because of their complexity. Until now the analytical methods, which base on the Fokker-Planck equation and the theory of Markov-Process, are still limited to simple, particular cases, such as SDOF systems or weakly nonlinear MDOF systems. Therefore various approximation procedures have been developed for engineering uses.

One of the approximated solutions to mention, which is the most widely applied in practice, is the *Equivalent Statistical Linearization* (ESL) proposed by Caughey [15]. Because this method is easy to deal with and is very useful for the pre-study by construction designs, enormous literature about ESL are available and a comprehensive introduction of ESL can be read in [65]. The basic concept of ESL is to determine the linearization coefficients by minimizing the mean square error between the linearized system and the original nonlinear system. To simplify the mathematical evaluation, the standard ESL assumes a normally distributed response of the nonlinear system, which, however, is not necessarily true. Therefore, further extensions of ESL to assume non-Gaussian properties of the response have been achieved, e.g., by Pradlwarter and Schuëller [59]. A short review of various approximated procedures and the comparison of ESL with other methods can be found in the benchmark study [75].

For the application of systems with arbitrary characters and loading conditions, the only thing to fall back on, which is also the simplest one in concept, is the simulation method, i.e., the direct Monte Carlo Simulation (MCS), which is also used to provide the reference solutions in [75]. The accuracy of the direct MCS is in principle independent of the system non-linear type and its dimensionality, but depends on the number of realizations. Therefore the major disadvantage of direct MCS is the unpractical requirement of large sample sizes to estimate the low probability regions, which are important for reliability analyses. To raise the the accuracy of MCS on the tail of probability distribution with feasible sample sizes, the advanced MCS, e.g., importance sampling [66], adaptive and selective sampling [56] [57], and MCS combined with the Controlled Simulation Techniques, such as Double and Clump [60], Russian Roulette and Splitting [58], etc., have been developed.

1.2.3 Reduction Strategies of System DOF

All the algorithms for NSD problems introduced above, no matter whether analytical, approximated or simulated, have a difficulty in common, namely the difficulty to be performed on systems with a large number of degrees of freedom, which are familiar in

the engineering practices. This is because, - as the yielding occurs - correspondingly there will be enhanced deformations, i.e., discontinuity of the deformation derivatives, concentrated locally at the yielding locations. In contrast to elastic dynamics, by which the system responses can be accurately enough approximated through only a few eigenvectors, the plastic deformations resulted from yielding have to be formulated through the superposition of high frequency modes according to the modal analysis method. In other words, all the eigenmodes, whose number conforms to the system degrees of freedom, have to be used in the classical modal analysis of a dynamic, physically nonlinear system.

To overcome this drawback and make the stochastic analysis also feasible for large scale systems, some reduction strategies of the modal bases for nonlinear systems have been developed. For example:

- The *Static Correction Procedure* and the *Mode Acceleration Method* [17], which consider the nonlinear part of system responses as quasi-static and determine them statically through the geometrical, time invariant function of the loading as the superposition of high frequency modes. Then this static mode will be multiplied with the time variant function of the loading and added as the correction into the elastic dynamic solutions resulted from the lower modes. This method is applied to the nonlinear problems by Schuëller, Pradlwarter and Schenk in the works [61], [74] and [69], in which the internal hysteretic restoring forces are treated as external loadings.

- The *Nonlinear Galerkin Method*, which can be derived from the concept "slaving principle" after [35]. In this procedure the higher modes will be replaced by static shape functions, whose time variant weighting coefficients are assumed to be a function of the elastic responses resulted from the lower modes. If this function were linear, then this method is the same as the static correction procedure, otherwise it is generally called nonlinear Galerkin method. The determination of such nonlinear weighting coefficients can be found in [46] and the variance of this method, the so-called "postprocessed" Galerkin method is proposed in [11].

- The Component Mode Synthesis (CMS) method [76], [62], which divides the large system into small components, so that the eigenvalue problem with enormous degrees of freedom (DOF) can be reduced to several eigenvalue problems with less DOF. According to the yielding locations, sub-systems will be separated by introducing rigid boundary conditions at the cutting off positions and the corresponding eigenforms will be determined. The entire system will be composed together through the CMS-matrix with consideration of the nonlinear equations.

Instead of using corrections or assumptions to approach the contributions of the high frequency modes to the nonlinear system responses, a completely new concept, the *Plastic Mode* was first suggested by Grundmann in [31]. Under the concept of *Plastic Mode*, which is also called the *Plastic Shape Function* (PSF) in the present work or "Plastische Formfunktion" in German literature, the contributions of all the higher eigenmodes will be 'freezed' into only a few particular shape functions according to the

yielding locations, and such plastic shape functions can be directly added in the reduced modal bases as their extensions for the common modal analysis methods. In this way the system DOF, no matter how large it is originally, can be extremely reduced to only a small number of eigenmodes for the description of elastic system responses plus a few plastic shape functions for particular yieldings.

In [31] and [27] the concept of PSF for the shear beam system, which is simulated as the discretized swing mass chain, is introduced and the investigation with corresponding examples is assembled in [26]. The further development of PSF for continuous bending beam is achieved in [42]. The application of PSF to hysteretic 2-D frame system can be found in [32] and further, in [33], the nonlinear dynamic analysis of 3-D large frame system under stochastic excitations is also performed through the utilization of PSFs.

1.3 Objectives and Scope

As already exhibited in the various research mentioned above, the plastic shape function can efficiently reduce the system dimensions by replacing the high frequency eigenmodes in the modal analysis without significant loss of accuracy. Therefore it is worth and necessary to do further research about the plastic shape functions, so that this procedure can be generalized for more extensive applications on various constructions.

The further development of the PSF, which is also the objective of this work, is its application for flat-plate systems, which is a basis and a gateway to more complicated surface structures, e.g., lateral loaded walls, shells and membranes. For this purpose a systematical derivation of the PSFs relying on the foundations of the Finite Element Method (FEM) is very important, since the FEM is the most general and useful numerical tool for the analysis of large scale systems. In other words, a general principle should be proposed and by following it compatible PSFs for most kind of plate elements utilized in the FEM should be derived.

Besides the development of PSFs, a directly applicable nonlinear material model for the plane stress state based on the Bouc-Wen hysteretic model, with its noticeable absence in literature, still has to be derived and implanted efficiently into the finite element representation of the entire system. In this part of work the stiffness matrix of the yielding related plate elements will be split into an elastic and a plastic one, while the former is the weighted common stiffness matrix corresponding to the nodal deformations, the latter is a curvature related stiffness matrix for hysteretic variables. Considering the consistency of the virtual energies the plastic stiffness matrix should be compatible with the usual elastic stiffness matrix, so that the entire virtual works resulting from these two parts wouldn't be falsified under elastic unloading states.

The entire nonlinear mechanical model will be built on the mathematical language

software “MATLAB”, which serves as the system platform in this work. For solving the nonlinear differential equation of examples in this work the package of differential equation solvers in MATLAB will be used, especially the solver “ode15s” [77] [78], which is based on the numerical differentiation formulas (NDFs) and the backward differentiation formulas (BDFs, or called as Gear’s method).

The stochastic seismic excitations will be considered as the filtered Gaussian White Noise using the Kanai-Tajimi-Model [39], [94] and applied to an RC slab with a large number of DOF. To predict the probabilistic values of this nonlinear dynamic system, such as the mean value, the standard deviation of the nonlinear responses or the probabilistic distribution of the maximal curvatures at the yielding locations, the direct Monte Carlo Simulation - which has no further technic of raising the efficiency - will be utilized, so that the performance of the PSFs can be realized in a straightforward manner, since a large sample sizes of the direct MCS are needed for a convincing result.

1.4 Outline

This work is composed of three major subjects, i.e., the nonlinear material model, the modified FE representation, the development of PSFs, and of two numerical examples. The three major subjects, discussed in chapter 2, 3, and 4. respectively, are on the one hand connected together in the numerical examples, but on the other hand they are also independent with each other according to their individual concepts and can be read separately. A preview of each chapters is given in the following.

Chapter 2.

First, two major subjects of the classical theory of plasticity, namely the yielding criteria and the constitutive equation of hardening materials, will be introduced. Reviews of the von Mises criterion and the Ziegler’s kinematic hardening model are given. According to the work of Park (1986) and of Simulescu (1989), a two-dimensional hysteretic model in the principal stress plane (2D-HMiPSP) is derived as the basis of the nonlinear plate element utilized in chapter 3. To verify the validity of the 2D-HMiPSP, it will be compared with the model of classical plasticity theory based on the von Mises yielding criteria and the Ziegler’s constitutive equation. Through numerical examples the results of the classical and hysteretic models, i.e., the yielding boundaries and the hardening characteristics, are compared.

Chapter 3.

This chapter begins with a brief introduction of the ‘Kirchhoff Plate Theory’, which is adopted in this work to simplify the considerations of the nonlinear stress-strain relationship, since a directly applicable hysteretic material model for neither the Kirch-

hoff's nor the Mindlin's plate theory has been found by the author in the literature. Applying the 'Principle of Virtual Work', which is generally used in the FEM to derive the elementary equilibrium equations, the internal virtual works of a plate element are separated into an elastic and a plastic part by introducing the hysteretic variables.

For the sake of building the finite element model of the global system a translation of the hysteretic variables from the principal stress plane to the Cartesian coordinate system is performed and verified through a control example. Further the stress-strain relation has to be translated to the moment-curvature relation through the integration across the plate section, which means that the same modification of the nonlinear variables in the Cartesian coordinate system should also also be done. But because an analytic integration of the hysteretic variables relying on the stress-strain level is impossible without extensive mathematic support, a hysteretic moment-curvature relation of plate is postulated. This assumption is then certified through the comparison with the nonlinear fiber model.

Corresponding to the hysteretic moment equations, which have two bending and one twisting curvatures as independent variables, the compatible rectangular 4-nodes *Schäfer plate element* (or known as *BFS-element*) with 4 DOF (1 vertical deflection, 2 rotation angles and 1 twisting angle) per node is chosen in this work. According to these degrees of freedom, 16 *bi-cubic* deformation shape functions and the corresponding elastic stiffness matrix can be determined. Since a bi-cubic deflection distribution is selected, an equivalent representation of the curvature fields is imperative, so that the consistency of the virtual works can be ensured. Consequently for the hysteretic variables of moment-curvature relations (Y-variables), the additional interpolation functions, which are compatible with the second derivatives of deformation shape functions, are derived. Based on these interpolation functions of Y-variables, the *curvature related stiffness matrices* (also named as stiffness matrices of hysteresis in this work) can be established. These matrices are not only indispensable for establishing the nonlinear differential equations but are also the kernels for the development of PSFs.

In the last section of this chapter some reduction strategies of the system DOF in the literature are reviewed. In order to avoid the unnecessary evaluations of the Y-variables under the consideration that yielding occurs only at some particular locations in the entire system, the *Patch* and *Split* methods are proposed. The original concept of the PSF, which is also a possibility of reducing the DOF of plate system, is briefly described at the end.

Chapter 4.

The basic considerations and requirements of the plastic shape function are intensively discussed at the beginning of this chapter by means of a most simple example – the elongating bar. A verification of the accuracy of PSFs, which simulate the contributions of high frequency eigenmodes, is also performed on this example. Although the PSFs of

discretized bending beam are already suggested in [42], the development of such PSFs is illustrated again in the second part of this chapter, but according to the new concept of the curvature related stiffness matrices. Since the same PSFs are derived as from previous works, proof of validity through numerical examples is abolished. With the experiences of the bending beam the development of PSFs for laterally loaded plate is then proposed in the last section.

Chapter 5.

This chapter serves as the essential verifications of the accuracy and efficiency of PSFs for flat-plate system. Various examples of different yielding conditions are illustrated with a simple supported rectangular steel plate. On this small plate structure reference solutions, resulted from the application of all eigenmodes, can be earned and direct comparisons of the PSF applied solutions with them are made.

Chapter 6.

In the first section of this chapter a brief review of the stochastic mechanics is given at the beginning. Then two procedures of estimating the stochastic system responses, namely MCS and ESL, are discussed with indications of corresponding literature. At the end of this section the generation of White Gaussian Noises is explicitly interpreted for further modifications.

In the second part of this chapter the FE model of a large RC flat slab is built. Vertical seismic excitations considered as the filtered Gaussian White Noises after the Kanai-Tajimi-Model are put on this system. While investigating the nonlinear system responses by one single random process, unexpected high divergences of the twisting curvature at the corner of the column support between the solutions with or without applying PSFs are detected. Therefore an independent inspection of this phenomenon, which is named as the nonlinear column support effects, is supplemented through a small system with reference solutions. Relying on this independent certification, Monte Carlo simulations with $10,000$ sample sizes are performed on the large RC slab to show the remarkable efficiency achieved by this procedure.

Chapter 2

Elasto-Plastic Material Behavior

Under the objectives of present work, the first step is to find a reasonable mathematical model to describe the phenomenological macroscopic nature of plastically deformed materials, and this model should be able to be modified for further applications of flat slabs. The commonly used materials in the engineering constructions are concrete and steel, whose plastic behavior differ widely from each other; the former has the nature of strain softening (brittle) while the latter has the strain hardening character (ductile). In order to avoid a suddenly collapse of the structure, by designing of reinforced concrete structures the reinforcement steel is demanded to yield before the concrete fails, i.e., the so-called *secondary compression failure* is required. Consequently the ductile characteristic of steel dominates the plastic behavior of the RC constructions. Therefore in the present work the consideration of elasto-plastic material behavior will focus on the construction steel.

2.1 Classical Theory of Plasticity

To certify the validity of the hysteretic model derived in the present work (cf. 2.3.1), the following constituents of the classical plasticity theory, i.e., the yielding criterion and the constitutive equation of kinematic hardening materials, are used as references. Details of the classical plasticity theory can be found in [41], [16] and a brief introduction about this theory is given in the appendix A.

2.1.1 von Mises Yielding Criterion

The material considered in this work is assumed to be isotropic, as a result the yielding is independent of the direction of the principal stresses. According to the von Mises criterion (1913), the distinction between the elastic and the plastic material behavior can be formulated as

$$F(\sigma_{ij}) = J_2' - k^2 \begin{cases} = 0 & \text{for yielding or plastic deformation} \\ < 0 & \text{for elastic deformation} \end{cases}, \qquad (2.1)$$

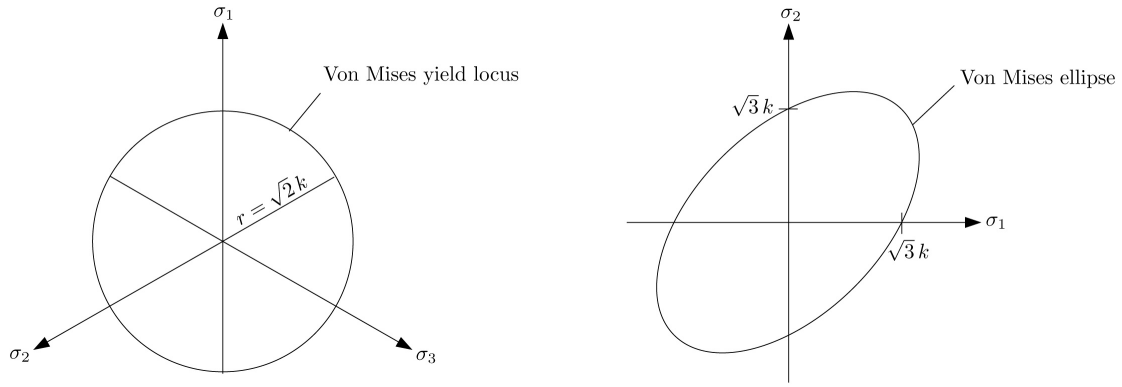

(a) Deviatoric Stress Plane (b) Principal Stress Plane

Figure 2.1: von Mises Yielding Criterion

where $F(\sigma_{ij})$ is the yield function, J_2' is the second invariant of the deviatoric stress tensor $\mathbf{S}$ and k^2 is a critical value of the material.

For the yielding state this expression can be rewritten in terms of principal stress components as

$$J_2' = \tfrac{1}{6}\left[(\sigma_1 - \sigma_2)^2 + (\sigma_2 - \sigma_3)^2 + (\sigma_3 - \sigma_1)^2\right] = k^2 \ . \tag{2.2}$$

Through a simple tension test or a pure shear test, the value of k in (2.2) can be determined as

$$k = \frac{\sigma_Y}{\sqrt{3}} = \tau_Y \ . \tag{2.3}$$

Under the condition of plane stress ($\sigma_3 = 0$), equation (2.2) can be reduced to

$$\sigma_1^2 - \sigma_1\sigma_2 + \sigma_2^2 = 3k^2 \ . \tag{2.4}$$

A graphical representation of the von Mises yield locus on the deviatoric stress plane, which is perpendicular to the hydrostatic pressure axis ($\sigma_1 = \sigma_2 = \sigma_3$), is given in Fig. 2.1 (a). The von Mises ellipse on the two-dimensional principal stress plane is represented in Fig. 2.1 (b).

2.1.2 Constitutive Equation of Ziegler's Hardening Model

In order to have a comparison with the post-yielding stiffness defined in the hysteretic material model, the kinematic hardening rule is utilized, whose yield function can be generally expressed as

$$F(\boldsymbol{\sigma}, \boldsymbol{\alpha}^h) = f(\boldsymbol{\sigma} - \boldsymbol{\alpha}^h) - \tilde{k} = 0 \ , \tag{2.5}$$

where $\boldsymbol{\alpha}^h$ is a tensorial hardening parameter (the so-called *back stress*) and $\tilde{k}$ is a material constant. Through $\boldsymbol{\alpha}^h$ and $\tilde{k}$ the geometrical center and the size of the yield

surface can be determined respectively.

According to the kinematic hardening model proposed by Ziegler in 1959, the increment of the hardening parameter is formulated as

$$d\boldsymbol{\alpha}^h = (\boldsymbol{\sigma} - \boldsymbol{\alpha}^h)d\mu \ , \tag{2.6}$$

where $d\mu$ is a proportional scalar constant determined by the yield criterion. Consequently, the moving direction of the yield surface is assumed to be parallel to the vector $\boldsymbol{\sigma} - \boldsymbol{\alpha}^h$ in the Ziegler's hardening model. The graphical representation of this hardening rule can be found in Fig. A.2.

Using the consistency assumption proposed by Prager (s. (A.28)) the proportional scalar $d\mu$ and the derivative of the hardening parameter $d\boldsymbol{\alpha}^h$ can be evaluated as

$$d\mu = \frac{\partial f/\partial \boldsymbol{\sigma} : d\boldsymbol{\sigma}}{\partial f/\partial \boldsymbol{\sigma} : (\boldsymbol{\sigma} - \boldsymbol{\alpha}^h)} \tag{2.7a}$$

and

$$d\boldsymbol{\alpha}^h = \frac{(\boldsymbol{\sigma} - \boldsymbol{\alpha}^h)}{\partial f/\partial \boldsymbol{\sigma} : (\boldsymbol{\sigma} - \boldsymbol{\alpha}^h)}\, l \ , \tag{2.7b}$$

with

$$l = \frac{\partial f}{\partial \boldsymbol{\sigma}} : d\boldsymbol{\sigma} \ .$$

By introducing the associated flow rule, the plastic strain rate $\dot{\boldsymbol{\epsilon}}^p$ can be determined as

$$\dot{\epsilon}^p_{ij} = \dot{\lambda}\frac{\partial F(\sigma_{ij})}{\partial \sigma_{ij}} \ , \tag{2.8}$$

where $\dot{\lambda}$ is a proportional positive scalar factor.

On the other hand, if the normality condition of the associated flow rule is considered, $d\boldsymbol{\epsilon}^p$ is then parallel to the component, which is normal to the yield surface, of stress increment $d\boldsymbol{\sigma}$, and can be formulated as

$$d\boldsymbol{\epsilon}^p = \frac{1}{K^P}\left(\mathbf{n} : d\boldsymbol{\sigma}\right)\mathbf{n} = \frac{1}{K^P}\,\frac{l}{\partial f/\partial \boldsymbol{\sigma} : \partial f/\partial \boldsymbol{\sigma}}\,\frac{\partial f}{\partial \boldsymbol{\sigma}} \ . \tag{2.9}$$

where $\mathbf{n}$ is the normal vector of yield surface and $K^P > 0$ is a proportional factor.

Comparing (2.8) with (2.9) the proportionality parameter $d\lambda$ can be determined as

$$d\lambda = \frac{1}{K^P}\,\frac{l}{\partial f/\partial \boldsymbol{\sigma} : \partial f/\partial \boldsymbol{\sigma}} \ . \tag{2.10}$$

Applying the von Mises yield criterion the parameter K^P can be calculated through the uniaxial tension test as [41]

$$\frac{1}{K^P} = \frac{3}{2}\left(\frac{1}{E^t} - \frac{1}{E}\right) \ , \tag{2.11}$$

where E is the Young's modulus and E^t is the tangential stiffness, i.e., the post-yielding strength for linear hardening. And K^P is considered as plastic modulus.

2.2 Hysteretic Model in 2D Principal Stress Plane

One of the basic assumptions of Kirchhoff's plate theory is the neglection of deformations due to transverse shear stresses, which means that the transverse shear has no influences on the lateral deflection(details about the plate theory s. section 3.1). The consequence of this assumption is that the shear stress, which is perpendicular to the middle plane, has no effects on the yielding of plate and can be neglected by the limit analysis, if the the plane stress state is considered [68].

This postulate can also be found in reference [16], in which the interaction between the shear force and bending moment for the yielding of beam is also demonstrated. Through the illustrations of beam element in [16], the following two conclusions can be made, with which the limit analysis of plate can be understood better.

- under the state of contained plastic flow (the cross-section is only partially yielded) the vertical shear stress is merely distributed in the region of the elastic normal stress. Therefore the yielding of the outer fibers is determined only by the normal stress.
- for the entire cross-section the effect of shear force V on the yielding is negligible when the length of the beam is more than 10 times its height, for which the Bernoulli beam theory is valid.

Therefore it is reasonable to assume that the yielding of plate is dominated by the plane stresses, i.e., by normal stresses in x- and y-direction corresponding to bending moments and by the in-plane shear stress resulted from twist moment. Furthermore, the plane stresses can be translated into the principal stresses, which means that only two additional hysteretic variables are needed for describing the yielding of a plate.

To establish the hysteretic model with two variables for the plate, the work of Park et al. [53] and the work of Simulescu et al. [88] are used as the bases. A more detailed exposition of the hysteretic model and its developments can be found in appendix B.

In [53] the biaxial hysteretic equations of the two-dimensionally excited column are proposed by Park as

$$\begin{aligned} \dot{z}_x &= A\,\dot{u}_x - \beta\,|\dot{u}_x\,z_x|\,z_x - \gamma\,\dot{u}_x\,z_x^2 - \beta\,|\dot{u}_y\,z_y|\,z_x - \gamma\,\dot{u}_y\,z_x\,z_y \\ \dot{z}_y &= A\,\dot{u}_y - \beta\,|\dot{u}_y\,z_y|\,z_y - \gamma\,\dot{u}_y\,z_y^2 - \beta\,|\dot{u}_x\,z_x|\,z_y - \gamma\,\dot{u}_x\,z_x\,z_y\ , \end{aligned} \tag{2.12}$$

where z_x, z_y are hysteretic variables, u_x, u_y are displacements and A, β, γ are material constants.

The total restoring forces can be expressed in the matrix form as

$$[Q] = \alpha\,[K]\,[u] + (1-\alpha)\,[K]\,[z]\ , \tag{2.13}$$

where $[K]$ is the initial stiffness matrix and $[Q]$, $[u]$ and $[z]$ are vectors.

If $A = 1$ and $\beta = \gamma$ is assumed, the following equation can be derived (cf. appendix B.3):

$$\beta = \frac{1}{2}\,(\frac{1}{z_L})^2 \ , \tag{2.14}$$

where z_L is the plastic limit of the deformation.

In [88] the hysteretic constitutive equation for the three-dimensional continua in tensorial level is suggested by Simulescu as

$$\sigma_{ij} = \lambda \left[\, \alpha^* \, \epsilon_{kk} + (1 - \alpha^*)\, \xi_{kk} \right] \delta_{ij} + 2\,\mu \left[\, \alpha_{ij}\, \epsilon_{ij} + (1 - \alpha_{ij})\, \xi_{ij} \right] \ , \tag{2.15}$$

where λ and μ are the Lamé's constants, δ_{ij} is the Kronecker's delta and the term α_{ij} is a symmetric tensor with the definition of $\alpha^* = \alpha_{11} = \alpha_{22} = \alpha_{33}$. The Einstein summation convention is also applied in this equation. The hysteretic variable ξ_{ij} in this equation is then proposed as

$$\dot{\xi}_{ij} = -b_{ij}\,\dot{\epsilon}_{ij} - c_{ij}|\dot{\epsilon}_{ij}|\,|\xi_{ij}|^{n_{ij}-1}\,\xi_{ij} - d_{ij}\,\dot{\epsilon}_{ij}\,|\xi_{ij}|^{n_{ij}} \ , \tag{2.16}$$

where b_{ij}, c_{ij}, d_{ij} and $n_{ij} \geq 1$ are material constants.

Under the plane stress condition ($\sigma_{33} = 0$) the equation (2.15) can be rewritten as

$$\begin{aligned} \sigma_1 &= \alpha\,\frac{E}{1-\nu^2}\,(\epsilon_1 + \nu\,\epsilon_2) + (1-\alpha)\,\frac{E}{1-\nu^2}\,(\xi_1 + \nu\,\xi_2) \\ \sigma_2 &= \alpha\,\frac{E}{1-\nu^2}\,(\nu\,\epsilon_1 + \epsilon_2) + (1-\alpha)\,\frac{E}{1-\nu^2}\,(\nu\,\xi_1 + \xi_2) \ , \end{aligned} \tag{2.17}$$

As the aim of this work is not to propose a new hysteretic material model, but to develop a reduction strategy of modal dimensions for the large scale FEM system, therefore a simplified two-dimensional hysteretic equations in the principal stress plane, which bases on the tensorial formulation (2.16) and the biaxial model (2.12), is suggested by the author for the further applications in the present work as

$$\begin{aligned} \dot{\xi}_1 &= \dot{\epsilon}_1 - \beta\,|\dot{\epsilon}_1\,\xi_1|\,\xi_1 - \beta\,\dot{\epsilon}_1\,\xi_1^2 - \beta\,|\dot{\epsilon}_2\,\xi_2|\,\xi_1 - \beta\,\dot{\epsilon}_2\,\xi_1\,\xi_2 \\ \dot{\xi}_2 &= \dot{\epsilon}_2 - \beta\,|\dot{\epsilon}_2\,\xi_2|\,\xi_2 - \beta\,\dot{\epsilon}_2\,\xi_2^2 - \beta\,|\dot{\epsilon}_1\,\xi_1|\,\xi_2 - \beta\,\dot{\epsilon}_1\,\xi_1\,\xi_2 \ , \end{aligned} \tag{2.18}$$

with the assumptions of the material constants in equation (2.12) that $A = 1$ and $\beta = \gamma$. Consequently through equation (2.14) is

$$\beta = \frac{1}{2}\,(\frac{1}{\epsilon_Y})^2 = \frac{1}{2}\,(\frac{E}{\sigma_Y})^2 \ , \tag{2.19}$$

in which the yield strain $\epsilon_Y = \sigma_Y / E$ takes the place of the yield limit z_L.

The equation (2.18) together with the equation (2.17) is named as the *two-dimensional hysteretic model in principal stress plane – 2D-HMiPSP.*

2.3 Comparison between Classical Theory and 2D-HMiPSP

In this section two essential perspectives, namely the yield criterion and the hardening behavior, will be used to give comparisons between the classical plasticity theory and the 2D-HMiPSP.

First the graphical representation of the yield boundary of the two-dimensional hysteretic model will be performed (which is absent in the most literature), to have a comparison with the von Mises's yield ellipse in the principal stress plane. Then the hardening characteristic of the hysteretic model, i.e., the translation of the yield boundary, will be studied in comparison with the Ziegler's hardening models.

2.3.1 Yield Boundary of 2D-HMiPSP

In order to find the yield boundary of the 2D-HMiPSP set $\alpha = 0$ in equation (2.17), which gives the elastic perfectly-plastic principal stress like

$$\begin{aligned} \sigma_1 &= \frac{E}{1-\nu^2}\,(\xi_1 + \nu\,\xi_2) \\ \sigma_2 &= \frac{E}{1-\nu^2}\,(\nu\,\xi_1 + \xi_2)\ . \end{aligned} \tag{2.20}$$

Since the yield boundary can be found only the under loading state, the symbol of absolute value in equation (2.18) can be neglected. By using $\dot{\xi}_1 = 0$ and $\dot{\xi}_2 = 0$ as the yield conditions of the 2D-HMiPSP it follows

$$\frac{\dot{\epsilon}_2}{\dot{\epsilon}_1} = \frac{1 - 2\,\beta\,\xi_1^2}{2\,\beta\,\xi_1\,\xi_2} = \frac{2\,\beta\,\xi_1\,\xi_2}{1 - 2\,\beta\,\xi_2^2} \tag{2.21a}$$

and leads to the yield criterion of 2D-HMiPSP

$$(1 - 2\,\beta\,\xi_1^2)\,(1 - 2\,\beta\,\xi_2^2) - (2\,\beta\,\xi_1\,\xi_2)^2 = 0\ . \tag{2.21b}$$

To simulate the quasi-static non-cyclic loading, the controlled principal strain rate is defined as

$$\dot{\epsilon}_1 = C\cos\theta \quad \text{and} \quad \dot{\epsilon}_2 = C\sin\theta\ , \tag{2.22}$$

in which the amplitude C is a small constant and denotes the monotonic increase of strain. The ratio of $\dot{\epsilon}_1$ to $\dot{\epsilon}_2$ is then given by θ. In the procedure of determining the yield stress couple the strains will keep increasing until the fulfillment of the yield criterion (2.21b) is made sure. In such procedure is θ a constant and a particular couple of yield stress can be determined. As θ changes from 0 to 2π the corresponding yield boundary can be found, and it is shown in Fig. 2.2 for various Poisson's ratio ν in comparison with the von Mises's yield ellipse.

It can be seen in this figure that the yield boundary of the two-dimensional hysteretic model (2.18) extends in the 45^o direction as the Poisson's ratio ν increases. With $\nu = 0.3$, which is about the Poisson's ratio of steel, the yield locus is quite similar to the von Mises yield ellipse.

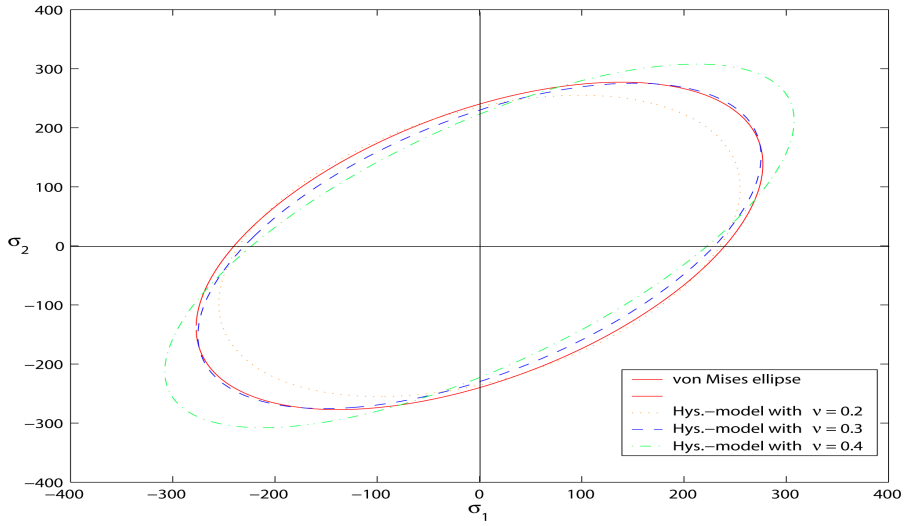

Figure 2.2: von Mises Ellipse and Yield Boundary of 2D-HMiPSP

2.3.2 Hardening Characteristics

With this point of view, the main difference between the hysteretic model and the classical plasticity theory is that the former has no explicit definition of the onset of yielding, because of its smooth transition from elastic to plastic region. Therefore, the yielding onset of the 2D-HMiPSP is defined in this work at the points, which are the affine positions of the corners in the corresponding bilinear models. For example, using (2.22) with monotonic increasing C and $\theta = 30^o$, Fig. 2.3 shows the yielding onset points A and B for σ_1 and σ_2 of the 2D-HMiPSP respectively. The points A and B are defined on a same vertical line, because the hysteretic model is symmetric with respect to ξ_1 and ξ_2.

The next to establish is a mathematical criterion, which should represent the yielding onset defined above. Suppose that points A and B in Fig. 2.3 have the values $\dot{\xi}_1 = C_1\,\dot{\epsilon}_1$ and $\dot{\xi}_2 = C_2\,\dot{\epsilon}_2$, in which C_1 and C_2 are nonzero constants, and setting them in the equation (2.18), so that similar to the equation (2.21b) the following expression can be derived

$$(1 - 2\,\beta\,\xi_1^2)\,(1 - 2\,\beta\,\xi_2^2) - (2\,\beta\,\xi_1\,\xi_2)^2 = C_2\,(1 - 2\,\beta\,\xi_1^2) + C_1\,(1 - 2\,\beta\,\xi_2^2) \neq 0\ . \quad (2.23)$$

Using the same procedure of determining the yield boundary in section 2.3.1, this critical value of (2.23) at the yielding onset point, which is called the yielding determinant of the 2D-HMiPSP, can be evaluated through interpolation under variant θ values.

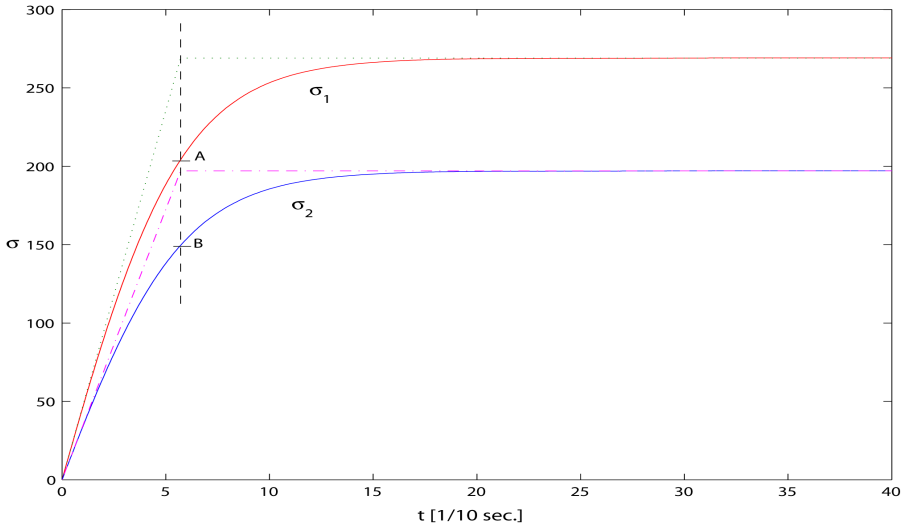

Figure 2.3: Definition of Yielding Onset Point of 2D-HMiPSP with $\theta = 30^o$

Fig. 2.4 shows the yielding determinants depending on the θ values. It can be seen that this figure is symmetric to the axes of $\theta = 45^o, 135^o, 225^o$ and 315^o. These values spread in a quite small range between 0.42 to 0.43 and are numerically very sensitive, therefore the mean with 0.424 is used as the yielding onset value for the following examples in this section. Together with the equation (2.21b) it can be concluded that the value of the yielding determinate (VYD) has the following indication

$$\text{VYD} = (1-2\,\beta\,\xi_1^2)\,(1-2\,\beta\,\xi_2^2)-(2\,\beta\,\xi_1\,\xi_2)^2 = \begin{cases} 0\ , & \text{limit values of yielding} \\ 0.424\ , & \text{onset of yielding} \end{cases} \tag{2.24}$$

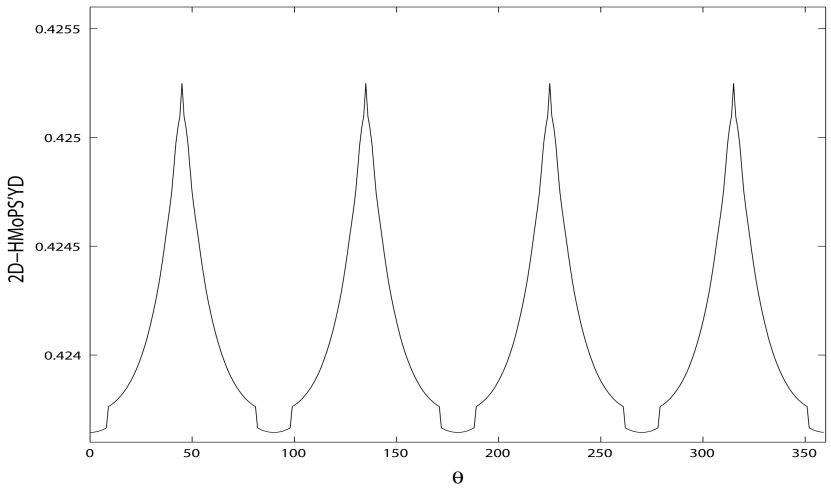

Figure 2.4: Yielding Determinants of 2D-HMiPSP

With these preparations the comparison of hardening characteristics between the classical theory and the hysteretic model will be first performed on a simple example. In

this example the cyclic input is defined through the given strain rate, in which $\dot{\epsilon}_1$ is a sine-like function of time and $\dot{\epsilon}_2 = -\nu\,\dot{\epsilon}_1$. The factor of post-yielding stiffness is set as $\alpha = 0.05$. For the numerical evaluation with the classical theory the equations in section 2.1.2 are used. For the hysteretic model the rate of the hardening parameter $\dot{\alpha}^h$ and of the plastic strain $\dot{\epsilon}^p$, which are not explicitly indicated in the literature, are defined here as

$$\begin{aligned} \dot{\alpha}_1^h &= H(0.424 - \mathrm{VYD})\, H(\dot{\epsilon}_1\,\xi_1)\, H(\dot{\epsilon}_2\,\xi_2)\, \alpha\, \tfrac{E}{1-\nu^2}\,(\dot{\epsilon}_1 + \nu\,\dot{\epsilon}_2) \\ \dot{\alpha}_2^h &= H(0.424 - \mathrm{VYD})\, H(\dot{\epsilon}_1\,\xi_1)\, H(\dot{\epsilon}_2\,\xi_2)\, \alpha\, \tfrac{E}{1-\nu^2}\,(\nu\,\dot{\epsilon}_1 + \dot{\epsilon}_2) \end{aligned} \tag{2.25a}$$

and

$$\begin{aligned} \dot{\epsilon}_1^p &= \dot{\epsilon}_1 - (\dot{\sigma}_1/E - \nu\,\dot{\sigma}_2/E) \\ \dot{\epsilon}_2^p &= \dot{\epsilon}_2 - (-\nu\,\dot{\sigma}_1/E + \dot{\sigma}_2/E) \end{aligned} \tag{2.25b}$$

In Fig. 2.5 the results of stress is shown at the top, results of the hardening parameter is given in the middle and results of the plastic strain locates at the bottom.

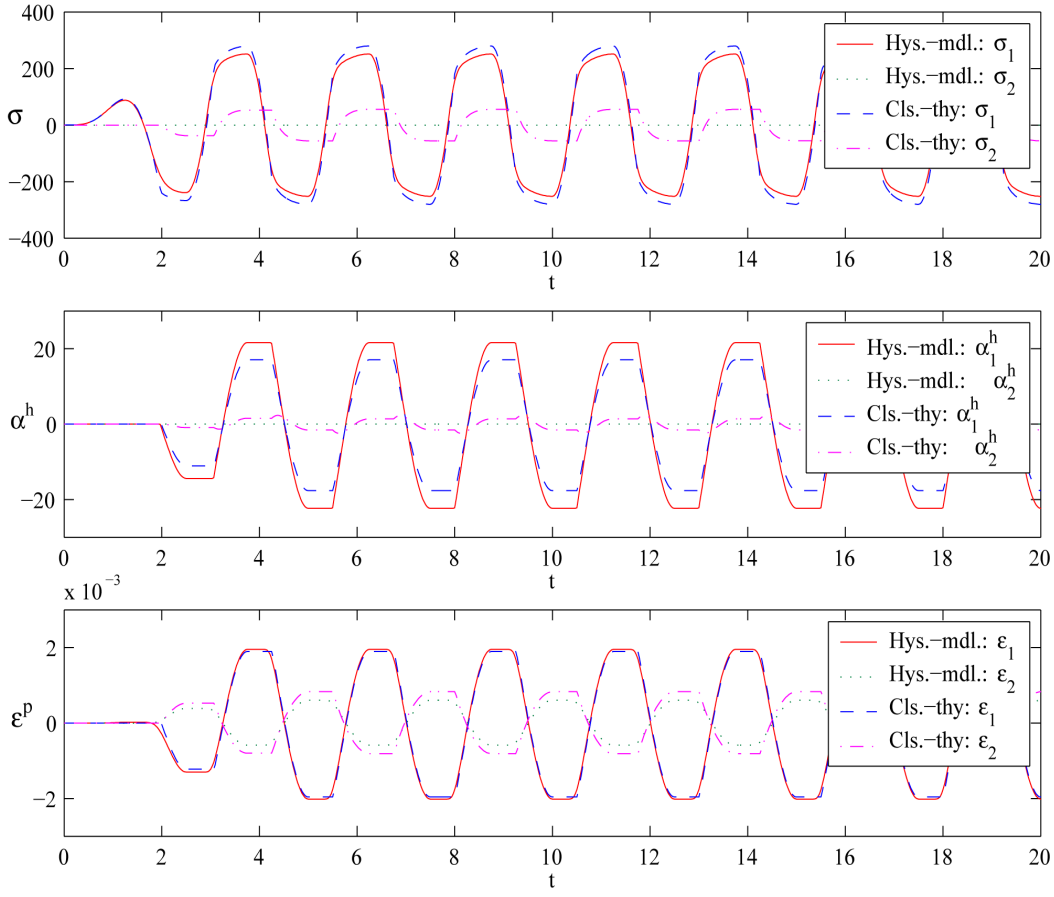

Figure 2.5: Comparison of Classical Theory to Hysteretic Model under Cyclic Loading with $\epsilon_2 = -\nu\,\epsilon_1$ and $\nu = 0.3$

In this case ($\epsilon_2 = -\nu\,\epsilon_1$) it is to expect that σ_2 should be nonzero under the plastic deformation. Because under the plastic deformation is $\epsilon_2 = -\nu\,\epsilon_1^e - \frac{1}{2}\,\epsilon_1^p \neq -\nu\,\epsilon_1$,

and since ϵ_2 is given/constrained, the resistance stress will arise. But this effect is not observed in the hysteretic model, as its σ_2 is always equal to zero. This deficiency comes from that the Poisson's ratio ν in the equation (2.17) is being unchanged during the elasto-plastic deformations, which means the hysteretic model doesn't obey the associated flow rule. Besides, because the bilinear and the smooth transition models have very different characters, the results of σ_1 and α^h between these two models are not identical. With further investigations σ_1 of the hysteretic model in this example will be closer to the results of the classical theory as the power number n in the hysteretic model increases. Generally the accuracy of the hysteretic model is still acceptable, since it follows different considerations.

In the next example the strain rate $\dot{\epsilon}_1$ and $\dot{\epsilon}_2$ are both given as sine-like functions of time with arbitrarily selected amplitudes and frequencies respectively. The results of the stress, the hardening parameter and the plastic strain are represented in Fig. 2.6 (a), (b) and (c). It is explained in appendix A.3 that the classical theory can not predict the elasto-plastic behaviors well under cyclic loadings. Therefore the frequencies of the designated strain rate should keep small, otherwise the divergence between the classical and hysteretic model is to expect.

It can be read directly in Fig. 2.6 (b) that the hardening behaviors of these two models are quite different. The first reason is that the yielding ellipse will not move until its boundary is touched according to the classical theory, while by the hysteretic model the yielding boundary starts to move at the begin of the smooth elastic-plastic transition (s. Fig. 2.3). The second reason is that the translation direction of the yield boundary in the hysteretic model is a function of $\dot{\boldsymbol{\sigma}}$ according to the equation (2.25a), while it is a function of $\boldsymbol{\sigma} - \boldsymbol{\alpha}^h$ in the classical theory according to the equation (2.6). Nevertheless, the resultant total stresses and the plastic strains of the hysteretic model are quite similar to those of the classical theory. Besides, the hysteretic model has also following advantages:

- adaptability for various materials
- prediction of the cyclic loading effects
- mathematical compatibility, which makes it easy to be placed in the differential equations and reduces the numerical computing efforts.

Therefore this hysteretic model is convincing enough for the needs of this work.

It is to remind that in this chapter only a simply modified, but not a new hysteretic model is suggested for this work, since this model is merely requested to represent the yielding characters of the plate reasonably, so that the nonlinear dynamic equations for developing the PSF can be established. This hysteretic model can be replaced by a better one, if available, at any time.

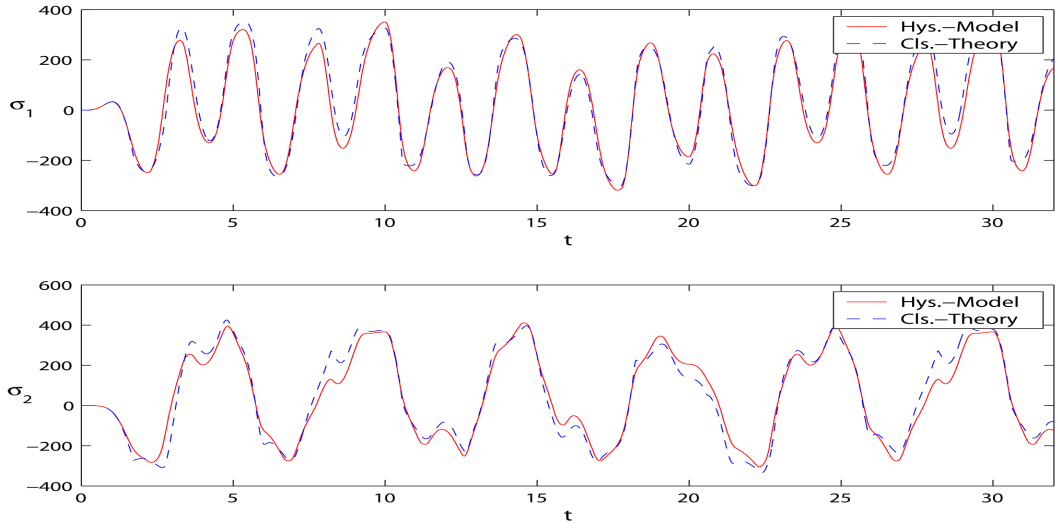

(a) Stress

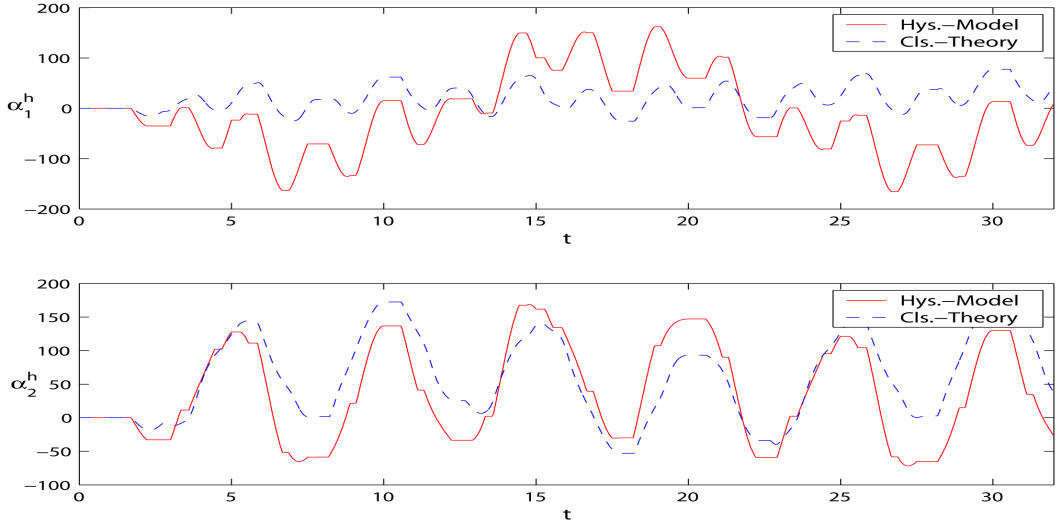

(b) Hardening Parameter

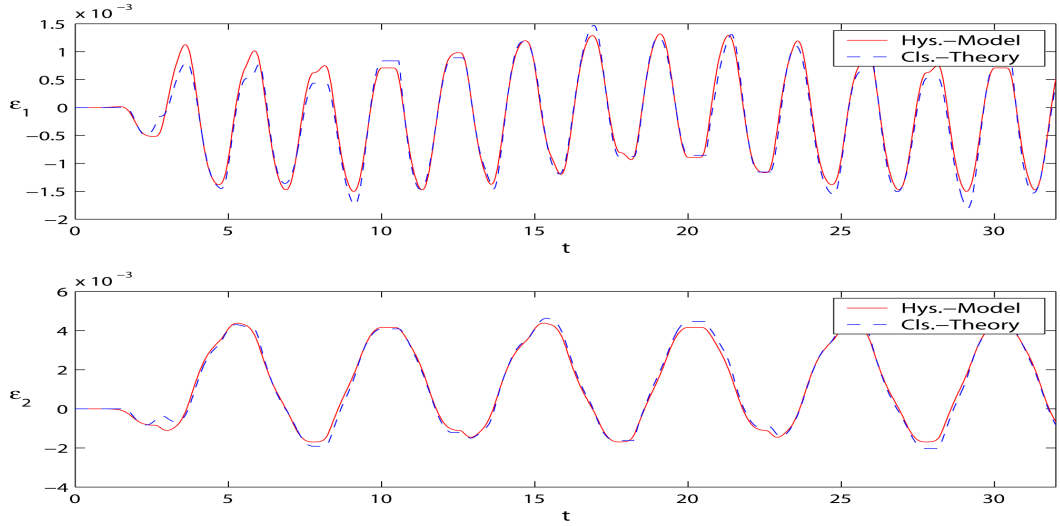

(c) Plastic Strain

Figure 2.6: Comparison of Classical Theory to Hysteretic Model under Arbitrary Cyclic Loading

Chapter 3

Mathematical Model of Plates with Hysteresis

3.1 Kirchhoff Plate Theory

3.1.1 General Assumptions and Sign Conventions

The structure concerned in the present work is the *Stiff Plate*, which is a thin plate with flexural rigidity that carry loads two-dimensionally by bending moments, torsional moments and transverse shears. In the following 'plate' is understood to mean the stiff plate, unless otherwise specified. Since this work extends the idea of the *plastic shape function*, which will be explained in detail in Chapter 4, of the Bernoulli beam in [33] and [42], the Kirchhoff plate theory is chosen to serve as the contrast. The main assumptions of the Kirchhoff plate theory are [93]:

1. The thickness of the plate is small compared to its other dimensions, which are at least ten times larger than the its thickness.

2. The deflections are small compared to the plate thickness. The maximum deflection is about 1/10 to 1/5 of the thickness.

3. Straight lines perpendicular to the middle surface before deformation remain straight after deformation.

4. transverse normals remain perpendicular to the middle surface after deformation. (Together with point 3. the deformations due to transverse shear will be neglected.)

5. The deflection of the plate is produced by the displacement of the middle surface in the normal direction to its initial plane.

6. The stresses normal to the middle surface are negligible ($\sigma_z = 0$) and the transverse normals do not experience elongation ($\epsilon_z = 0$).

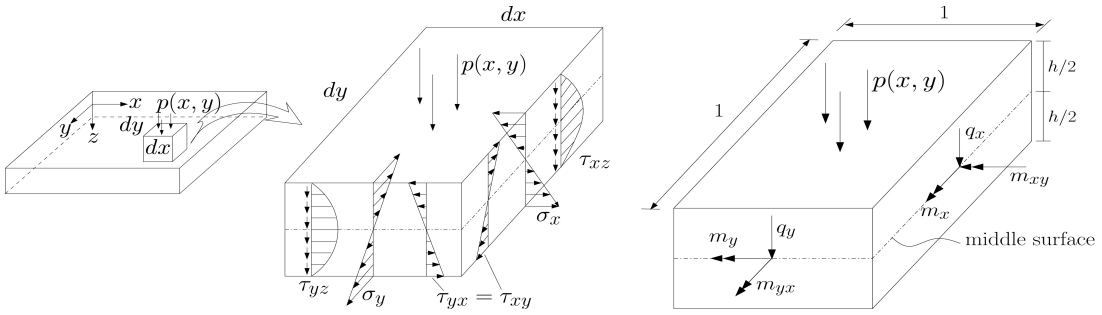

(a) Stress (b) Stress Resultants/unit length

Figure 3.1: Positive Definition of Stresses and Stress Resultants

The difference between the Kirchhoff's and the Reissner-Mindlin's theory is that the latter considers the transverse shear deformation, i.e. without the assumption 4. listed above. The primarily linear elastic assumed material behavior in the plate theory will be modified through the hysteretic model.

In the Cartesian coordinate system the positive stress resultants are so defined that on the positive cutting surface the stresses of fibers, which have positive z coordinate, point toward the positive coordinate directions. According to this the stresses and the stress resultants per unit length are plotted in Fig. 3.1 (a) and (b) respectively, in which σ_x and σ_y are the normal stresses due to bending moments m_x and m_y; τ_{xy} and τ_{yx} are the shear stresses due to torsional moments m_{xy} and m_{yx}; τ_{xz} and τ_{yz} are the shear stresses due to transverse shear forces q_x and q_y.

3.1.2 Static Equilibrium and Kinematics of Plate Elements

To establish the basic differential equation of the plate element, the force equilibriums will be used. By considering the equilibrium of shear forces $\sum V = 0$ (s. Fig. 3.2 (a)) and the equilibrium of moments $\sum M_x = 0$, $\sum M_y = 0$ (s. Fig. 3.2 (b)) at the infinitesimal element the differential equation of plate can be derived as [93]

$$\frac{\partial^2 m_x}{\partial x^2} + \frac{\partial^2 (m_{xy} + m_{yx})}{\partial x \, \partial y} + \frac{\partial^2 m_y}{\partial y^2} = p\,(x, y)\ . \tag{3.1}$$

The deformations of plates can be described through the deflection $w(x, y)$ and the rotation angles $\psi_x(x, y)$ and $\psi_y(x, y)$. The deflection is positive defined in the positive z-direction and the positive rotation angles are counterclockwise defined (s. Fig. 3.3).

According to the shear-rigid assumption are $\gamma_{xz} = 0$ and $\gamma_{yz} = 0$, therefore the rotation angles of the plate cross section are functions of the deflection, which are

$$\psi_x = -\frac{\partial w}{\partial x} \quad \text{and} \quad \psi_y = -\frac{\partial w}{\partial y}\ , \tag{3.2}$$

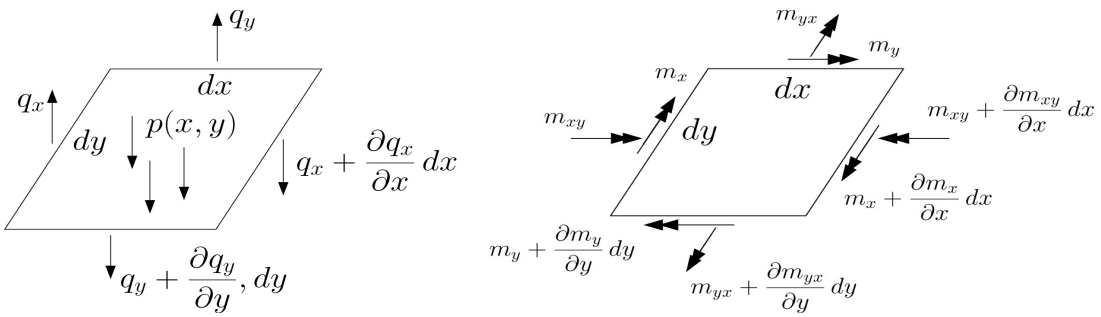

(a) shear forces equilibrium (b) moments equilibrium

Figure 3.2: Equilibrium of Infinitesimal Plate Element

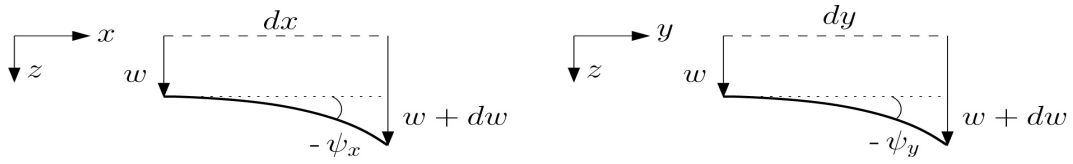

Figure 3.3: Positive Definitions of Deflection and Rotation Angles

so that the only degree of freedom of Kirchhoff's plate theory is the deflection $w(x, y)$.

The curvatures are defined as

$$\kappa_x = \frac{\partial^2 w}{\partial x^2} = -\frac{\partial \psi_x}{\partial x}\,, \quad \kappa_y = \frac{\partial^2 w}{\partial y^2} = -\frac{\partial \psi_y}{\partial y}\,, \quad \text{and} \quad \kappa_{xy} = \frac{\partial^2 w}{\partial x\,\partial y} = -\frac{\partial \psi_x}{\partial y} = -\frac{\partial \psi_y}{\partial x}\,. \tag{3.3}$$

Similar to the Bernoulli beam theory the elastic moment-curvature relations of plate can be expressed as

$$\begin{aligned} m_x &= -\frac{E\,h^3}{12\,(1-\nu^2)}\,(\kappa_x + \nu\,\kappa_y) \\ m_y &= -\frac{E\,h^3}{12\,(1-\nu^2)}\,(\nu\,\kappa_x + \kappa_y)\,, \end{aligned} \tag{3.4a}$$

where h is the thickness of plate. Due to the equilibrium the adjacent twisting moments across the corner of the infinitesimal element are of the same magnitude ($m_{xy} = m_{yx}$). The elastic twisting moment can be formulated as

$$m_{xy} = -\frac{E\,h^3}{12\,(1-\nu^2)}\,(1-\nu)\,\kappa_{xy} \tag{3.4b}$$

Putting (3.4) in (3.1), the differential equation of plate element can be rewritten as

$$\frac{\partial^4 w}{\partial x^4} + 2\,\frac{\partial^4 w}{\partial x^2\,\partial y^2} + \frac{\partial^4 w}{\partial y^4} = p(x,y)/K_b\,, \tag{3.5}$$

where $K_b = (Eh^3)/(12\,(1-\nu^2))$ is the bending stiffness of plate.

With using of the kinematic relations defined above the strains of plate can be expressed through the curvatures as

$$\begin{aligned} \epsilon_x &= \frac{\partial u(x,y,z)}{\partial x} = z\,\frac{\partial \psi_x}{\partial x} = -z\,\frac{\partial^2 w}{\partial x^2} = -z\,\kappa_x \\ \epsilon_y &= \frac{\partial v(x,y,z)}{\partial y} = z\,\frac{\partial \psi_y}{\partial y} = -z\,\frac{\partial^2 w}{\partial y^2} = -z\,\kappa_y \\ \gamma_{xy} &= \frac{\partial u}{\partial y} + \frac{\partial v}{\partial x} = z\,(\frac{\partial \psi_x}{\partial y} + \frac{\partial \psi_y}{\partial x}) = -2\,z\,\frac{\partial^2 w}{\partial x\,\partial y} = -2\,z\,\kappa_{xy}\ , \end{aligned} \tag{3.6}$$

where $u(x,y,z)$ and $v(x,y,z)$ are the elongations in x- and y-direction respectively.

3.2 Principle of Virtual Work

To establish the dynamic differential equation of the plate element, the principle of virtual work is utilized, which states

$$\delta W = \delta W_i + \delta W_e = 0\ , \tag{3.7}$$

where δW, δW_i and δW_e are the total, internal and external virtual work respectively.

Generally the external virtual work δW_e results from four external loadings, which are the body force f_B, the surface load f_S, the single load F_i and the D'ALEMBERT's inertial force f_T. And δW_e can be evaluated as [54], [7]

$$\delta W_e = \int_V \delta U^T f_B\,dV + \int_S \delta U_S^T f_S\,dS + \sum_i \delta U_i^T F_i - \int_V \delta U^T f_T\,dV\ , \tag{3.8}$$

where δU is the vector of the virtual displacements, which are small, compatible and hold the fundamental boundary conditions. The lower indexes S and i denote the virtual displacements on the surface and on the single points respectively.

By using the Kirchhoff plate theory the only degree of freedom is the deflection $w(x,y,t)$, therefore δU in the equation above can be substituted by δw. Furthermore it will be assumed that there are no body forces and no single loads, which can result in singularity on plate, so that the first and the third term on the right hand side of equation (3.8) will be eliminated.

The internal virtual work, which is always negative, is formulated as

$$\delta W_i = -\int_V \delta\boldsymbol{\epsilon}^T \boldsymbol{\sigma}\,dV\ , \tag{3.9}$$

where $\delta\boldsymbol{\epsilon}$ is the vector of the virtual strain corresponding to the virtual deflection δw.

The hysteretic material behavior can be taken into consideration, if the internal virtual work is formulated in the principal direction by using (2.17) as

$$\begin{aligned}\delta W_i =& -\int_V (\delta\epsilon_1\sigma_1 + \delta\epsilon_2\sigma_2)dV \\ =& -\alpha\int_V [\,\delta\epsilon_1\ \delta\epsilon_2]\,\frac{E}{1-\nu^2}\begin{bmatrix}1 & \nu\\ \nu & 1\end{bmatrix}\begin{bmatrix}\epsilon_1\\ \epsilon_2\end{bmatrix}dV \\ & -(1-\alpha)\int_V [\,\delta\epsilon_1\ \delta\epsilon_2]\,\frac{E}{1-\nu^2}\begin{bmatrix}1 & \nu\\ \nu & 1\end{bmatrix}\begin{bmatrix}\xi_1\\ \xi_2\end{bmatrix}dV\ ,\end{aligned} \tag{3.10}$$

where the auxiliary hysteretic equations (2.18) are required for ξ_1 and ξ_2.

It can be seen that (3.10) is not directly suitable for the general kinematic formulations of the Kirchhoff plate theory and is not convenient for applying the finite element method (FEM). Therefore (3.10) should be rewritten in the Cartesian coordinate system and the auxiliary hysteretic equations (2.18) have to be correspondingly modified. This modifications are performed in the next section.

3.2.1 Hysteretic Model of Plates in Cartesian Coordinates

According to the transformation rules of the plane stress state the principal stresses σ_1 and σ_2 can be derived from the plane stresses σ_x, σ_y and τ_{xy} as

$$\begin{aligned}\begin{bmatrix}\sigma_1\\ \sigma_2\end{bmatrix} &= \begin{bmatrix}\dfrac{1+\cos 2\theta}{2} & \dfrac{1-\cos 2\theta}{2} & \sin 2\theta\\ \dfrac{1-\cos 2\theta}{2} & \dfrac{1+\cos 2\theta}{2} & -\sin 2\theta\end{bmatrix}\begin{bmatrix}\sigma_x\\ \sigma_y\\ \tau_{xy}\end{bmatrix} \\ &= T_\theta\begin{bmatrix}\sigma_x\\ \sigma_y\\ \tau_{xy}\end{bmatrix}\ , \qquad \text{with} \quad \tan 2\theta = \frac{\tau_{xy}}{(\sigma_x-\sigma_y)/2}\ .\end{aligned} \tag{3.11a}$$

The principal strains ϵ_1 and ϵ_2 can be obtained from the plane strains ϵ_x, ϵ_y and γ_{xy} as

$$\begin{aligned}\begin{bmatrix}\epsilon_1\\ \epsilon_2\end{bmatrix} &= \begin{bmatrix}\dfrac{1+\cos 2\tilde{\theta}}{2} & \dfrac{1-\cos 2\tilde{\theta}}{2} & \dfrac{\sin 2\tilde{\theta}}{2}\\ \dfrac{1-\cos 2\tilde{\theta}}{2} & \dfrac{1+\cos 2\tilde{\theta}}{2} & \dfrac{-\sin 2\tilde{\theta}}{2}\end{bmatrix}\begin{bmatrix}\epsilon_x\\ \epsilon_y\\ \gamma_{xy}\end{bmatrix} \\ &= T_{\tilde{\theta}}\begin{bmatrix}\epsilon_x\\ \epsilon_y\\ \gamma_{xy}\end{bmatrix}\ , \qquad \text{with} \quad \tan 2\tilde{\theta} = \frac{\gamma_{xy}}{\epsilon_x-\epsilon_y}\ .\end{aligned} \tag{3.11b}$$

Considering a plate element, if the material behaves purely elastic, the principal stress angle θ will coincide with the principal strain angle $\tilde{\theta}$. But according to the loading history dependency of the plastic deformations these two angles are generally different to each other under plastic material behaviors. These angles overlap only exceptionally,

i.e., as the stresses of the plate element are proportional to each other all the time, so that the principal stress angle keeps a constant. Consequently there is no shear strain on this principal direction during the whole loading history. But with the studies made in chapter 2. it can be concluded that the hysteretic equations (2.17) are still suitable to describe the plastic constructive relations between the principal stresses and strains directly, even when $\theta \neq \tilde{\theta}$ under general loadings.

According to (2.15), the constitutive equations of plane stresses in the Cartesian coordinate system can be formulated as

$$\begin{aligned}
\sigma_x &= \alpha \frac{E}{1-\nu^2}(\epsilon_x + \nu\,\epsilon_y) + (1-\alpha)\frac{E}{1-\nu^2}(\xi_x + \nu\,\xi_y) \\
\sigma_y &= \alpha \frac{E}{1-\nu^2}(\nu\,\epsilon_x + \epsilon_y) + (1-\alpha)\frac{E}{1-\nu^2}(\nu\,\xi_x + \xi_y) \\
\tau_{xy} &= \alpha \frac{E}{2(1+\nu)}\,\gamma_{xy} + (1-\alpha)\,\frac{E}{2(1+\nu)}\,\xi_{xy}\ .
\end{aligned} \tag{3.12}$$

Instead of directly applying (2.16), which is too general to use, the still unknown differential equations of the hysteretic variables ξ_x, ξ_y and ξ_{xy} above will be derived from (2.18).

In order to establish the hysteretic model of the Cartesian coordinate system, an inverse transformation of strains from the principal space to the Cartesian coordinate system is needed, which is

$$\begin{bmatrix} \epsilon_x \\ \epsilon_y \\ \gamma_{xy} \end{bmatrix} = \begin{bmatrix} \dfrac{1+\cos 2\tilde{\theta}}{2} & \dfrac{1-\cos 2\tilde{\theta}}{2} \\ \dfrac{1-\cos 2\tilde{\theta}}{2} & \dfrac{1+\cos 2\tilde{\theta}}{2} \\ \sin 2\tilde{\theta} & -\sin 2\tilde{\theta} \end{bmatrix} \begin{bmatrix} \epsilon_1 \\ \epsilon_2 \end{bmatrix} = T'_{\tilde{\theta}} \begin{bmatrix} \epsilon_1 \\ \epsilon_2 \end{bmatrix}\ . \tag{3.13}$$

It is to note that for (3.13) the angle $\tilde{\theta}$ has to be known, while in (3.11b) the information about $\tilde{\theta}$ is already included in the vector $[\,\epsilon_x\ \epsilon_y\ \gamma_{xy}\,]^T$. In the practices the inverse transformation matrix $T'_{\tilde{\theta}}$ can always be determined, since the strains ϵ_x, ϵ_y and γ_{xy} are always calculated first. Differentiating (3.13) with respect to time its rate form can be expressed as

$$\begin{bmatrix} \dot{\epsilon}_x \\ \dot{\epsilon}_y \\ \dot{\gamma}_{xy} \end{bmatrix} = T'_{\tilde{\theta}} \begin{bmatrix} \dot{\epsilon}_1 \\ \dot{\epsilon}_2 \end{bmatrix} + \dot{T}'_{\tilde{\theta}} \begin{bmatrix} \epsilon_1 \\ \epsilon_2 \end{bmatrix}\ . \tag{3.14}$$

Multiplying (2.18) by $T'_{\tilde{\theta}}$ on both sides and rewriting in vector form it follows

$$T'_{\tilde{\theta}} \begin{bmatrix} \dot{\xi}_1 \\ \dot{\xi}_2 \end{bmatrix} = T'_{\tilde{\theta}} \begin{bmatrix} \dot{\epsilon}_1 \\ \dot{\epsilon}_2 \end{bmatrix} - \beta(|\dot{\epsilon}_1\xi_1| + |\dot{\epsilon}_2\xi_2|)\, T'_{\tilde{\theta}} \begin{bmatrix} \xi_1 \\ \xi_2 \end{bmatrix} - \beta(\dot{\epsilon}_1\xi_1 + \dot{\epsilon}_2\xi_2)\, T'_{\tilde{\theta}} \begin{bmatrix} \xi_1 \\ \xi_2 \end{bmatrix}\ ,$$

then applying (3.14) in this equation, so that

$$T'_{\tilde{\theta}}\begin{bmatrix}\dot{\xi}_1\\ \dot{\xi}_2\end{bmatrix} = T'_{\tilde{\theta}}\begin{bmatrix}\dot{\epsilon}_1\\ \dot{\epsilon}_2\end{bmatrix} + \dot{T}'_{\tilde{\theta}}\begin{bmatrix}\epsilon_1\\ \epsilon_2\end{bmatrix} - \beta(|\dot{\epsilon}_1\xi_1| + |\dot{\epsilon}_2\xi_2|)T'_{\tilde{\theta}}\begin{bmatrix}\xi_1\\ \xi_2\end{bmatrix} - \beta(\dot{\epsilon}_1\xi_1 + \dot{\epsilon}_2\xi_2)T'_{\tilde{\theta}}\begin{bmatrix}\xi_1\\ \xi_2\end{bmatrix} - \dot{T}'_{\tilde{\theta}}\begin{bmatrix}\epsilon_1\\ \epsilon_2\end{bmatrix}$$
$$= \begin{bmatrix}\dot{\epsilon}_x\\ \dot{\epsilon}_y\\ \dot{\gamma}_{xy}\end{bmatrix} - \beta(|\dot{\epsilon}_1\xi_1| + |\dot{\epsilon}_2\xi_2|)T'_{\tilde{\theta}}\begin{bmatrix}\xi_1\\ \xi_2\end{bmatrix} - \beta(\dot{\epsilon}_1\xi_1 + \dot{\epsilon}_2\xi_2)T'_{\tilde{\theta}}\begin{bmatrix}\xi_1\\ \xi_2\end{bmatrix} - \dot{T}'_{\tilde{\theta}}\begin{bmatrix}\epsilon_1\\ \epsilon_2\end{bmatrix} \ . \tag{3.15}$$

Because ξ_1 and ξ_2, which have no physical meanings, are auxiliary hysteretic variables of ϵ_1 and ϵ_2, and generally is $\tilde{\theta} \neq \theta$, therefore the values of ξ_1 and ξ_2 should also be transformed with the matrix $T'_{\tilde{\theta}}$ into the Cartesian coordinate. As a result the transformation $T'_{\tilde{\theta}}\ [\xi_1\ \xi_2]^T$ can be seen in (3.15). In order to derive the unknown hysteretic equations in the Cartesian coordinate system, the new hysteretic variables ξ_x, ξ_y and ξ_{xy} are defined according to this transformation as

$$\begin{bmatrix}\xi_x\\ \xi_y\\ \xi_{xy}\end{bmatrix} = T'_{\tilde{\theta}}\begin{bmatrix}\xi_1\\ \xi_2\end{bmatrix} \ , \tag{3.16a}$$

which leads to

$$T'_{\tilde{\theta}}\begin{bmatrix}\dot{\xi}_1\\ \dot{\xi}_2\end{bmatrix} = \begin{bmatrix}\dot{\xi}_x\\ \dot{\xi}_y\\ \dot{\xi}_{xy}\end{bmatrix} - \dot{T}'_{\tilde{\theta}}\begin{bmatrix}\xi_1\\ \xi_2\end{bmatrix} \ , \tag{3.16b}$$

where

$$\dot{T}'_{\tilde{\theta}} = 2\,\dot{\tilde{\theta}}\begin{bmatrix}\frac{-\sin 2\tilde{\theta}}{2} & \frac{\sin 2\tilde{\theta}}{2}\\ \frac{\sin 2\tilde{\theta}}{2} & \frac{-\sin 2\tilde{\theta}}{2}\\ \cos 2\tilde{\theta} & -\cos 2\tilde{\theta}\end{bmatrix} \tag{3.17a}$$

with

$$2\,\dot{\tilde{\theta}} = \frac{d\ \arctan\left(\gamma_{xy}/\epsilon_x - \epsilon_y\right)}{dt} = \frac{\dot{\gamma}_{xy}(\epsilon_x - \epsilon_y) - (\dot{\epsilon}_x - \dot{\epsilon}_y)\gamma_{xy}}{(\epsilon_x - \epsilon_y)^2 + \gamma_{xy}^2} \ . \tag{3.17b}$$

Introducing then this definition in (3.15), the hysteretic equations in the Cartesian coordinate system can be derived as

$$\begin{bmatrix}\dot{\xi}_x\\ \dot{\xi}_y\\ \dot{\xi}_{xy}\end{bmatrix} = \begin{bmatrix}\dot{\epsilon}_x\\ \dot{\epsilon}_y\\ \dot{\gamma}_{xy}\end{bmatrix} - \beta(|\dot{\epsilon}_1\xi_1| + |\dot{\epsilon}_2\xi_2|)\begin{bmatrix}\xi_x\\ \xi_y\\ \xi_{xy}\end{bmatrix} - \beta(\dot{\epsilon}_1\xi_1 + \dot{\epsilon}_2\xi_2)\begin{bmatrix}\xi_x\\ \xi_y\\ \xi_{xy}\end{bmatrix} - \dot{T}'_{\tilde{\theta}}\begin{bmatrix}\epsilon_1 - \xi_1\\ \epsilon_2 - \xi_2\end{bmatrix} \ . \tag{3.18}$$

In (3.18) $\dot{\epsilon}_1$ and $\dot{\epsilon}_2$ can be calculated through the first derivative of (3.11b) as

$$\begin{aligned}
\begin{bmatrix} \dot{\epsilon}_1 \\ \dot{\epsilon}_2 \end{bmatrix} &= T_{\tilde{\theta}} \begin{bmatrix} \dot{\epsilon}_x \\ \dot{\epsilon}_y \\ \dot{\gamma}_{xy} \end{bmatrix} + \dot{T}_{\tilde{\theta}} \begin{bmatrix} \epsilon_x \\ \epsilon_y \\ \gamma_{xy} \end{bmatrix} \\
&= T_{\tilde{\theta}} \begin{bmatrix} \dot{\epsilon}_x \\ \dot{\epsilon}_y \\ \dot{\gamma}_{xy} \end{bmatrix} + 2\,\dot{\tilde{\theta}} \begin{bmatrix} -\dfrac{\sin 2\tilde{\theta}}{2} & \dfrac{\sin 2\tilde{\theta}}{2} & \dfrac{\cos 2\tilde{\theta}}{2} \\ \dfrac{\sin 2\tilde{\theta}}{2} & -\dfrac{\sin 2\tilde{\theta}}{2} & -\dfrac{\cos 2\tilde{\theta}}{2} \end{bmatrix} \begin{bmatrix} \epsilon_x \\ \epsilon_y \\ \gamma_{xy} \end{bmatrix} \\
&= T_{\tilde{\theta}} \begin{bmatrix} \dot{\epsilon}_x \\ \dot{\epsilon}_y \\ \dot{\gamma}_{xy} \end{bmatrix} + 2\,\dot{\tilde{\theta}} \begin{bmatrix} \gamma_{12} \\ -\gamma_{12} \end{bmatrix} = T_{\tilde{\theta}} \begin{bmatrix} \dot{\epsilon}_x \\ \dot{\epsilon}_y \\ \dot{\gamma}_{xy} \end{bmatrix} + 2\,\dot{\tilde{\theta}} \begin{bmatrix} 0 \\ 0 \end{bmatrix} \\
&= T_{\tilde{\theta}} \begin{bmatrix} \dot{\epsilon}_x \\ \dot{\epsilon}_y \\ \dot{\gamma}_{xy} \end{bmatrix} .
\end{aligned} \tag{3.19}$$

In comparison with (3.14), the reason for the absence of the term $\dot{T}_{\tilde{\theta}}\,[\,\epsilon_x\ \epsilon_y\ \gamma_{xy}\,]^T$ in (3.19) is that the vector $[\,\epsilon_x\ \epsilon_y\ \gamma_{xy}\,]^T$ includes already the information about the principal strain angle $\tilde{\theta}$, whereas the vector $[\,\epsilon_1\ \epsilon_2\,]^T$ in (3.14) does not.

According to the definition (3.16a) the ξ_1 and ξ_2 of (3.18) can be determined as

$$\begin{bmatrix} \xi_1 \\ \xi_2 \end{bmatrix} = T_{\tilde{\theta}} \begin{bmatrix} \xi_x \\ \xi_y \\ \xi_{xy} \end{bmatrix} . \tag{3.20}$$

To verify the validity of (3.18), a numerical example with predefined plane strain rates $\dot{\epsilon}_x$, $\dot{\epsilon}_y$ and $\dot{\gamma}_{xy}$, which are sine-like functions with arbitrary amplitudes and frequencies for each, is performed. In this example two independent calculation procedures are done. The first one determines the plane stresses σ_x, σ_y and τ_{xy} through (3.12) with (3.18), (3.19) and (3.20) directly from the given strain rates $\dot{\epsilon}_x$, $\dot{\epsilon}_y$ and $\dot{\gamma}_{xy}$. Then the corresponding principal stresses σ_1 and σ_2 will be calculated through the stress transformation (3.11a). And the so-called principal hysteretic variables ξ_1 and ξ_2 will be evaluated according to (3.20). Results of this procedure are shown in Fig. 3.4 with the red dashed line and denoted as '*Trans.-Hy.*'.

In the second procedure the principal strain rates $\dot{\epsilon}_1$ and $\dot{\epsilon}_2$ will be first determined through (3.19) from the given plane strain rates. Then the principal stresses will be calculated by using (2.17) and (2.18). The results of the principal stresses and the hysteretic variables are shown in Fig. 3.4 with the blue solid line and denoted as '*2D-HMiPSP*'.

It can be seen that the results from these two processes are almost identical, so that the hysteretic material model in Cartesian coordinate system for the plane stress state is established for further application.

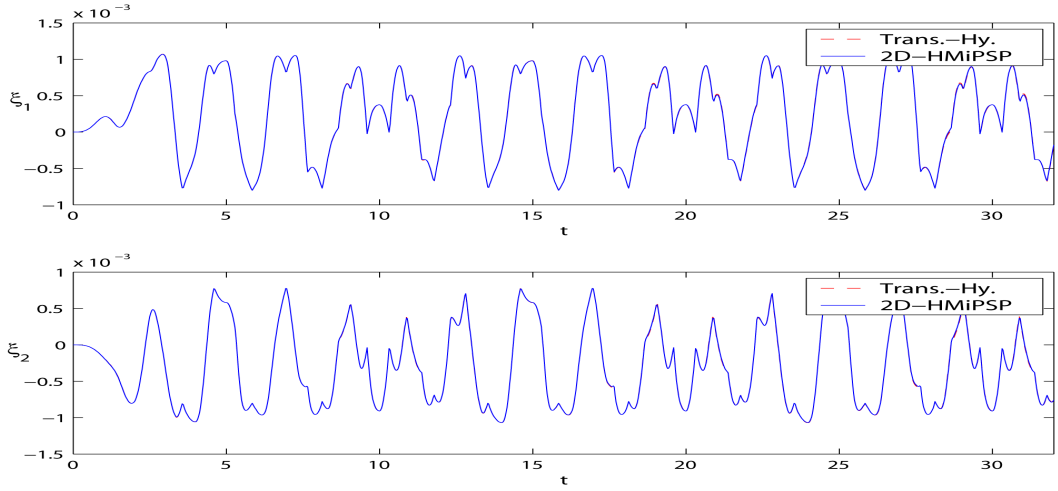

(a) Principal Hysteretic Variables

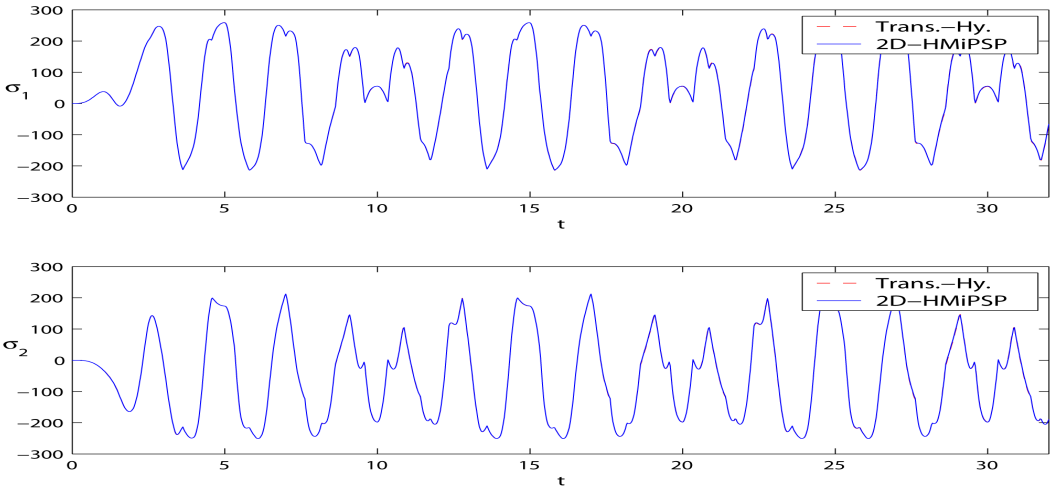

(b) Principal Stresses

Figure 3.4: Comparison of 2D-HMiPSP with Transformed Plane Stress Hysteretic Model

The internal virtual work can be formulated now as

$$\begin{aligned}\delta W_i &= -\int_V (\delta\epsilon_x\sigma_x + \delta\epsilon_y\sigma_y + \delta\gamma_{xy}\tau_{xy})dV \\ &= -\alpha\int_V [\,\delta\epsilon_x\ \delta\epsilon_y\ \delta\gamma_{xy}]\,\frac{E}{1-\nu^2}\begin{bmatrix}1 & \nu & 0\\ \nu & 1 & 0\\ 0 & 0 & \frac{1-\nu}{2}\end{bmatrix}\begin{bmatrix}\epsilon_x\\ \epsilon_y\\ \gamma_{xy}\end{bmatrix}dV \\ &\quad -(1-\alpha)\int_V [\,\delta\epsilon_x\ \delta\epsilon_y\ \delta\gamma_{xy}]\,\frac{E}{1-\nu^2}\begin{bmatrix}1 & \nu & 0\\ \nu & 1 & 0\\ 0 & 0 & \frac{1-\nu}{2}\end{bmatrix}\begin{bmatrix}\xi_x\\ \xi_y\\ \xi_{xy}\end{bmatrix}dV\ .\end{aligned} \tag{3.21}$$

After the elastic theory the next step is to perform the integration of the internal virtual work in the z-direction with using of the kinematic relations (3.6). But obviously it is difficult to perform the analytical integration of the hysteretic variables ξ in (3.21). Therefore it is necessary to derive a multi-variables hysteretic moment-curvature relation.

3.2.2 Hysteretic Moment-Curvature Relations

Since the stresses (3.12) have elastic and hysteretic components, it is reasonable to assume that the moments of the cross-section per unit length, which are the stress resultants, are also composed of an elastic and a hysteretic parts and can be expressed as

$$\begin{aligned}
m_x &= \int_{-h/2}^{h/2} \sigma_x \, z \, dz \simeq \alpha \, \frac{-Eh^3}{12(1-\nu^2)}(\kappa_x + \nu\,\kappa_y) + (1-\alpha)\frac{-Eh^3}{12(1-\nu^2)}(Y_x + \nu\, Y_y) \\
m_y &= \int_{-h/2}^{h/2} \sigma_y \, z \, dz \simeq \alpha \, \frac{-Eh^3}{12(1-\nu^2)}(\nu\,\kappa_x + \kappa_y) + (1-\alpha)\frac{-Eh^3}{12(1-\nu^2)}(\nu\, Y_x + Y_y) \\
m_{xy} &= \int_{-h/2}^{h/2} \tau_{xy} \, z \, dz \simeq \alpha \, \frac{-Eh^3}{12(1-\nu^2)}\,(1-\nu)\,\kappa_{xy} + (1-\alpha)\,\frac{-Eh^3}{12(1-\nu^2)}\,(1-\nu)\,Y_{xy} \;,
\end{aligned} \tag{3.22}$$

where Y_x, Y_y and Y_{xy} are defined as the hysteretic variables of moment.

The nonlinear equations for these hysteretic variables of moment are assumed to have the same form as (3.18) like

$$\begin{bmatrix} \dot{Y}_x \\ \dot{Y}_y \\ \dot{Y}_{xy} \end{bmatrix} = \begin{bmatrix} \dot{\kappa}_x \\ \dot{\kappa}_y \\ \dot{\kappa}_{xy} \end{bmatrix} - \beta_M(|\dot{\kappa}_1 Y_1| + |\dot{\kappa}_2 Y_2|) \begin{bmatrix} Y_x \\ Y_y \\ Y_{xy} \end{bmatrix} - \beta_M(\dot{\kappa}_1 Y_1 + \dot{\kappa}_2 Y_2) \begin{bmatrix} Y_x \\ Y_y \\ Y_{xy} \end{bmatrix} - \dot{T}'_\kappa \begin{bmatrix} \kappa_1 - Y_1 \\ \kappa_2 - Y_2 \end{bmatrix} , \tag{3.23}$$

where β_M is a unknown parameter concerning with the curvature yielding limit.

According to the kinematic relations (3.6) and the transformation equation (3.13) the following relations can be derived

$$\begin{bmatrix} \kappa_x \\ \kappa_y \\ \kappa_{xy} \end{bmatrix} = T'_\kappa \begin{bmatrix} \kappa_1 \\ \kappa_2 \end{bmatrix} \quad \text{with} \quad T'_\kappa = \begin{bmatrix} \dfrac{1+\cos 2\tilde{\theta}}{2} & \dfrac{1-\cos 2\tilde{\theta}}{2} \\ \dfrac{1-\cos 2\tilde{\theta}}{2} & \dfrac{1+\cos 2\tilde{\theta}}{2} \\ \dfrac{\sin 2\tilde{\theta}}{2} & -\dfrac{\sin 2\tilde{\theta}}{2} \end{bmatrix} , \tag{3.24a}$$

where

$$\tan 2\tilde{\theta} = \frac{\gamma_{xy}}{\epsilon_x - \epsilon_y} = \frac{2\,\kappa_{xy}}{\kappa_x - \kappa_y} \quad \text{and} \quad 2\,\dot{\tilde{\theta}} = \frac{2\dot{\kappa}_{xy}(\kappa_x - \kappa_y) - (\dot{\kappa}_x - \dot{\kappa}_y)\,2\kappa_{xy}}{(\kappa_x - \kappa_y)^2 + (2\kappa_{xy})^2} \;. \tag{3.24b}$$

So that $\dot{T}'_\kappa$ in (3.23) is

$$\dot{T}'_\kappa = 2\,\dot{\tilde{\theta}} \begin{bmatrix} \dfrac{-\sin 2\tilde{\theta}}{2} & \dfrac{\sin 2\tilde{\theta}}{2} \\ \dfrac{\sin 2\tilde{\theta}}{2} & \dfrac{-\sin 2\tilde{\theta}}{2} \\ \dfrac{\cos 2\tilde{\theta}}{2} & \dfrac{-\cos 2\tilde{\theta}}{2} \end{bmatrix} . \tag{3.25}$$

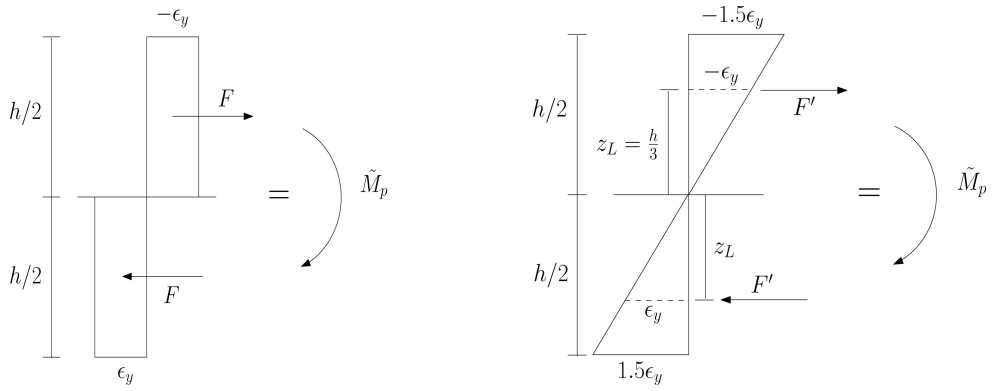

(a) Ideal (b) Linear Equivalent

Figure 3.5: Ideal / Equivalent Plastic Limit of Moment

Setting (3.6) in (3.11b) it follows

$$\begin{bmatrix} \kappa_1 \\ \kappa_2 \end{bmatrix} = \begin{bmatrix} \frac{1+\cos 2\tilde{\theta}}{2} & \frac{1-\cos 2\tilde{\theta}}{2} & \sin 2\tilde{\theta} \\ \frac{1-\cos 2\tilde{\theta}}{2} & \frac{1+\cos 2\tilde{\theta}}{2} & -\sin 2\tilde{\theta} \end{bmatrix} \begin{bmatrix} \kappa_x \\ \kappa_y \\ \kappa_{xy} \end{bmatrix} = T_\kappa \begin{bmatrix} \kappa_x \\ \kappa_y \\ \kappa_{xy} \end{bmatrix} . \tag{3.26}$$

And similar to (3.19) the relation below can be found

$$\begin{bmatrix} \dot{\kappa}_1 \\ \dot{\kappa}_2 \end{bmatrix} = T_\kappa \begin{bmatrix} \dot{\kappa}_x \\ \dot{\kappa}_y \\ \dot{\kappa}_{xy} \end{bmatrix} . \tag{3.27}$$

From (3.11b) and (3.20) it can be seen that the same transformation matrix is used both for strains ϵ_i and for their corresponding hysteretic variable ξ_i. Analogically it is assumed that the Y-variables have also the same transformation relations as the curvatures, so that Y_1 and Y_2 can be evaluated as

$$\begin{bmatrix} Y_1 \\ Y_2 \end{bmatrix} = T_\kappa \begin{bmatrix} Y_x \\ Y_y \\ Y_{xy} \end{bmatrix} . \tag{3.28}$$

The last unknown in (3.23) is the yielding parameter β_M. According to the limit analysis mentioned in the appendix B.2 the maximal carrying moment of the cross-section is the plastic limit $\tilde{M}_p$, by which the whole section is loaded with the yield stress σ_y. Correspondingly the ideal plastic limit of moment per unit length is

$$\tilde{m}_p = \frac{\sigma_y h^2}{4} , \tag{3.29a}$$

which is schematically illustrated in Fig. 3.5 (a). In Fig. 3.5 (b) an equivalent plastic limit of curvature $\bar{\kappa_p}$, which has a linear strain distribution and has the same magnitude of plastic moment $\tilde{m}_p$, can be determined as

$$\bar{\kappa_p} = \frac{m_p}{EI} = \frac{\sigma_y h^2/4}{Eh^3/12} = \frac{3\,\sigma_y}{Eh} \tag{3.29b}$$

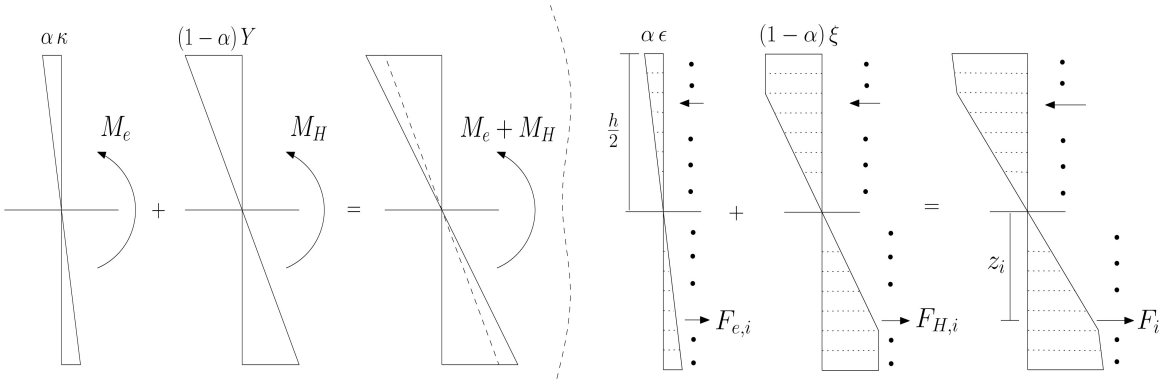

(a) Whole Section Model (b) Fiber Model

Figure 3.6: Hysteretic Cross-Section Moments

Using (2.19) and exchanging the yield strain ϵ_Y by $\bar{\kappa_p}$, the material parameter β_M is determined as

$$\beta_M = \frac{1}{2}\,(\frac{1}{\bar{\kappa_p}})^2 = \frac{1}{2}\,(\frac{Eh}{3\,\sigma_y})^2\ . \tag{3.30}$$

In order to verify the hysteretic moment-curvature relation (3.22) and (3.23), two independent procedures are performed on a fictive plate element with a thickness of $40\,mm$ to give comparisons. In the first procedure the moments m_x, m_y and m_{xy} are determined from the given curvature rates $\dot{\kappa}_x$, $\dot{\kappa}_y$ and $\dot{\kappa}_{xy}$ by using (3.22) and (3.23). This procedure is schematically shown in Fig. 3.6 (a).

In the second procedure the fiber model of the plate cross-section is built, in which the cross-section is divided into 100 fibers and the derivative of fiber strains is calculated through the differentiation of (3.6) using the same curvature rates as in the first procedure. For each fiber the corresponding stress is determined after (3.12) and (3.18) and the cross-section moment is then the resultant of all fiber forces F_i. This model is schematically represented in Fig. 3.6 (b).

The numerical results for the 1-dimensional case, in which $\dot{\kappa}_y = -\nu\,\dot{\kappa}_x$ and $\dot{\kappa}_{xy} = 0$ are assumed, is shown in Fig. 3.7 (a). In this figure the result of the hysteretic moment-curvature model (3.22) is indicated with the red dashed line and denoted as '*Whole Section*'. The blue solid line, which denoted as '*Fiber Model*', is the result of using the hysteretic stress-strain relation (3.12). The black dotted line is the elastic limit of moment, by which the most outer fiber just reaches the yield stress. It can be seen that for the fiber model the nonlinear moment appears above the elastic limit, as part of the section yields (Fig. 3.6 (b)) . For the whole section model, although the smooth hysteretic model is used, its shape is more angular at the elastic-plastic transition region than the fiber model. This is because that the assumption of the linear distributed $\bar{\kappa}_p$ in the cross-section is adopted and consequently the moment in the transition region is overestimated. But the maximum stresses of these two models match with each other quite well; the error of the maximum stress is about 0.7 %.

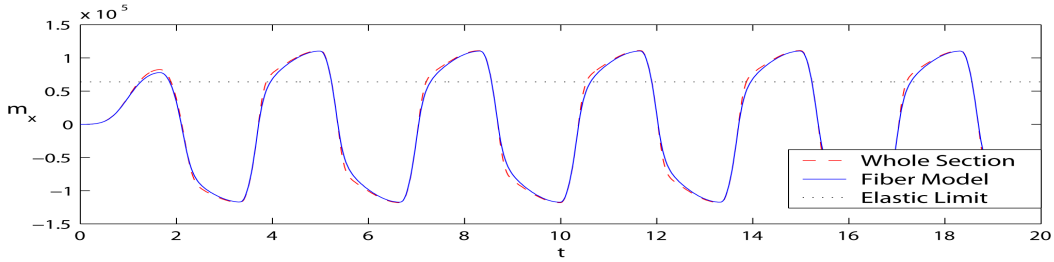

(a) 1-Dimensional Case

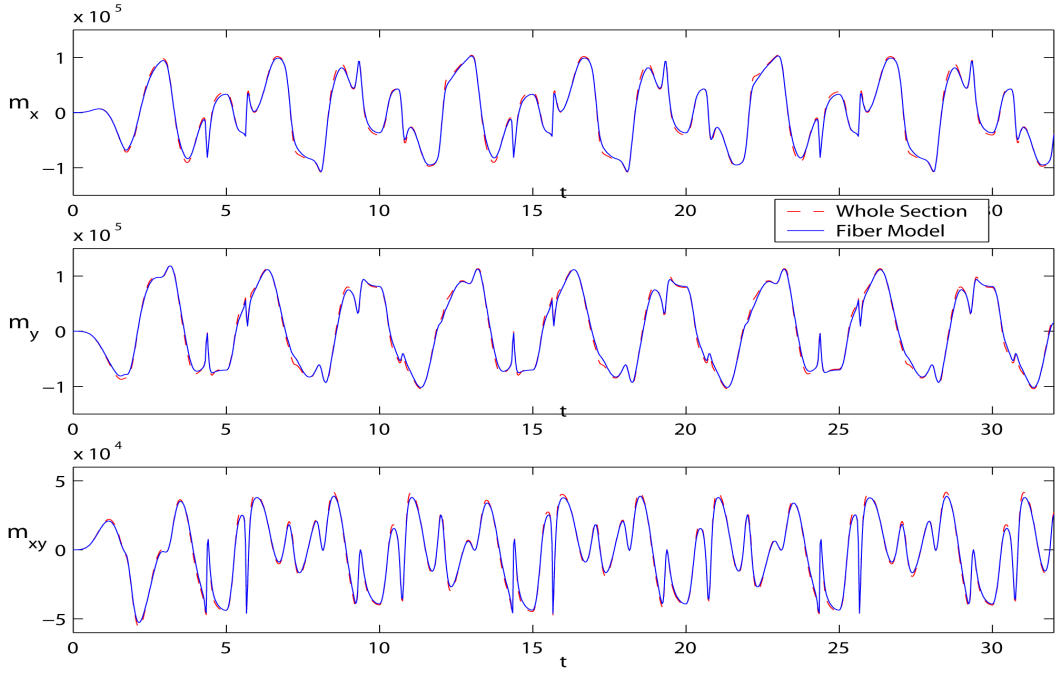

(b) Arbitrary Plane Stresses Case

Figure 3.7: Comparison of Whole Section Model with Fiber Model

To have a general comparison of these two models, Fig. 3.7 (b) shows the results of another example, in which the arbitrary amplitude and frequency of $\dot{\kappa}_x$, $\dot{\kappa}_y$ and $\dot{\kappa}_{xy}$ are applied. From the good acceptable results the hysteretic moment-curvature relation is verified. And consequently the internal virtual work of the plate element can be further developed in the moment-curvature expression as

$$\begin{aligned}
\delta W_i &= -\int_V (\delta\epsilon_x\sigma_x + \delta\epsilon_y\sigma_y + \delta\gamma_{xy}\tau_{xy})dV \\
&= -\alpha\int_A [\,\delta\kappa_x\ \delta\kappa_y\ 2\,\delta\kappa_{xy}]\,\frac{Eh^3}{12(1-\nu^2)}\begin{bmatrix} 1 & \nu & 0 \\ \nu & 1 & 0 \\ 0 & 0 & \frac{1-\nu}{2} \end{bmatrix}\begin{bmatrix} \kappa_x \\ \kappa_y \\ 2\kappa_{xy} \end{bmatrix} dxdy \\
&\quad -(1-\alpha)\int_A [\,\delta\kappa_x\ \delta\kappa_y\ 2\,\delta\kappa_{xy}]\,\frac{Eh^3}{12(1-\nu^2)}\begin{bmatrix} 1 & \nu & 0 \\ \nu & 1 & 0 \\ 0 & 0 & \frac{1-\nu}{2} \end{bmatrix}\begin{bmatrix} Y_x \\ Y_y \\ 2Y_{xy} \end{bmatrix} dxdy\ .
\end{aligned} \tag{3.31}$$

3.3 FEM – Curvature related Stiffness Matrix

To be able to solve the complex nonlinear dynamic problems numerically, the *Finite Element Method* (FEM) is chosen, with which the continuous functions will be discretized through the nodal degree of freedoms with corresponding interpolation functions (also called as shape functions). According to the kinematic relations (3.3) the curvatures can be expressed as the second derivatives of the deflection $w(x, y)$, therefore the discretization will be performed on the plate deflection function.

3.3.1 BFS/Schäfer Plate Element

To develop the *Plastic Shape Function* of plates, which is the main objective of this work, the compatible 4-nodes rectangular plate element with 16 DOF, i.e., BFS- or Schäfer-element [8], is chosen for the system discretization, so that a convenient adoption of the Kirchhoff plate theory can be achieved. Each node of the Schäfer-element has four degrees of freedom, which are the deflection w, the rotation angles ψ_x and ψ_y, and the twisting curvature $\psi_{xy} = -\partial^2 w/\partial x \partial y$ as shown in Fig. 3.8 (a).

The field of the deflection is then described as a bi-cubic function with the polynomial terms given in Fig. 3.8 (b) and can be written as [103]

$$\begin{aligned} w(x,y) = {} & a_1 + a_2\,x + a_3\,y + a_4\,x^2 + a_5\,xy + a_6\,y^2 + a_7\,x^3 + a_8\,x^2y + a_9\,xy^2 \\ & + a_{10}\,y^3 + a_{11}\,xy^3 + a_{12}\,x^3y + a_{13}\,x^2y^2 + a_{14}\,x^2y^3 + a_{15}\,x^3y^2 + a_{16}\,x^3y^3 \ . \end{aligned} \tag{3.32}$$

The deflection function $w(x, y)$ can be further discretized as the linear combination of the nodal deformations multiplied with the shape functions like

$$\begin{aligned} w(x,y) = {} & N_1(x,y)\,w_1 + N_2(x,y)\,\psi_{x1} + N_3(x,y)\,\psi_{y1} + N_4(x,y)\,\psi_{xy1} \\ & + N_5(x,y)\,w_2 + N_6(x,y)\,\psi_{x2} + N_7(x,y)\,\psi_{y2} + N_8(x,y)\,\psi_{xy2} \\ & + N_9(x,y)\,w_3 + N_{10}(x,y)\,\psi_{x3} + N_{11}(x,y)\,\psi_{y3} + N_{12}(x,y)\,\psi_{xy3} \\ & + N_{13}(x,y)\,w_4 + N_{14}(x,y)\,\psi_{x4} + N_{15}(x,y)\,\psi_{y4} + N_{16}(x,y)\,\psi_{xy4} \\ = {} & \sum_{i=1}^{16} N_i(x,y)\,w_{e,i} \ , \end{aligned} \tag{3.33}$$

where $N_i(x, y)$ are the shape functions corresponding to the unit deformation of each nodal degrees of freedom respectively. The details about the shape functions N_i can be found in appendix C.1. The $w_{e,i}$ are the components of the nodal deformations vector, which is

$$\mathbf{w}_e = [\, w_1 \ \psi_{x1} \ \psi_{y1} \ \psi_{xy1} \ w_2 \ \psi_{x2} \ \psi_{y2} \ \psi_{xy2} \ w_3 \ \psi_{x3} \ \psi_{y3} \ \psi_{xy3} \ w_4 \ \psi_{x4} \ \psi_{y4} \ \psi_{xy4} \,]^T \ . \tag{3.34}$$

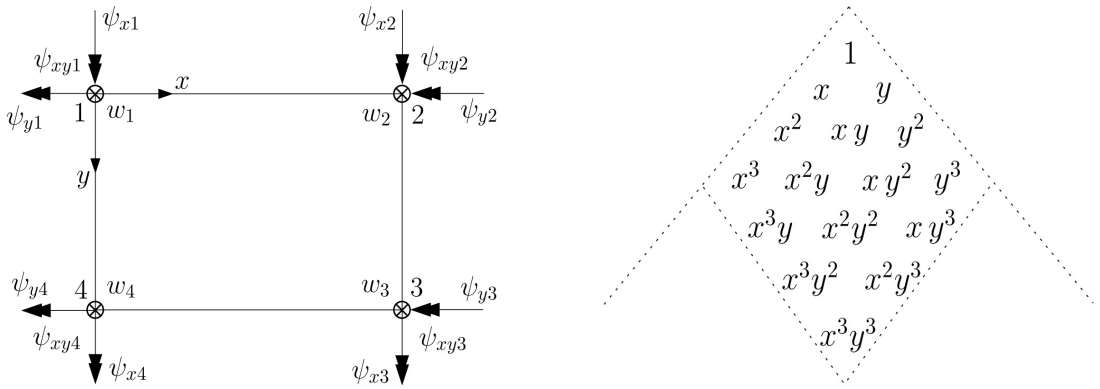

(a) DOF (b) Bi-cubic Polynomials

Figure 3.8: Schäfer Plate Element

Setting (3.33) in (3.3) the curvatures can be formulated as

$$\kappa_x(x,y) = \sum_{i=1}^{16} B_{x,i}(x,y)\, w_{e,i}\ , \qquad \kappa_y(x,y) = \sum_{i=1}^{16} B_{y,i}(x,y)\, w_{e,i}$$
$$\text{and} \qquad \kappa_{xy}(x,y) = \sum_{i=1}^{16} B_{xy,i}(x,y)\, w_{e,i}\ , \tag{3.35a}$$

where

$$B_{x,i} = \frac{\partial^2 N_i}{\partial x^2}\ , \qquad B_{y,i} = \frac{\partial^2 N_i}{\partial y^2} \qquad \text{and} \qquad B_{xy,i} = \frac{\partial^2 N_i}{\partial x \partial y}\ . \tag{3.35b}$$

The interpolation functions of curvatures $B_{x,i}$, $B_{y,i}$ and $B_{xy,i}$ are given in appendix C.1 in detail.

With (3.35) the elastic part of (3.31) can be discretized. For the nonlinear part of the internal virtual work it was suggested in [33] that a discrete formulation is more advantageous than a continuous one of the hysteretic variables, as long as an appropriate interpolation function of the hysteretic variable is chosen and the size of the discrete element is also small enough. Therefore the key point is to find out what kind of interpolation functions should be used for the Y-variables in (3.31), as the deformation shape functions are already selected.

3.3.2 Interpolation Functions of Y-Variables

The requirement of the interpolation function of Y-variables is that it must be compatible with the second derivatives of the shape function N_i, i.e., the curvature shape functions in (3.35b), because as the system elastically behaves, is $Y(x,y) \simeq \kappa(x,y)$ and (3.31) should be able to return into pure elastic formulation in view of the consistency of virtual works. The variable Y can be actually treated as a kind of hysteretic curvature which has the upper and lower yielding bound.

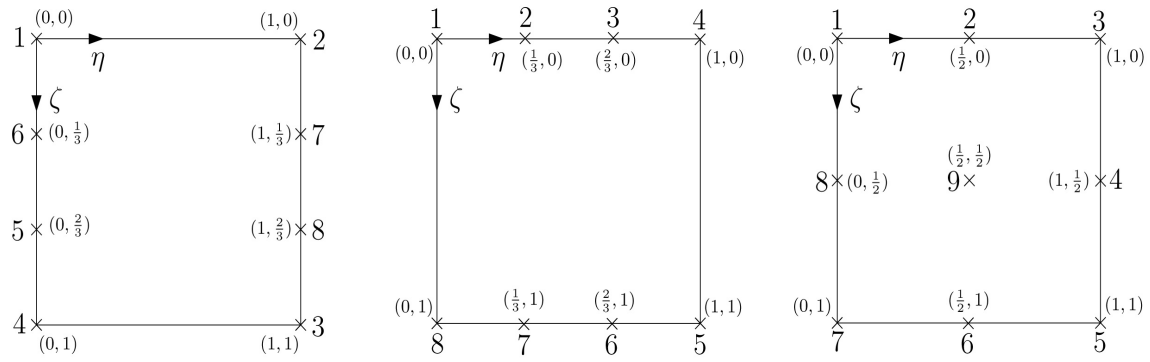

(a) κ_{ex} / Y_{ex} Itp. Nodes (b) κ_{ey} / Y_{ey} Itp. Nodes (c) κ_{exy} / Y_{exy} Itp. Nodes

Figure 3.9: New κ / Y Interpolation Nodes

Considering the function B_x of the curvature κ_x for example, it can be seen from (C.2a) that under the use of the bi-cubic deformation shape function is B_x linear in the x-direction and cubic in the y-direction. The field of κ_x can be expressed generally with 8 polynomial terms as

$$\kappa_x(x,y) = a_1 + a_2\,x + a_3\,y + a_4\,x\,y + a_5\,y^2 + a_6\,x\,y^2 + a_7\,y^3 + a_8\,x\,y^3 \ . \tag{3.36}$$

This curvature field can be discretely formulated through at least 8 nodal curvatures multiplied with corresponding interpolation functions, which are linear independent with each other, as

$$\begin{aligned} \kappa_x(x,y) &= \tilde{N}^*_{x,1}\kappa_{ex,1} + \tilde{N}^*_{x,2}\kappa_{ex,2} + \cdots + \tilde{N}^*_{x,8}\kappa_{ex,8} \\ &= \sum_{i=1}^{8} \tilde{N}^*_{x,i}\,\kappa_{ex,i} \ , \end{aligned} \tag{3.37}$$

where $\tilde{N}^*_{x,i}$ are the new unknown interpolation functions for $\kappa_x(x,y)$. The $\kappa_{ex,i}$ is the curvature value of the node i, which is defined in Fig. 3.9 (a).

Using (3.35a) the curvature of node i in Fig. 3.9 (a) can be calculated as

$$\kappa_{x,i} = \kappa_x(\eta_i,\zeta_i) = \sum_{j=1}^{16} B_{x,j}(\eta_i,\zeta_i)\,w_{e,j} \ , \tag{3.38}$$

where η_i and ζ_i are the natural coordinates of the node i.

Setting (3.38) in (3.37) it follows

$$\begin{aligned}\kappa_x(x,y) &= \tilde{N}^*_{x,1}(\sum_{j=1}^{16} B_{x,j}(\eta_1,\zeta_1)\, w_{e,j}) + \tilde{N}^*_{x,2}(\sum_{j=1}^{16} B_{x,j}(\eta_2,\zeta_2)\, w_{e,j}) + \cdots \\ &\quad \cdots + \tilde{N}^*_{x,8}(\sum_{j=1}^{16} B_{x,j}(\eta_8,\zeta_8)\, w_{e,j}) \\ &= \sum_{i=1}^{8} \tilde{N}^*_{x,i}\big[\sum_{j=1}^{16} B_{x,j}(\eta_i,\zeta_i)\, w_{e,j}\big] \\ &= \sum_{j=1}^{16} \big[\sum_{i=1}^{8} \tilde{N}^*_{x,i}\, B_{x,j}(\eta_i,\zeta_i)\big]\, w_{e,j}\ .\end{aligned} \tag{3.39}$$

Under the condition of compatibility setting (3.39) equal to the expression of $\kappa_x(x,y)$ in (3.35a) and the following equation can be found

$$\sum_{i=1}^{8} B_{x,j}(\eta_i,\zeta_i)\, \tilde{N}^*_{x,i}(x,y) = B_{x,j}(x,y)\ . \tag{3.40}$$

These equations can be collected in the matrix form as

$$\begin{bmatrix} B_{x,1}(\eta_1,\zeta_1) & B_{x,1}(\eta_2,\zeta_2) & \dots & B_{x,1}(\eta_8,\zeta_8) \\ B_{x,2}(\eta_1,\zeta_1) & B_{x,2}(\eta_2,\zeta_2) & \dots & B_{x,2}(\eta_8,\zeta_8) \\ \vdots & \vdots & \ddots & \vdots \\ B_{x,16}(\eta_1,\zeta_1) & B_{x,16}(\eta_2,\zeta_2) & \dots & B_{x,16}(\eta_8,\zeta_8) \end{bmatrix}_{16\times 8} \begin{bmatrix} \tilde{N}^*_{x,1} \\ \tilde{N}^*_{x,2} \\ \vdots \\ \tilde{N}^*_{x,8} \end{bmatrix}_{8\times 1} = \begin{bmatrix} B_{x,1} \\ B_{x,2} \\ \vdots \\ B_{x,16} \end{bmatrix}_{16\times 1} \tag{3.41}$$

Since $\kappa_x(x,y)$ is a polynomial with 8 terms, the maximum number of the linear independent functions of $B_{x,i}$ should also be 8. From (C.2a) it can be found that the linear independent functions of $B_{x,i}$ are

$$B_{x,2}\ ,\ B_{x,4}\ ,\ B_{x,6}\ ,\ B_{x,8}\ ,\ B_{x,10}\ ,\ B_{x,12}\ ,\ B_{x,14} \text{ and } B_{x,16}\ . \tag{3.42}$$

So that (3.41) is reduced to

$$\begin{bmatrix} B_{x,2}(\eta_1,\zeta_1) & B_{x,2}(\eta_2,\zeta_2) & \dots & B_{x,2}(\eta_8,\zeta_8) \\ B_{x,4}(\eta_1,\zeta_1) & B_{x,4}(\eta_2,\zeta_2) & \dots & B_{x,4}(\eta_8,\zeta_8) \\ \vdots & \vdots & \ddots & \vdots \\ B_{x,16}(\eta_1,\zeta_1) & B_{x,16}(\eta_2,\zeta_2) & \dots & B_{x,16}(\eta_8,\zeta_8) \end{bmatrix}_{8\times 8} \begin{bmatrix} \tilde{N}^*_{x,1} \\ \tilde{N}^*_{x,2} \\ \vdots \\ \tilde{N}^*_{x,8} \end{bmatrix}_{8\times 1} = \begin{bmatrix} B_{x,2} \\ B_{x,4} \\ \vdots \\ B_{x,16} \end{bmatrix}_{8\times 1}$$

$$\Longrightarrow$$

$$\Big[\, BxM \,\Big]_{8\times 8} \cdot \Big[\, \tilde{N}^*_x(x,y) \,\Big]_{8\times 1} = \Big[\, B^*_x(x,y) \,\Big]_{8\times 1} \tag{3.43}$$

It is to note that $[BxM]$ is a scalar matrix as $[\tilde{N}^*_x(x,y)]$ and $[B^*_x(x,y)]$ are vectors of function.

Finally the compatible interpolation functions can be determined as

$$\left[\tilde{N}_x^*(x,y)\right] = \left[BxM\right]^{-1}\left[B_x^*(x,y)\right] \ . \tag{3.44}$$

Considering the dependency of $Y_x(x,y)$ on $\kappa_x(x,y)$ given in (3.23), it is reasonable also to use $\tilde{N}_x^*(x,y)$ as the interpolation function of $Y_x(x,y)$, so that the hysteretic variable $Y_x(x,y)$ can be discretized as

$$\begin{aligned} Y_x(x,y) &= \tilde{N}_{x,1}^* Y_{ex,1} + \tilde{N}_{x,2}^* Y_{ex,2} + \cdots + \tilde{N}_{x,8}^* Y_{ex,8} \\ &= \sum_{i=1}^{8} \tilde{N}_{x,i}^*\, Y_{ex,i} \ , \end{aligned} \tag{3.45}$$

where $Y_{ex,i}$ are the values of Y_x on the nodes defined in Fig. 3.9 (a).

Similarly for $\kappa_y(x,y)$, its compatible interpolation functions $\tilde{N}_{y,i}^*(x,y)$ can be calculated according to the nodes defined in Fig. 3.9 (b) as

$$\left[\tilde{N}_y^*(x,y)\right]_{8\times 1} = \left[ByM\right]_{8\times 8}^{-1}\left[B_y^*(x,y)\right]_{8\times 1} \ , \tag{3.46a}$$

with

$$\left[\tilde{N}_y^*(x,y)\right] = \begin{bmatrix} \tilde{N}_{y,1}^*(x,y) & \tilde{N}_{y,2}^*(x,y) & \cdots & \tilde{N}_{y,8}^*(x,y) \end{bmatrix}^T \ , \tag{3.46b}$$

and

$$\left[B_y^*(x,y)\right] = \begin{bmatrix} B_{y,3} & B_{y,4} & B_{y,7} & B_{y,8} & B_{y,11} & B_{y,12} & B_{y,15} & B_{y,16} \end{bmatrix}^T \ , \tag{3.46c}$$

which is the vector composed of the linear independent functions of $B_{y,i}$. The corresponding scalar matrix is

$$\left[ByM\right] = \begin{bmatrix} B_{y,3}(\eta_1,\zeta_1) & B_{y,3}(\eta_2,\zeta_2) & \dots & B_{y,3}(\eta_8,\zeta_8) \\ B_{y,4}(\eta_1,\zeta_1) & B_{y,4}(\eta_2,\zeta_2) & \dots & B_{y,4}(\eta_8,\zeta_8) \\ B_{y,7}(\eta_1,\zeta_1) & \cdots & \dots & B_{y,7}(\eta_8,\zeta_8) \\ \vdots & \vdots & \ddots & \vdots \\ B_{y,16}(\eta_1,\zeta_1) & B_{y,16}(\eta_2,\zeta_2) & \dots & B_{y,16}(\eta_8,\zeta_8) \end{bmatrix} \ . \tag{3.46d}$$

It is to emphasize that the nodal coordinates (η_i,ζ_i) used in the matrix $[ByM]$ are defined according to Fig. 3.9 (b). Then the hysteretic variable $Y_y(x,y)$ can be discretized as

$$\begin{aligned} Y_y(x,y) &= \tilde{N}_{y,1}^* Y_{ey,1} + \tilde{N}_{y,2}^* Y_{ey,2} + \cdots + \tilde{N}_{y,8}^* Y_{ey,8} \\ &= \sum_{i=1}^{8} \tilde{N}_{y,i}^*\, Y_{ey,i} \ , \end{aligned} \tag{3.47}$$

where $Y_{ey,i}$ are the values of Y_y on the nodes defined in Fig. 3.9 (b).

Under the bi-cubic deflection approach the twisting function $\kappa_{xy}(x,y)$ is bi-quadratic, which means that 9 independent, compatible interpolation functions $\tilde{N}^*_{xy}$ corresponding to the nodes defined in Fig. 3.9 (c) can be found. And the 9 linear independent functions of $B_{xy,i}$ are

$$B_{xy,1}\ ,\ B_{xy,2}\ ,\ B_{xy,3}\ ,\ B_{xy,4}\ ,\ B_{xy,6}\ ,\ B_{xy,8}\ ,\ B_{xy,12}\ ,\ B_{xy,15} \text{ and } B_{xy,16}\ . \tag{3.48}$$

So that $\tilde{N}^*_{xy,i}(x,y)$ can be determined as

$$\left[\tilde{N}^*_{xy}(x,y)\right]_{9\times 1} = \left[BxyM\right]^{-1}_{9\times 9}\left[B^*_{xy}(x,y)\right]_{9\times 1}\ , \tag{3.49a}$$

with

$$\left[\tilde{N}^*_{xy}(x,y)\right] = \begin{bmatrix}\tilde{N}^*_{xy,1}(x,y) & \tilde{N}^*_{xy,2}(x,y) & \cdots & \tilde{N}^*_{xy,9}(x,y)\end{bmatrix}^T\ , \tag{3.49b}$$

and

$$\left[B^*_{xy}(x,y)\right] = \begin{bmatrix}B_{xy,1} & B_{xy,2} & B_{xy,3} & B_{xy,4} & B_{xy,6} & B_{xy,8} & B_{xy,12} & B_{xy,15} & B_{xy,16}\end{bmatrix}^T \tag{3.49c}$$

The corresponding scalar matrix is

$$\left[BxyM\right] = \begin{bmatrix} B_{y,1}(\eta_1,\zeta_1) & B_{y,1}(\eta_2,\zeta_2) & \dots & B_{y,1}(\eta_9,\zeta_9) \\ \vdots & \vdots & \ddots & \vdots \\ B_{y,4}(\eta_1,\zeta_1) & \dots & \dots & B_{y,4}(\eta_9,\zeta_9) \\ B_{y,6}(\eta_1,\zeta_1) & \dots & \dots & B_{y,6}(\eta_9,\zeta_9) \\ \vdots & \vdots & \ddots & \vdots \\ B_{y,16}(\eta_1,\zeta_1) & B_{y,16}(\eta_2,\zeta_2) & \dots & B_{y,16}(\eta_9,\zeta_9) \end{bmatrix}\ . \tag{3.49d}$$

Similarly the hysteretic variable $Y_{xy}(x,y)$ can be discretized as

$$\begin{aligned} Y_{xy}(x,y) &= \tilde{N}^*_{xy,1}Y_{exy,1} + \tilde{N}^*_{xy,2}Y_{exy,2} + \cdots + \tilde{N}^*_{xy,9}Y_{exy,9} \\ &= \sum_{i=1}^{9}\tilde{N}^*_{xy,i}\,Y_{exy,i}\ , \end{aligned} \tag{3.50}$$

where $Y_{exy,i}$ are the values of Y_{xy} on the nodes defined in Fig. 3.9 (c).

The detailed functions of $\tilde{N}^*_{x,i}$, $\tilde{N}^*_{y,i}$ and $\tilde{N}^*_{xy,i}$ are given in appendix (C.3a), (C.3b) and (C.3c) respectively.

It can be seen from Fig. 3.9 that because of the different distribution characters of κ_x, κ_y and κ_{xy}, the discrete nodes needed for a compatible interpolation of Y_x, Y_y and Y_{xy} are not unitary. Such inconsistency of the nodal nets will give rise to difficulties by applying the FEM. On the other hand these three hysteretic variables are coupled together according to (3.23), which means all these three values have to be calculated

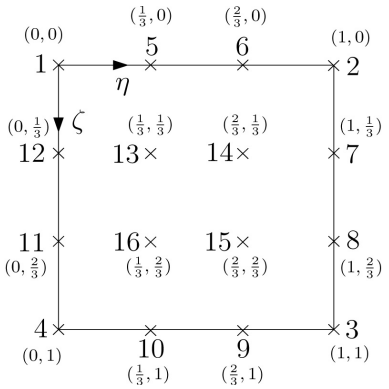

Figure 3.10: Common nodal Net of Y_x, Y_y and Y_{xy}

for every single node appearing in Fig. 3.9 (a) to (c). Therefore a unified nodal net for Y_x, Y_y and Y_{xy} is advantageous and defined in Fig. 3.10. This unified nodal net will called as the *Y-nodal net* in following.

Corresponding to the Y-nodal net the original interpolation function groups $\tilde{N}^*_{x,i}(x,y)$, $\tilde{N}^*_{y,i}(x,y)$ and $\tilde{N}^*_{xy,i}(x,y)$ have to be expanded to $\tilde{N}_{x,i}(x,y)$, $\tilde{N}_{y,i}(x,y)$ and $\tilde{N}_{xy,i}(x,y)$ respectively, so that each of them has 16 linear dependent components. Taking $\tilde{N}^*_{x,i}(x,y)$ for example, two additional nodes for each row (x-direction), i.e., totally 8 additional nodes, have to be included to establish $\tilde{N}_{x,i}(x,y)$ in regard to nodes defined in Fig. 3.10. This means that for each row of Fig. 3.9 (a), the linear function of η will be described through 4 nodal values with 4 dependent interpolation functions, as the part of the ζ polynomial remains unchanged.

Considering a linear function of η expressed as

$$\begin{aligned} f(\eta) &= a_1 + a_2\,\eta \\ &= f(0)(1-\eta) + f(1)\,\eta \end{aligned} \tag{3.51a}$$

and introducing the following relations of nodal values that

$$\begin{aligned} f(0) &= 2\,f(1/3) - f(2/3) \\ f(1) &= -f(1/3) + 2\,f(2/3)\ , \end{aligned} \tag{3.51b}$$

since $f(1/3)$ and $f(2/3)$ should be added into the interpolation.

So the linear function $f(\eta)$ can be decomposed for example as

$$\begin{aligned} f(\eta) &= f(0)(1-\eta) + f(1)\,\eta \\ &= f(0)\frac{1-\eta}{2} + f(0)\frac{1-\eta}{2} + f(1)\frac{\eta}{2} + f(1)\frac{\eta}{2} \\ &= f(0)\frac{1-\eta}{2} + (2\,f(1/3) - f(2/3))\frac{1-\eta}{2} + (-f(1/3) + 2\,f(2/3))\frac{\eta}{2} + f(1)\frac{\eta}{2} \\ &= f(0)\frac{1-\eta}{2} + f(1/3)\frac{2-3\,\eta}{2} + f(2/3)\frac{-1+3\,\eta}{2} + f(1)\frac{\eta}{2}\ . \end{aligned} \tag{3.51c}$$

Consequently, for the interpolation functions

$$\begin{aligned} \tilde{N}^*_{x,1} &= (1-\eta)(1-5.5\,\zeta+9\,\zeta^2-4.5\,\zeta^3) \\ \tilde{N}^*_{x,2} &= \eta\,(1-5.5\,\zeta+9\,\zeta^2-4.5\,\zeta^3)\ , \end{aligned} \tag{3.52a}$$

which are on a same row, the linear function $1-\eta$ and η will be split up into 4 dependent functions according to (3.51c) and each of them will multiply with the same polynomial of ζ to produce 4 new interpolation functions like

$$\begin{aligned} \tilde{N}_{x,1} &= (1-\eta)(0.5-2.75\,\zeta+4.5\,\zeta^2-2.25\,\zeta^3) \\ \tilde{N}_{x,5} &= (2-3\,\eta)(0.5-2.75\,\zeta+4.5\,\zeta^2-2.25\,\zeta^3) \\ \tilde{N}_{x,6} &= (-1+3\,\eta)(0.5-2.75\,\zeta+4.5\,\zeta^2-2.25\,\zeta^3) \\ \tilde{N}_{x,2} &= \eta\,(0.5-2.75\,\zeta+4.5\,\zeta^2-2.25\,\zeta^3)\ , \end{aligned} \tag{3.52b}$$

which belong to the Y-nodal net.

Finally the hysteretic variables $Y_x(x,y)$, $Y_y(x,y)$ and $Y_{xy}(x,y)$ will be discretized according to Fig. 3.10 as

$$\begin{aligned} &Y_x(x,y)=\sum_{i=1}^{16}\tilde{N}_{x,i}\,Y_{ex,i}\ , \qquad Y_y(x,y)=\sum_{i=1}^{16}\tilde{N}_{y,i}\,Y_{ey,i} \\ &\text{and} \qquad Y_{xy}(x,y)=\sum_{i=1}^{16}\tilde{N}_{xy,i}\,Y_{exy,i}\ . \end{aligned} \tag{3.53}$$

The complete $\tilde{N}_{x,i}(x,y)$, $\tilde{N}_{y,i}(x,y)$ and $\tilde{N}_{xy,i}(x,y)$ for $i=1\ldots16$ are given in appendix (C.4), (C.5) and (C.6), in which the expansion procedure of $\tilde{N}^*_{xy,i}(x,y)$ to $\tilde{N}_{xy,i}(x,y)$ is illustrated in detail.

3.3.3 Differential Equation of Motion with Hysteresis

Local Equation of Element

With use of (3.35) and (3.53) the continuous formulation of the internal virtual work of a plate element (3.31) can be discretized according to FEM as

$$\begin{aligned} \delta W_i = &-\delta\mathbf{w}_e^T\left(\alpha\int_A \mathbf{B}^T\,\mathbf{D}\,\mathbf{B}\,dxdy\right)\mathbf{w}_e \\ &-\delta\mathbf{w}_e^T\left((1-\alpha)\int_A \mathbf{B}^T\,\mathbf{D}\,\tilde{\mathbf{N}}_x\,dxdy\right)\mathbf{Y}_{ex} \\ &-\delta\mathbf{w}_e^T\left((1-\alpha)\int_A \mathbf{B}^T\,\mathbf{D}\,\tilde{\mathbf{N}}_y\,dxdy\right)\mathbf{Y}_{ey} \\ &-\delta\mathbf{w}_e^T\left((1-\alpha)\int_A \mathbf{B}^T\,\mathbf{D}\,\tilde{\mathbf{N}}_{xy}\,dxdy\right)\mathbf{Y}_{exy}\ , \end{aligned} \tag{3.54a}$$

where

$$\mathbf{B} = \begin{bmatrix} \partial^2 N_1/\partial x^2 & \partial^2 N_2/\partial x^2 & \partial^2 N_3/\partial x^2 & \cdots & \partial^2 N_{16}/\partial x^2 \\ \partial^2 N_1/\partial y^2 & \partial^2 N_2/\partial y^2 & \partial^2 N_3/\partial y^2 & \cdots & \partial^2 N_{16}/\partial y^2 \\ 2\,\partial^2 N_1/(\partial x \partial y) & 2\,\partial^2 N_2/(\partial x \partial y) & 2\,\partial^2 N_3/(\partial x \partial y) & \cdots & 2\,\partial^2 N_{16}/(\partial x \partial y) \end{bmatrix}_{3\times 16}$$

$$\mathbf{D} = \frac{Eh^3}{12(1-\nu^2)} \begin{bmatrix} 1 & \nu & 0 \\ \nu & 1 & 0 \\ 0 & 0 & \frac{1-\nu}{2} \end{bmatrix}_{3\times 3}$$

$$\tilde{\mathbf{N}}_x = \begin{bmatrix} \tilde{N}_{x,1} & \tilde{N}_{x,2} & \tilde{N}_{x,3} & \cdots & \tilde{N}_{x,16} \\ 0 & 0 & 0 & \cdots & 0 \\ 0 & 0 & 0 & \cdots & 0 \end{bmatrix}_{3\times 16}; \qquad \mathbf{Y}_{ex} = \begin{bmatrix} Y_{ex,1} \\ Y_{ex,2} \\ Y_{ex,3} \\ \vdots \\ Y_{ex,16} \end{bmatrix}_{16\times 1}$$

$$\tilde{\mathbf{N}}_y = \begin{bmatrix} 0 & 0 & 0 & \cdots & 0 \\ \tilde{N}_{y,1} & \tilde{N}_{y,2} & \tilde{N}_{y,3} & \cdots & \tilde{N}_{y,16} \\ 0 & 0 & 0 & \cdots & 0 \end{bmatrix}_{3\times 16}; \qquad \mathbf{Y}_{ey} = \begin{bmatrix} Y_{ey,1} \\ Y_{ey,2} \\ Y_{ey,3} \\ \vdots \\ Y_{ey,16} \end{bmatrix}_{16\times 1}$$

$$\tilde{\mathbf{N}}_{xy} = \begin{bmatrix} 0 & 0 & 0 & \cdots & 0 \\ 0 & 0 & 0 & \cdots & 0 \\ 2\tilde{N}_{xy,1} & 2\tilde{N}_{xy,2} & 2\tilde{N}_{xy,3} & \cdots & 2\tilde{N}_{xy,16} \end{bmatrix}_{3\times 16}; \qquad \mathbf{Y}_{exy} = \begin{bmatrix} Y_{exy,1} \\ Y_{exy,2} \\ Y_{exy,3} \\ \vdots \\ Y_{exy,16} \end{bmatrix}_{16\times 1}. \tag{3.54b}$$

It is to note that the elastic curvature $\kappa(x, y)$ is discretized with the nodal degrees of freedom defined in Fig. 3.8 (a), while the discretization of the hysteretic variable $Y(x, y)$ is achieved according to a different nodal net defined in Fig. 3.10. It can be seen that the total degrees of freedom of Y is $3 \times 16 = 48$, which will raise certain complexities in the numerical computing. But the use of the Y-nodal net can ensure the compatibility between $\kappa(x, y)$ and $Y(x, y)$ and also improves the accuracy of the interpolation of $Y(x, y)$ with the nodes inside the plate element.

To establish the differential equation of motion, the external virtual work will be taken into consideration now. For a plate element, if the body force and the single load, which will cause singularity, are neglected, its external virtual work is resulted from the distributed area load and the d'Alembert's inertia force and can be expressed according to (3.8) as

$$\begin{aligned}\delta W_e &= \int_A \delta w(x,y)\,\bar{p}(x,y,t)dxdy - \int_V \delta w(x,y)\,(\rho\,\ddot{w}(x,y))dV \\ &= \delta\mathbf{w}_e^T\left(\int_A \mathbf{N}^T\,\bar{p}(x,y,t)\,dxdy\right) - \delta\mathbf{w}_e^T\left(\rho\,h\int_A \mathbf{N}^T\,\mathbf{N}\,dxdy\right)\ddot{\mathbf{w}}_e\ ,\end{aligned} \tag{3.55a}$$

where $\bar{p}(x,y,t)$ is the dynamic area load, ρ is the density, $\ddot{\mathbf{w}}_e$ is the vector of nodal accelerations and

$$\mathbf{N} = \begin{bmatrix} N_1 & N_2 & N_3 & \cdots & N_{16} \end{bmatrix}_{1\times 16} \tag{3.55b}$$

Setting (3.54a) and (3.55a) in (3.7) and eliminating $\mathbf{w}_e^T$, since the virtual nodal deformations are arbitrary and unequal zero, the differential equation of motion can be formulated as

$$\mathbf{M}_e\,\ddot{\mathbf{w}}_e + \alpha\,\mathbf{K}_e\,\mathbf{w}_e + (1-\alpha)(\mathbf{K}_{ex}\mathbf{Y}_{ex} + \mathbf{K}_{ey}\mathbf{Y}_{ey} + \mathbf{K}_{exy}\mathbf{Y}_{exy}) = \bar{\mathbf{P}}_e(t)\ , \tag{3.56a}$$

plus the auxiliary vectors of hysteretic equations

$$\dot{\mathbf{Y}}_{ex} = \mathbf{H}_{ex}(\dot{\kappa}_{ex}, Y_{ex}), \quad \dot{\mathbf{Y}}_{ey} = \mathbf{H}_{ey}(\dot{\kappa}_{ey}, Y_{ey}) \quad \text{and} \quad \dot{\mathbf{Y}}_{exy} = \mathbf{H}_{exy}(\dot{\kappa}_{exy}, Y_{exy})\ , \tag{3.56b}$$

where

$$\begin{aligned}\mathbf{M}_e &= \rho\,h\int_A \mathbf{N}^T\,\mathbf{N}\,dxdy \\ \mathbf{K}_e &= \int_A \mathbf{B}^T\,\mathbf{D}\,\mathbf{B}\,dxdy \\ \mathbf{K}_{ex} &= \int_A \mathbf{B}^T\,\mathbf{D}\,\tilde{\mathbf{N}}_x\,dxdy \\ \mathbf{K}_{ey} &= \int_A \mathbf{B}^T\,\mathbf{D}\,\tilde{\mathbf{N}}_y\,dxdy \\ \mathbf{K}_{exy} &= \int_A \mathbf{B}^T\,\mathbf{D}\,\tilde{\mathbf{N}}_{xy}\,dxdy \\ \bar{\mathbf{P}}_e(t) &= \int_A \mathbf{N}^T\,\bar{p}(x,y,t)\,dxdy\ .\end{aligned} \tag{3.56c}$$

According to (3.23) each discrete node defined in Fig. 3.10 has three coupled hysteretic equations for $Y_{ex,i}$, $Y_{ey,i}$ and $Y_{exy,i}$. These hysteretic equations are separately collected in the vectors $\mathbf{H}_{ex}$, $\mathbf{H}_{ey}$ and $\mathbf{H}_{exy}$, which are therefore also coupled together and each of them has the dimension of 16×1. The same as in the elastic dynamics, $\mathbf{M}_e$ is the mass matrix, and $\mathbf{K}_e$ is the stiffness matrix, which is related to the nodal deformations. $\bar{\mathbf{P}}_e(t)$ is the so called equivalent element nodal forces.

In contrast with the elastic dynamics the differential equation (3.56a) are equipped with the curvature related matrices $\mathbf{K}_{ex}$, $\mathbf{K}_{ey}$ and $\mathbf{K}_{exy}$, i.e., the stiffness matrices of hysteresis, which are based on the nodal curvatures instead of the nodal deformations. The differential equation self remains linearly formulated, while the nonlinear properties are collected in the auxiliary equations of hysteresis (3.56b).

If the damping nature of the material is considered, e.g., the viscous damping, the differential equation of motion can be formulated as

$$\mathbf{M}_e\,\ddot{\mathbf{w}}_e + \mathbf{C}_e\,\dot{\mathbf{w}}_e + \alpha\,\mathbf{K}_e\,\mathbf{w}_e + (1-\alpha)(\mathbf{K}_{ex}\mathbf{Y}_{ex} + \mathbf{K}_{ey}\mathbf{Y}_{ey} + \mathbf{K}_{exy}\mathbf{Y}_{exy}) = \bar{\mathbf{P}}_e(t)\ , \quad (3.57a)$$

where

$$\mathbf{C}_e = æ \int_A \mathbf{N}^T\,\mathbf{N}\,dxdy \qquad \text{is the viscous damping matrix} \quad (3.57b)$$

and æ is the element damping coefficient [7].

Global Equation of System

For the entire plate structure the corresponding damped differential equation of motion can be built through the global nodal forces equilibrium and expressed as

$$\mathbf{M}\,\ddot{\mathbf{w}} + \mathbf{C}\,\dot{\mathbf{w}} + \alpha\,\mathbf{K}\,\mathbf{w} + (1-\alpha)(\mathbf{K}_{gx}\mathbf{Y}_{gx} + \mathbf{K}_{gy}\mathbf{Y}_{gy} + \mathbf{K}_{gxy}\mathbf{Y}_{gxy}) = \bar{\mathbf{P}}(t)\ , \quad (3.58a)$$

with

$$\dot{\mathbf{Y}}_{gx} = \mathbf{H}_x(\dot{\kappa}_{gx}, Y_{gx}), \quad \dot{\mathbf{Y}}_{gy} = \mathbf{H}_y(\dot{\kappa}_{gy}, Y_{gy}) \quad \text{and} \quad \dot{\mathbf{Y}}_{gxy} = \mathbf{H}_{xy}(\dot{\kappa}_{gxy}, Y_{gxy})\ , \quad (3.58b)$$

where all the vectors and matrices are related to the global degrees of freedom.

In the practice it is difficult, if not impossible, to determine the element damping coefficient æ for an arbitrary element-grouping, especially because the damping's magnitude is frequency-dependent. Therefore the global damping matrix $\mathbf{C}$ will not be established through the summation of the element damping matrix $\mathbf{C}_e$, but through the application of the global mass matrix $\mathbf{M}$ and the stiffness matrix $\mathbf{K}$ in conjunction with the experimentally determined values of damping [7]. The determination of matrix $\mathbf{C}$ will be described in section 3.4.2.

3.4 Reduction Strategies of Differential Equations

To analyze the dynamic responses of a system with hundreds of thousand DOF, an appropriate reduction's strategy of the system dimension is indispensable. In the following strategies of reducing the number of the hysteretic variables, which demand the most computing efforts, will be first proposed. Then the methods of reducing the deformation degrees of freedom in the literature and the concept of the plastic shape function will be briefly introduced.

3.4.1 Patch & Split Methods

According to (3.53) each plate elements has 48 Y-variables, hence for a complex plate structure the number of the hysteretic variables in (3.58a) is enormous and unacceptable. Fortunately, not all of the Y-variables are really nonlinear in a large scale system,

since generally the plastifications occur on only a few locations, while the most parts of the structure behave elastically. The following two methods can be used to reduce the number of the Y-variables in the system.

Patch Method

If the yielding locations in a finite element mesh are identified through a pre-analysis or are known because the pre-damages of the structure, the original yielding related element, which has only the elastic stiffness matrix $\mathbf{K}_e$, will be replaced by the elastic-plastic patch element with additional hysteretic stiffness matrices $\mathbf{K}_{ex}$, $\mathbf{K}_{ey}$ and $\mathbf{K}_{exy}$ during the establishment of the global differential equation. The global nodal degrees of freedom can be therefore sorted in an elastic group $\mathbf{w}_a$ and a plastic group $\mathbf{w}_b$, so that the global differential equation can be written as

$$\begin{bmatrix} \mathbf{M}_{aa} & \mathbf{M}_{ab} \\ \mathbf{M}_{ba} & \mathbf{M}_{bb} \end{bmatrix} \begin{bmatrix} \ddot{\mathbf{w}}_a \\ \ddot{\mathbf{w}}_b \end{bmatrix} + \begin{bmatrix} \mathbf{C}_{aa} & \mathbf{C}_{ab} \\ \mathbf{C}_{ba} & \mathbf{C}_{bb} \end{bmatrix} \begin{bmatrix} \dot{\mathbf{w}}_a \\ \dot{\mathbf{w}}_b \end{bmatrix} + \begin{bmatrix} \mathbf{K}_{aa} & \mathbf{K}_{ab} \\ \mathbf{K}_{ba} & \mathbf{K}_{bb} \end{bmatrix} \begin{bmatrix} \mathbf{w}_a \\ \mathbf{w}_b \end{bmatrix}$$
$$- (1-\alpha) \begin{bmatrix} 0 & 0 \\ 0 & \mathbf{K}_{bb} \end{bmatrix} \begin{bmatrix} \mathbf{w}_a \\ \mathbf{w}_b \end{bmatrix} + (1-\alpha) \begin{bmatrix} 0 & 0 & 0 \\ \mathbf{K}_{bx} & \mathbf{K}_{by} & \mathbf{K}_{bxy} \end{bmatrix} \begin{bmatrix} \mathbf{Y}_{bx} \\ \mathbf{Y}_{by} \\ \mathbf{Y}_{bxy} \end{bmatrix} = \begin{bmatrix} \bar{\mathbf{P}}_a(t) \\ \bar{\mathbf{P}}_b(t) \end{bmatrix} \tag{3.59a}$$

with

$$\dot{\mathbf{Y}}_{bx} = \mathbf{H}_{bx}(\dot{\kappa}_{bx}, Y_{bx}), \quad \dot{\mathbf{Y}}_{by} = \mathbf{H}_{by}(\dot{\kappa}_{by}, Y_{by}) \quad \text{and} \quad \dot{\mathbf{Y}}_{bxy} = \mathbf{H}_{bxy}(\dot{\kappa}_{bxy}, Y_{bxy}) \ . \tag{3.59b}$$

The subindex a denotes the affiliated matrices or vectors of the elastic nodal degrees of freedom, while subindex b is for the plastic ones. With this method, if the total number of the yielding related elements is n, the maximum number of hysteretic variables to be concerned is then $48 \times n$.

This idea is applied in [33] for the elastic-plastic frame structure under the condition that the yielding locations are predefined. As a result the unknowns in the global differential equation keep unchanged during the whole analysis procedure. But if the yielding locations are identified within the calculation process instead of previously defined, the patch method has difficulties to catalogue the hysteretic variables by programming, since they are not always present in the differential equation. With the split method described below this drawback can be overcome.

Split Method

Considering that each of the vectors $\mathbf{Y}_{gx}$, $\mathbf{Y}_{gy}$ and $\mathbf{Y}_{gxy}$ in (3.58a) has the dimension N_Y, which is the total number of curvature degrees of freedom and is generally unequal to the number of deformation degrees of freedom N. Actually in these Y-vectors only the components, which correspond directly to the yielding nodes, have to be considered as hysteretic, while the others are equal the elastic curvatures κ_i , since the yielding appears only on certain nodes. Therefore the vector $\mathbf{Y}$ for the entire system can be

split up into a pure hysteretic and a pure elastic vector.

For example, if two yielding nodes, e.g. j and k, are identified in the system, i.e., $n_p = 2$, the vector $\mathbf{Y}_{gx}$ can be split as

$$\begin{aligned}\Big[\mathbf{Y}_{gx}\Big]_{N_Y\times 1} &= \begin{bmatrix} 0 \\ \vdots \\ Y_{gx,j} \\ \vdots \\ Y_{gx,k} \\ \vdots \\ 0 \end{bmatrix} + \begin{bmatrix} \kappa_{gx,1} \\ \vdots \\ 0 \\ \vdots \\ 0 \\ \vdots \\ \kappa_{gx,N_Y} \end{bmatrix} \\ &= \mathbf{T}_s\,\mathbf{Y}_x + (\mathbf{I}_y - \mathbf{T}_s\,\mathbf{T}_s^T)\boldsymbol{\kappa}_{gx} \\ &= \mathbf{T}_s\,\mathbf{Y}_x + (\mathbf{I}_y - \mathbf{T}_s\,\mathbf{T}_s^T)\mathbf{B}_{gx}\,\mathbf{w}\end{aligned} \tag{3.60a}$$

where

$$\mathbf{T}_s = \begin{bmatrix} 0 & 0 \\ \vdots & \vdots \\ 1 & \vdots \\ \vdots & \vdots \\ \vdots & 1 \\ \vdots & \vdots \\ 0 & 0 \end{bmatrix}_{N_Y\times n_p} \begin{matrix} \\ \\ \leftarrow \text{j-row} \\ \\ \\ \leftarrow \text{k-row} \\ \\ \\ \end{matrix} \quad , \quad \mathbf{Y}_x = \begin{bmatrix} Y_{gx,j} \\ Y_{gx,k} \end{bmatrix} \quad , \quad \mathbf{I}_y = \text{identity matrix}_{\,(N_Y\times N_Y)} \; . \tag{3.60b}$$

$\boldsymbol{\kappa}_{gx}$ is the assembling vector of the elastic curvatures $\kappa_{gx,i}$, which are determined on the nodes according to the global numbering of $Y_{gx,i}$ $(i = 1 \ldots N_Y)$.
And $\boldsymbol{\kappa}_{gx} = \mathbf{B}_{gx}\,\mathbf{w}$, where $\mathbf{B}_{gx}$ is the summation of the local curvature determination matrix $\mathbf{B}_{ex}$.

According to (3.35a), $\mathbf{B}_{ex}$ satisfies

$$\boldsymbol{\kappa}_{ex} = \mathbf{B}_{ex}\,\mathbf{w}_e \quad \text{with} \quad \mathbf{B}_{ex,\,ij} = B_{x,j}(\eta_i, \zeta_i) \; , \tag{3.60c}$$

where $\boldsymbol{\kappa}_{ex}$ is the vector of the local curvatures corresponding to the nodes defined in Fig. 3.10. In (3.60c) the subindex $i = 1 \ldots 16$ denotes the node number, as $j = 1 \ldots 16$ denotes the curvature shape function.

Similarly the hysteretic vectors $\mathbf{Y}_{gy}$ and $\mathbf{Y}_{gxy}$ can be also split as

$$\begin{aligned}\mathbf{Y}_{gy} &= \mathbf{T}_s\,\mathbf{Y}_y + (\mathbf{I}_y - \mathbf{T}_s\,\mathbf{T}_s^T)\mathbf{B}_{gy}\,\mathbf{w} \\ \mathbf{Y}_{gxy} &= \mathbf{T}_s\,\mathbf{Y}_{xy} + (\mathbf{I}_y - \mathbf{T}_s\,\mathbf{T}_s^T)\mathbf{B}_{gxy}\,\mathbf{w}\end{aligned} \tag{3.60d}$$

The prerequisite of applying this method is the compatibility described in section 3.3.2, otherwise the potential energy calculated through the nodal curvatures is unequal the one through the nodal deformations, i.e., $\mathbf{K}_e\,\mathbf{w}_e \neq \alpha\,\mathbf{K}_e\,\mathbf{w}_e + (1-\alpha)(\mathbf{K}_{ex}\boldsymbol{\kappa}_{ex} + \mathbf{K}_{ey}\boldsymbol{\kappa}_{ey} + \mathbf{K}_{exy}\boldsymbol{\kappa}_{exy})$.

A disadvantage of this method is the large dimension of the matrices $\mathbf{B}_{gx}$, $\mathbf{B}_{gy}$ and $\mathbf{B}_{gxy}$, which will occupy additional working memories of the computer. But if the yielding locations are predetermined the patch method can be first used to filter out the yielding related elements, then the split method can be further applied on these elements, so that the number of the hysteretic variables and the dimension of the corresponding matrices can be minimized. Such applications will be illustrated in chapter 5.

3.4.2 Modal Transformation

The next step of reducing the size of the differential equation will be undertaken with deformation degrees of freedom $\mathbf{w}$, which is fixed by the physical arrangement of the structure; in general all of these degrees of freedom would be involved in the static analysis. On the other hand, not all of them need to be considered as independent variables in the response analysis of an arbitrary dynamic loading [17].

Using the discrete FE-formulation, the eigenvectors can construct a multidimensional modal space, in which all kind of deformation figures (limited by the FE-discretization) can be represented as the linear combination of the basic vectors, no matter whether the material behavior is elastic or plastic. Therefore the modal analysis, which has the following advantages, is chosen as a foundation of reducing the DOF :

1. Orthogonality - The elastic parts of the differential equations will be decoupled because of the orthogonality of the mode shapes.
2. Efficiency - Under equally distributed loadings, which are the most cases in dynamics, the elastic system responses can be described with sufficient accuracy by employing only a few modal degrees of freedom.

With the modal transformation the geometrical deformation vector $\mathbf{w}$ can be expressed through the linear combination of all eigenvectors ϕ_i as

$$\mathbf{w} = \phi_1\, w_1^* + \phi_2\, w_2^* + \cdots + \phi_N\, w_N^* = \Phi\,\mathbf{w}^* \;, \tag{3.61}$$

where N is system degrees of freedom, Φ is the mode-shape matrix, whose i column is the eigenvector ϕ_i, and $\mathbf{w}^*$ is the vector of the generalized degrees of freedom w_i^*.

The eigenvalues and eigenvectors will be determined from the general eigenvalue problem

$$\mathbf{K}\phi_i = \lambda_i\,\mathbf{M}\phi_i \;, \tag{3.62}$$

where $\mathbf{K}$ and $\mathbf{M}$ are symmetric, positive definite, $N \times N$ system matrices. The natural frequency of the system is $\omega_i = \sqrt{\lambda_i}$.

If the eigenvectors are normalized according to $\mathbf{M}$, the following orthogonality can be found

$$\phi_i^T \mathbf{M} \phi_j = \delta_{ij} \quad \text{and} \quad \phi_i^T \mathbf{K} \phi_j = \lambda_i \, \delta_{ij} \ , \tag{3.63}$$

where δ_{ij} is the Kronecker delta.

Setting (3.60a), (3.60d) and (3.61) in (3.58), then multiplying the whole differential equation from left by Φ^T, the following equation can be derived

$$\begin{aligned}
&\big(\Phi^T \mathbf{M} \Phi\big)\ddot{\mathbf{w}}^* + \big(\Phi^T \mathbf{C} \Phi\big)\dot{\mathbf{w}}^* + \alpha\big(\Phi^T \mathbf{K} \Phi\big)\mathbf{w}^* \\
&+ (1-\alpha)\big(\Phi^T \mathbf{K}_{gx}(\mathbf{I}_y - \mathbf{T}_s\,\mathbf{T}_s^T)\mathbf{B}_{gx}\Phi\big)\mathbf{w}^* + (1-\alpha)\big(\Phi^T \mathbf{K}_{gx}\mathbf{T}_s\big)\mathbf{Y}_x \\
&+ (1-\alpha)\big(\Phi^T \mathbf{K}_{gy}(\mathbf{I}_y - \mathbf{T}_s\,\mathbf{T}_s^T)\mathbf{B}_{gy}\Phi\big)\mathbf{w}^* + (1-\alpha)\big(\Phi^T \mathbf{K}_{gy}\mathbf{T}_s\big)\mathbf{Y}_y \\
&+ (1-\alpha)\big(\Phi^T \mathbf{K}_{gxy}(\mathbf{I}_y - \mathbf{T}_s\,\mathbf{T}_s^T)\mathbf{B}_{gxy}\Phi\big)\mathbf{w}^* + (1-\alpha)\big(\Phi^T \mathbf{K}_{gxy}\mathbf{T}_s\big)\mathbf{Y}_{xy} = \Phi^T \bar{\mathbf{P}}(t)
\end{aligned}$$

$\Longrightarrow$

$$\begin{aligned}
\mathbf{M}^*\ddot{\mathbf{w}}^* + \mathbf{C}^*\dot{\mathbf{w}}^* + \alpha\,\mathbf{K}^*\mathbf{w}^* + (1-\alpha)(\mathbf{K}_{rx}^* + \mathbf{K}_{ry}^* + \mathbf{K}_{rxy}^*)\mathbf{w}^* \\
+ (1-\alpha)(\mathbf{K}_{Yx}^*\mathbf{Y}_x + \mathbf{K}_{Yy}^*\mathbf{Y}_y + \mathbf{K}_{Yxy}^*\mathbf{Y}_{xy}) = \bar{\mathbf{P}}^*(t)
\end{aligned} \tag{3.64a}$$

with the auxiliary vectors of nonlinear equations

$$\dot{\mathbf{Y}}_x = \mathbf{H}_x(\dot{\kappa}_x, Y_x), \quad \dot{\mathbf{Y}}_y = \mathbf{H}_y(\dot{\kappa}_y, Y_y) \quad \text{and} \quad \dot{\mathbf{Y}}_{xy} = \mathbf{H}_{xy}(\dot{\kappa}_{xy}, Y_{xy}) \ , \tag{3.64b}$$

where the definitions of the generalized (*) matrices are

$$\begin{aligned}
&\mathbf{M}^* = \Phi^T \mathbf{M} \Phi \qquad \mathbf{C}^* = \Phi^T \mathbf{C} \Phi \qquad \mathbf{K}^* = \Phi^T \mathbf{K} \Phi \qquad \bar{\mathbf{P}}^*(t) = \Phi^T \bar{\mathbf{P}}(t) \\
&\mathbf{K}_{rx}^* = \Phi^T \mathbf{K}_{gx}(\mathbf{I}_y - \mathbf{T}_s\,\mathbf{T}_s^T)\mathbf{B}_{gx}\Phi \qquad \mathbf{K}_{ry}^* = \Phi^T \mathbf{K}_{gy}(\mathbf{I}_y - \mathbf{T}_s\,\mathbf{T}_s^T)\mathbf{B}_{gy}\Phi \\
&\mathbf{K}_{rxy}^* = \Phi^T \mathbf{K}_{gxy}(\mathbf{I}_y - \mathbf{T}_s\,\mathbf{T}_s^T)\mathbf{B}_{gxy}\Phi \\
&\mathbf{K}_{Yx}^* = \Phi^T \mathbf{K}_{gx}\mathbf{T}_s \qquad \mathbf{K}_{Yy}^* = \Phi^T \mathbf{K}_{gy}\mathbf{T}_s \qquad \mathbf{K}_{Yxy}^* = \Phi^T \mathbf{K}_{gxy}\mathbf{T}_s
\end{aligned} \tag{3.64c}$$

According to (3.63) $\mathbf{M}^*$ is an identity matrix and $\mathbf{K}^*$ a diagonal matrix of the eigenvalues λ_i. In order to avoid the complexity of the damping nature the Rayleigh damping matrix, i.e., proportional to mass- and stiffness-matrix,

$$\mathbf{C} = a\,\mathbf{M} + b\,\mathbf{K} \tag{3.65}$$

is introduced, where a and b are constants. This leads to the diagonalization of the generalized damping matrix $\mathbf{C}^*$. On the other hand, with the definition of the modal damping $C_i^* = 2\,\omega_i\,\zeta_i\,M_i^*$ the damping ratio of the Rayleigh damping is

$$\zeta_i = \frac{a}{2\,\omega_i} + \frac{b\,\omega_i}{2} \ . \tag{3.66}$$

As a result the material constants a and b can be evaluated in the practices by two measurement data pairs of (ζ, ω) from the system.

In contrast with the elastic dynamics there are two significant disadvantages in the nonlinear differential equation (3.64):

- Totally decoupling of this differential equation through the modal transformation is not available.

  Although the correction matrices of the elastic curvatures $\mathbf{K}^*_{rx}$, $\mathbf{K}^*_{ry}$ and $\mathbf{K}^*_{rxy}$ are $N \times N$ square, but in general they are off-diagonally populated. Besides, the modified stiffness matrices of hysteresis $\mathbf{K}^*_{Yx}$, $\mathbf{K}^*_{Yy}$ and $\mathbf{K}^*_{Yxy}$ are non-square and have the dimension $N \times n_p$, where n_p is the number of the yielding nodes.

  But as long as the system responses can be reasonably simulated by a few modal coordinates, i.e., if the modal degrees of freedom can be reduced, the numerical computing costs resulted from this shortcoming is not intolerable.

- A simple modal reduction used in the most elastic cases, i.e., the approximation of the system responses through the few low frequency modes according to the frequency and the distribution of the external excitations, is not adequate for this nonlinear equation.

  As pointed out in [33] concerning the physically nonlinear dynamic system of 3-D frame, when the yielding occurs, the locally enhanced curvature distributions will arise, which can not be accurately described by the few low frequency modes. The internal hysteretic forces generate responses in high frequency range. The same phenomenon can also be expected in the plate structure.

Consequently, the number of modal degrees of freedom involved in a dynamic analysis of a complex plate structure with nonlinear material properties are enormous and a common numerical calculation is infeasible under this circumstance.

3.4.3 Correction's Method of Higher Modes

Before introducing the correction's methods, it should be recalled that the entire dynamic analysis procedure involves two basic approximations:

- The selection of the finite element and the corresponding mesh, which approximates the true strain distribution only in a virtual work sense.
- The modal transformation and reduction, which approximate the physical deformations of the large number of a finite-element system.

If the full set of modal coordinates is included in the modal-superposition, it will give an *exact* solution within the limits of the finite-element assumptions; in other words, the differential equation (3.64) can be solved exactly by superposing all the mode shapes, if possible. Otherwise, the modal truncation errors should be considered and corrected, as the contributions of the higher modes to the system response are no more negligible.

In the literature several methods can be found, in which static deformation figures are added to the superposition of the eigenvectors, to decrease the truncation errors by using the reduced modal basis. One of these methods is briefly interpreted below.

Static Correction Procedure

With the study of modal contributions it can be concluded that, for the higher modes of the system, the resistance tends toward purely static behavior and inertial effects are negligible [17]. Therefore the dynamic system response can be approximately divided into a dynamic part $\mathbf{w}_d$, which is the sum of the lower mode contributions, and a quasi-static part $\mathbf{w}_s$, which is the superposition of the remaining higher modes, as following

$$\mathbf{w}(t) \simeq \mathbf{w}_d(t) + \mathbf{w}_s(t) = \sum_{i=1}^{n_{red}} \phi_i \, w^*_{d,i}(t) + \sum_{i=n_{red}+1}^{N} \phi_i \, w^*_{s,i}(t) = \Phi_r \, \mathbf{w}^*_d(t) + \Phi_h \, \mathbf{w}^*_s(t) \; , \quad (3.67)$$

where n_{red} is the number of the reduced mode shapes. The reduced modal basis is so chosen that the lowest frequency of the neglected modes is wide beyond the highest frequency of the excitations.

Applying this procedure in the nonlinear model established previously the system dynamic response can be determined by using the reduced modal basis through the differential equation

$$\begin{aligned} \mathbf{M}^*\ddot{\mathbf{w}}^*_d + \mathbf{C}^*\dot{\mathbf{w}}^*_d + \alpha\,\mathbf{K}^*\mathbf{w}^*_d + (1-\alpha)(\mathbf{K}^*_{rx} + \mathbf{K}^*_{ry} + \mathbf{K}^*_{rxy})\mathbf{w}^*_d \\ + (1-\alpha)(\mathbf{K}^*_{Yx}\mathbf{Y}_x + \mathbf{K}^*_{Yy}\mathbf{Y}_y + \mathbf{K}^*_{Yxy}\mathbf{Y}_{xy}) = \bar{\mathbf{P}}^*(t) \end{aligned} \quad (3.68)$$

with the auxiliary nonlinear equations (3.64b). It is to note that all the generalized matrices are now calculated through the reduced mode-shape matrix Φ_r instead of Φ after (3.64c).

Then the system response is corrected by adding the quasi-static part, whose modal coordinates can be obtained by ordinary static analysis as

$$w^*_{s,i}(t) = \frac{\bar{P}^*_i(t)}{K^*_i} = \frac{\phi_i^T \, \bar{\mathbf{P}}(t)}{\omega_i^2} \; , \quad \text{so that} \quad \mathbf{w}_s(t) = \sum_{i=n_{red}+1}^{N} \frac{\phi_i \, \phi_i^T}{\omega_i^2} \, \bar{\mathbf{P}}(t) \; . \quad (3.69)$$

To avoid the evaluation of the higher mode shapes, this quasi-static part can be expressed through the total static response given by all modes and subtracting the static

response developed in the first n_{red} modes as

$$\mathbf{w}_s(t) = \mathbf{K}^{-1}\,\bar{\mathbf{P}}(t) - \sum_{i=1}^{n_{red}} \frac{\phi_i\,\phi_i^T}{\omega_i^2}\,\bar{\mathbf{P}}(t)\ . \tag{3.70}$$

This concept is adopted in [61] and [74], in which the internal nonlinear restoring forces, comparable with the $\mathbf{Y}$ terms in (3.68), are moved to the right hand side of the equation and treated as the external loadings.

Another methods such as the *Mode Acceleration Method* [17], which is similar to the *Static Correction Procedure* but was developed several decades earlier following a different line of reasoning, and the *Modal Augmentation Method* [36] serve also the purpose of avoiding certain higher mode errors. A discussion of them can be found in [33].

3.4.4 Plastic Shape Function

The methods mentioned in previous section have one thing in common – the contribution of higher modes is statically approximated, i.e., their inertia and damping effects are neglected. But generally the inertial and damping forces will arise from the disproportionately increased curvature under yielding.

In order to make the evaluation of the higher mode contributions in a nonlinear dynamic analysis more accurately and more efficiently, the concept of *Plastic-Shape-Function* (PSF) was first proposed by Grundmann [31], who suggests that the locally amplified curvature distribution and its corresponding deformation figure resulted from yielding could be condensed within particular PSFs in accordance with the plastification locations . So that the few PSFs can replace the higher eigenmodes in the modal analysis and be added on the reduced modal bases as extended modes. Until now this concept is already successfully applied on the nonlinear 3-D frame structure. About the developing history of the PSF is reported in section 1.2.

Therefore the other possibility to reduce the degrees of freedom of (3.64) for a nonlinear plate system and to maintain the accuracy of solutions at the same time is to extend the reduced basis, which is used in elastic dynamics, with the adaptable PSFs for the plate structure. The quality of solutions depends then directly on how well the PSF can reproduce the curvature distribution of yielding, i.e., how well the PSF can simulate the contribution of higher eigenmodes. The basic considerations, the requirements and the evolution of the plastic shape function is illustrated in the next chapter.

Chapter 4

Development of Plastic-Shape-Functions

4.1 Basic Requirements and Concept

In order to ensure that the PSF can reasonably substitute the higher modes needed in the modal analysis of a nonlinear system and provide a reliable solution, the PSF should satisfy the following basic requirements:

- Satisfaction of the boundary conditions – the PSFs should fulfill the essential and the natural boundary conditions of the system, since they are used as the modal vectors to build the virtual displacement, which corresponds to the test function in the Galerkin Method.
- Reconstruction of the curvature distribution – the PSFs should be able to describe the local curvature distribution specific to the yielding.
- Orthogonality – the PSFs should be orthogonalized with respect to the lower modes, which are used for the elastic part of the system responses, so that they can serve as independent new bases to expand the modal space for the nonlinear dynamic problems.

The basic concept of PSF is : Under the dynamic process, the yielding specific deformation and the corresponding stress distribution of a part of the system can be described as the multiplication of a time-variant amplitude with a basic geometrical figure, which has a unit plastic deformation. This basic deformation figure can be used as a kind of modal vector and its time-variant amplitude is then the generalized degree of freedom. And this basic deformation figure is the so-called *Plastic Shape Function*.

To illustrate this concept, taking a one-side restrained elongating bar as an example. Considering that this bar has a weak zone 'b1', which has a lower yield limit $\sigma_{Y,b1}$ and a post-yielding stiffness αE, as the others 'b2' have the same material properties but a

higher yield limit $\sigma_{Y,b2}$. The system and the $\sigma - \epsilon$ diagram, which is simplified as the bi-linear hardening model, are shown in Fig. 4.1 (a) and (b).

Supposed that at a particular time the bar has the internal stress σ_n, which is smaller than $\sigma_{Y,b2}$ but higher than $\sigma_{Y,b1}$, that just the weak zone 'b1' yields and has a unit plastic strain $\epsilon_{p,b1}$. The corresponding stress and strain distribution is shown in Fig. 4.1 (c).

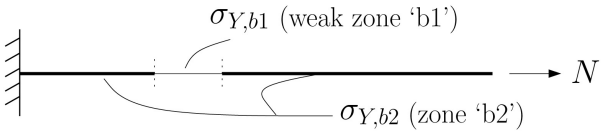

(a) System

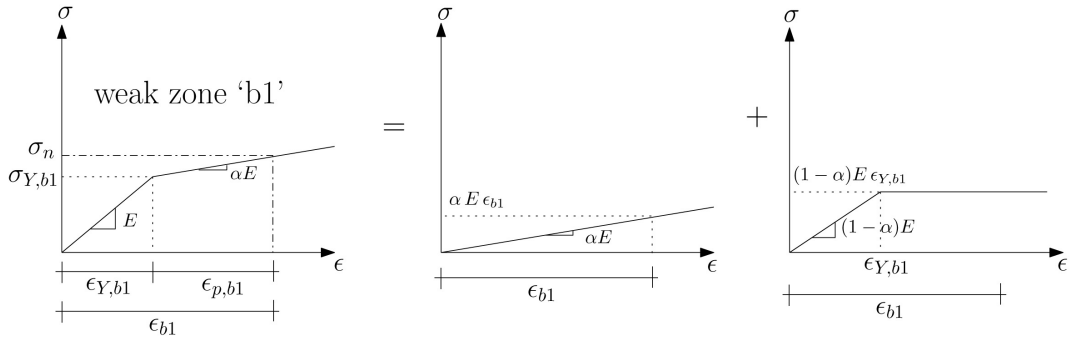

(b) Material Properties

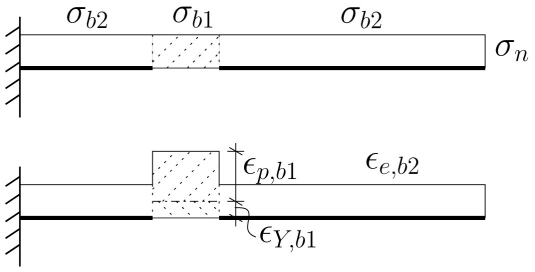

(c) Stress / Strain

Figure 4.1: Elongating Bar

The total strain and stress in zone 'b1' and 'b2' are separately

$$\begin{cases} \epsilon_{b1} = \epsilon_{Y,b1} + \epsilon_{p,b1} \\ \sigma_{b1} = E\,\epsilon_{Y,b1} + \alpha E\,\epsilon_{p,b1} = \sigma_n \end{cases} \qquad \begin{cases} \epsilon_{b2} = \epsilon_{e,b2} + 0 = \epsilon_n \\ \sigma_{b2} = E\,\epsilon_{e,b2} + 0 = \sigma_n \end{cases} \tag{4.1}$$

Separating out the plastic strain and the post-yielding stress, the corresponding distributions as given in Fig. 4.2 are what the PSF should simulate in this particular example. It is to note that this PSF can be further normalized, so that various plastic strains, as long as the size and the position of the weak zone remains the same, can be simulated by the normalized PSF together with a weighting coefficient.

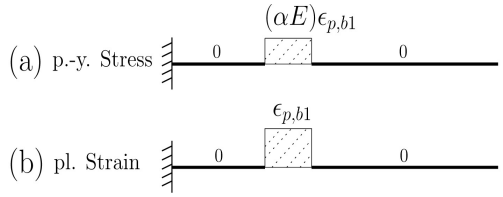

Figure 4.2: Post-Yielding Stress / Pl. Strain

To reproduce this strain distribution and to find its static deformation figure, imagining that only the part 'b1' of the same bar has an elastic strain with the magnitude $\epsilon_{p,b1}$ under a particular circumstance. This part 'b1' will be cut off and loaded by fictive external compression forces $N_p = -EA\,\epsilon_{p,b1}$ as shown in Fig. 4.3, so that its strain reduces to zero. Then the clipped 'b1' will be put back on the system. Subsequently the whole system will be released and loaded by the fictive reaction forces.

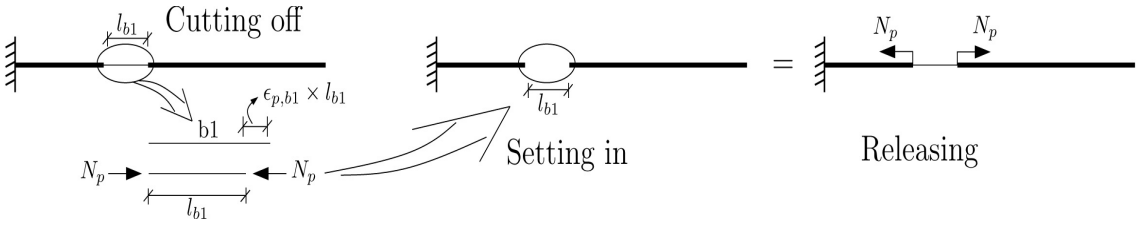

Figure 4.3: Reproduction of pl. Strain

This statically loaded system in Fig. 4.3 has then the same strain distribution as the plastic portion shown in Fig. 4.2 (b). The next question: does this system also provide the exact stress distribution as given in Fig. 4.2 (a) ? At first sight the fictive reaction forces result in the elastic stress $E\epsilon_{p,b1}$, which is unequal to the desired post-yielding stress $\alpha E\epsilon_{p,b1}$, in the yield zone 'b1'.

But actually, as the part 'b1' yields, the stress inside 'b1' will be evaluated according the hysteretic equation:

$$\sigma = \alpha E\epsilon + (1-\alpha)E\,\xi\ , \tag{4.2}$$

therefore the post-yielding stress distribution is also correct. In other words, the plastic part of the strain distribution is indeed calculated linear elastically, but its corresponding stress distribution is determined nonlinearly.

Satisfying the distribution of the plastic strain and the post-yielding stress, the deformation figure that resulted from the statically loaded system given in Fig. 4.3 is the plastic shape function needed for this example. Normalizing this plastic shape function and equipping it with a weighting coefficient, then it can serve as a kind of modal vector for the dynamic analysis.

4.1.1 Elongating Bar

To verify this derivation, a numerical analysis of the system given in Fig. 4.1 (a) is performed. It is assumed that the steel bar has the length $L_b = 1\ [m]$ and is discretized in 100 elements with a element length of $L_e = 0.01\ [m]$. The other material and system constants are defined as:

$$E = 2.1{\cdot}10^5\ [N/mm^2], \quad \sigma_Y = 240\ [N/mm^2], \quad A = 100\ [mm^2] \quad \text{and} \quad \mu = 0.008\ [kg/m]\ .$$

The bar is loaded in the horizontal direction on the $76'th$ to $81'th$ elements by the distributed load $p(t)$ shown in Fig. 4.4, in which $H(t)$ is the Heaviside function. The total loading time is $t_{max} = 16\ [s]$, the sampling time span is $\Delta t = 1/32\ [s]$ and the loading frequency is $\omega = 0.4\ [rad/s]$.

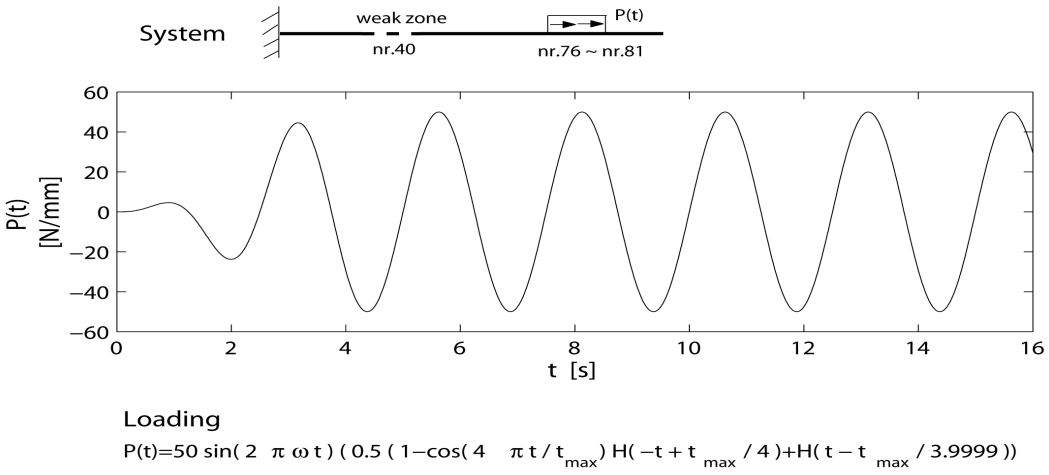

Figure 4.4: System / Loading Function of Elongating Bar

The weak zone 'b1' is set on the element Nr.40, which has a ten times lower yielding strain $\epsilon_{Y,40} = (\sigma_Y/E)/10$ than the other elements to emphasize the yielding. In this discrete system the internal element elongation is assumed to be linear and can be interpolated as

$$u_e(x) = (1 - x/L_e)\, u_{e,l} + (x/L_e)\, u_{e,r} = N_1\, u_{e,l} + N_2\, u_{e,r}\ , \tag{4.3}$$

where $u_{e,l}$ and $u_{e,r}$ are the nodal displacements.

Under this assumption, the strain is constant inside the element, hence only one hysteretic variable z_e according to the Bouc-Wen's model (B.4) is needed per element and the compatible interpolation function of z_e is then $\tilde{N} = 1$. Using the principle of virtual work the local differential equation can be formulated as

$$\mathbf{M}_e\ddot{u} + \mathbf{C}_e\,\dot{u} + \alpha\,\mathbf{K}_e\,u + (1-\alpha)\mathbf{K}_{ex}\,z_e = \bar{\mathbf{P}}_e(t) \tag{4.4a}$$

where

$$\begin{aligned}
\mathbf{M}_e &= \mu \int \begin{bmatrix} N_1 \\ N_2 \end{bmatrix} \begin{bmatrix} N_1 & N_2 \end{bmatrix} dx \\
\mathbf{K}_e &= EA \int \begin{bmatrix} \partial N_1/\partial x \\ \partial N_2/\partial x \end{bmatrix} \begin{bmatrix} \partial N_1/\partial x & \partial N_2/\partial x \end{bmatrix} dx \\
\mathbf{K}_{ex} &= EA \int \begin{bmatrix} \partial N_1/\partial x \\ \partial N_2/\partial x \end{bmatrix} \begin{bmatrix} 1 \end{bmatrix} dx \\
\mathbf{C}_e &= \mathbf{K}_e/500 \qquad \bar{\mathbf{P}}_e(t) = \int \begin{bmatrix} N_1 \\ N_2 \end{bmatrix} p(t)\,dx\ .
\end{aligned} \tag{4.4b}$$

Considering the force equilibrium the global system matrices, i.e., $\mathbf{M}$, $\mathbf{C}$, $\mathbf{K}$, $\mathbf{K}_{gx}$ and $\bar{\mathbf{P}}$ can be established. Then applying the modal transformation the global differential equation in modal space can be written as

$$\mathbf{M}^*\ddot{u}^* + \mathbf{C}^*\,\dot{u}^* + \alpha\,\mathbf{K}^*\,u^* + (1-\alpha)\mathbf{K}^*_{rx}\,z = \bar{\mathbf{P}}^*(t) \tag{4.5a}$$

where u^* is the modal coordinate and according to section 3.4.2, the generalized system matrices are defined as

$$\begin{aligned}
&\mathbf{M}^* = \Phi^T\mathbf{M}\Phi \qquad \mathbf{C}^* = \Phi^T\mathbf{C}\Phi \qquad \mathbf{K}^* = \Phi^T\mathbf{K}\Phi \\
&\mathbf{K}^*_{rx} = \Phi^T\mathbf{K}_{gx}(\mathbf{I}_y - \mathbf{T}_s\,\mathbf{T}_s^T)\mathbf{B}_{gx}\Phi \qquad \bar{\mathbf{P}}^*(t) = \Phi^T\bar{\mathbf{P}}(t)\ .
\end{aligned} \tag{4.5b}$$

As the reference solution all eigenvectors are used in the mode-shape matrix Φ and the strain distribution at time point $t = 10.75s$ is given as the red solid line in the upper part of Fig. 4.5. Analyzing the modal coordinate values at this moment, which is shown in the second part of Fig. 4.5, it can be seen that the first 8 modal shapes almost dominate the system reaction. Therefore the result of using the first 8 modes, which are collected in the reduced basis matrix Φ_{red} to replace Φ as commonly applied in elastic dynamics, is also performed and indicated by the green dashed line. As expected, it can be seen that the locally raised strain due to the yielding can not be covered by the reduced modal basis.

According to the method mentioned in previous section the PSF – ψ_p needed for this example can be calculated through the force vector $\bar{\mathbf{P}}_p$, which has only two opposite single loads $\pm N_p$ on the left and right nodes of the element Nr.40 as shown in Fig. 4.3, under the global degrees of freedom as

$$\psi_p = \mathbf{K}^{-1}\,\bar{\mathbf{P}}_p\ . \tag{4.6}$$

To ensure the orthogonality of the PSF with the reduced bases, the contributions of the reduced bases have to be subtracted from the PSF, since it can be formulated

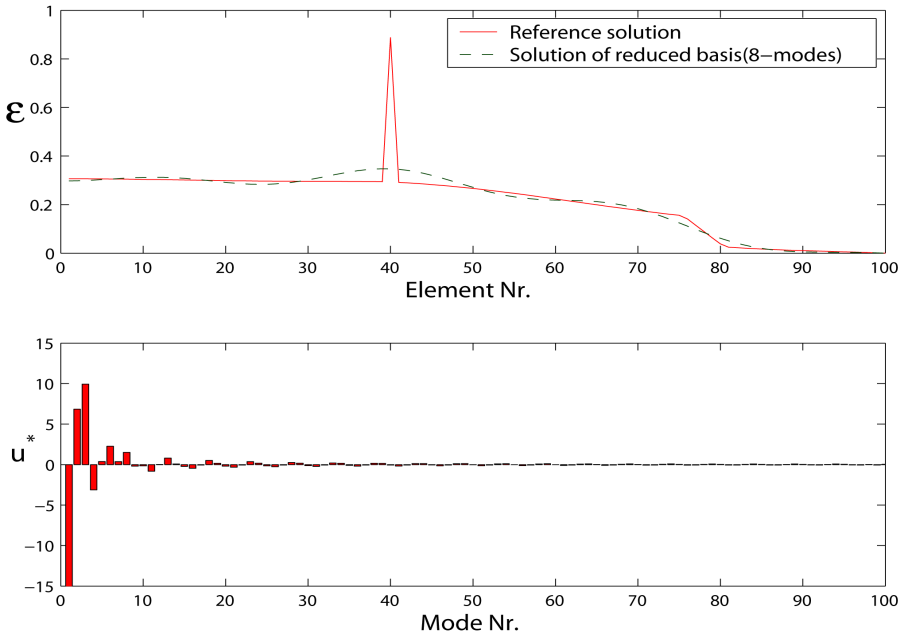

Figure 4.5: Strain Distribution and Modal Contributions of Elongating Bar

as the linear superposition of all the eigenmodes. According to [42] or the so-called Gram-Schmidt method in [17] the orthogonalized PSF can be determined as

$$\tilde{\psi}_p = \psi_p - \Phi_{red}(\Phi_{red}^T \mathbf{M}\, \psi_p) \ . \tag{4.7}$$

In Fig. 4.6 the PSF, which is merely normalized with respect to the mass matrix but unmodified, and the further orthogonalized PSF with respect to the reduced bases Φ_{red} are represented.

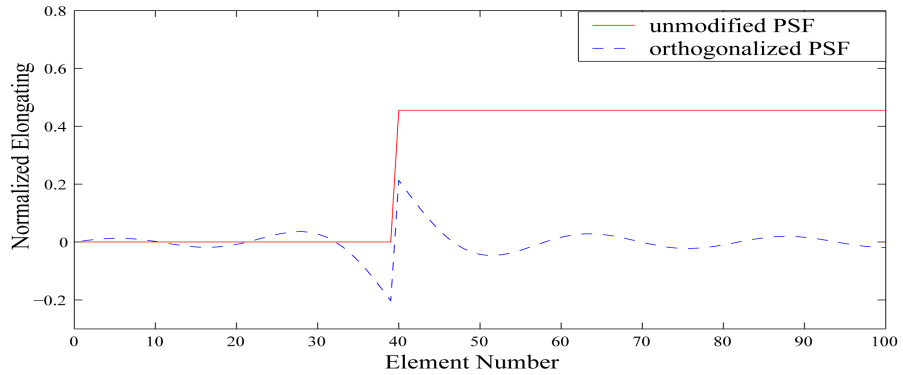

Figure 4.6: Unmodified / Orthogonalized PSF of Elongating Bar

Then the reduced modal space will be extended by adding the PSF in it as

$$\tilde{\Phi}_{red} = \left[\ \phi_1 \quad \phi_2 \quad \ldots \quad \phi_8 \quad \tilde{\psi}_p \ \right] \ . \tag{4.8}$$

Replacing Φ in (4.5) by $\tilde{\Phi}_{red}$, the results of applying the PSF in comparison with the reference solution by different observation time is given in Fig. 4.7. It can be seen that

no matter the displacement or the strain are well rebuilt by using of the PSF under yielding. With only a slight loss of accuracy in comparing to reference solutions, the total modal degrees of freedom is strongly reduced from 100 to 8 and the spending time of numerical evaluation is about 6-times compressed.

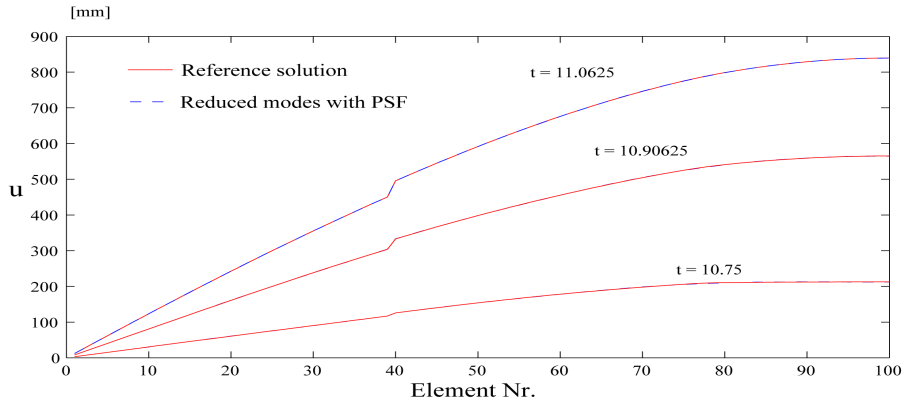

(a) Displacement

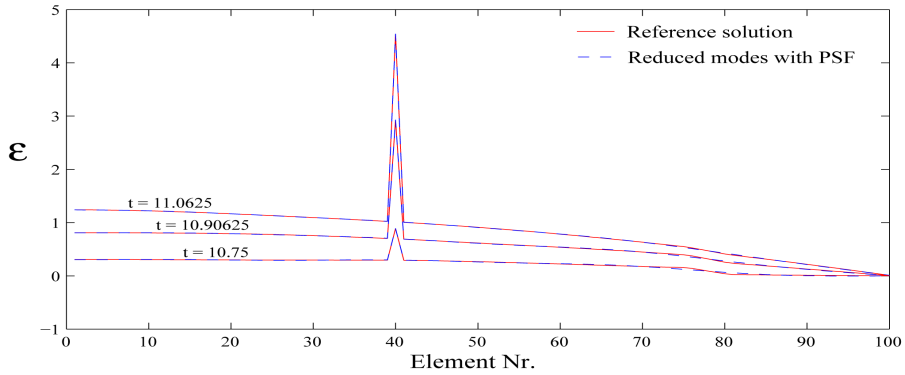

(b) Strain

Figure 4.7: Reference / PSF Applied Solutions of Elongating Bar

Conclusion:

- The Plastic-Shape-Function can be found by the statically deformation analysis of the original system loaded by a force group, which is the opposite of the force group needed for counteracting a unit plastic deformation of the yield zone.
- Only the pure geometrical deformation figure of such static analysis is adopted as the PSF; the internal stresses of the PSF will be determined according to the elastic-plastic constructive material law.
- The PSF can only replace the higher mode contributions which resulted from yielding. The other factors that excite the higher modes, such as the unequally distributed loading, single loads or impulse loading, need to be treated especially.

4.2 PSF of FE Discrete Bending Beam

To extend the concept of the PSF for a general finite element system and to show the systematic determination of the force group needed for producing the PSF, the bending beam is considered in this section. Although the PSF of bending beam has been already developed in [42] and extended for 3-D framework in [33], at this place the PSF of bending beam will be derived from a different way, i.e., from the curvature related stiffness matrix.

Under the ultimate state the beam cross section is fully yielded and forms a hinge with the moment capacity $\tilde{M}_p$ after the theory of plastic hinge. According to this assumption there is a discontinuity of the curvature at the yielding location and the idealized plastic curvature is schematically represented as the dashed line in Fig. 4.8 (a). Depending on the system (statically determinate or indeterminate) and on the loading property (static or dynamic) the enhanced curvature of the plastic hinge can be finite or infinite.

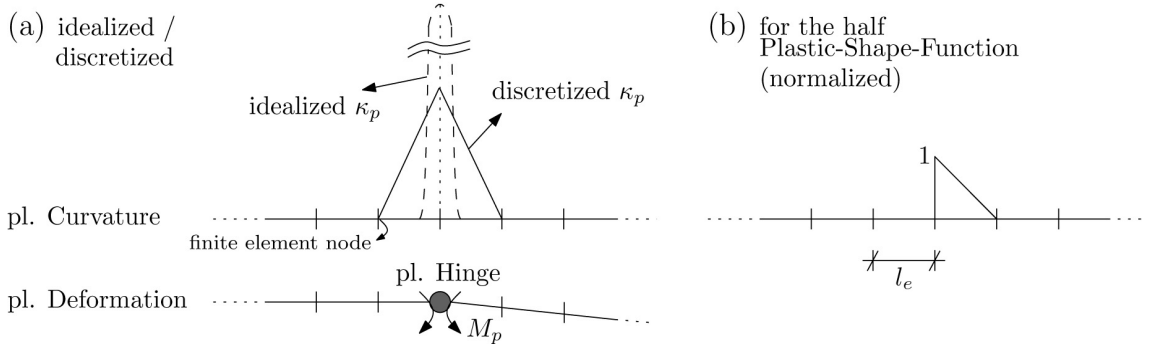

Figure 4.8: pl. Curvature Distribution

In a discrete finite element system this locally concentrated curvature distribution can only be simulated through the derivatives of the deformation shape functions. With the Bernoulli beam theory the typical deformation shape function is the Hermite's interpolation function, which is a third order polynomial. Its second derivative for the curvature is then linear. Therefore the idealized curvature distribution will be approximated through the triangle as shown with the solid line in Fig. 4.8 (a) in a FE-system. It is also to note that in the discretized system the plastic hinge always locates on the nodal point, since the element internal values can only be interpolated, and the minimal detectable *yielding zone* is the discrete element length. Consequently, the enclosed area of the discretized plastic curvature is overestimated, which is an inevitable shortcoming of the FE-discretization, in comparison with the idealized plastic curvature distribution.

The accuracy of this approximation depends on the quality of the deformation shape function and on the fineness of the discretization. Therefore within the limit of the FEM the PSF should and can only reproduce the discretized curvature distribution, but not the 'exact' one. It can be seen from Fig. 4.8 (a) that two adjacent elements are involved with the plastic hinge and have the mirrored plastic curvature distribution of

right triangle form. Hence only one element has to be considered to develop the half PSF.

According to the conclusion made in previous section, the normalized curvature distribution as shown in Fig. 4.8 (b) can be reproduced by a force group, whose opposite results in a negative unit curvature on the left node of the yielding related element on the right hand side. To determine such force group, the concept of the curvature related stiffness matrix introduced in the subsection 3.3.3 can be very useful.

With use of the Hermite's interpolation function the compatible interpolation functions of the curvature $\kappa_x(x) = \tilde{N}_{x,1}\,\kappa_x(0) + \tilde{N}_{x,2}\,\kappa_x(l_e)$ are

$$\tilde{N}_{x,1} = 1 - \frac{x}{l_e} \quad \text{and} \quad \tilde{N}_{x,2} = \frac{x}{l_e}\ , \quad \text{for} \quad 0 \le x \le l_e\ , \tag{4.9}$$

where l_e is the element length. And comparing with (3.56c), the curvature related stiffness matrix of the bending beam can be evaluated as

$$\mathbf{K}_{ex} = \int \mathbf{B}_{4\times1}^{T}(EI)\,\tilde{\mathbf{N}}_{x,1\times2}\,dx = \frac{EI}{{l_e}^3}\begin{bmatrix} -{l_e}^2 & {l_e}^2 \\ {l_e}^3 & 0 \\ {l_e}^2 & -{l_e}^2 \\ 0 & -{l_e}^3 \end{bmatrix}\ , \tag{4.10}$$

where $\tilde{\mathbf{N}}_{x,1\times2} = [\,\tilde{N}_{x,1}\ \tilde{N}_{x,2}\,]$ and $\mathbf{B}_{1\times4}$ is the matrix of the second derivatives of the deformation shape function as given in (D.2b).

As a result the force group $\bar{\mathbf{P}}_{p,r}$, which produces the wished nodal curvature $[\,-1\ 0\,]^T$, can be evaluated as

$$\bar{\mathbf{P}}_{p,r} = \mathbf{K}_{ex}\begin{bmatrix} -1 \\ 0 \end{bmatrix} = \frac{EI}{{l_e}^3}\begin{bmatrix} {l_e}^2 \\ -{l_e}^3 \\ -{l_e}^2 \\ 0 \end{bmatrix}\ . \tag{4.11}$$

It can be proved that this force group can also be obtained through the multiplication of the deformation stiffness matrix $\mathbf{K}_e$ (s. (D.3)) with one of various nodal deformation sets, such as $[\,0\ \frac{-l_e}{3}\ 0\ \frac{l_e}{6}\,]^T$, which can also produce the same nodal curvature $[\,-1\ 0\,]^T$. But such combinations of nodal deformations are not unified and can not be directly embedded in the global system to find the PSF, especially when the system is statically indeterminate.

For the element on the left hand side of the plastic hinge the corresponding force group can be found as $\bar{\mathbf{P}}_{p,l} = \mathbf{K}_{ex}[\,0\ -1\,]$. Combining the opposite of $\bar{\mathbf{P}}_{p,r}$ and the opposite of $\bar{\mathbf{P}}_{p,l}$ as the external forces $\bar{\mathbf{P}}_p$ acting on the beam, which is a vector under the global degrees of freedom as shown in Fig. 4.9, the complete Plastic-Shape-Function ψ_p can be determined through the static analysis as

$$\psi_p = \mathbf{K}^{-1}\bar{\mathbf{P}}_p\ , \tag{4.12}$$

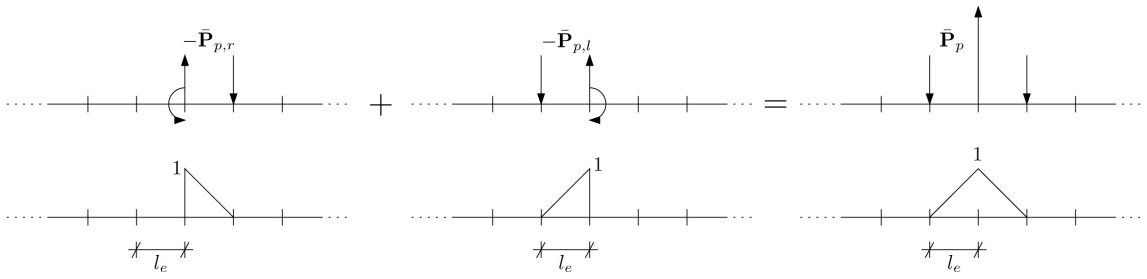

Figure 4.9: Force Group of Producing the PSF of Beam

where $\mathbf{K}$ is the global stiffness matrix of the entire system. The orthogonal PSF $\tilde{\psi}_p$ with respect to the reduced modal bases can be found analogically as (4.7).

In [42] identical PSFs of bending beam as derived in this section are also developed but following different considerations and the numerical examples of this work have verified the accuracy of such PSFs. Examples of the 3-D frame structure by using similar concept of PSF, which show especially the efficiency of PSF, can be found in [33].

Conclusion:

- Within the finite element system the idealized plastic curvature distribution can only be discretely approximated through the second derivatives of the deformation shape function.
- The exact extent of yielding, in which the plastic limit moment $\tilde{M}_p$ is reached, is not explicitly defined. The yielding can only be distinguished on the element nodes and the yielding range inside the element will be linear interpolated (s. [33]). To overcome this deficiency, the FE-net has to be refined around the yielding nodes.
- According to this discrete formulation a chain of plastic hinges will form as the yielding zone incessantly expands.
- Only if the curvature related stiffness matrix $\mathbf{K}_{ex}$ is determined by using the compatible interpolation functions, is the potential energy of yielding exactly formulated within the limit of FEM.
- The force group needed to produce a unit curvature on the left or right element node can be read directly from the corresponding column of the curvature related matrix $\mathbf{K}_{ex}$.
- This method of developing the PSF can be applied not only on the statically determinate system but also on the indeterminate system, since the force group is obtained from the cutting-off element but acts on the complete system, i.e., the boundary conditions of supports are always considered. So that the effects of redundant forces in the statically indeterminate system are automatically included in the PSF.

4.3 PSF of Laterally Loaded Plate

With use of the Kirchhoff plate theory the yielding involves with three curvatures, namely κ_x, κ_y and κ_{xy}. At the yielding location these curvatures have a certain inter-relationship depending on the loading condition and the material property, but on the other hand these three curvatures have their own distribution function and are from this point of view independent of each other.Therefore it is assumed in the present work that there exist three independent plastic shape functions for simulating the plastic curvatures $\kappa_{x,p}$, $\kappa_{y,p}$ and $\kappa_{xy,p}$, which are defined as the portion of curvatures beyond the yielding limit by the strain-hardening material.

Because of the two-dimensional nature of plate and various combinations of the yielding stresses, it is not easy to represent the real distribution of the plastic curvatures graphically. But similar to the concept of the plastic hinge, the yielding zone of plate can be idealized as a concentrated small point at the beginning. As a result,depending on the principal stress direction, each of the plastic curvatures $\kappa_{x,p}$, $\kappa_{y,p}$ and $\kappa_{xy,p}$ under this idealization could have a peak-shaped distribution.

As mentioned in the previous section the yielding can only be described discretely and starts from a node in the FE formulation. For example it can be the joint node of four adjacent elements, and is enclosed by them, while the other elements still behave elastically. To illustrate such discrete simulation, Fig. 4.10 shows the plastic curvature $\kappa_{x,p}$ of a yielding element corner node. It can be seen that under the use of bi-cubic deformation shape function, the discrete $\kappa_{x,p}$ is linear in x- and cubic in y-direction and is also symmetric with respect to these to axes.

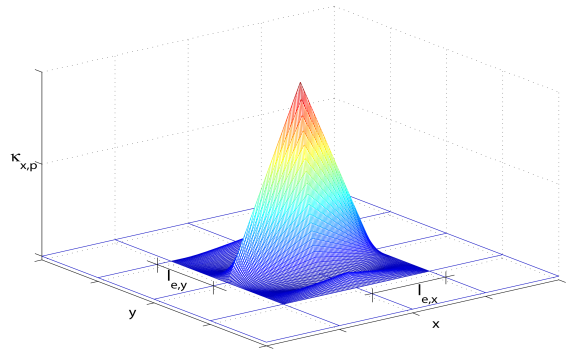

Figure 4.10: Discretized Plastic Curvature $\kappa_{x,p}$

To rebuild the curvature distribution given in Fig. 4.10 through the PSF, only one of the four yielding related elements has to be considered by using the symmetry conditions. Taking the element Nr.1 in Fig. 4.11 (a) as example, the PSFs of this element should have a unit curvature at the local node Nr.3 with corresponding distributions for $\kappa_{x,p}$, $\kappa_{y,p}$ and $\kappa_{xy,p}$ respectively, which are shown in Fig. 4.11 (b)$\sim$(d).

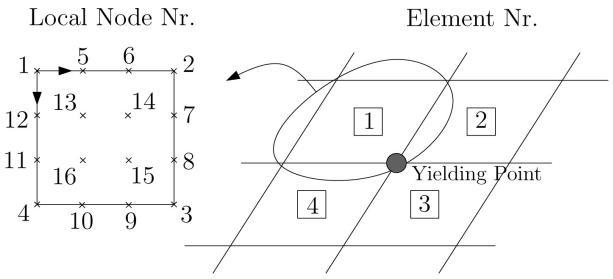

(a) Local Node Nr. / Element Nr.

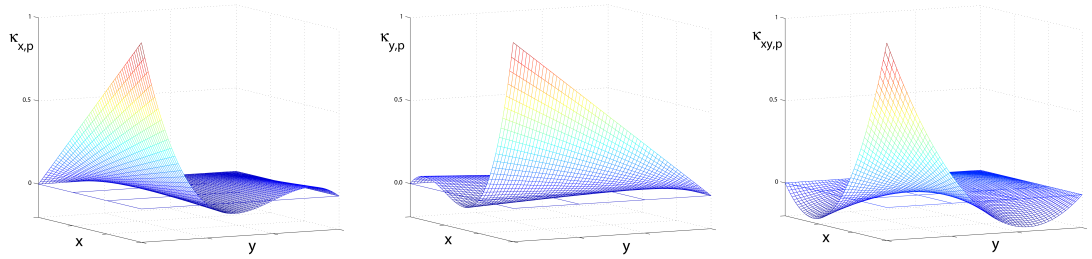

(b) $\kappa_{x,p}$ (c) $\kappa_{y,p}$ (d) $\kappa_{xy,p}$

Figure 4.11: Nodal Plastic Curvatures of One Single Element

According to the conclusion made in section 4.2, the static force group needed to create such compatible unit curvature distribution can be determined through the stiffness matrix of hysteresis. It can be read from Fig. 4.11 (b) that the nodal curvature values are $\kappa_{x,p3} = 1$, $\kappa_{x,p9} = 2/3$ and $\kappa_{x,p10} = 1/3$, by which the numeral index is the node number, as the other nodal values are equal to zero. Collecting these nodal curvatures in the vector $\boldsymbol{\kappa}_{u3} = \begin{bmatrix} 0 & 0 & 1 & 0 & 0 & 0 & 0 & 0 & 2/3 & 1/3 & 0 & 0 & 0 & 0 & 0 & 0 \end{bmatrix}^T$, so that the force group $\bar{\mathbf{P}}_{xp,u3}$, which has the dimension of 16×1, for a unit curvature at node Nr.3 of element Nr.1 can be determined as

$$\bar{\mathbf{P}}_{xp,u3} = \mathbf{K}_{ex}\, \boldsymbol{\kappa}_{u3} \ , \tag{4.13}$$

where $\mathbf{K}_{ex}$ comes from (3.56c).

The curvature interpolation functions derived from section 3.3.2 have the following relationship

$$\tilde{N}_{x,3} + \frac{2}{3}\,\tilde{N}_{x,9} + \frac{1}{3}\,\tilde{N}_{x,10} = 2\,\tilde{N}_{x,3} = \eta\,(\zeta - 4.5\,\zeta^2 + 4.5\,\zeta^3) \ , \tag{4.14}$$

since κ_x is linear in the x-direction. Therefore the columns of the matrix $\mathbf{K}_{ex}$ are also dependent on each other corresponding to the relation of curvature interpolation functions $\tilde{N}_{x,i}$. It can be verified that the force group $\bar{\mathbf{P}}_{xp,u3}$ is equal to two times of the *3rd* column of $\mathbf{K}_{ex}$, which is the force vector corresponding to the single unit curvature of node Nr.3. This indicates that each column of $\mathbf{K}_{ex}$ can serve directly as the static force group needed for producing the PSF of the corresponding node, because only the geometrical figure is relevant for the modal vector.

To rebuild the discretized plastic curvature $\kappa_{x,p}$ as shown in Fig. 4.10 and to find its corresponding PSF – ψ_{xp} , the 3rd, the 4th, the 1st and the 2nd columns of $\mathbf{K}_{ex}$ have to be used as the loading vectors on the element Nr.1, Nr.2, Nr.3 and Nr.4, which are according to the element numbering given in Fig. 4.11 (a), respectively. So that a global loading vector $\bar{\mathbf{P}}_{xp}$ will be established and the PSF can be determined as

$$\psi_{xp} = \mathbf{K}^{-1}\bar{\mathbf{P}}_{xp} \ , \tag{4.15}$$

where $\mathbf{K}$ is the deformation stiffness matrix of the global system.

Beside the PSF ψ_{xp} for the plastic curvature $\kappa_{x,p}$ the other two PSFs ψ_{yp} and ψ_{xyp}, which are corresponding to $\kappa_{y,p}$ and $\kappa_{xy,p}$, should also be determined, since the yielding of plate involves with these three curvatures. Similarly the PSFs ψ_{yp} and ψ_{xyp} will be created by setting the force groups, which can be read directly from the hysteretic stiffness matrix $\mathbf{K}_{ex}$ and $\mathbf{K}_{exy}$ in (3.56c) respectively, on the corresponding elements to form the global force vectors $\bar{\mathbf{P}}_{yp}$ and $\bar{\mathbf{P}}_{xyp}$, and then can be evaluated statically as

$$\psi_{yp} = \mathbf{K}^{-1}\bar{\mathbf{P}}_{yp} \qquad \text{and} \qquad \psi_{xyp} = \mathbf{K}^{-1}\bar{\mathbf{P}}_{xyp} \ . \tag{4.16}$$

The orthogonal PSFs $\tilde{\psi}_{xp}$, $\tilde{\psi}_{yp}$ and $\tilde{\psi}_{xyp}$ with respect to the reduced modal bases Φ_{red} can be determined analogically according to (4.7).

Because of the curvature interpolation nodes defined in Fig. 3.10, the yielding can be distinguished not only on the corner nodes, whose PSF has been developed above, but also on the nodes on the edges and inside the element. The PSFs for the latter two cases can also be developed by applying the same procedure illustrated in this section. It is to note that the yielding on the element edge involves two elements, while the internal yielding node concerns with only one element.

Conclusion:

1. Under the FE-formulation of the plate each discrete node has three independent PSFs, which are corresponding to the plastic curvature $\kappa_{x,p}$, $\kappa_{y,p}$ and $\kappa_{xy,p}$ respectively.

2. The static loading group needed to create the local PSF for a particular node of a single element, i.e., the local force group, is the node number coincident column vector of the hysteretic stiffness matrices $\kappa_{x,p}$, $\kappa_{y,p}$ or $\kappa_{xy,p}$, depending on which PSF is looked for.

3. According to the location of the yielding node, i.e., on the corner, on the edge or inside of the element, different local force groups obtained from point 2. will be put on the corresponding elements to establish the complete force vector of the global system. Then the PSF of the global system can be determined through the static analysis by using the stiffness matrix K.

4. Because of the nature of the curvature interpolation functions $\tilde{N}(x, y)$, not all the local PSFs are linear independent with each other. For example, $\psi_{xp,n5}$, which is the PSF corresponding to $\kappa_{x,p}$ for the local node Nr.5, can be expressed through the combination of $\psi_{xp,n1}$ and $\psi_{xp,n2}$, which are PSFs for node Nr.1 and Nr.2 respectively. And for the twisting curvature $\kappa_{xy,p}$ are the PSFs: $\psi_{xyp,n5} = \psi_{xyp,n6}$, $\psi_{xyp,n13} = \psi_{xyp,n14} = \psi_{xyp,n15} = \psi_{xyp,n16}$, ... and so forth.

Detailed investigations of applying the PSFs for the nonlinear dynamic analysis of plate will be given in chapter 5 by means of various numerical examples.

Chapter 5

Numerical Verification of PSFs

In order to verify the accuracy and the efficiency of applying the plastic shape functions, the nonlinear dynamic analysis of a rectangular steel plate under harmonic loading with considerations of various yielding conditions will be illustrated in this chapter.

5.1 System and Loading

As represented in Fig. 5.1 the rectangular plate is assumed to be simple supported at its four sides. This plate system discretized in a 10×10 finite element net, which has totally 400 degrees of freedom by using the Schäfer plate element introduced in section 3.3.1.

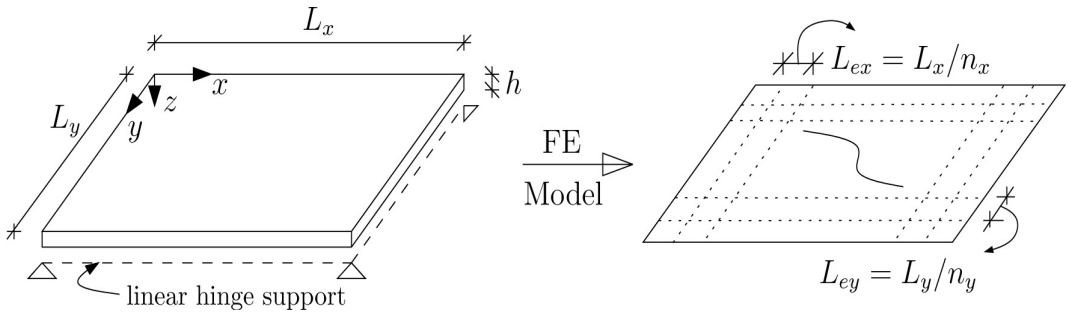

Figure 5.1: Simply Supported Plate System / FE Discretization

The system dimensions and material parameters, i.e., construction steel 'S 235' after the norm [1], are

$$L_x = 2.0\,[m], \qquad L_y = 1.2\,[m], \qquad h = 0.002\,[m], \qquad n_x = 10, \qquad n_y = 10$$

$$E = 210 \cdot 10^6\,[kN/m^2], \qquad \sigma_Y = 235 \cdot 10^3\,[kN/m^2], \qquad \nu = 0.3, \qquad \rho = 78.5\,[kN/m^3]$$

This plate system is oscillated by a uniformly distributed harmonic loading over the entire area, which is formulated as

$$\bar{p}(x,y,t) = P_a \sin(2\pi f t)\Big[0.5\big(1-\cos(\frac{4\pi t}{t_{max}})\big)H(-t+\frac{t_{max}}{4}) + H(t-\frac{t_{max}}{3.9999})\Big] \ , \quad (5.1)$$

where P_a is the maximal loading amplitude, f is the loading frequency, t_{max} is the loading duration and $H(.)$ is the Heaviside function. This loading function with $P_a = 2.5\,[kN/m^2]$, $f = 0.9$ and $t_{max} = 16\,[sec.]$ is schematically illustrated in Fig. 5.2.

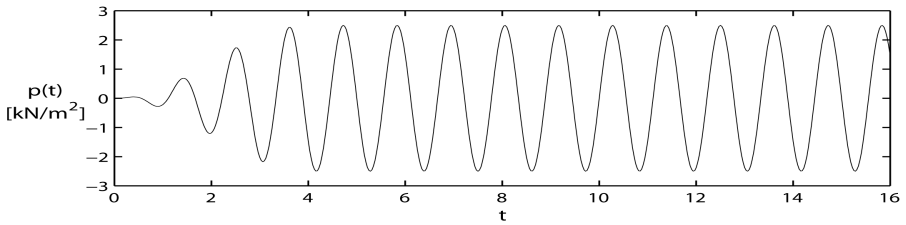

Figure 5.2: Harmonic loading

5.2 Reduced Nonlinear Differential Equation

Generally, if any node in the FE model is considered as possible to yield, then each node has three nonlinear variables, i.e., Y_x, Y_y and Y_{xy}, and the maximal number of the Y-variables of the system defined above is 2759, when the Y-nodal net of the element is specified after Fig. 3.10. Such number of Y-variables is much higher than the deformation DOF ($N = 400$) to be calculated by a commercial PC. But fortunately not all the nodes have to be calculated nonlinearly, since only a part of them will yield even under the limit state of the plate.

In the following studies of different yielding conditions it is always assumed that the locations of the yielding nodes are known and the number of the additional nonlinear differential equations for the hysteretic variables will be correspondingly reduced. First the patch method will be applied to establish the global stiffness matrix. With this method only the yielding related elements will be equipped with elastic and hysteretic stiffness parts as

$$\alpha\,\mathbf{K}_e\,\mathbf{w}_e + (1-\alpha)(\mathbf{K}_{ex}\mathbf{Y}_{ex} + \mathbf{K}_{ey}\mathbf{Y}_{ey} + \mathbf{K}_{exy}\mathbf{Y}_{exy}) \ , \quad (5.2)$$

while the unmodified stiffness matrix $\mathbf{K}_e$ is used for the other purely elastic elements. This procedure of the patch method is represented schematically in Fig. 5.3.

According to (3.59a), the global nonlinear differential equation of motion can be simplified as

$$\mathbf{M}\,\ddot{\mathbf{w}} + \mathbf{C}\,\dot{\mathbf{w}} + \mathbf{K}_{mod}\,\mathbf{w} + (1-\alpha)(\mathbf{K}_{bx}\mathbf{Y}_{bx} + \mathbf{K}_{by}\mathbf{Y}_{by} + \mathbf{K}_{bxy}\mathbf{Y}_{bxy}) = \bar{\mathbf{P}}(t) \ , \quad (5.3)$$

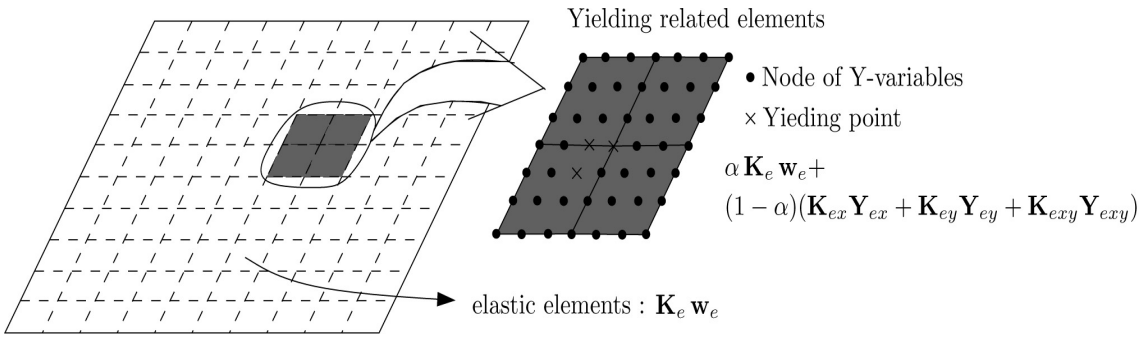

Figure 5.3: Patch Method

where $\mathbf{K}_{mod}$ is the modified elastic stiffness matrix of the system and

$$\begin{aligned}\mathbf{K}_{mod} &= \mathbf{K} - (1-\alpha)\mathbf{K}_{Psub} \\ &= \begin{bmatrix} \mathbf{K}_{aa} & \mathbf{K}_{ab} \\ \mathbf{K}_{ba} & \mathbf{K}_{bb} \end{bmatrix} - (1-\alpha)\begin{bmatrix} 0 & 0 \\ 0 & \mathbf{K}_{bb} \end{bmatrix} ,\end{aligned} \tag{5.4}$$

in which $\mathbf{K}$ is the usual elastic stiffness matrix of the global system and $\mathbf{K}_{Psub}$ is the elastic sub stiffness matrix of the yielding related elements.

It is to note that the dimension of Y-variable vectors, e.g., $\mathbf{Y}_{bx}$, is $N_Y \times 1$. If the yielding related elements are defined as in Fig. 5.3, then is $N_Y = 49$. Although the number of the hysteretic variables is reduced from 2759 to 49×3, the reduction is still not optimal, since not all 49 nodes equipped with Y-variables in the yielding related elements really behave nonlinearly.

Therefore the split method can be added on these hysteretic vectors to reduce the dimension of the hysteretic part in (5.3) again. For example the vector $\mathbf{Y}_{bx}$ can be split up according to (3.60) as

$$\begin{aligned}\mathbf{Y}_{bx} &= \mathbf{T}_s\,\mathbf{Y}_x + (\mathbf{I}_y - \mathbf{T}_s\,\mathbf{T}_s^T)\boldsymbol{\kappa}_{bx} \\ &= \mathbf{T}_s\,\mathbf{Y}_x + (\mathbf{I}_y - \mathbf{T}_s\,\mathbf{T}_s^T)\mathbf{B}_{bx}\,\mathbf{w} ,\end{aligned} \tag{5.5}$$

in which $\mathbf{T}_s$ is after (3.60b) and $\mathbf{Y}_x$ has the dimension of $n_p \times 1$, e.g., $n_p = 4$ according to Fig. 5.3.

Similarly $\mathbf{Y}_{by}$ and $\mathbf{Y}_{bxy}$ will also be split up into pure elastic and pure hysteretic vectors. Further applying the modal transformation $\mathbf{w} = \Phi\,\mathbf{w}^*$ the global differential equation (5.3) can be developed as

$$\begin{aligned}&\big(\Phi^T\mathbf{M}\Phi\big)\ddot{\mathbf{w}}^* + \big(\Phi^T\mathbf{C}\Phi\big)\dot{\mathbf{w}}^* + \big(\Phi^T\mathbf{K}_{mod}\Phi\big)\mathbf{w}^* \\ &+ (1-\alpha)\big(\Phi^T\mathbf{K}_{bx}(\mathbf{I}_y - \mathbf{T}_s\,\mathbf{T}_s^T)\mathbf{B}_{bx}\Phi\big)\mathbf{w}^* + (1-\alpha)\big(\Phi^T\mathbf{K}_{bx}\mathbf{T}_s\big)\mathbf{Y}_x \\ &+ (1-\alpha)\big(\Phi^T\mathbf{K}_{by}(\mathbf{I}_y - \mathbf{T}_s\,\mathbf{T}_s^T)\mathbf{B}_{by}\Phi\big)\mathbf{w}^* + (1-\alpha)\big(\Phi^T\mathbf{K}_{by}\mathbf{T}_s\big)\mathbf{Y}_y \\ &+ (1-\alpha)\big(\Phi^T\mathbf{K}_{bxy}(\mathbf{I}_y - \mathbf{T}_s\,\mathbf{T}_s^T)\mathbf{B}_{bxy}\Phi\big)\mathbf{w}^* + (1-\alpha)\big(\Phi^T\mathbf{K}_{bxy}\mathbf{T}_s\big)\mathbf{Y}_{xy} = \Phi^T\bar{\mathbf{P}}(t) ,\end{aligned} \tag{5.6a}$$

together with the auxiliary vectors of nonlinear equations

$$\dot{\mathbf{Y}}_x = \mathbf{H}_x(\dot{\kappa}_x, Y_x), \quad \dot{\mathbf{Y}}_y = \mathbf{H}_y(\dot{\kappa}_y, Y_y) \quad \text{and} \quad \dot{\mathbf{Y}}_{xy} = \mathbf{H}_{xy}(\dot{\kappa}_{xy}, Y_{xy}) \ , \tag{5.6b}$$

whose components come from (3.23). It is to note that in the following study cases the principal strain angle $\tilde{\theta}$ is time invariant under the harmonic loading, i.e., $\dot{\tilde{\theta}} = 0$. By numerical simulations $\dot{\tilde{\theta}}$ is never exactly equal to '0' but equal to a very small number, which would result in numerical instabilities in trigonometric functions, therefore the last term of (3.23) on the right hand side is neglected in the following numerical examples.

5.3 Numerical Examples of Different Yielding Conditions

In this section cases of different yielding locations in the plate will be studied to certify the validity of the plastic shape function. If it isn't especially mentioned, the loading for each cases is assumed to have $P_a = 2.5\,[kN/m^2]$, $f = 0.9\,[Hz]$ and $t_{max} = 16\,[sec]$ after (5.1). For the numerical integration the discrete time step $\Delta t = 1/32\,[sec]$ is chosen.

The solution of using the extended modal bases (plastic shape functions included)

$$\tilde{\Phi}_{red} = \left[\ \phi_1 \quad \phi_2 \quad \dots \quad \phi_{n_{red}} \quad \tilde{\psi}_{xp,1} \quad \tilde{\psi}_{yp,1} \quad \tilde{\psi}_{xyp,1} \quad \dots \quad \tilde{\psi}_{xyp,n_p} \ \right] \ , \tag{5.7}$$

taking the place of Φ in (5.6a), will be compared with the *reference solution*, for which all eigenvectors are utilized in the mode-shape matrix Φ of (5.6a). In order to control the approximation error of the reduced modal bases on the elastic system response and to show the error part of PSFs properly, a pre-study of pure elastic system responses is performed and the number of the adopted eigenmodes $n_{red} = 20$ is selected.

As shown in Fig. 5.4 the difference of the elastic curvatures between the reference solution (400 modes) and the reduced modal solution (20 modes) is about 3.3% for κ_x and 1.5% for κ_y in the plate middle under the maximal deflection. Such error ratio is defined as

$$\text{Error}(i,j) = \left| \frac{Rs(i,j) - As(i,j)}{Rs_{max}} \right| \times 100\% \ , \tag{5.8}$$

where $Rs(i,j)$ is the discrete reference value, $As(i,j)$ is the approximated value and Rs_{max} is the maximal reference value. It is to note that by using the deformation FE method the accuracy of the deformations is much better than that of the curvatures, since the curvatures are the second derivative of the deformations, and the error ratio of the deformations is generally smaller than 0.5% for this elastic case except the twisting angle at the corners.

Fig. 5.5 shows the different plastification conditions investigated in the following and the yielding nodes defined in each case are nodes with lower yield stress of $\sigma_Y/10$. For

the group A the yielding related elements locate on the centrum of the plate, where the bending moment dominates. In each subcase of this group, i.e., A.1, A.2 and A.3, it is assumed that the number of the yielding nodes is 1, 2 and 4 respectively, which develops along the x-direction. For the group B the yielding related elements are then located near the corner on the diagonal. In each subcase B.1, B.2 and B.3 the number of the yielding nodes is also assumed to be 1, 2 and 4, but developed in the diagonal direction.

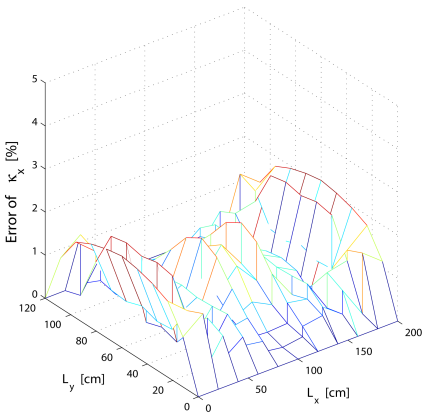

(a) Error of κ_x[%]

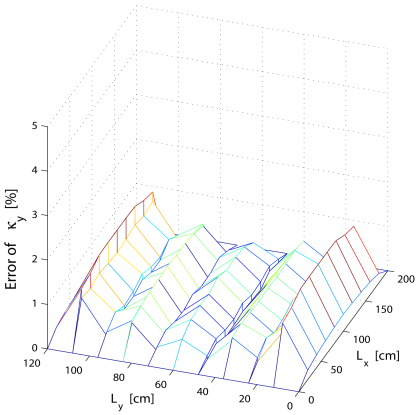

(b) Error of κ_y[%]

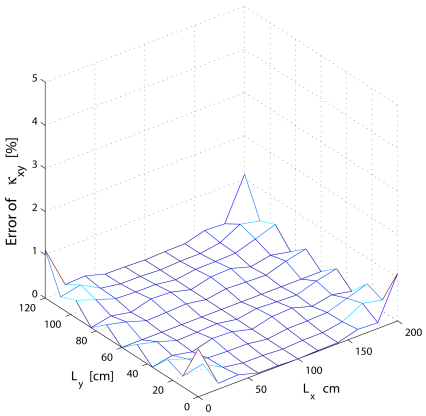

(c) Error of κ_{xy}[%]

Figure 5.4: Error Ratio of Curvatures – 20-modes/reference by Pure Elastic Case

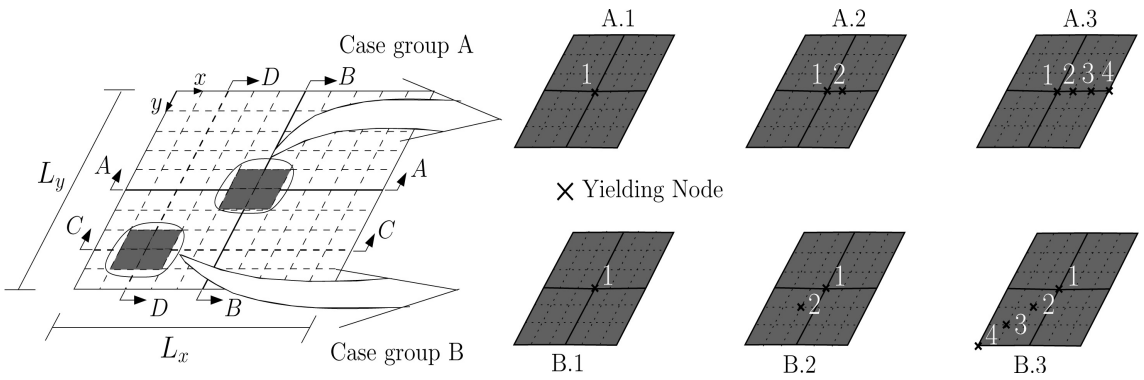

Figure 5.5: Study Cases

5.3.1 Case A.1 - One yielding node in plate middle

In this subcase it is assumed that there is only one yielding node locating at the cross point of four yielding related elements in the middle of the plate. In Fig. 5.6 the curvatures and the moments of the reference solution along the section $A-A$ and $B-B$, which are defined in Fig. 5.5, is given at the time $t = 8.625\,sec.$ of the maximal deflection. It can be seen that the curvatures increase locally. And there are discontinuities in the curvature distribution near the yielding node because of reaching the moment capacities.

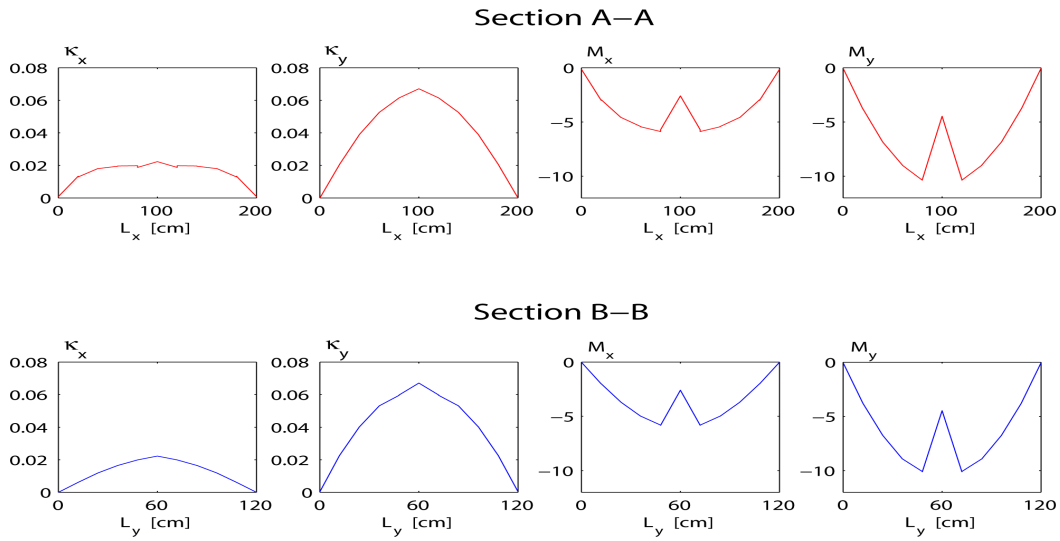

Figure 5.6: Curvatures and Moments of Section A-A/B-B at $t = 8.625\,sec$

Just as expected the solution of applying merely 20 eigenmodes can not represent the enhanced curvatures at the yielding location. To show the improvement achieved by PSFs, it is necessary to interpret the error between the reference solutions and the results of the first 20 eigenmodes. The distribution of the curvatures of the reference solution and the error ratio of the 20-modes solution with respect to them is represented in Fig. 5.7, which correspond to the maximal deflection at $t = 8.625\,sec.$ All the following demonstrations are relating to this time point, unless additionally specified. In comparison with Fig. 5.4 it can be recognized that the error ratio increases several times around the yielding point.

Now the solution will be improved by applying the PSFs developed in section 4.3. For one yielding node three independent plastic shape functions are needed and the reduced modal bases is extended with these PSFs as

$$\tilde{\Phi}_{red} = \left[\begin{array}{ccccccc} \phi_1 & \phi_2 & \dots & \phi_{20} & \tilde{\psi}_{xp,1} & \tilde{\psi}_{yp,1} & \tilde{\psi}_{xyp,1} \end{array} \right] , \tag{5.9}$$

which has a total dimension of 23. Similar to Fig. 5.7 the error ratio of the curvatures between the reference and the PSFs applied solutions is given in Fig. 5.8. It can be seen that the error of the curvatures near the yielding point is significantly reduced with this procedure and has about the same level as by the elastic case.

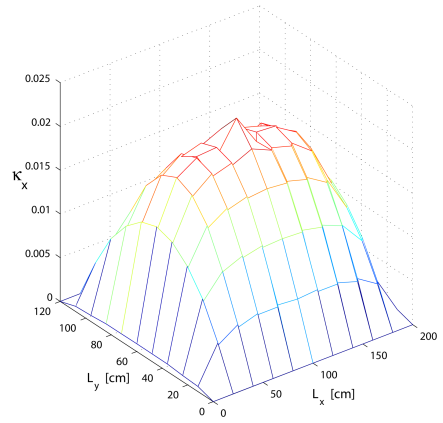

(a) κ_x

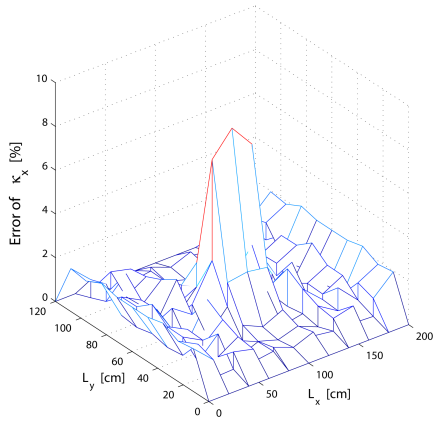

(d) Error of κ_x[%]

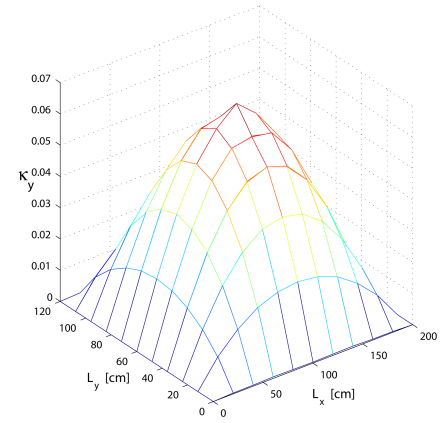

(b) κ_y

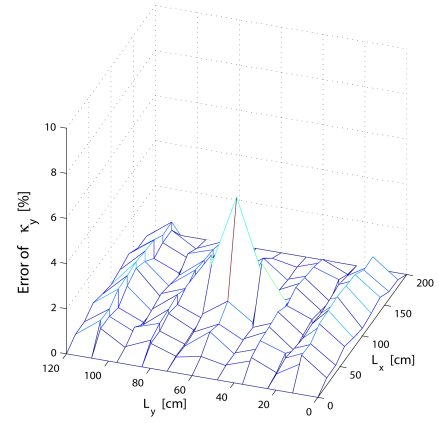

(e) Error of κ_y[%]

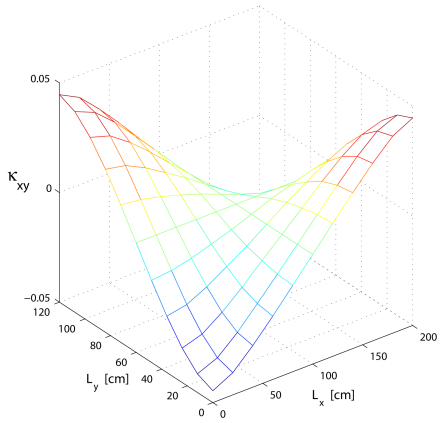

(c) κ_{xy}

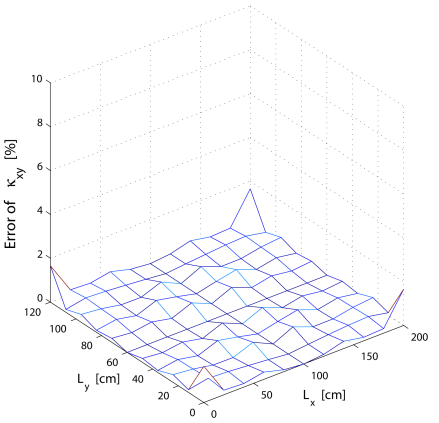

(f) Error of κ_{xy}[%]

Figure 5.7: Reference Curvatures and Error Ratio – 20-modes/reference by Case A.1

To have more aspects of the improvement of PSFs, some other results are also represented. Fig. 5.9 shows the comparison of κ_x, κ_y along the section $A-A$ and the κ_{xy} along the diagonal at $t = 8.625\,sec$ between the reference, 20-modes and the PSFs applied solutions. The comparison of the moment time histories, i.e., $M_x(t)$ and $M_y(t)$, of the yielding node between these three solutions is demonstrated in Fig. 5.10. The error ratio of the deformations between the reference and the PSFs applied solutions is also

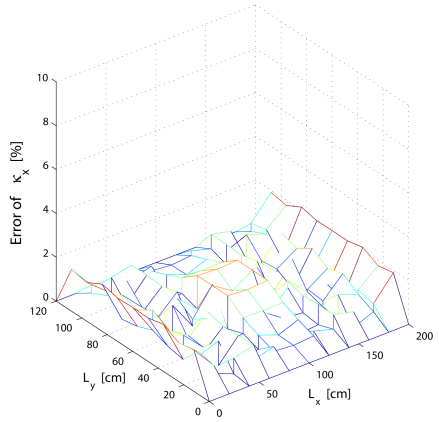

(a) Error of κ_x[%]

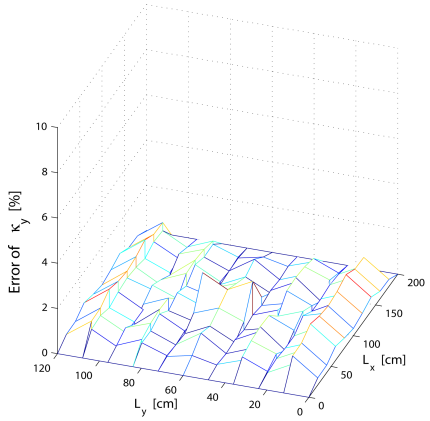

(b) Error of κ_y[%]

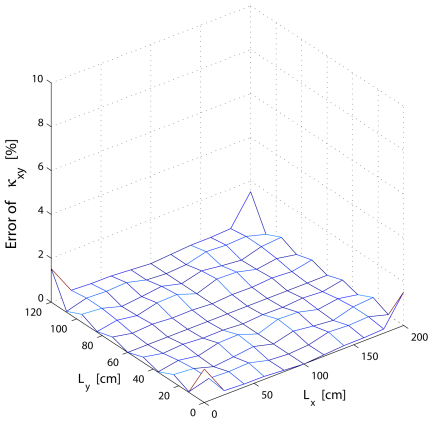

(c) Error of κ_{xy}[%]

Figure 5.8: Error Ratio of Curvatures – (20-modes+PSFs)/reference by Case A.1

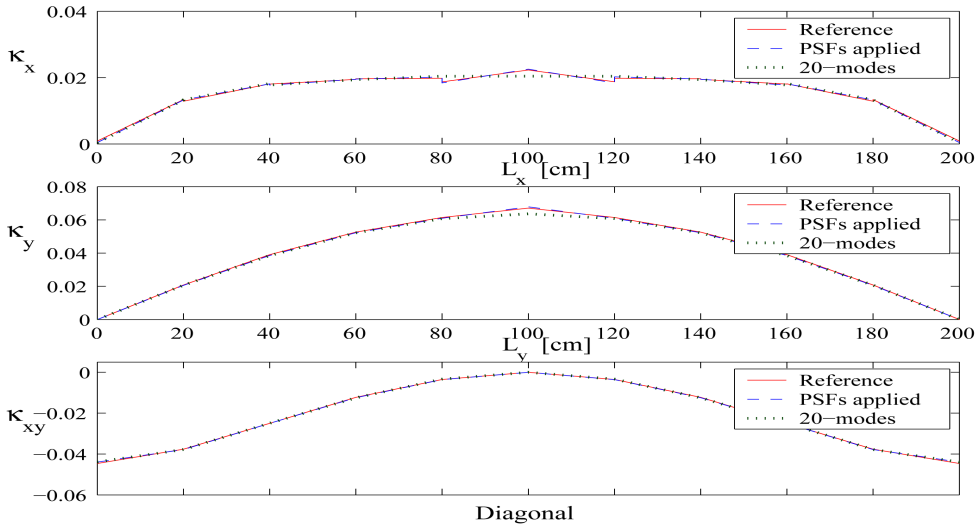

Figure 5.9: Comparisons of κ_x, κ_y on Section $A-A$ and κ_{xy} on Diagonal, A.1

given in Fig. 5.11 out of the interest. These error ratios are generally smaller than 0.5% of the pure elastic case except the twisting angle at the corner, whose error is inherited from the approximation of the elastic system responses by using the first 20 eigenmodes.

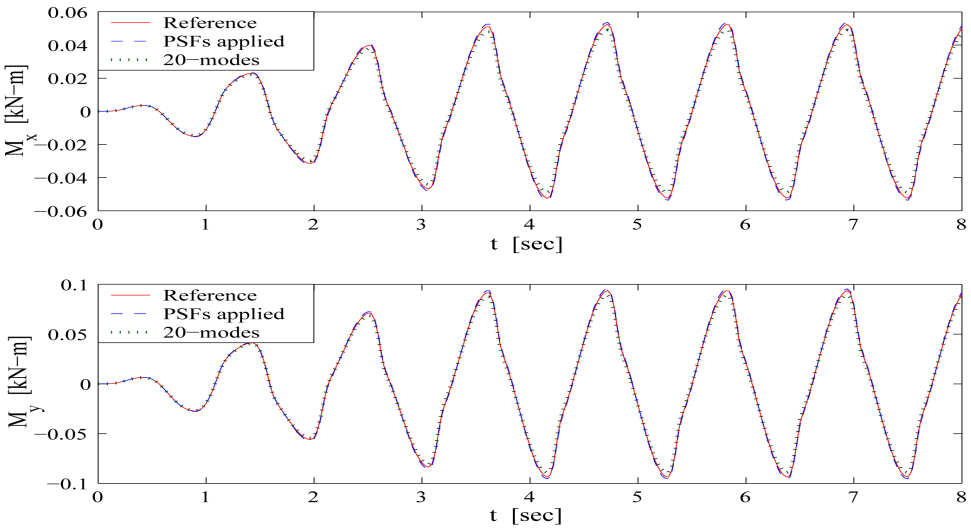

Figure 5.10: Comparison of M_x and M_y of the Yielding Node – Case A.1

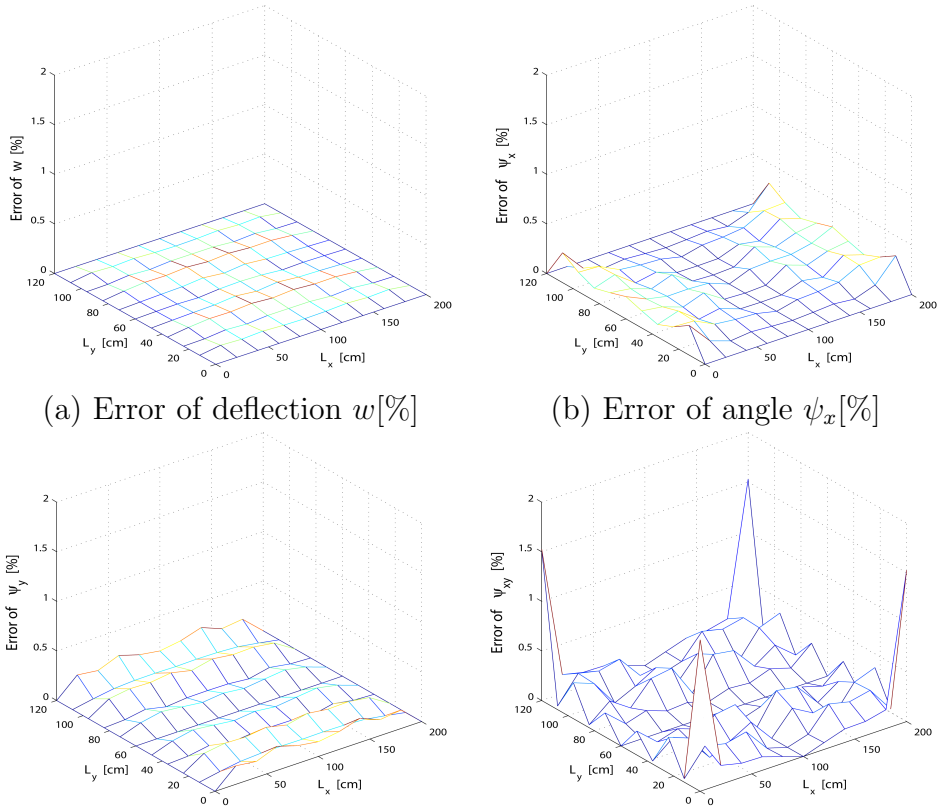

(a) Error of deflection w[%]

(b) Error of angle ψ_x[%]

(c) Error of angle ψ_y[%]

(d) Error of twist ψ_{xy}[%]

Figure 5.11: Error Ratio of Deformations – (20-modes+PSFs)/reference – Case A.1

The accuracy of the PSFs has been exposed by these demonstrations, but the most significance lies in the efficiency of the PSFs. By using the same computer it needs about 3000 *sec.* to carry out the calculation of the reference solution, i.e., calculation of 400 linear plus 3 nonlinear differential equations. To perform the PSFs applied solution, i.e., evaluating 23 linear and 3 nonlinear differential equations, the calculation time is about 100 *sec.*, which is only 3.33% of the cost of the reference solution.

This efficiency will be even higher when the system dimension expands. For example, if the FE net of this case is extended to 20×20, which has a total DOF of 1600, and the yielding condition remains the same, i.e., only one yielding node locates on the middle point of the plate, the curvature distributions of the reference solution under the same loading are represented in Fig. 5.12 (a)-(c). It is interesting to find that the enhance of the curvature at the yielding node is very small, i.e., only a slight plastic deformation occurs. This is because the total area of the yielding related elements reduces to 1/4 under the 20×20 FE net, so that the portion of the plastic deformation energy is also reduced. Under this circumstance the curvatures will be overestimated by using the PSFs as shown in Fig. 5.12 (d)-(f). It is to mention that the first 40 eigenmodes plus three PSFs are used in this case for the PSF applied solution, since the FE resolution is increased.

In order to emphasize the yielding phenomenon the loading of this 20×20 FE system is five times increased and the reference curvatures is shown in Fig. 5.13 (a)-(c). As expected, the enhance and the discontinuity of the curvatures around the yielding node are more apparent under the increased loading. This reference solution will be approached by the extended modal bases (first 40 eigenmodes plus three PSFs) and the error ratio of the curvatures is given in Fig. 5.13 (d)-(f), which is much better than that by small plastic deformation. It should be noted again that even under the 5 times loading the plate behaves elastically except the one single yielding node as assumed.

The key point of these two examples with refined FE net is to realize the efficiency of the PSFs. While the calculation time of the reference solution with 1600 DOF raises to about $8.3 \times 10^4 sec.$, the time needed for the PSF applied solution is only about $615 sec.$ under the same computational conditions. This means the efficiency of the PSFs is about 135-fold. From these examples the following two conclusions can also be made:

- The number of the required plastic shape functions is independent of the system dimension. The PSF can provide a reliable approximation, even when the system dimension is too huge to obtain a reference solution.
- The PSF simulates merely the curvatures resulted from the yielding. By using the PSFs the plastic deformations will be overestimated when they are too small, but the estimation is still on the safe side for the engineering application.

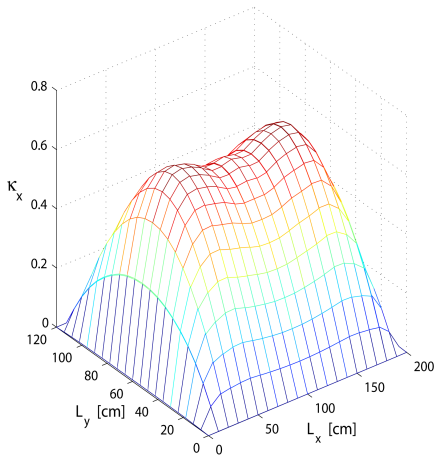

(a) κ_x

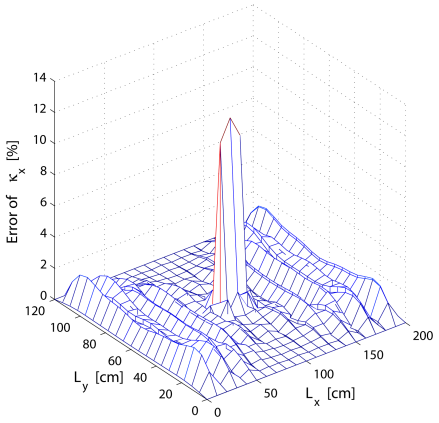

(d) Error of κ_x[%]

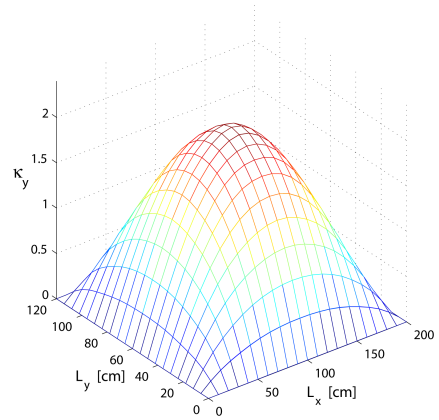

(b) κ_y

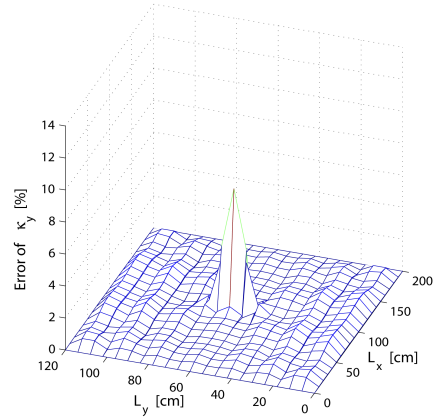

(e) Error of κ_y[%]

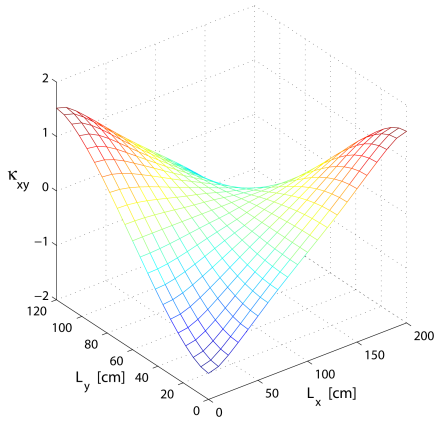

(c) κ_{xy}

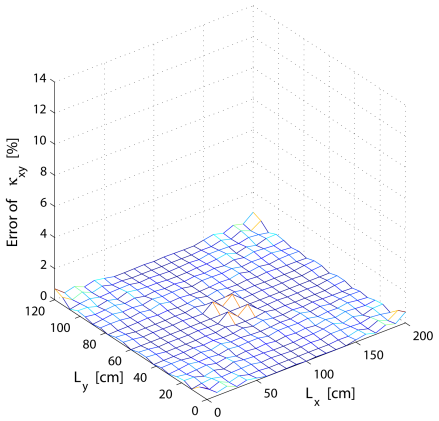

(f) Error of κ_{xy}[%]

Figure 5.12: Reference Curvatures and Error Ratio – (40-modes+PSFs)/reference of 20×20 FE Net under Original Loading

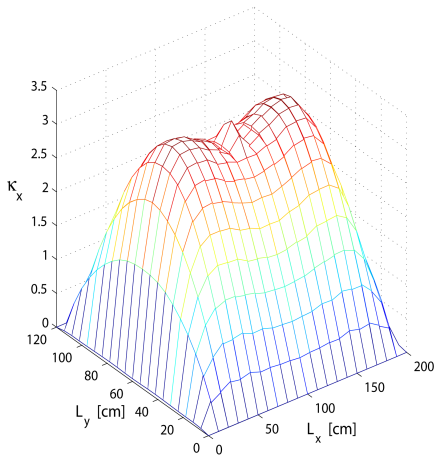

(a) κ_x

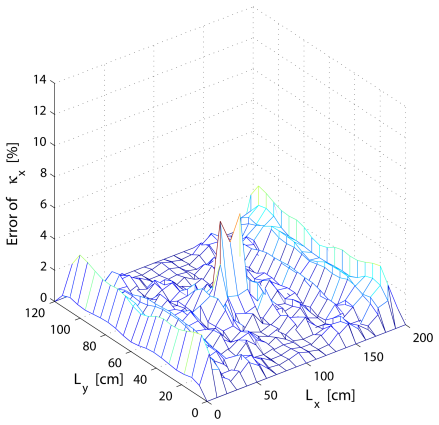

(d) Error of κ_x[%]

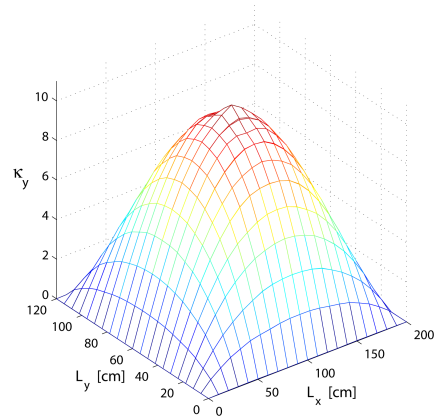

(b) κ_y

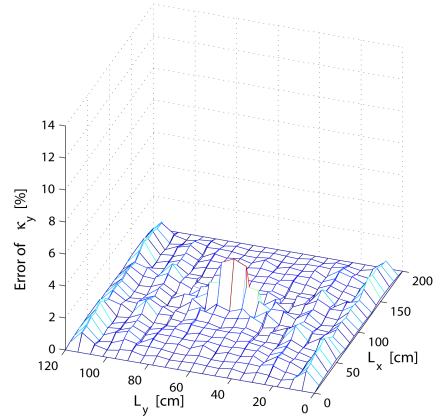

(e) Error of κ_y[%]

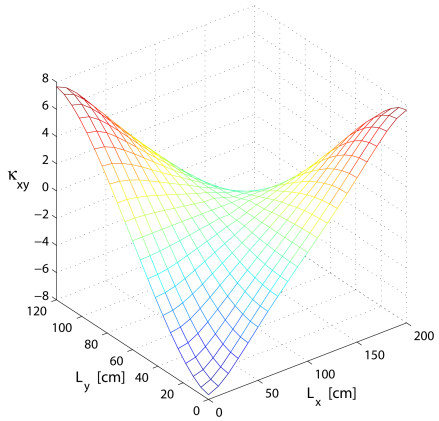

(c) κ_{xy}

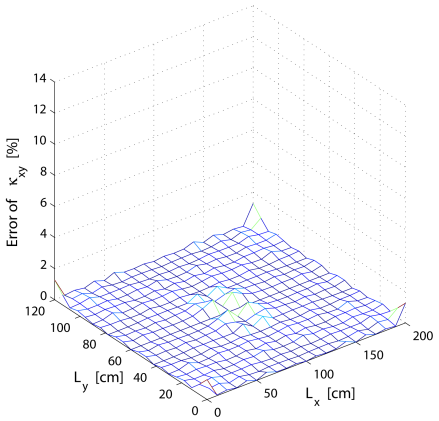

(f) Error of κ_{xy}[%]

Figure 5.13: Reference Curvatures and Error Ratio – (40-modes+PSFs)/reference of 20×20 FE net under 5 Times Loading

5.3.2 Case A.2 - Two yielding nodes in plate middle

In this subcase two yielding nodes are defined in the middle of the plate as shown in Fig. 5.5. This assumption causes higher discontinuity and asymmetry of the curvature distribution in x-direction as shown in Fig. 5.14 (a)-(c). As expected, the error of the approach with merely 20 eigenmodes is much larger than that of case A.1 especially by κ_x. It is to note that the z-scale is up 50% in Fig. 5.14 (d)-(f).

The results will be improved by extending the reduced modal bases, i.e., the first 20 eigenmodes, with 3 PSFs for each of the yielding nodes 1. and 2. while solving (5.6), so that the reduced modal system has a total of 26 DOF. The calculation time of this reduced system is about 5.38% of the time needed for the reference solution. Although this time-spending ratio is a little higher than that in case A.1, since three more PSFs and three more Y-variables are required, the improvement of the curvatures error ratio is much more significant than that in case A.1, which can be observed directly by comparing Fig. 5.14 and Fig. 5.15. For this purpose 50% is selected also as the maximal z-scale in Fig. 5.15. The average error ratio around the yielding elements is about 3.5% for κ_x, 3% for κ_y and 3.5% for κ_{xy} under applications of the PSFs in this study case.

Fig. 5.16 represents the comparison of κ_x, κ_y on the cross-section $A - A$ and the comparison of κ_{xy} along the diagonal under the maximal deflection between the reference, 20-modes and the PSFs applied solutions. It can be seen that the discontinuity of κ_x and κ_y can not be simulated by the lower frequency modes at all. And the comparison of the moment time history of M_x and M_y for the yielding node 1. and 2. is given in Fig. 5.17 (a), (b) respectively.

The the error ratio of the deformations between the reference and PSFs applied solution is then represented in Fig. 5.18. Obviously the error ratio of the twisting angle ψ_{xy} is relative higher than the other deformations, whose error ratios are less than 0.5%. But the two peaks in Fig. 5.18 (d) do not locate on the assumed yielding positions and are actually inherited from the approximation of first 20 eigenmodes, if Fig. 5.14 (f) is reviewed.

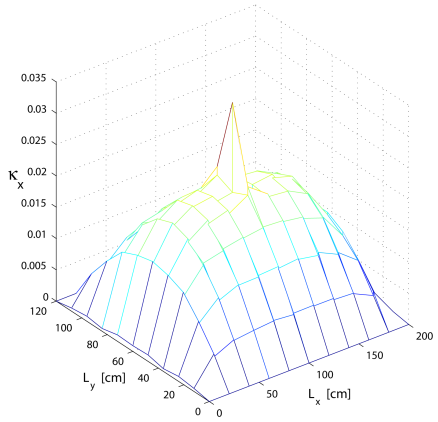

(a) κ_x

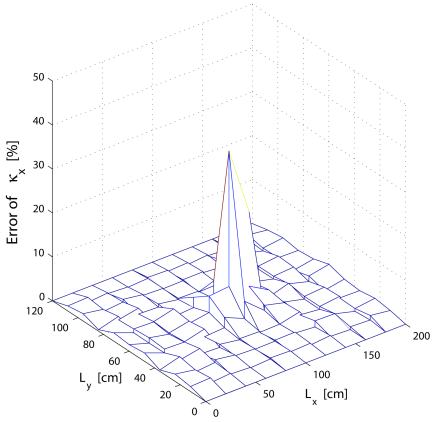

(d) Error of κ_x[%]

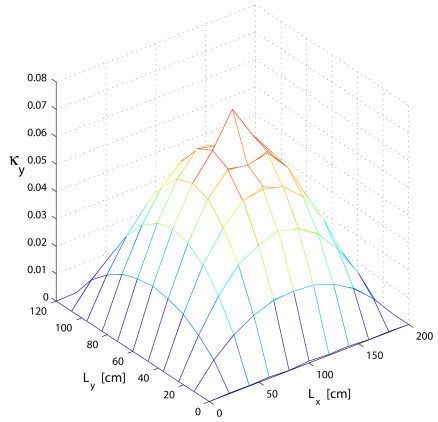

(b) κ_y

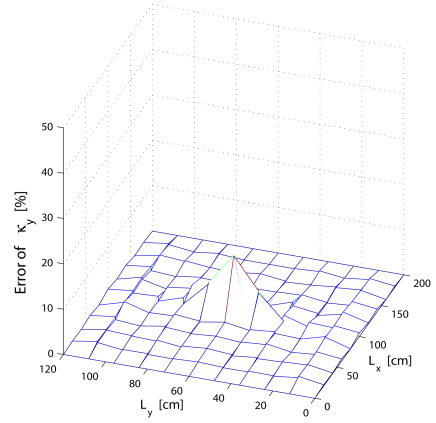

(e) Error of κ_y[%]

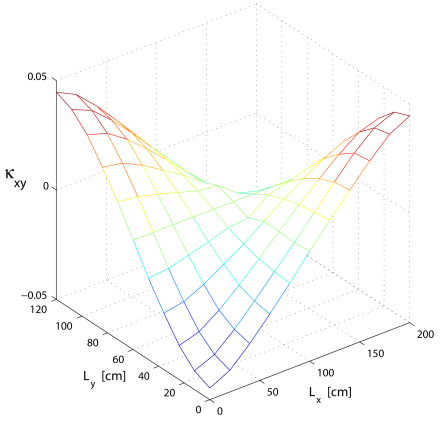

(c) κ_{xy}

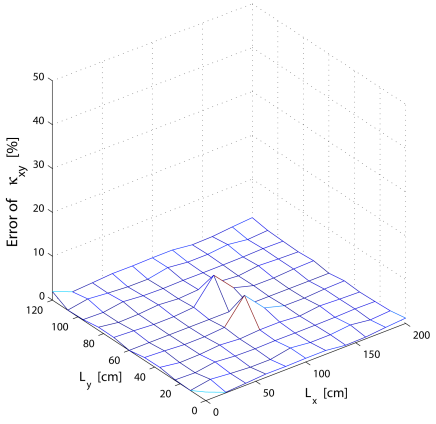

(f) Error of κ_{xy}[%]

Figure 5.14: Reference Curvatures and Error Ratio – 20-modes/reference – Case A.2

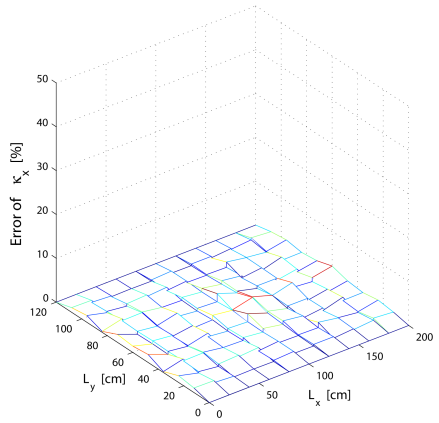

(a) Error of κ_x[%]

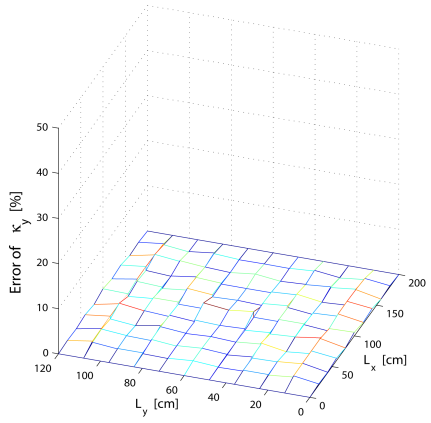

(b) Error of κ_y[%]

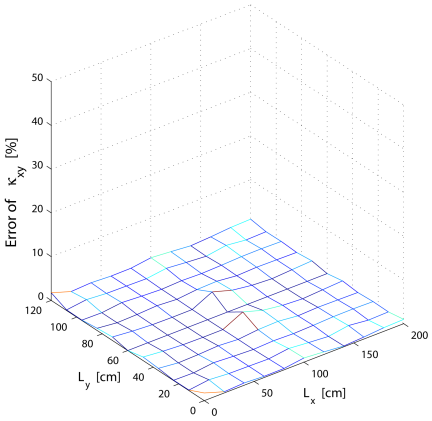

(c) Error of κ_{xy}[%]

Figure 5.15: Error Ratio of Curvatures – (20-modes+PSFs)/reference – Case A.2

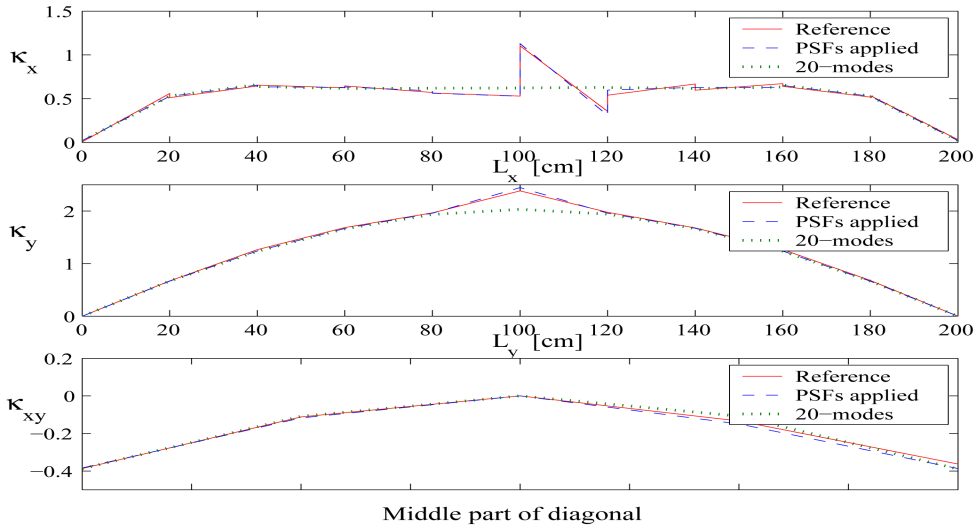

Figure 5.16: Comparison of κ_x, κ_y on Section $A-A$ and κ_{xy} on Diagonal – Case A.2

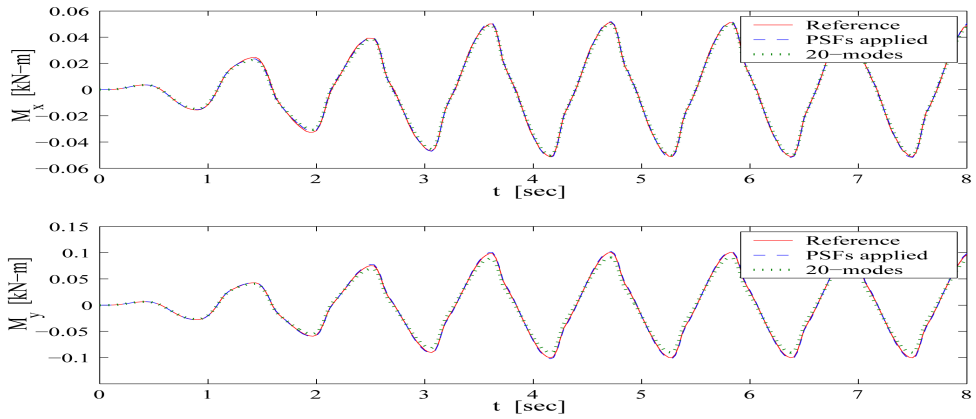

(a) Yielding Node Nr.1

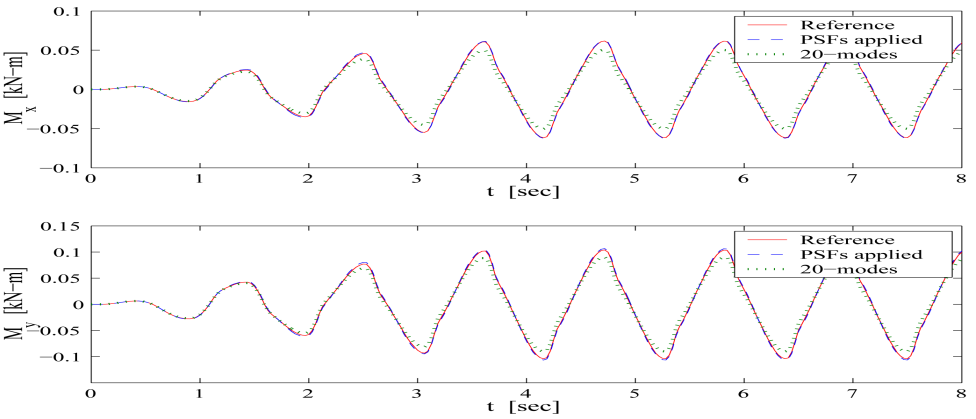

(b) Yielding Node Nr.2

Figure 5.17: Comparison of M_x and M_y of Yielding Nodes – Case A.2

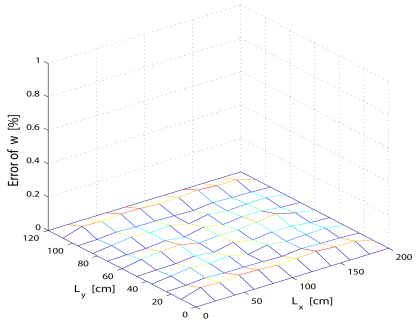

(a) Error of deflection w[%]

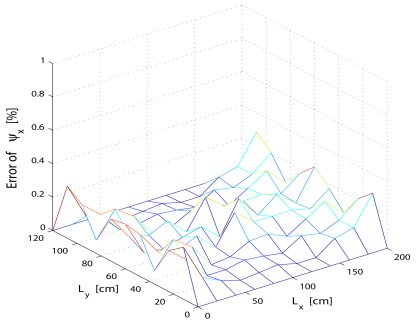

(b) Error of angle ψ_x[%]

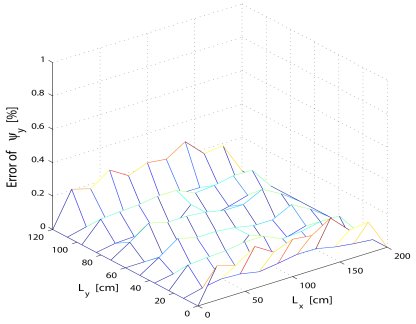

(c) Error of angle ψ_y[%]

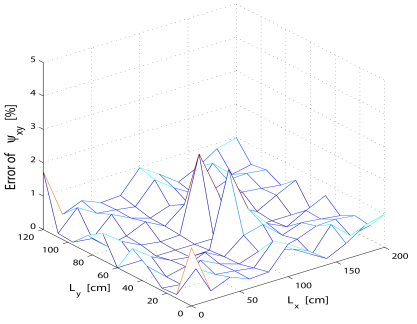

(d) Error of twist ψ_{xy}[%]

Figure 5.18: Error Ratio of Deformations – (20-modes+PSFs)/reference – Case A.2

5.3.3 Case A.3 - Four yielding nodes in plate middle

In this study case four yielding points as defined in Fig. 5.5 are assumed. For these four yielding nodes there are totally $3(PSFs) \times 4(nodes) - 1 = 11$ PSFs needed, since the plastic shape function for κ_{xy} of the node Nr.2 and Nr.3 are identical. Extending the first 20 eigenmodes with these PSFs the reduced system has then a dimension of 31. In Fig. 5.19 (a)-(c) the reference curvatures by the maximal deflection ($t = 8.625\,sec$) is given and (d)-(c) shows the error ratio of the curvatures between the reference and the PSFs applied solution directly, since it is clear that merely the first 20 eigenmodes can not correctly represent the locally enhanced curvatures.

Again it can be seen that the curvatures around the yielding nodes are well approximated through the PSFs. The moment time history of M_x and M_y for the four yielding nodes are represented in Fig. 5.20, from which it can be verified that the hysteretic variables of these two solutions are almost identical, since they are functions of curvatures and the error ratio of the curvatures is about 2% averaging on the yielding nodes.

According to the definition given in Fig. 3.10 it is possible to determine the yielding not only on the element corner nodes but also the nodes on the edge and inside of the element. This benefit of a finer yielding resolution will turn into a disadvantage when the number of the yielding nodes increases, i.e., the system dimension will be overloaded by the required PSFs and the corresponding hysteretic equations. Therefore it will be attempted to reduce the number of the required PSFs. Considering that the plastic shape function of Y_x for the yielding node Nr.2 and Nr.3 in Fig. 5.5 are linear dependent on that of node Nr.1 and Nr.4 (s. section 3.3.2 and section 4.3), an other approximation with 9 PSFs, which are listed in the following, is also performed.

- 3×2 PSFs, which correspond to Y_x, Y_y and Y_{xy}, for yielding node Nr.1 and Nr.4 respectively.
- 2×1 PSFs of Y_y for yielding node Nr.2 and Nr.3 respectively.
- 1 PSF of Y_{xy} for both yielding node Nr.2 and Nr.3, since their PSFs of Y_{xy} are identical.

The error ratio of the curvatures by applying these 9 PSFs is given in Fig. 5.21. It can be seen that the error ratio of κ_x around the yielding nodes is increased. This is because of the PSFs used on node Nr.1 and Nr.4 are the summation of four sub-PSFs of four elements around the yielding node. Therefore the curvature κ_x between node Nr.1 and Nr.4 is bounded with the parts on the left of node Nr.1 and the right of Nr.4, so that it can not be correctly regulated. However this increased error is still acceptable when considering its improved efficiency under large number of yielding nodes.

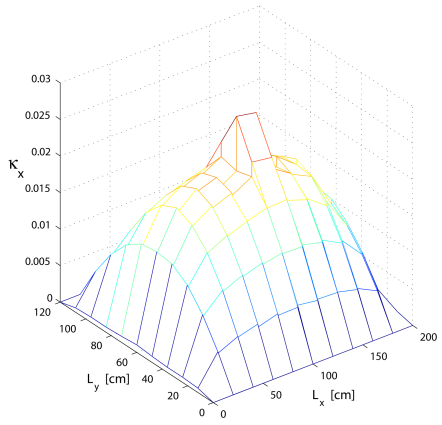

(a) κ_x

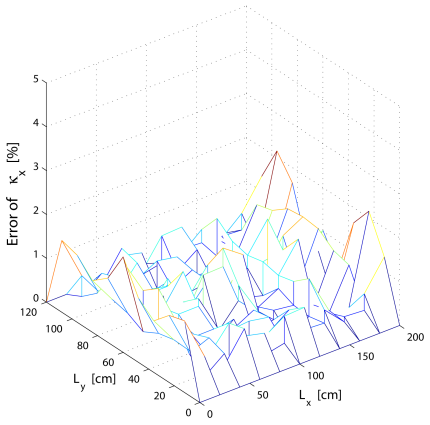

(d) Error of κ_x[%]

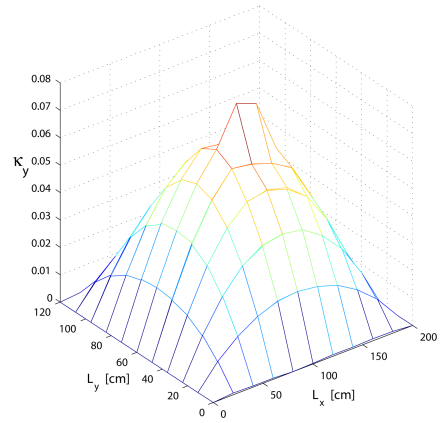

(b) κ_y

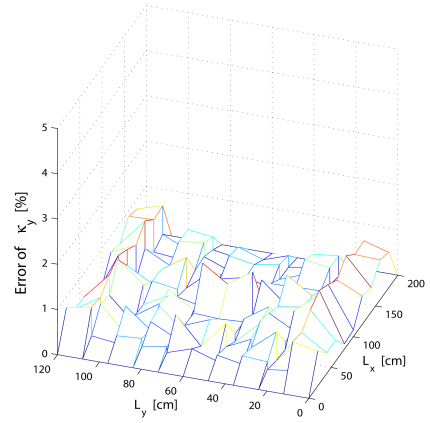

(e) Error of κ_y[%]

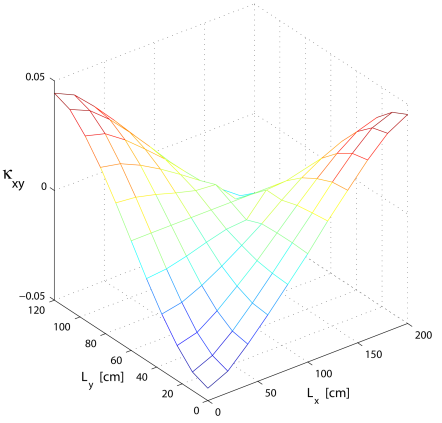

(c) κ_{xy}

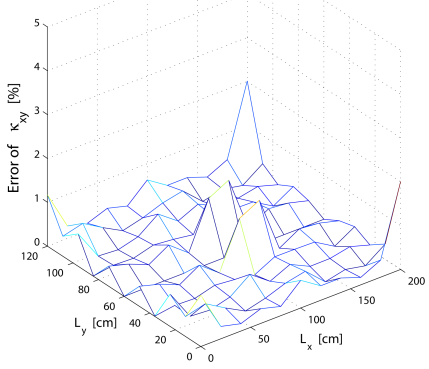

(f) Error of κ_{xy}[%]

Figure 5.19: Reference Curvatures and Error Ratio – (20-modes+11 PSFs)/reference – Case A.3

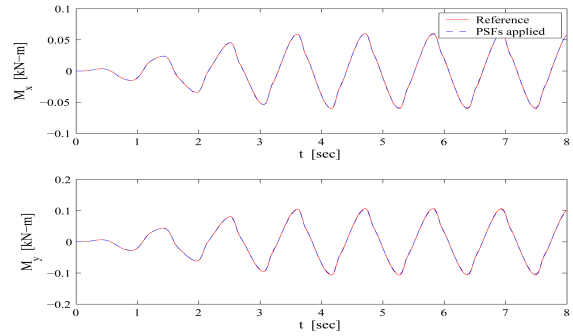

(a) Yielding Node Nr.1

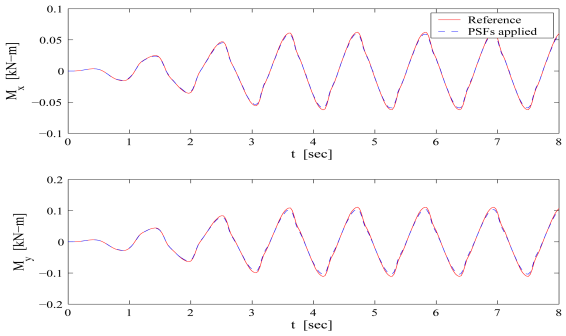

(b) Yielding Node Nr.2

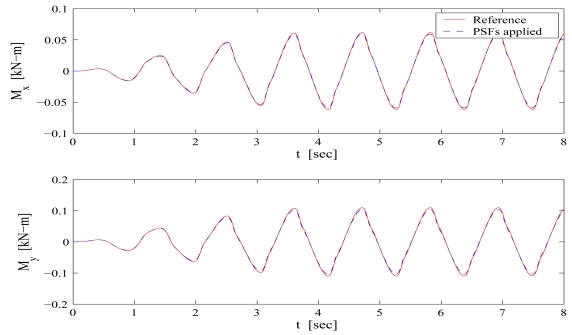

(c) Yielding Node Nr.3

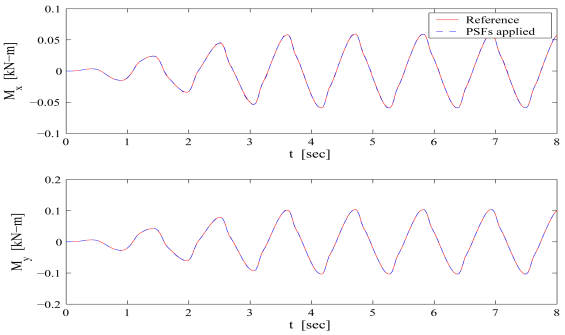

(d) Yielding Node Nr.4

Figure 5.20: Comparison of M_x and M_y of Yielding Nodes – Case A.3

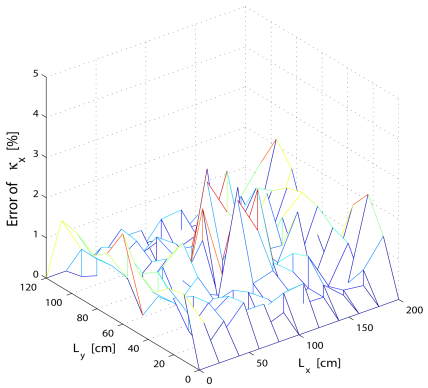

(a) Error of κ_x[%]

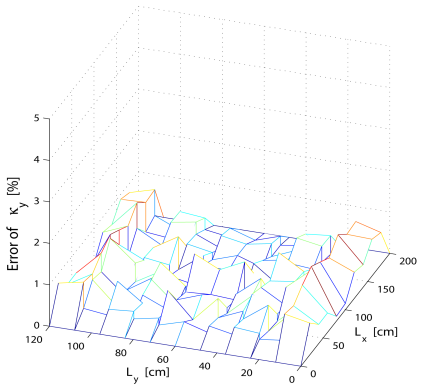

(b) Error of κ_y[%]

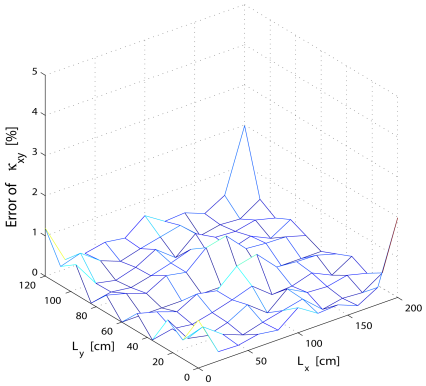

(c) Error of κ_{xy}[%]

Figure 5.21: Error Ratio of Curvatures – (20-modes+9 PSFs)/reference – A.3

5.3.4 Case B.1 - One yielding node at plate corner

In the subcase group B the yielding nodes are assumed to be located near the corner of the plate, where the twisting moments dominate the yielding occurrence. As defined in Fig. 5.5, case B.1 has only one yielding node, which locates at the cross point of the four yielding related elements. Because only one single yielding node is assumed near the plate corner instead of several nodes, which can build a yielding zone, the discontinuity of curvatures is insignificant under the equally distributed loading. Therefore the loading amplitude is raised to $P_a = 12.5\,[kN/m^2]$ to emphasize the yielding phenomenon near the plate corner. Although the loading concentrating on a small area can produce locally enlarged curvatures, such loading could also result in undesired curvature jumps around the loading bounds, therefore the concentrated loading is inappropriate for the use of this example. Since the purpose of this example is to verify the pure performance of PSFs for the yielding on a single node, which is dominated by the twisting moments, it is necessary to raise the loading without considering the reality. The curvatures of the reference solution by the maximal deflection at $t = 8.625\,sec.$ is given in Fig. 5.22 (a)-(c), and the error ratio of the curvatures between the reference and the errors of the first 20-modes solution is also represented in (d)-(f) to serve as a control.

To improve the curvature errors resulted from the yielding, the reduced modal bases of the first 20 eigenmodes will be enlarged by three PSFs corresponding to the given yielding node like (5.9). The curvature errors of the PSF applied solution with respect to the reference solution is demonstrated in Fig. 5.23.

Obviously, the PSFs adjust the curvatures near the yielding node quite well, while the error ratios outside this region remain the same level as by the 20-modes solution. Then the moments variation of the yielding node are compared between the reference, the 20-modes and the PSF applied solution in Fig. 5.24.

The error ratio of the deformations between the reference and the PSF applied solution is shown in Fig. 5.25. In comparison with other deformations the twisting angle ψ_{xy} has a higher error ratio of 1.8%. Part of this error is resulted from the existence of the interactions between the plastic shape functions. In other words, by building the plastic shape function $\tilde{\psi}_{xp}$, which should merely approximate the plastic curvature $\kappa_{x,p}$, two redundant curvature distributions $\kappa_{y,\tilde{\psi}_{xp}}$ and $\kappa_{xy,\tilde{\psi}_{xp}}$ will attach on this plastic shape function and influence the approximation of $\kappa_{y,p}$ and $\kappa_{xy,p}$. In the same way $\tilde{\psi}_{yp}$ and $\tilde{\psi}_{xyp}$ have also undesired effects on the approximation of plastic curvatures belonging not to themselves. But such interactions are not critical for the reliability of the PSFs as can be verified from the results of this example.

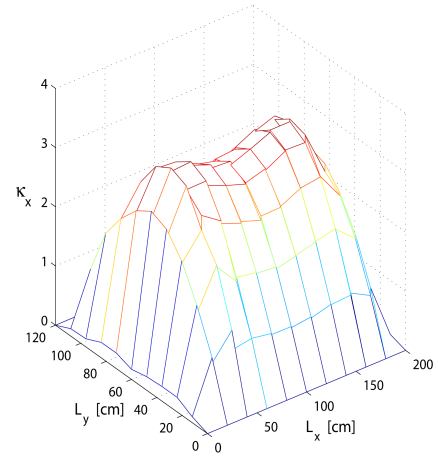

(a) κ_x

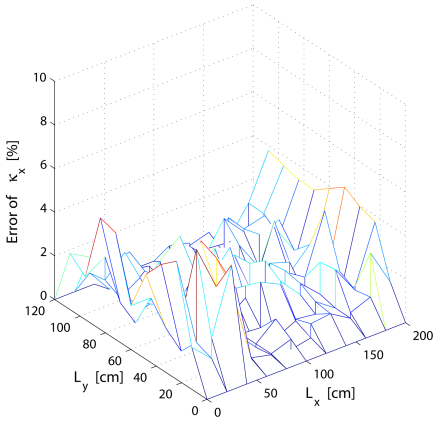

(d) Error of $\kappa_x[\%]$

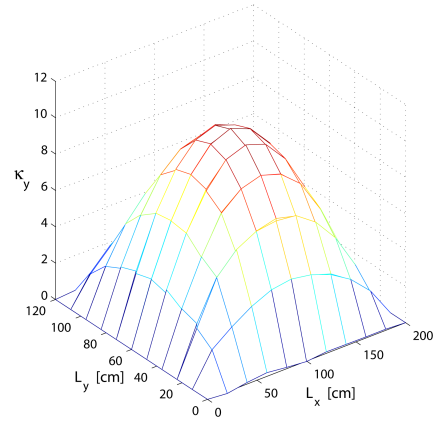

(b) κ_y

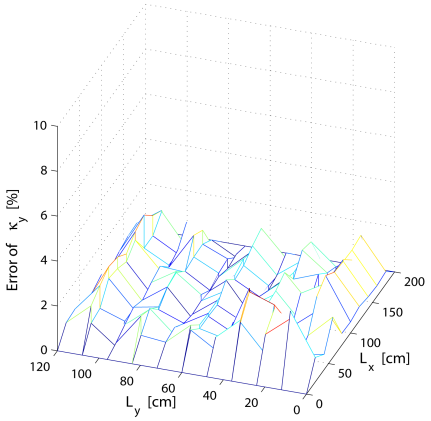

(e) Error of $\kappa_y[\%]$

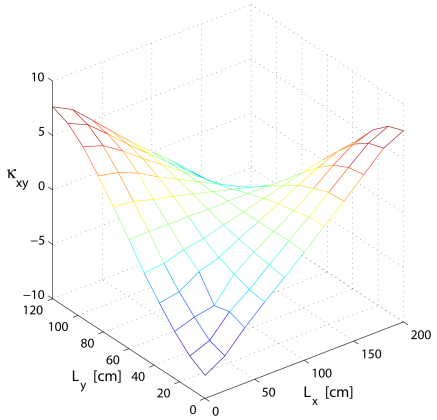

(c) κ_{xy}

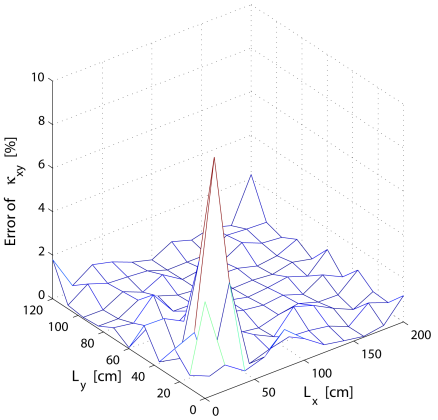

(f) Error of $\kappa_{xy}[\%]$

Figure 5.22: Reference Curvatures and Error Ratio – 20-modes/reference – Case B.1

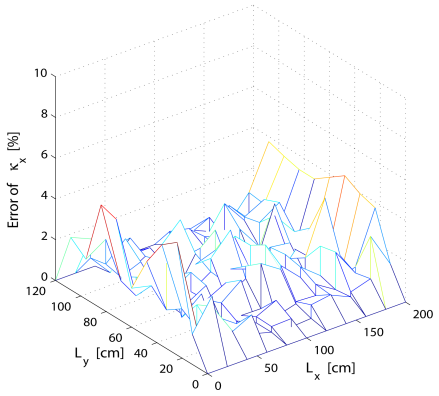

(a) Error of κ_x[%]

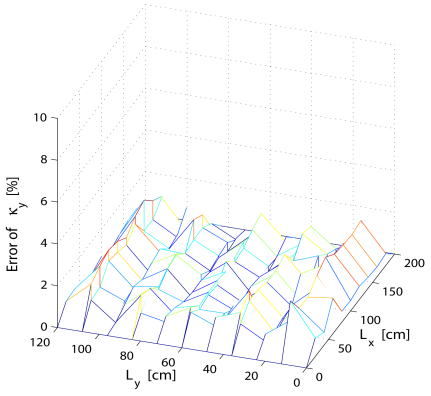

(b) Error of κ_y[%]

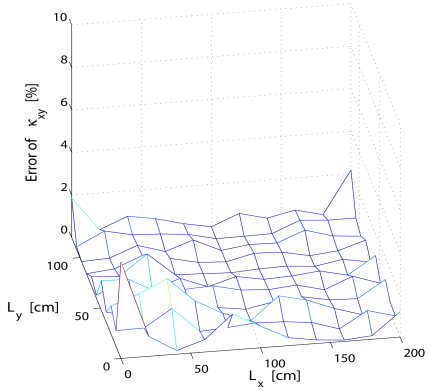

(c) Error of κ_{xy}[%]

Figure 5.23: Error Ratio of Curvatures – (20-modes+PSFs)/reference – Case B.1

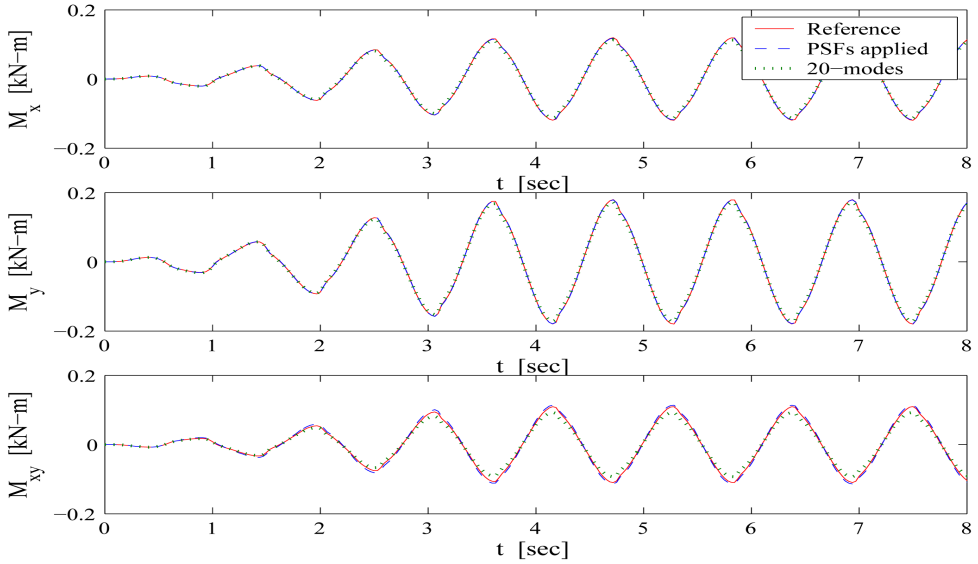

Figure 5.24: Comparison of M_x, M_y and M_{xy} of Yielding Node – Case B.1

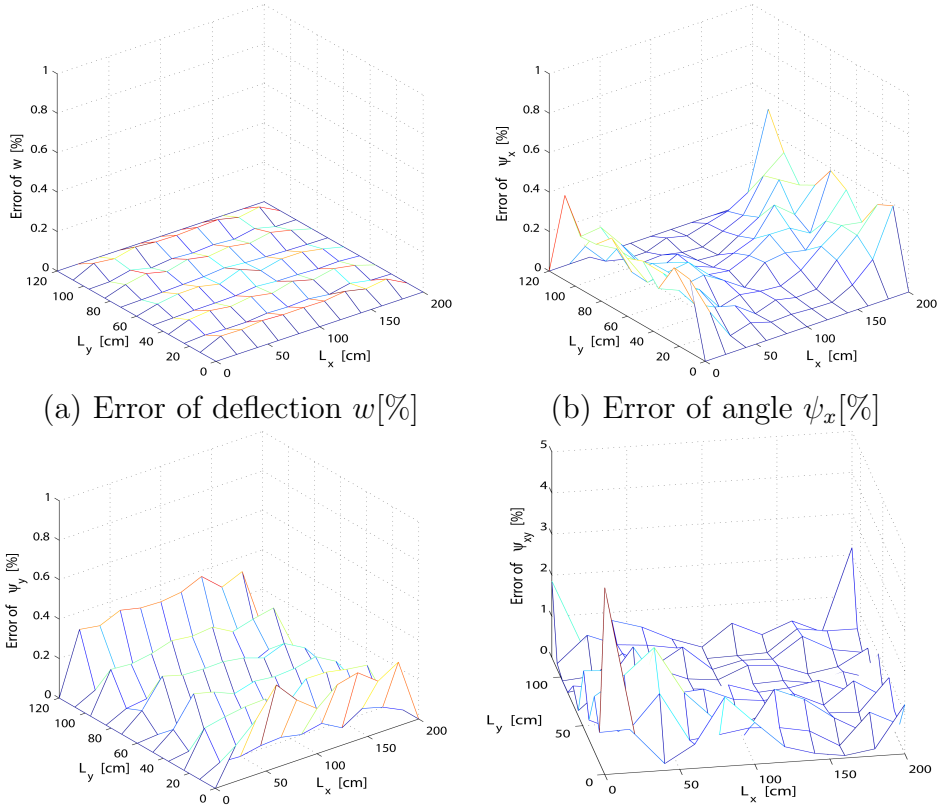

(a) Error of deflection w[%] (b) Error of angle ψ_x[%]

(c) Error of angle ψ_y[%] (d) Error of twist ψ_{xy}[%]

Figure 5.25: Error Ratio of Deformations – (20-modes+PSFs)/reference – Case B.1

5.3.5 Case B.2 - Two yielding nodes at plate corner

Under this subcase one more yielding node is defined on the diagonal of the plate as defined in Fig. 5.5 and a loading amplitude with $P_a = 5\,[kN/m^2]$ is used, since a small yielding zone can be built and the curvature discontinuity is more significant than previous example. Again, in order to realize the performance of PSFs, the reference curvatures and the error ratio of the 20-modes approach under the maximal deflection is shown in Fig. 5.26 first. It is to note that the maximal z-scalar in Fig. 5.26 (d)-(f) is up to 50%.

For this subcase six independent PSFs, i.e., three PSFs per yielding nodes Nr.1 and Nr.2, are adopted in the reduced modal bases of the first 20 eigenmodes. The curvature error ratios of the PSF applied solution with respect to the reference solution is represented in Fig. 5.27 also with a maximal z-scalar of 50% to give a direct impression of the remarkable improvements. The curvature error ratios near the yielding nodes are generally under 5% by applying the PSFs. Not only the accuracy but also the efficiency of the PSFs should be mentioned here – the computation time for the PSF applied solution is just about 4% of the time needed for the reference solution.

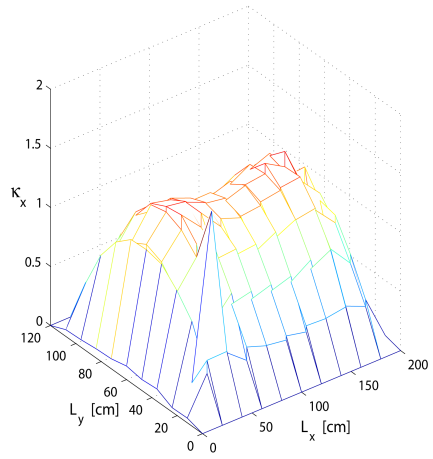

(a) κ_x

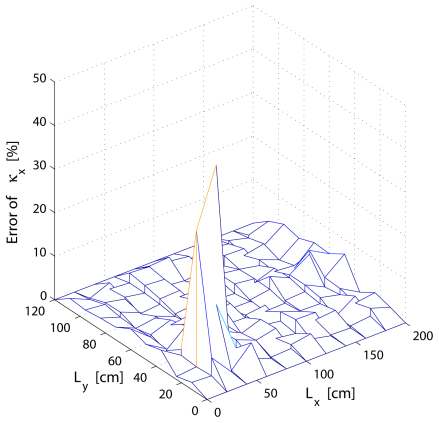

(d) Error of κ_x[%]

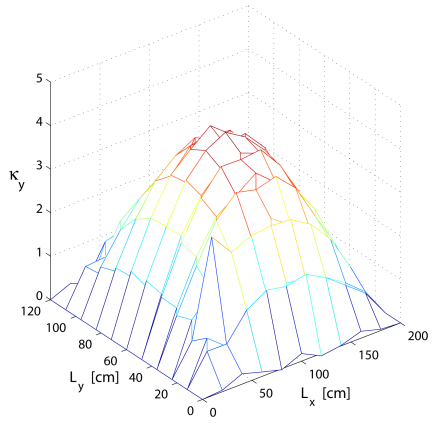

(b) κ_y

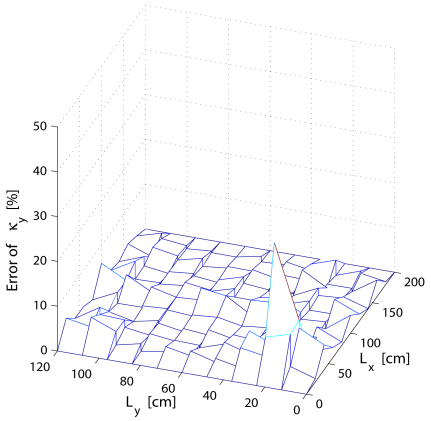

(e) Error of κ_y[%]

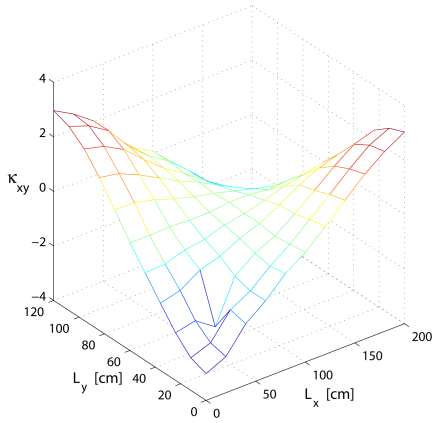

(c) κ_{xy}

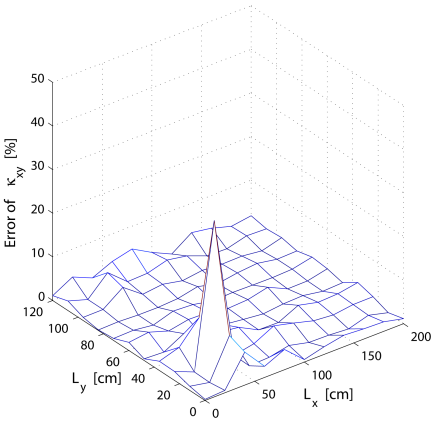

(f) Error of κ_{xy}[%]

Figure 5.26: Reference Curvatures and Error Ratio – 20-modes/reference – Case B.2

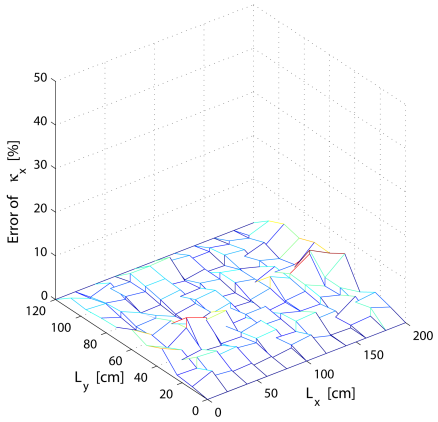

(a) Error of κ_x[%]

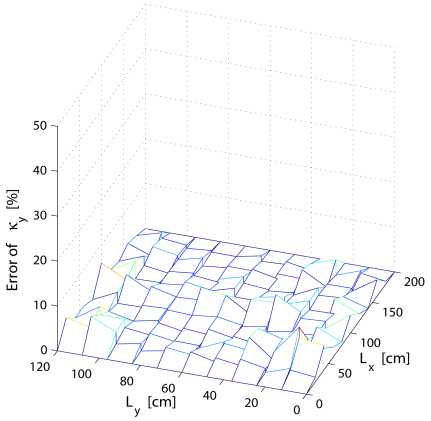

(b) Error of κ_y[%]

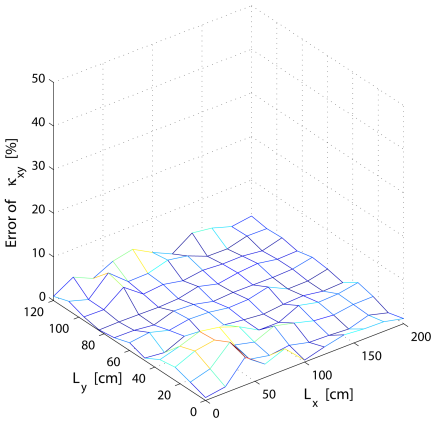

(c) Error of κ_{xy}[%]

Figure 5.27: Error Ratio of Curvatures – (20-modes+PSFs)/reference – Case B.2

To gain more confidence of the PSFs, the time-variation of the moment of the yielding nodes is controlled in Fig. 5.28 (a) and (b).

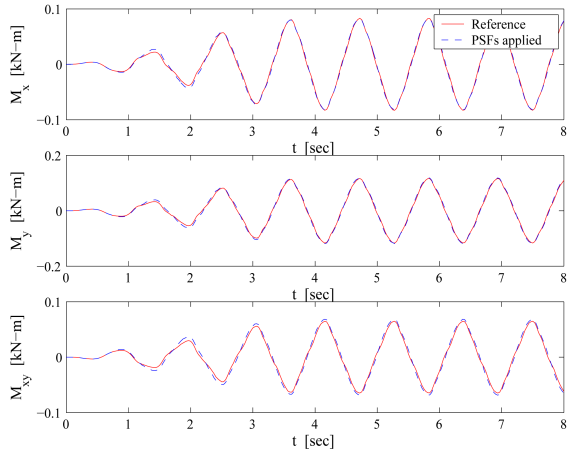

(a) Yielding Node Nr.1

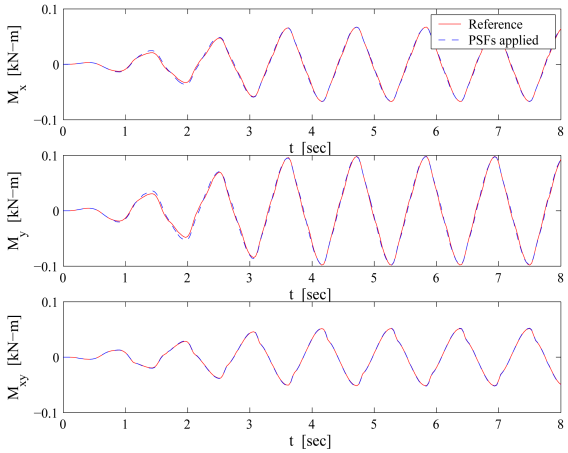

(b) Yielding Node Nr.2

Figure 5.28: Comparison of M_x, M_y and M_{xy} of Yielding Nodes – Case B.2

5.3.6 Case B.3 - Four yielding nodes at plate corner

In this subcase four yielding nodes are assumed to be located along the diagonal near the plate corner as shown in Fig. 5.5 and loaded with $P_a = 5\,[kN/m^2]$. At this place it is no more necessary to show the error of solutions using the first 20-eigenmodes, since its poor approximation of the plastic deformations can be expected. Under this yielding condition totally $3(PSFs) \times 4(nodes) - 1 = 11$ PSFs will be implanted in the reduced modal bases of the first 20 eigenmodes, since the plastic shape function for κ_{xy} of yielding node Nr.2 and Nr.3 are identical. As a result, a PSF applied modal system with 31 DOF, which is smaller than 1/10 of complete modal space, is established. The reference curvature distributions at $t = 8.625\,sec.$ of this subcase are represented in Fig. 5.29 (a)-(c) and the error ratios of the PSF applied solution are given in (d)-(f).

It can be seen that the curvatures of the yielding nodes are well approximated by the PSFs. Generally the curvature error ratios on the yielding nodes are smaller than 2.5%. The relative higher error ratios on the edges of the plate are partially resulting from the elastic approach with the first 20 eigenmodes, which can be realized from Fig. 5.4. It should be noted that even the reference solution is only an approximation after all, since the finite element method self is a numerical approach. For example, the analytical stress resultants, i.e., the curvatures, of the linear hinge supports should actually equal zero, but they are not zeros in the reference solution, which is a shortcoming of the FEM. On the contrary the curvatures of the hinge supports by the 20-modes and the PSF applied solutions are more closer to zero. Therefore the higher error ratios on the edges with respect to the reference solution don't have to mean a poor approach at this place.

With another aspect Fig. 5.30 (a)-(c) represent the plastic part of curvature distributions, which are contributed by the 21 to 400 eigenmodes, and (d)-(f) are curvatures resulted merely from the 11 PSFs. It can be seen that the results of plastic curvatures of these two independent formulations are almost identical, especially around the yielding zone. But the results of the high frequency modes are corrugated outside the yielding zone, while the corresponding results are almost flat by the PSFs approach. This is because that the PSFs are created by the concentrated force group, which is in equilibrium, and their curvatures focus only on the yielding related elements. Besides, it can be seen that the curvatures of the supports are closer to zero by the PSFs approach than the high frequency modes.

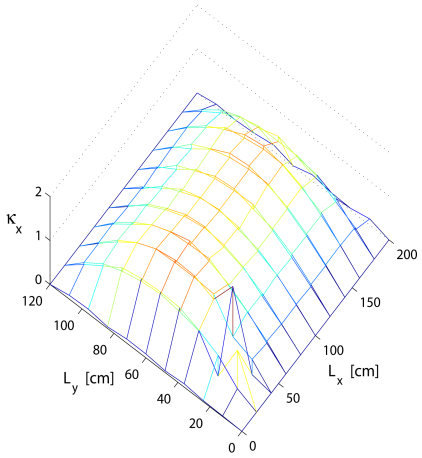

(a) κ_x

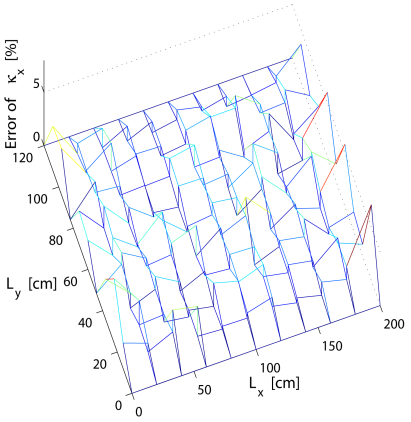

(d) Error of κ_x[%]

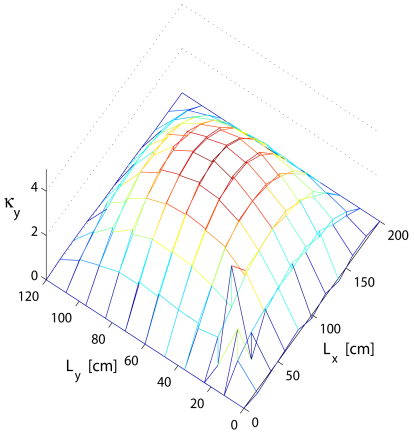

(b) κ_y

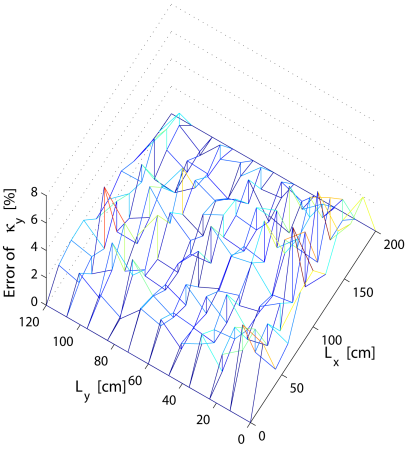

(e) Error of κ_y[%]

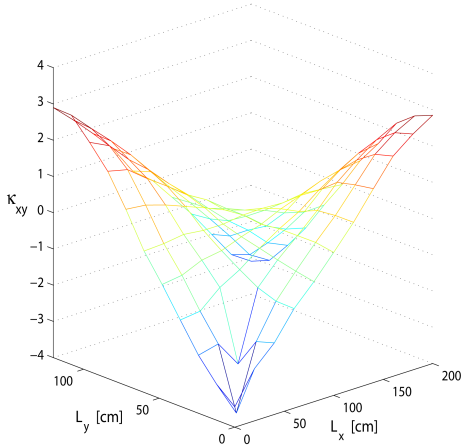

(c) κ_{xy}

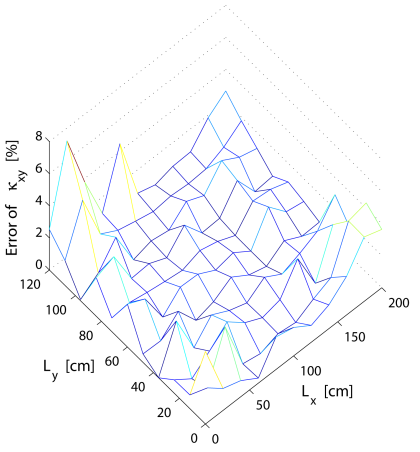

(f) Error of κ_{xy}[%]

Figure 5.29: Reference Curvatures and Error Ratio – (20-modes+PSFs)/reference – Case B.3

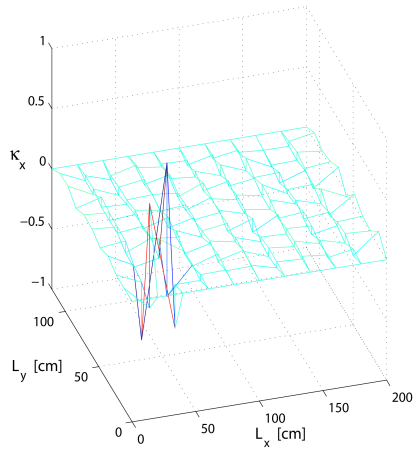

(a) Rf. $\kappa_{x,p}$

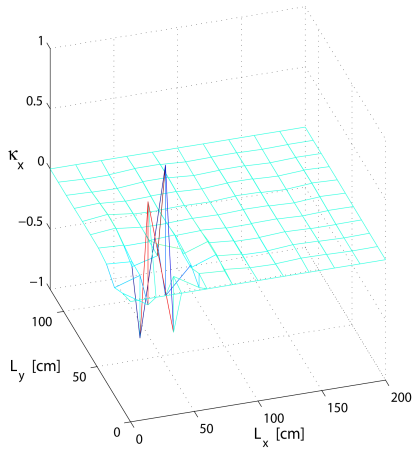

(d) PSF $\kappa_{x,p}$

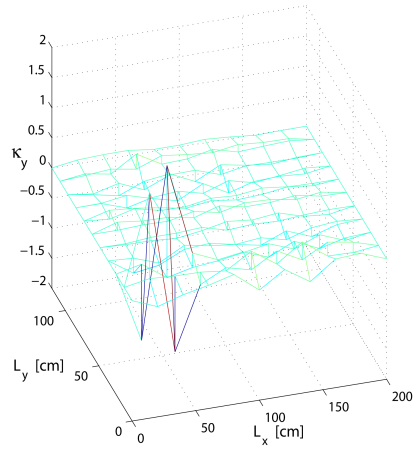

(b) Rf. $\kappa_{y,p}$

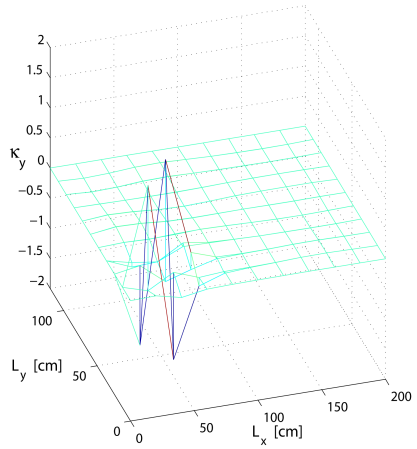

(e) PSF $\kappa_{y,p}$

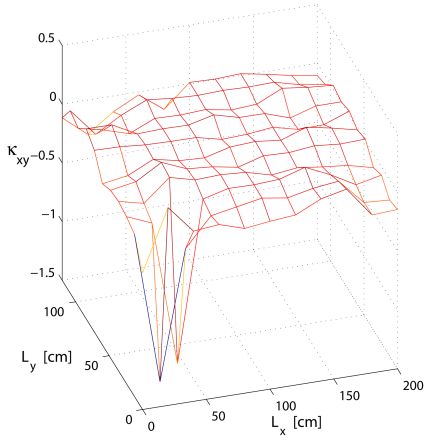

(c) Rf. $\kappa_{xy,p}$

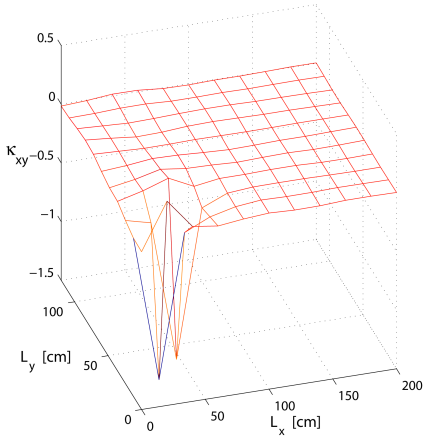

(f) PSF $\kappa_{xy,p}$

Figure 5.30: Plastic Curvatures of 21-400 Modes and of 11 PSFs – Case B.3

5.4 Example of Extreme Loading Conditions

In the previous sections the accuracy and the efficiency of the PSFs has been verified under the condition of a predefined small number of yielding nodes. But in order to have a more precise research of the subject it is necessary to put this plate system, which is given in section 5.1, under an extreme loading without predefining locations with lower yield stress, so that it can be verified if the development of the yielding zones of this model conforms to the classic limit theory of plate [68] and to see if the PSFs can still provide a reasonable approach under such extreme circumstances.

For this purpose a quasi-static loading distributing on a 4×4 elements area in the middle of the plate is used. After (5.1) with $P_a = 6\,[kN/m^2]$, $f = 0.95/64\,[Hz]$ and $t_{max} = 16\,[sec]$ the loading function is shown in Fig. 5.31. All the material properties and the geometrical boundary conditions of the system remain unchanged as in the prior examples. The system is also discretized in a 10×10 FE net, which has 400 deformation DOF and 961 curvature nodes.

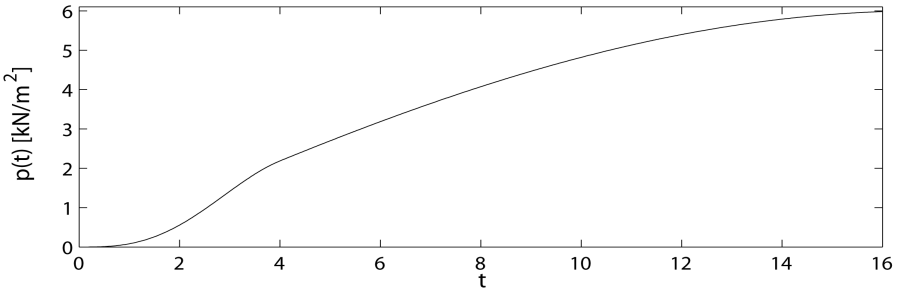

Figure 5.31: Quasi-static loading

As mentioned, no yielding nodes are predefined in this study case, therefore by each calculation step every curvature node has to be judged whether it is over the elastic limit κ_y. If any new yielding nodes are found in a particular calculation step, then this step will be recalculated with additional nonlinear equations corresponding to the new detected yielding nodes. Considering the time history dependency of the plastic deformations once a curvature node reaches the elastic limit, its auxiliary hysteretic equations, i.e., (3.23), have to be added in the differential equations and retained in the equation system to the end of the calculation. Since the vectors of the hysteretic variable $\mathbf{Y}_x$, $\mathbf{Y}_y$ and $\mathbf{Y}_{xy}$ are not invariant with respect to the integration intervals, only the split method introduced in section 3.4.1, but not the patch method, can be applied in this case to reduce the number of the nonlinear equations.

As the reference solution all the 400 eigenmodes are used from the beginning to the end for the calculation and the number, i.e., the location, of the yielding nodes will be automatic detected by the programming. Fig. 5.32 represents the development of the yielding zones of the reference solution. Each color, symbol in this figure denotes a yielding group belonging to a particular integration interval. It can be seen that

the yielding starts from the middle of the plate; as the loading increases gradually the yielding zone extends along the diagonal direction, then plate corners also yield. The final yielding zone with a kind of double Y-shape matches the figure of the yielding chain according to the limit load-carrying capacity theory of plate. Under this extreme loading condition there are totally 567 yielding nodes found at the end, i.e., 59.0% of the plate area is yielded. It is to note that by the last step of the numerical integration there are $567 \times 3 = 1701$ nonlinear auxiliary equations besides the system differential equation with 400 DOF to compute, and the total calculating time, which is performed on the Linux cluster of the Leibniz-Rechenzentrum (LRZ) in Munich, is about 41921*sec.*.

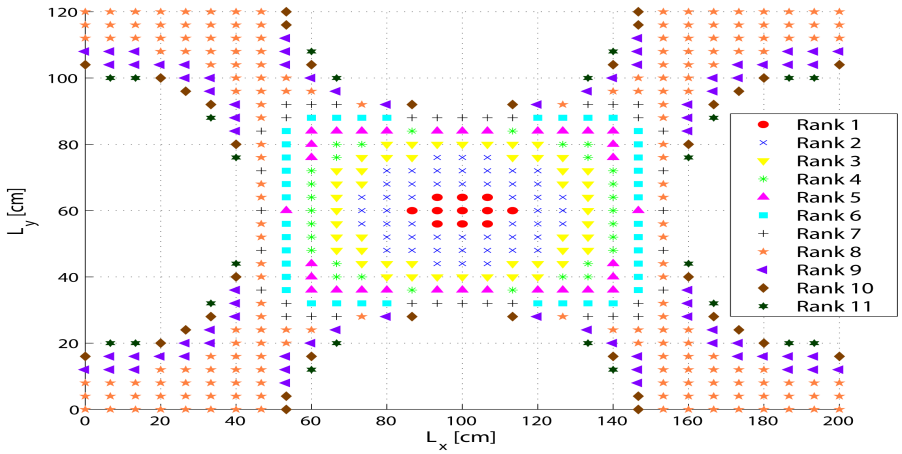

Figure 5.32: Ranking of the yielding zones

In Fig. 5.33 (a)-(c) the maximal curvature distributions at the time $t = 16.0\,sec.$ of the reference solution are represented. It can be seen that in this case the curvature distributions under yielding are not strongly discontinuous, i.e., there are no obvious peaks in the curvatures, since a great successive part of the plate yields. Therefore the error ratio of the curvatures resulted from the approach with the first 20 eigenmodes as represented in Fig. 5.33 (d)-(f) is not very high in comparison with previous examples.

It is to mention that by the approach with the first 20 eigenmodes there are 585 yielding nodes, which is 18 more than the reference solution, detected at the end of the calculation. And its total computation time is about 23088*sec.*, which is near 55.0% of the time needed for the reference solution, although the modal DOF is reduced to only 1/20. To realize why the calculation time is not proportionally decreased, as the system DOF are reduced by the modal transformation method, the system differential equation set (3.64) should be reviewed. It can be seen that although main linear differential equation (3.64a) and the nonlinear auxiliary equation (3.64b) are coupled together through the Y-variables and have to be solved iteratively by using the numerical method, the total computation time can still be roughly separated in two parts for the linear and nonlinear equations respectively. While the computing time of (3.64a) can be compressed by using the reduced modal bases, the time needed for (3.64b) are unmodifiable with the dimension reduction strategies introduced in section 3.4.

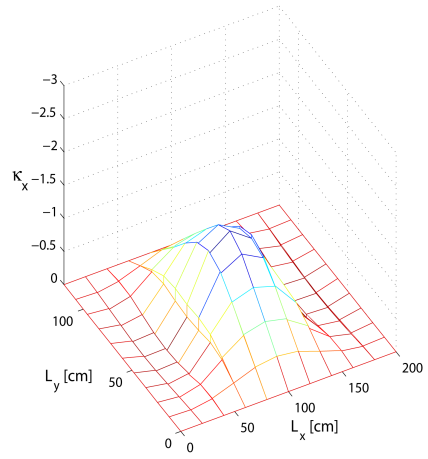

(a) κ_x

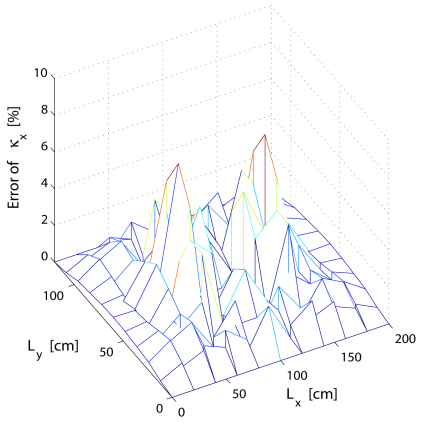

(d) Error of κ_x [%]

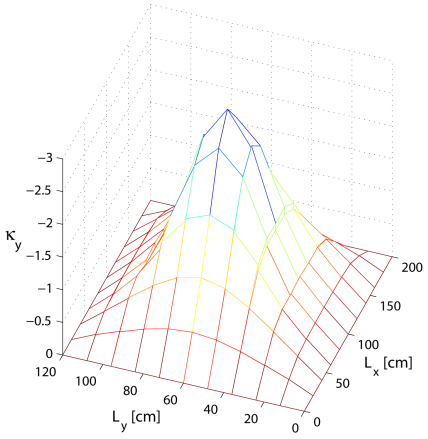

(b) κ_y

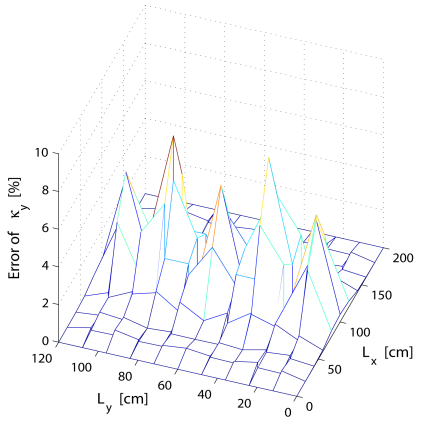

(e) Error of κ_y [%]

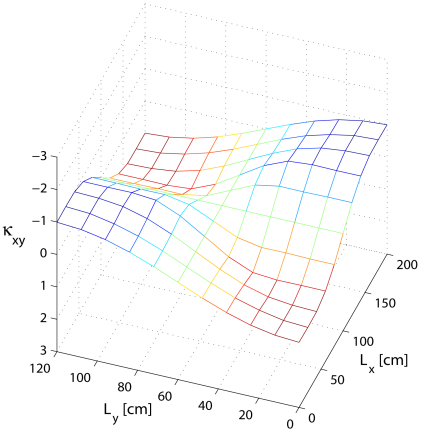

(c) κ_{xy}

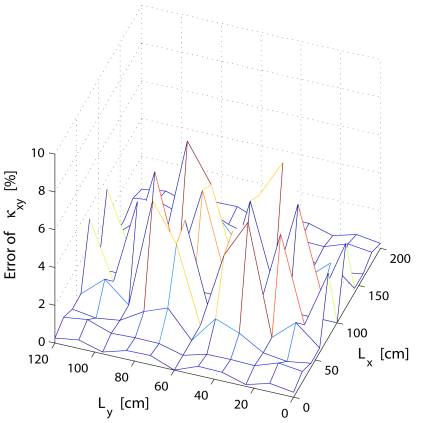

(f) Error of κ_{xy} [%]

Figure 5.33: Reference Curvatures and Error Ratio – 20-modes/reference under Extreme Loading

In Fig. 5.34 (a) and (b) the computing time of a single integration interval of 1*sec.* divided into 32 steps, which is performed on a commercial PC with 1.8 GHz CPU, and the corresponding statistic fitting curve for different conditions are shown. The former is the time–yielding nodes diagram computed with fixed 400 eigenmodes, whose

quadratic fitting curve has the function $f(x) = 0.009375\,x^2 + 2.709\,x + 56.61$ with 95% confidence bounds and has a root mean squared error of 8.449. The latter is the time–eigenmodes diagram computed with fixed 103 yielding nodes, whose quadratic fitting curve has the function $f(x) = 0.0005571\,x^2 + 0.5795\,x + 101.2$ with 95% confidence bounds and has a root mean squared error of 1.845. From these two figures it can be seen that the increase of the computing time by a rising number of yielding nodes is faster than that by a rising number of eigenmodes. Therefore, if the number of yielding nodes is relative high with respect to the total system DOF, such as in this case of study, there will be a great portion of computing time occupied by solving the hysteretic equations, which can not be compressed by the modal reduction, so that the efficiency of the modal transformation wouldn't be so remarkable.

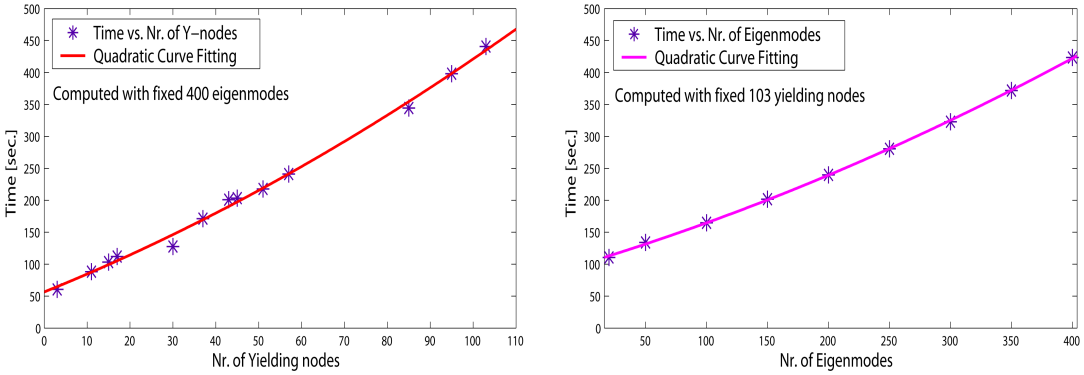

(a) Time – Yielding nodes (b) Time – Eigenmodes

Figure 5.34: Computing time of 1*sec.* integration interval

The approach with PSFs for this study case are also performed to improve the accuracy of solutions. Generally each yielding nodes has three independent PSFs that should be added as the modal vectors in the reduced bases. But considering the linear dependency of the PSFs illustrated in section 4.3 and to reduce the number of modal DOF, the PSFs of the yielding nodes inside the plate element, i.e., the node Nr.13 to Nr.16 in Fig. 3.10, are neglected in the following calculations.

According to the creating procedure of PSFs introduced in section 4.3 the PSFs of the corner nodes relate to four elements, while the PSFs of the edge nodes relate only to two elements, therefore the PSFs of the corner and the edge nodes are actually independent referring to the global system. But after various simulations it is found that the PSFs of the edge nodes could cause a kind of numerical instability as the number of used PSFs is too large and the edge node PSFs are numerically too close to each other, so that even when the rank of the system matrices shows the independency of the PSFs the numerical integration may not converge. To avoid this problem, the PSFs of the edge nodes will be replaced by those of the neighbor corner nodes. The results of this approach, i.e., the error ratio of the curvatures with respect to the reference solution, is shown in Fig. 5.35. Clearly the accuracy of the results are improved by applying the PSFs but the corresponding computing time costs about 32984 *sec.*, which saves only 22 % computing time in comparison with reference solution. On the one hand this is because of the large number of nonlinear equations, on the other hand 267 PSFs are

needed for this approach in addition to the first 20 eigenmodes. Table 5.1 lines up the modal DOF, the total number of detected yielding nodes and the computing time of these three approaches for a direct comparison.

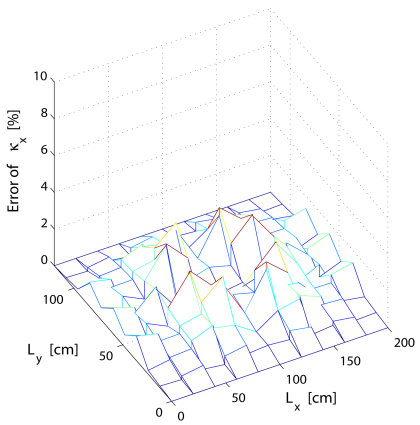

(a) Error of κ_x [%]

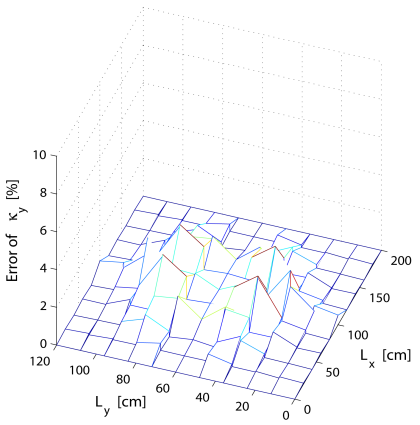

(b) Error of κ_y [%]

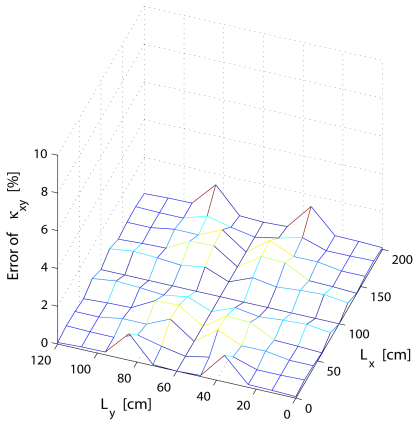

(c) Error of κ_{xy} [%]

Figure 5.35: Error Ratio of Curvatures – (20-modes+PSFs)/reference under Extreme Loading

	applied Modes	Yielding nodes	Time [sec.]
Reference	400	567	41921
Reduced	20	585	23088
PSFs applied	20+267 PSFs	573	32984

Table 5.1: Comparison of Reference, reduced Modal and PSFs applied Approaches

With this investigation the following conclusions could be made:

- Accuracy – The PSFs can well simulate the contribution of high frequency eigenmodes and provide a reasonable approximation. The improvement of accuracy achieved by PSFs is only then significant, when the yielding zone is locally concentrated instead of overall distributed. Or it can be said that the more discontinuous the yielding curvatures are, the greater is the improvement earned by the PSFs.

- Efficiency – The PSFs can only raise the efficiency through the reduction of the system dimensions, i.e., the modal DOF. When the proportion of the yielding nodes to the total system DOF is too high, the saving time through PSFs can not catch up the time consumed by calculating the nonlinear auxiliary functions, so that the efficiency achieved by the PSFs is no longer significant. A problem of this kind is not what the PSFs deal with. Such problem can perhaps be solved by proposing a new nonlinear material model or introducing a new concept to condense the number of yielding nodes.

Chapter 6

MCS of Large Scale Flat Slabs

6.1 Stochastic Mechanics

As a branch of the mechanics, the stochastic mechanics is concerned with the uncertain properties in the structural analysis. In the past half century this subject has gained more importance, since the risk of the civil engineering constructions rises gradually with their expanding dimensions.

In reality, neither the system characteristics, such as the material property, the damping character, the geometrical conditions ... etc., nor the external excitations are deterministic. Such uncertainties have to be considered, if the reliability of the constructions is relevant. Already 80 years ago, it was suggested that the uncertainties inherent in the analysis and design of structures should be modeled by the probability theory [47]. And *A.M. Freudenthal* has even envisaged, that "probabilistic reasoning and the application of statistical methods must become an integral part of the procedures of structural design and analysis" [24].

As mentioned in Chapter 1 only the random external excitations are considered in this work to simulate the stochastic property of a dynamic system. Two methods of solving the NSD problems are introduced in the following section, in which the MCS is adopted in the present work. Further expositions about the definition and the representation of stochastic processes are given in appendix E.

6.1.1 Estimation of Stochastic System Responses

Generally it is impossible to find the analytical solution of stochastic responses for nonlinear systems. In such cases the solution strategies are classified into two groups, i.e., the simulation and the approximation methods. In the benchmark study [75] it is shown that most of the computational methods developed in stochastic structural dynamics are quite limited with respect to the dimension of the problem and conse-

quently are not suitable to be applied to engineering problems of larger scale. Methods, such as numerical solutions based on the Fokker-Planck equation by path integration, increase in complexity at least exponentially with the system dimension.

It appears that the Monte-Carlo simulation and the Equivalent Statistical Linearization, which belong to simulation and approximation methods respectively, are more applicable to nonlinear dynamic systems with large size. Therefore these two methods are discussed briefly in the following. An overview and the comparison of them can be found in [73], [63].

Monte-Carlo Simulation (MCS)

In the publications [80] and [87] the Monte-Carlo simulation was first applied in stochastic structural mechanics. With this procedure, as its name indicates, the stochastic system response will be estimated through simulations. In other words, a collective of realizations of the input, which approximate the loading process with given statistic properties, will be generated independently and by using them the probability characters of the response will be determined such as the game of chance. This simplest form of MCS is also denoted as direct Monte-Carlo Simulation (DMCS). With the following benefits is the MCS certainly the most general approach among all available procedures [71].

1. Generality – MCS is applicable to linear and nonlinear problems in the same way, i.e., no distinction is required between linear and nonlinear problems.

2. Adaptability – All well developed deterministic procedures are adaptable to evaluate the system response by the MCS. Since each realization of the random process, which is a (deterministic) function of random numbers obtained from random number generator, is treated as the input of a deterministic calculation.

3. Dimension Independency – Contrary to other procedures, the accuracy of MCS is independent of the dimensionality of the problem. The influence factors of the accuracy are the sample size N_s and the capability of the random number generator to produce pseudo-statistically independent and equally distributed sets of random variables. The DMCS has an absolute estimation error that decreases with $N_s^{-1/2}$, independently of the system dimension N, whereas all other approaches have errors which decrease with $N_s^{-1/N}$ at best [22].

Therefore the MCS is especially suitable for analyzing large and strongly nonlinear structure systems, discretized by FE-models, under stochastic excitations. Generally a sample size of few hundred independent realizations is sufficient to obtain the basic information of the response distribution, e.g., the mean and variance values. For the reliability assessment, which requires the failure probabilities in the range of $10^{-7} < p_f < 10^{-4}$, the DMCS is inadequate to provide the needed information in the low probability tails of the distribution, unless the sample size N_s is greater than 10^6

(s. [73]).

Obviously such a large number of simulations is only performable for small and simple systems, since the dimension of the system, the complexity of the nonlinear structural models and especially the dynamic analysis will extremely increase the computational burdens. To improve the computational efficiency of the MCS, i.e., to reduce the sample size but keeping the accuracy, the so-called "variance reduction" methods were developed, e.g., importance sampling, adaptive sampling and controlled Monte-Carlo simulation [66], [57], [58]. These procedures can be summarized as methods that focus the analysis in the important domain, i.e., increase the sampling density in the low probability domain, where the realizations contribute most to the failure probability.

Equivalent Statistical Linearization

Contrary to the simulation method the equivalent statistical linearization (ESL), abbreviated as EQL in the literature, is certainly the most widely applied method to determine the response of nonlinear system under stochastic excitations approximately. As bases of the standard ESL technique, the work of Kazakov [40], Caughey [15] and Atalik Utku [4] are worth mentioning.

In the procedure of ESL the original nonlinear differential equation, e.g., (B.4), will be replaced by a approximate linear differential equation such as [101]

$$\dot{z}(t) = C_1(t)\,\dot{x}(t) + C_2(t)\,z(t) + C_3(t)\ , \tag{6.1}$$

where $C_1(t)$, $C_2(t)$ and $C_3(t)$ are linearization coefficients. These coefficients are determined according to the criterion that the error of the approximation $\varepsilon(t)$, i.e., the difference between the original and the linearized equation, is minimized in mean square sense

$$E\{\varepsilon^2(t)\} \to \min\ . \tag{6.2}$$

Under the stationary zero-mean Gaussian excitation the linearization coefficients C_1 and C_2 are independent of time and $C_3 = 0$. The determination of C_1 and C_2 for the one-dimensional Bouc-Wen hysteretic model can be found in [100] and [6]. For two- and three-dimensional cases the ESL procedure can be read in [53] and [88] respectively.

Already in [14] Caughey applied the ESL to analyze the single mass-spring system with bilinear hysteresis under white noise excitation. Recently the application of ESL for nonlinear 3-D framework is performed in [33]. The evolution of ESL, applying to various engineering problems, can be found in [98]. A detailed introduction of the ESL method and the hysteretic material behavior is given in the book by Roberts/Spanos [65]. An overview of this method can also be read in the work of Socha/Soong [90]. The comparison between the ESL approximation and the Monte-Carlo simulation is carried out in [63].

6.1.2 White Gaussian Noise

Usually the computational costs of determining the stochastic nonlinear responses of large FE systems by the direct Monte-Carlo simulation are so huge that such a job is not affordable for commercial PCs, although the direct MCS can provide a better solution than other approximate methods. Just for this reason, the direct Monte-Carlo simulation is chosen in the present work to demonstrate the tremendous efficiency obtained directly from the application of plastic shape functions in large nonlinear FE systems under stochastic excitations.

The first step of the MCS is to establish the realizations, which approximates the stochastic loading process, since they are the foundation of the simulation. The white noise spectrum, which is an idealized mathematical model due to its unbound spectral density function $\mathbf{S}(\omega)$, is chosen as a basis to represent the stochastic excitations. As indicated in [43] the white noise spectrum can well approximate the actual excitation spectral density, as long as it is wide-band in comparison with the system transfer function $|H(\omega)^2|$. Furthermore it is assumed that the loading process is Gaussian, so that the realizations can be created by the spectral method. In other words, the realization will be obtained from the discrete inverse Fourier transformation (DIFT) of its spectral signals. And such spectral signals are formulated as the multiplication of spectral amplitudes with random phase angles, which are equally distributed between $[0..2\pi]$ and can be created by a random number generator.

The magnitude of the discrete spectral amplitude in time average – $\langle|\tilde{P}_m|\rangle$, can be determined from the power spectral density as

$$\langle|\tilde{P}_m|\rangle = \sqrt{2\pi\, S_m / T_p} = \sqrt{S_m\, \Delta\omega}\ , \tag{6.3}$$

where S_m is the coefficient of the Fourier expansion of the periodic autocorrelation function $\tilde{R}_{per}(\tau)$ (cf. (E.9b)), and $T_p = 2\pi/\Delta\omega$ is the period of loading according to the discretized frequency $\omega_m = m\,\Delta\omega$, $m = 0, 1, 2\cdots$. The detailed explanation of deriving this equation is given in appendix E.3.

For the general white noise signals is the power spectral density $S_{xx}(\omega_m)$, i.e., S_m, a constant. For the filtered white noise, e.g., the ground motion considering the layer of earth, the well known Tajimi-Kanai spectrum [39], [94] can be used, which is introduced in section 6.2.2.

With (6.3) the spectral amplitude P_m of the periodic random loading $\tilde{p}_{per}(t)$ can be written as

$$P_m = \langle|\tilde{P}_m|\rangle\, e^{i\theta_m}\ , \tag{6.4}$$

where θ_m is the equally distributed random phase angle between $[0..2\pi]$.

Through the discrete inverse Fourier transformation the random loading can be reconstructed as

$$\tilde{p}_{per}(t) = \sum_{m=-\infty}^{\infty} \sqrt{S_m\,\Delta\omega}\, e^{i(\omega_m t+\theta_m)} \ . \tag{6.5}$$

To apply the numerical integration method, the time axis is also discretized, such that $t_n = n\,\Delta t$ for $n = 0, 1, 2 \ldots N$ and $N = T_p/\Delta t = 2\pi/(\Delta t \Delta\omega)$. Under this discretization is the sampling angular frequency $\omega_{smp} = 2\pi/\Delta t = N\Delta\omega$, and the maximal cutting-off frequency is defined as $\omega_{cut} = m\Delta\omega$. According to the *Nyquist-Shannon sampling theorem* [51], [79] the following criterion should be hold

$$\omega_{smp} \geq 2\,\omega_{cut} \ , \tag{6.6}$$

in order to avoid the aliasing effect. This leads to $m \leq N/2$. Therefore the discrete loading signals can be determined as

$$\begin{aligned} \tilde{p}_{per}(t_n) &= \sum_{m=-N/2}^{N/2} \sqrt{S_m\,\Delta\omega}\, e^{i(\omega_m t_n+\theta_m)} \\ &= 2\sqrt{S_m\,\Delta\omega}\,\Big[\,\frac{1}{2} + \sum_{m=1}^{N/2}\big[\cos(\frac{2\pi}{N}mn)\cos(\theta_m) - \sin(\frac{2\pi}{N}mn)\sin(\theta_m)\big]\Big] \ . \end{aligned} \tag{6.7}$$

6.2 Seismically Loaded RC Slab

Based on the project of a apartment building in Munich – *Arnulfpark München MI 1*, whose construction is designed by the engineering consultant "Henke & Rapolder Ingenieurgesellschaft mbH", a model of reinforced concrete slab is created in this section and loaded by a vertical seismic acceleration. Because of the limitation of computational capacities only about one-third of the actual floor slab is modelled with certain idealizations as the example used here. However, the purpose of this example is not to analyze a 'real' construction but to show the capability of the PSF applied method. Since for such a large model the nonlinear Monte Carlo Simulation of the seismic responses is inexecutable on commercial PCs because of the enormous degrees of freedom, if the general modal analysis is used.

6.2.1 Model of the RC Slab

Fig. 6.1 represents the model of slab with necessary information for the analyses such as dimensions, boundary conditions and reinforcement, etc.. According to the static analysis made by the engineering office a finite element with a size of $10\,cm \times 10\,cm$ is chosen for the stress concentrating areas and a size of $20\,cm \times 20\,cm$ is used for the fields. Because the limitation of the rectangular Schäfer element applied in this work, two transition elements of $10\,cm \times 20\,cm$ and $20\,cm \times 10\,cm$ are required, which inevitably cause curvature discontinuities at the transition boundary lines. The corresponding

FE discretization is represented in Fig. 6.2. This FE model has totally 7416 elements and 29536 DOF.

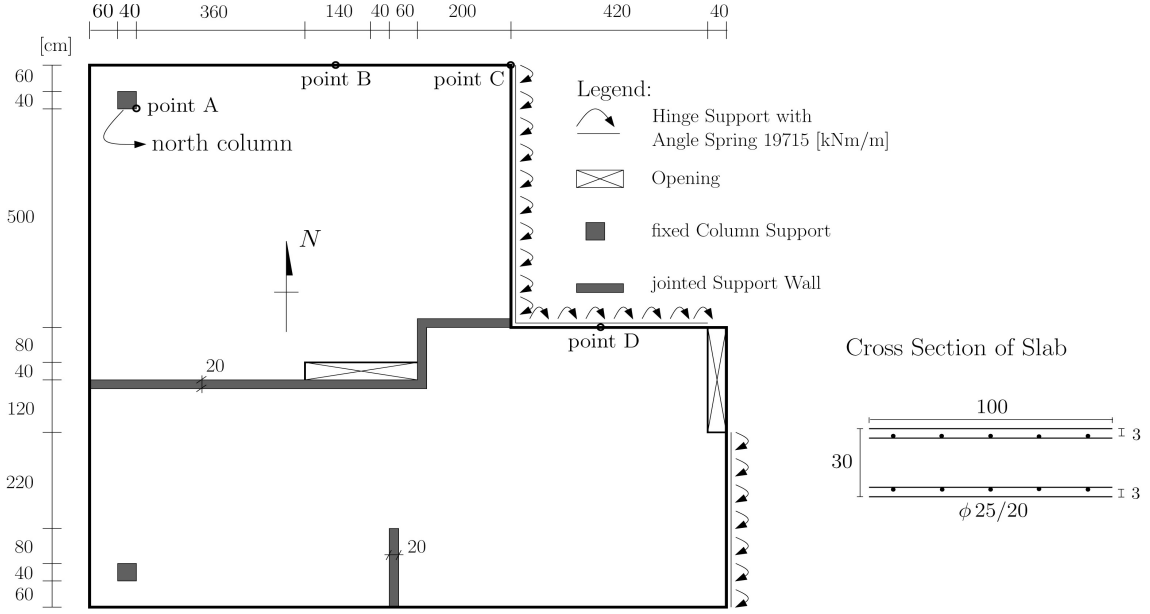

Figure 6.1: Model of RC Slab

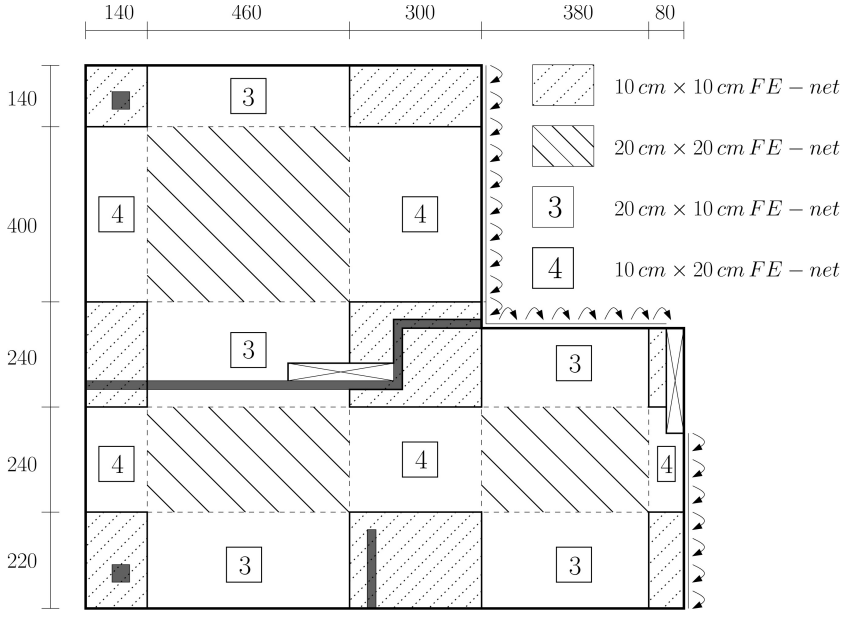

Figure 6.2: Finite Element Discretization

The construction materials used are C30/37 for concrete and BSt 500 S for reinforcement after the code [2]. The RC slab is assumed to be homogeneous and isotropic, so that the depth of concrete section under compression is about $6.5\,cm$ by the "state II" (cracks in concrete) [107] and the plastic limit of curvature is $\tilde{\kappa}_p = 0.0106$ as the reinforcement yields at the tension side.

Fig. 6.3 shows the static deformation and the corresponding curvatures distribution under a uniformly distributed loading of $5.0\,kN/m^2$. Obviously there are stress concentrations at the corners of the slab and around the column supports.

Considering the limitation of the computational memory capacity (1Gb RAM) it is necessary to indicate the yielding related elements, so that the number of the hysteretic variables can be confined by using the patch method. According to this static analysis 40 elements near the corners and column supports are regarded as elastic-plastic and 48 nodes in them could reach the yielding limit during the calculation.

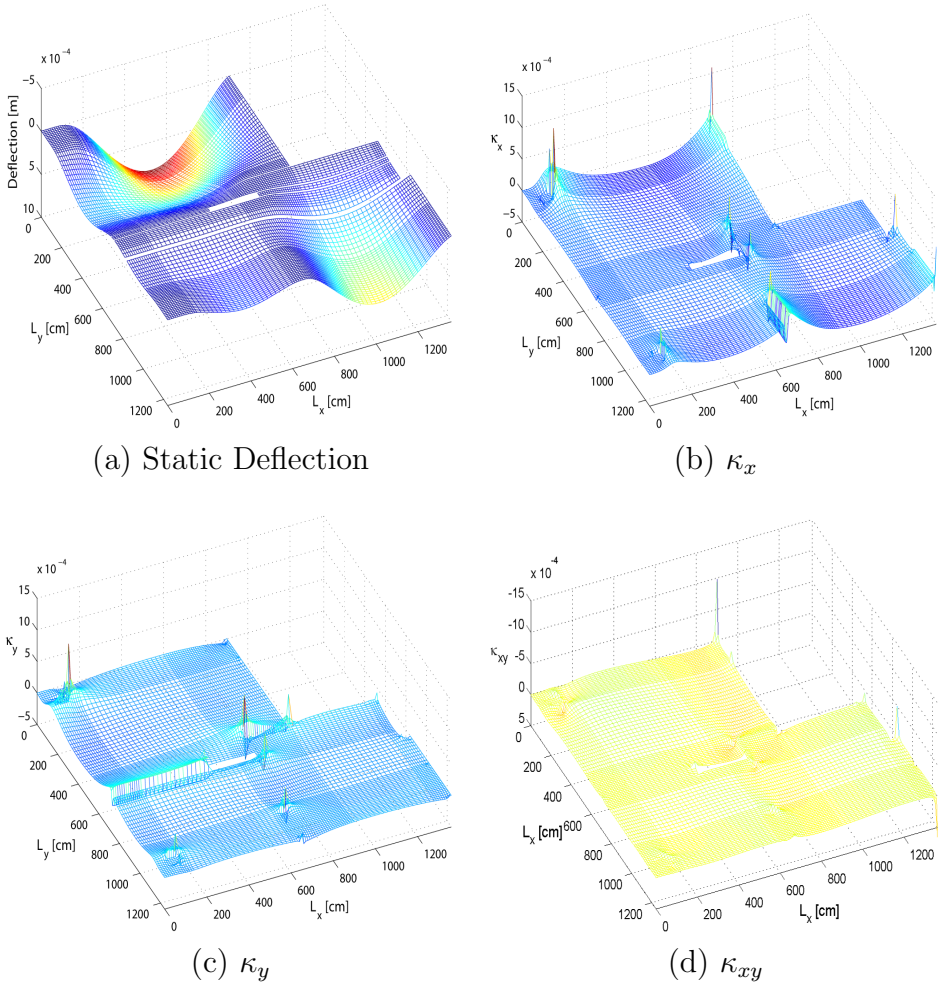

(a) Static Deflection (b) κ_x

(c) κ_y (d) κ_{xy}

Figure 6.3: Static Deflection and Curvatures under $5.0\,kN/m^2$ Loading

6.2.2 Formulation of Seismic Loadings

The time variance of the vertical seismic acceleration is formulated as the filtered Gaussian White Noise. The simplest filter model to approximate the characters of layered, depth dependent half-space is the Kanai-Tajimi-Model, which considers the

top layer of underground as a single oscillator excited from its bottom, so that the following differential equation can be built [39], [94].

$$\ddot{u}_1(t) + 2\,\beta_g\,\Omega_g\,\dot{u}_1(t) + \Omega_g^2\,u_1(t) = -\ddot{u}_0(t)\ , \tag{6.8}$$

where β_g, Ω_g are underground's damping and eigenfrequency values. And $\ddot{u}_0$ is the seismic excitation.

When $\ddot{u}_0$ is a stationary White Noise, the power spectrum of the acceleration in free field, i.e., the Kanai-Tajimi-Spectrum, can be formulated according to the random vibration theory as [48]

$$S_{KT}(\omega) = S_0\,\frac{\Omega_g^4 + 4\,\beta_g^2\,\Omega_g^2\,\omega^2}{(\Omega_g^2 - \omega^2)^2 + 4\,\beta_g^2\,\Omega_g^2\,\omega^2}\ , \tag{6.9}$$

where S_0 represents the strength of the earthquake.

Since the intensity of the seismic energies changes during the earthquake, the filtered acceleration signals are modulated with a intensity function $I(t)$, which can be considered to have a constant equivalent intensity for about 1/3 of the excitation time T_d and a short increasing but long decay stage for practical applications. These three stages can be for example defined as following

$$\begin{aligned} t < 0.15\,T_d: &\quad I(t) = \Big(\frac{t}{0.15\,T_d}\Big)^2 \\ 0.15\,T_d < t < 0.45\,T_d: &\quad I(t) = 1 \\ 0.45\,T_d < t: &\quad I(t) = e^{-c(t-0.45\,T_d)}\ , \end{aligned} \tag{6.10}$$

so that $\ddot{u}(t) = I(t)\,\ddot{u}_1(t)$.

If the central-European earthquake with underground class 'M' is considered, the following parameters of the Kanai-Tajimi-Spectrum can be used [48].

$$\beta_g = 0.7\ ; \quad \Omega_g = 15\,[rad/s]\ ; \quad T_d = 9\,[sec.]\ ; \quad c = 0.4\ . \tag{6.11}$$

With $S_0 = 0.5221\,[m^2/s^3]$, which corresponds to the MSK-Intensity scale 'X', the corresponding Spectrum and the intensity function used are shown in Fig. 6.4 (a), (b) respectively.

Replacing the constant power spectrum amplitude S_m in the first equation of (6.7) with the Kanai-Tajimi-Spectrum (6.9), by which a cutting off frequency $f_{cut} = 32$ [Hz] is used, then producing θ_m with a random number generator, so that the filtered white noise signals of seismic acceleration can be produced as shown in Fig. 6.5.

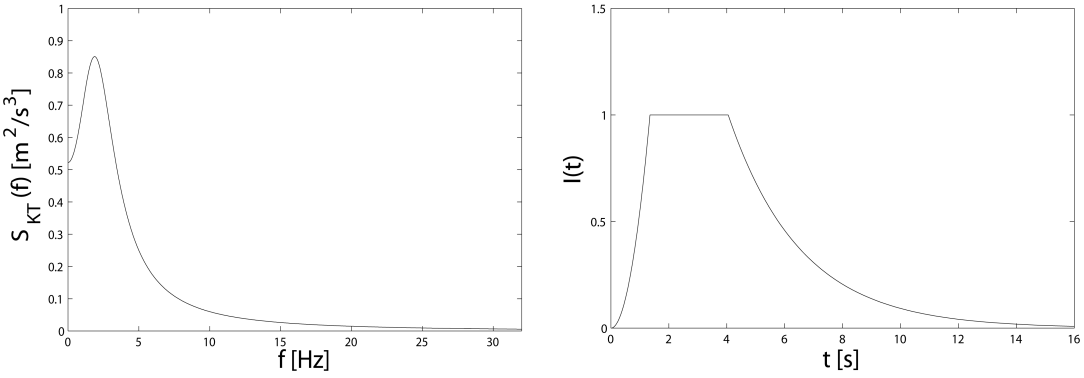

(a) (b)

Figure 6.4: Kanai-Tajimi-Spectrum & Intensity function

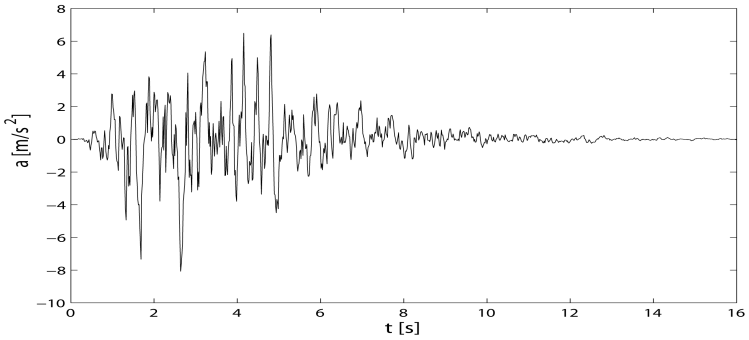

Figure 6.5: Pseudo Seismic Acceleration Signals

6.3 Numerical Results of One Single Random Process

Only the first 400 eigenmodes of the system are calculated because of the limitation of computational capacities (1Gb RAM). Before performing the Monte Carlo simulations some results of a single realization using the excitation as given in Fig. 6.5 still have to be discussed. In Fig. 6.6 the linear-elastic deformations resulted from the first 20 and 400 eigenmodes respectively are represented. According to the observation points A, B, C and D defined in Fig. 6.1, the figure 6.7(a) shows the twisting angle ψ_{xy} at the left under corner of the north column, 6.7(b) gives the max. deflection w of the north free edge, 6.7(c) indicates the rotation angle ψ_x at the northeast corner of the slab and 6.7(d) illustrates the rotation angle ψ_y in the middle of the simple supported edge.

It can be seen that the first 20 eigenmodes can well simulate the elastic system response, since the cut off frequency of random excitation lies on 32 [Hz] and the 20'th eigenfrequency is about 115 [Hz].

With the same random loading used above, the hysteretic material model (3.23) will be applied on this system with $\beta_M = 4450.0$ and with the post-yielding stiffness ratio $\alpha = 0.1$. A constant damping ratio of this system with $\zeta = 0.865\%$ is also assumed.

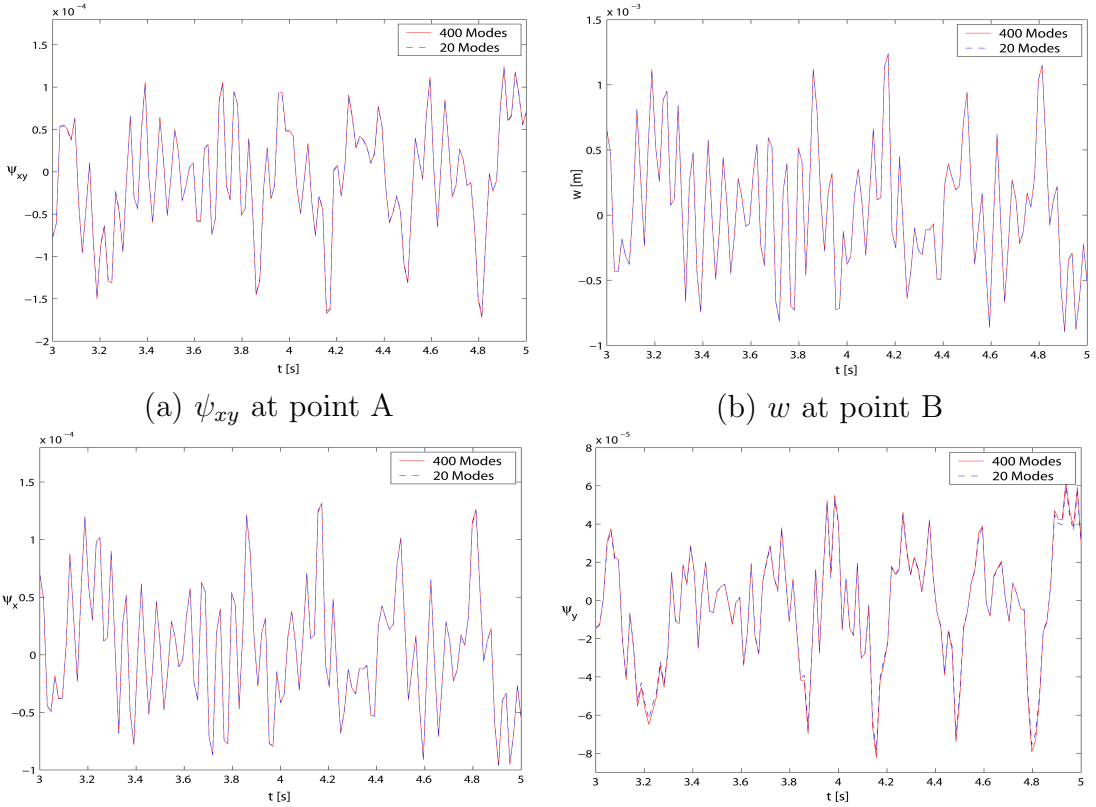

(a) ψ_{xy} at point A

(b) w at point B

(c) ψ_x at point C

(d) ψ_x at point D

Figure 6.6: Comparison of Elastic Deformations – 20/400 eigenmodes (ref. Fig. 6.1)

Three approaches, namely the approach with the first 20 eigenmodes, with the first 400 eigenmodes and with 20 eigenmodes plus 72 PSFs, are performed to give comparisons. Since the yielding locations are locally concentrated in small regions, the difference of deformations between the pure elastic and the elasto-plastic responses is insignificant in the global system. The distinction between these approaches is then obvious if the curvature distributions are considered, such as in Fig. 6.7 the curvature differences between the elastic solution with 400 eigenmodes and plastic solution with 20 modes + 72 PSFs are represented.

It can be seen clearly from this figure that the nonlinear behaviors locate on the single column corners, especially on the north column, and on the corner of the internal jointed support wall.

Fig. 6.8 (a)-(c) shows the curvature difference between the 20 modes and the 400 modes approaches under plastic system responses. When comparing this difference with the difference between the 20 modes and the 20 modes + 72 PSFs approaches, which is represented in Fig. 6.8 (d)-(f) and has a much larger z-scale (30%), under the same loading conditions, it is reasonable to use the first 20 modes as the reduced modal bases, so that the computing costs can be reduced several times without significant loss of accuracy in comparison of using 400 modes.

From Fig. 6.8 (d)-(f) it can be seen that there are two substantial yielding locations at the corner of the north column and of the internal support wall. Considering the "punching shear failure" of the flat slab system it is necessary to take a further investigation at the north column in this study case. Fig. 6.9 (a) gives a detailed sketch of the north column, which has 9 yielding related elements and 16 yielding nodes, in which are only 6×3 PSFs for the yielding corner nodes used as modal vectors. Fig. 6.9 (b)-(f) compare the time variance of the curvatures κ_x and κ_{xy} between the 20 modes and the PSFs applied solutions for the points A, E, F, G and H respectively.

Just as already shown in Fig. 6.8 (d) and (f) the difference of κ_{xy} between the 20 modes and the 20 modes + 72 PSFs solutions is clearly higher than that of κ_x. With detailed analyses at the north column remarkable observations were found that, the twisting curvature κ_{xy} of the point A and H have a completely reverse sign as shown in Fig. 6.9 (b) and (f). This is because that, as the edge at the right hand side of the north column yields, the yielding enhances the change of the rotation angle ψ_x on this edge. Clearly the first 20 eigenmodes can not describe such plastic deformations with the result that the twisting angle ψ_{xy} can not be evaluated correctly. Such phenomenon is called as the *Nonlinear Column Support Effect* in the following.

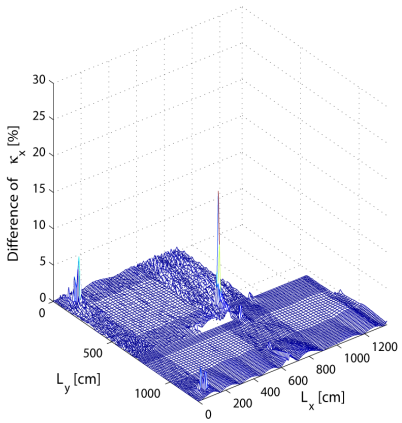

(a) Difference of κ_x

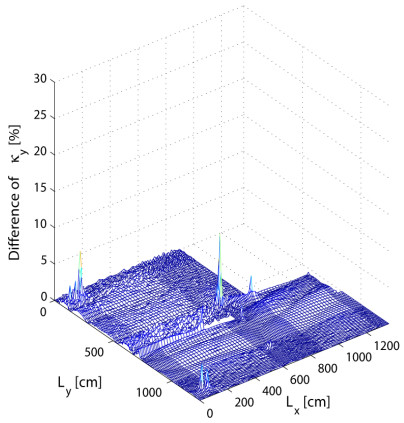

(b) Difference of κ_y

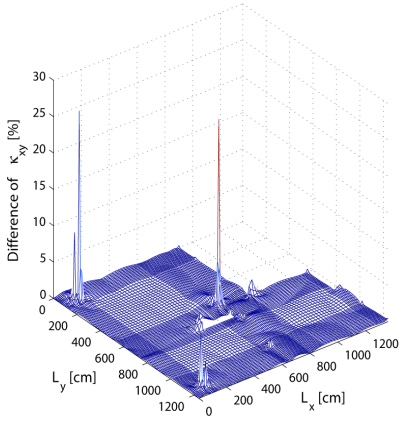

(c) Difference of κ_{xy}

Figure 6.7: Difference of curvatures – (el. 400 modes)/(pl. 20 modes + 72 PSFs)

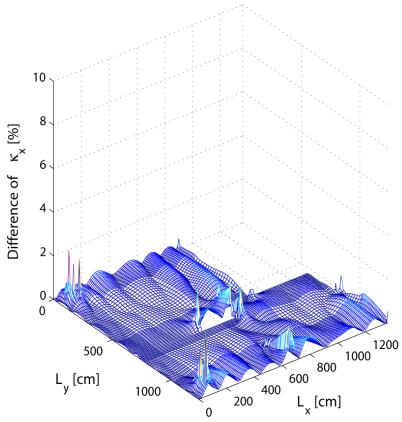

(a) Diff. of κ_x 20 mod./400 mod.

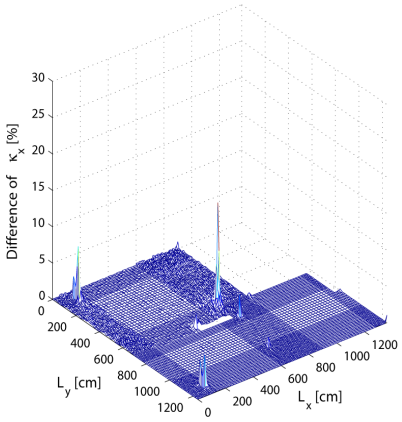

(d) Diff. of κ_x 20 mod./(20 mod.+72 PSFs)

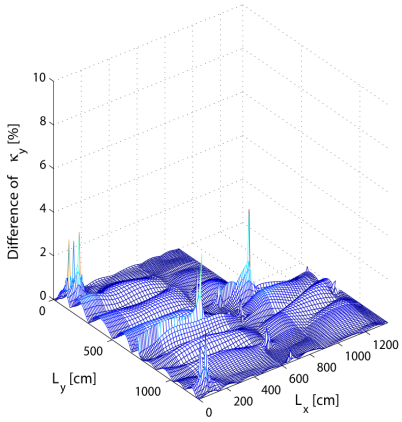

(b) Diff. of κ_y 20 mod./400 mod.

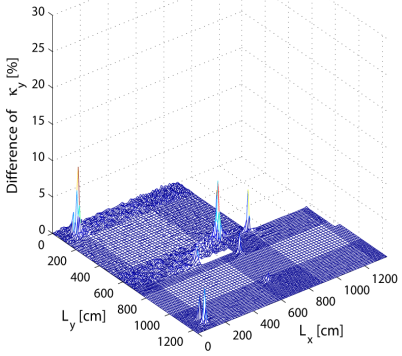

(e) Diff. of κ_y 20 mod./(20 mod.+72 PSFs)

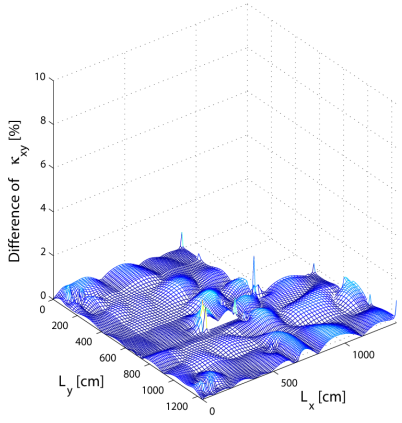

(c) Diff. of κ_{xy} 20 mod./400 mod.

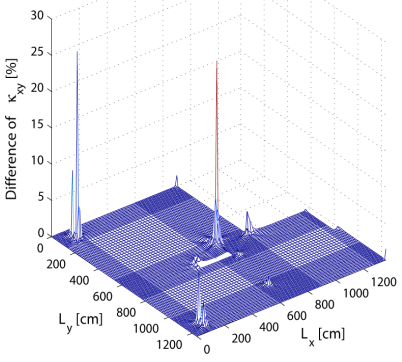

(f) Diff. of κ_{xy} 20 mod./(20 mod.+72 PSFs)

Figure 6.8: (a)-(c) Difference of Curvatures between pl. Solutions with 20 modes and with 400 modes. (d)-(f) Difference of Curvatures between pl. Solutions with 20 modes and with (20 modes + 72 PSFs)

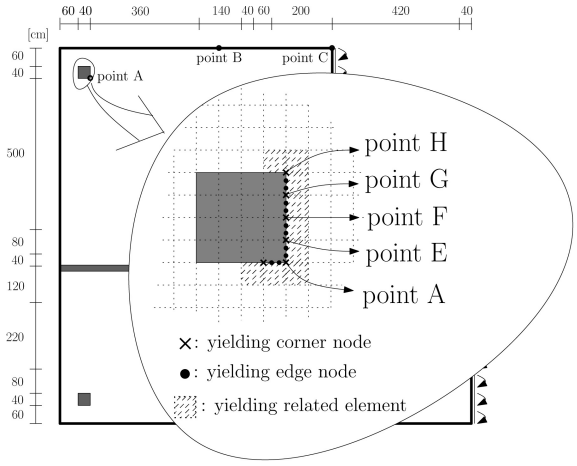

(a) Detail of North Column

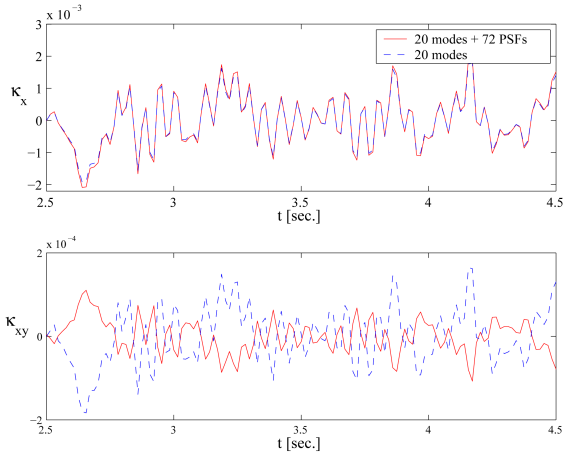

(b) comparison of curvatures at point A

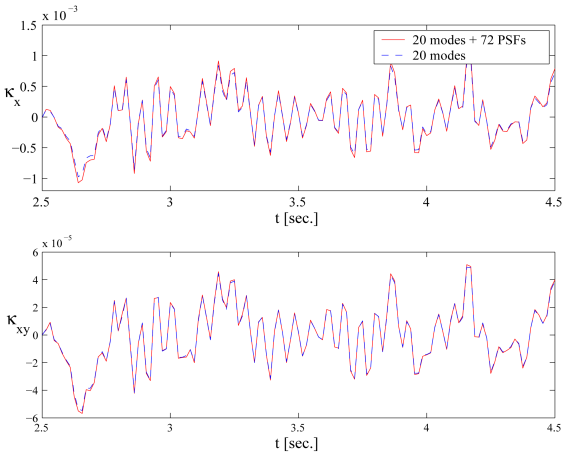

(c) comparison of curvatures at point E

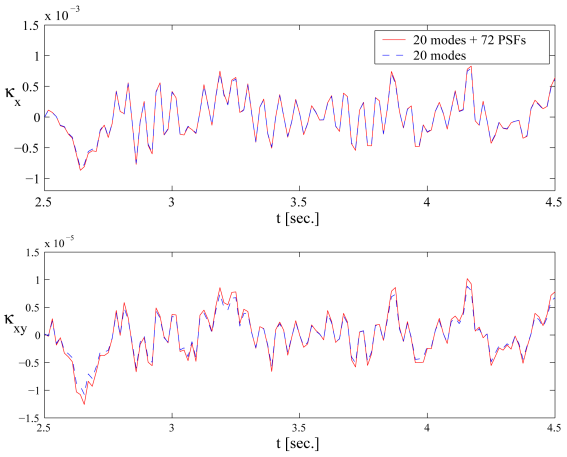

(d) comparison of curvatures at point F

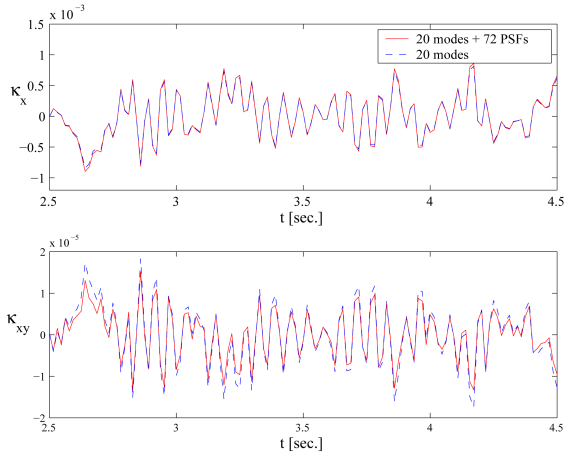

(e) comparison of curvatures at point G

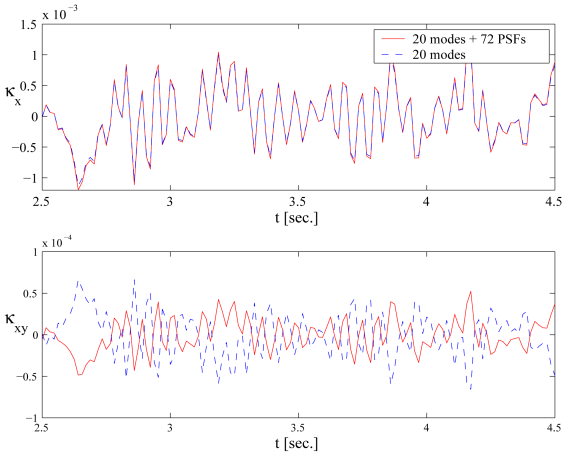

(f) comparison of curvatures at point H

Figure 6.9: Comparison of κ_x, κ_{xy} between Solutions with 20 modes and with (20 modes + 72 PSFs) on Points A, E, F, G, H of the North Column

6.3.1 Verification of Nonlinear Column Support Effects

The pure mechanical explanation of the nonlinear column support effects mentioned above doesn't seem to be persuasive enough to declare that such a great improvement can be achieved by the PSFs. Therefore it is necessary to verify this revelation on a independent system, on which a reference solution resulted from the utilization of all the eigenmodes can be earned and the approach of the PSFs can be compared with it. Fig. 6.10 shows the plate system to be investigated for this purpose. The steel plate is assumed to be $5\,mm$ thick and has the material properties of 'S 235'. This plate is simply supported at the right hand side through a linear hinge and has a fixed column support near the top left corner. A finite element with the dimension of $10\,cm \times 10\,cm$ is chosen for the discretization, which results in a numerical model of 320 elements with 1366 DOF. To simplify the calculation, a harmonic loading formulated by (5.1) with $P_a = 1.0\,[kN/m^2]$ and $f = 0.9$ is used for this example.

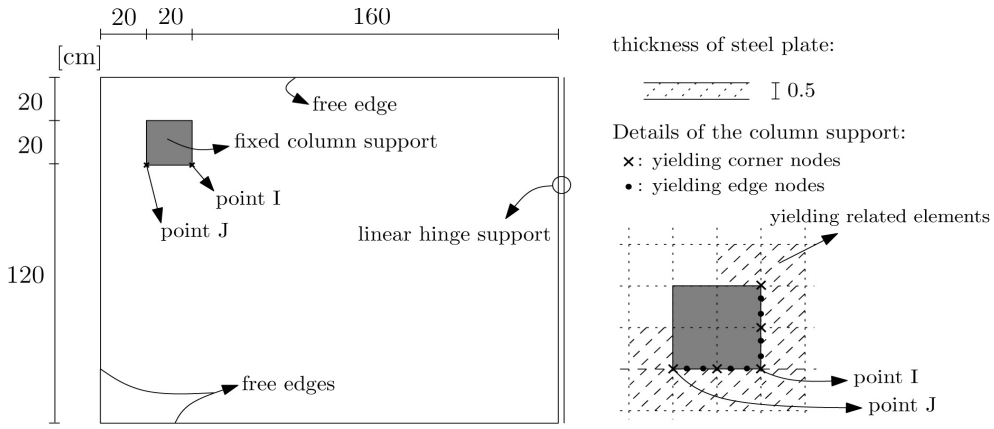

Figure 6.10: System for Investigating the Nonlinear Column Support Effects

According to the pre-studies 13 yielding nodes (5 corner nodes plus 8 edge nodes) are defined on the edges of the column as represented in the detail sketch of Fig. 6.10. As shown in Fig. 6.11 for an elasto-plastic analysis, there is also an extreme difference, i.e., a reverse sign, of the twisting angle κ_{xy} on the *point I* and *point J* in this case between the solution of the first 20 eigenmodes and that of 20 eigenmodes plus 18 PSFs, which are the PSFs of the yielding corner nodes only. By contrast, the curvatures κ_x and κ_y of the points I and J match quite well between the solutions with or without PSFs. It is to note that three PSFs, which are combined together for the yielding related elements (2 or 3 elements in this case), are generally applied on a particular yielding corner node, but for the point J totally six PSFs separated in two groups has to be used because of the discontinuity of curvatures in the y-direction at this corner.

To verify the accuracy of the PSFs applied solution and to see if the PSFs really can simulate the plastic deformations around the column support, which have to be formulated through the high frequency modes by the classical modal analysis, Fig. 6.12 shows the comparison between the reference solution (1366 eigenmodes) and the solution with 20 eigenmodes + 18 PSFs.

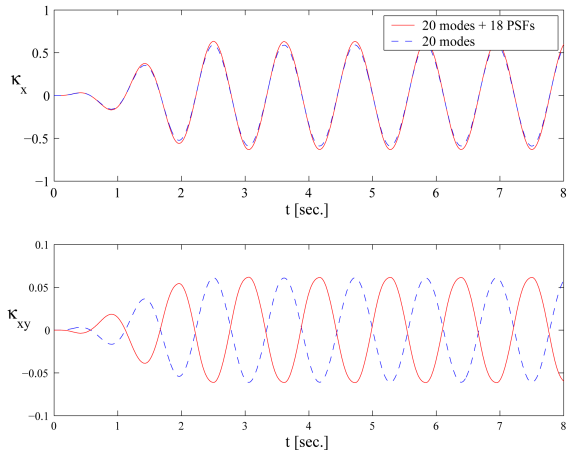

(a) comparison of curvatures at point I

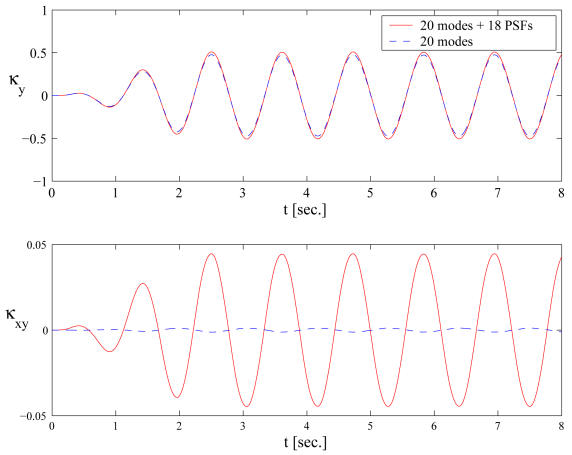

(b) comparison of curvatures at point J

Figure 6.11: Comparison of Curvatures between Solutions with 20 modes and with (20 modes + 18 PSFs) on Points I, J defined in Fig. 6.10

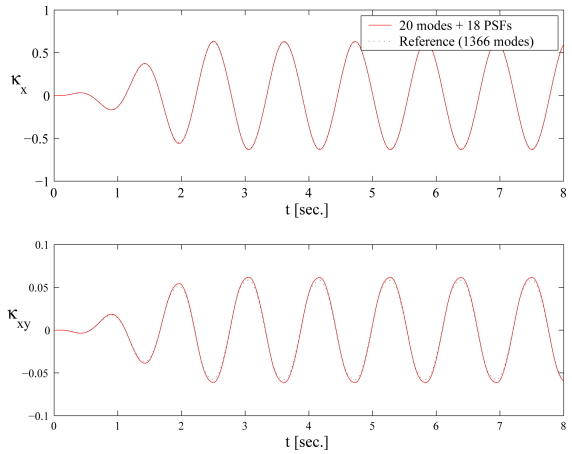

(a) comparison of curvatures at point I

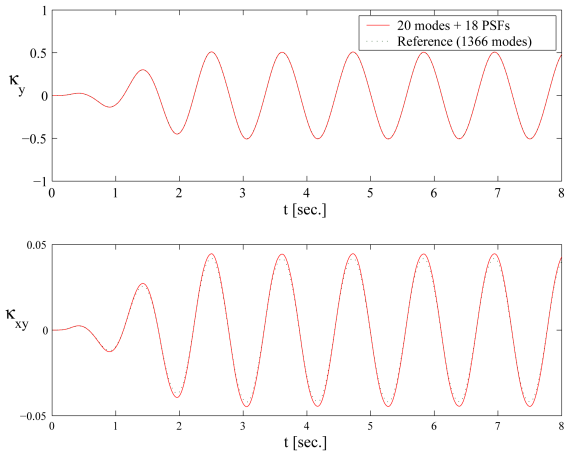

(b) comparison of curvatures at point J

Figure 6.12: Comparison of Curvatures between Solutions with (20 modes + 18 PSFs) and Reference Solutions (1366 modes) on Points I, J defined in Fig. 6.10

With Fig. 6.12 it can be concluded that the plastic deformation of the slab at the column support can only be formulated through the entire eigenvectors by the classical method, which costs about 16703 sec. in this case. And such nonlinear column support effects can be approached advantageously through the PSFs, since their solution accuracy is very high and the most important benefit of all is the efficiency of PSFs – for the PSFs applied solution (20 eigenmodes + 18 PSFs) the computing time is only about 80 sec..

The last thing to note for this case is that the accuracy of the PSFs applied solution can even be further improved, if the PSFs of the yielding edge nodes are also included

in the modal space. In this case there are 4 yielding related elements and each of them has 2 yielding edge nodes with 5 independent PSFs, because the PSFs of κ_{xy} for these two nodes are identical. At first sight 20 additional PSFs should be used in the calculation, but actually 2 of them are linear dependent with the others because of the nature of the linear-cubic curvature distribution. Therefore 20 eigenmodes + 18 PSFs of the yielding corner nodes + 18 PSFs of the yielding edge nodes are used for the new approach, whose results in comparison with the reference solution is represented in Fig. 6.13.

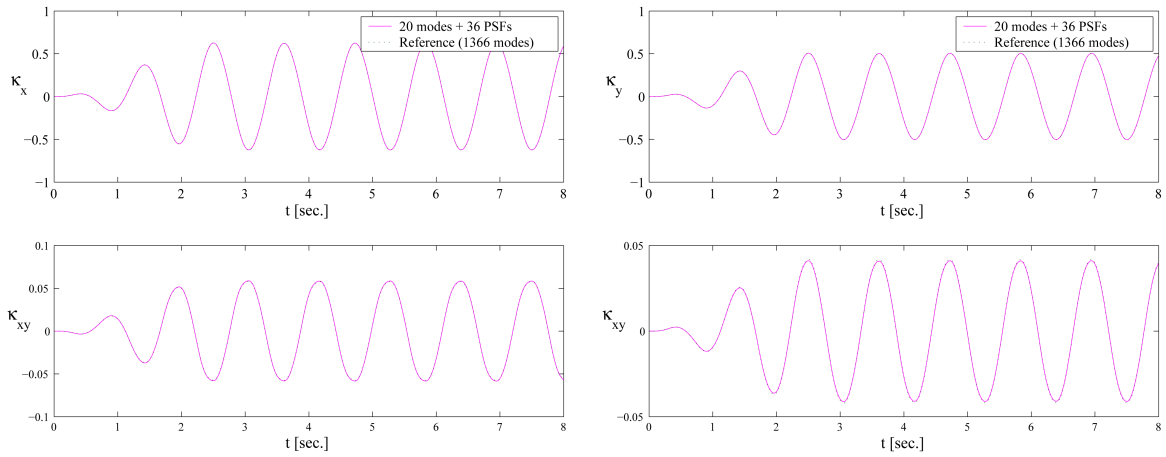

(a) comparison of curvatures at point I (b) comparison of curvatures at point J

Figure 6.13: Comparison of Curvatures between Solutions with (20 modes + 36 PSFs) and Reference Solutions (1366 modes) on Points I, J defined in Fig. 6.10

Comparing with the reference solution the absolute error ration of maximal κ_{xy} is from about 5 % of the 18-PSFs solution to 1.5 % of the 36-PSFs solution reduced, but the calculating time for the latter is double increased and an extra work to distinguish the linear independency of PSFs is also needed. Therefore for large systems it is suggested only to use the PSFs of the element corner nodes.

6.4 Results of Monte Carlo Simulations

After the verification of the nonlinear column support effects through an independent system in previous section the accuracy of the PSFs is again ensured. With this confidence the nonlinear stochastic analyses of the large RC flat slab are directly performed by using 20 eigenmodes plus 72 PSFs as the extended modal bases without further control through the reference solutions, since reference solutions are infeasible on the commercial PC of nowadays for systems with such a large DOF.

In order to present the unmanipulated efficiency achieved by PSFs, the direct Monte Carlo Simulation, i.e., without any reduction technics, is chosen to predict the probabilistic characteristics of the nonlinear system responses under seismic excitations

generated in section 6.2.2. As indicated in [22] large sample sizes are necessary by the direct Monte Carlo Simulation to obtain reasonable prognoses at the tail of the probability distribution, which is essential for the reliability analysis. Therefore *10,000* simulations are accomplished for this example to show that the procedure proposed in this work is sustainable for such a large number of simulations.

Because the limitation of the PC memory sizes (RAM sizes) and of the large solution data to be saved, only the first 8 seconds of the seismic accelerations, in which the maximal value occurs, are analyzed with a sampling frequency of 64 [Hz], i.e., 512 numerical integration steps for a single realization. With the same reasons only the nonlinear responses, i.e., the curvatures and the hysteretic Y-variables, of the column corner point A (s. Fig. 6.9 (a)) are recorded for the further statistical postprocessing. The computing time of one single simulation of the reduced system with 92 DOF and 144 auxiliary nonlinear equations is about 2 minutes on a commercial PC (AMD 64 Dual-Core 3.8 GHz CPU, 2 GB RAM), namely about 14 days are needed for $10,000$ simulations. Although it sounds to take a very long time but at least it is still feasible. With a rough assumption that the computing time is proportional to the system DOF, then for the unreduced system with 30000 DOF the entire simulations need more than 12 years to be performed on the same PC.

First the mean values and the corresponding standard deviations of the curvatures and the hysteretic Y-variables on point A from $0-8$ seconds are represented in Fig. 6.14. It can be seen that the standard deviation increases with the seismic accelerations and has a similar shape like the intensity function of the excitations (s. Fig. 6.4 (b)) as expected.

By considering the maximal curvatures Fig. 6.15 represents the probability histogram resulted from the Monte Carlo simulations together with the approximated Normal-distribution and Gumbel-distribution respectively. The Gumbel-distribution, which is developed from the extreme value theory, is suggested in [33] to approach the statistic characters of the nonlinear system responses and its probability density $f_G(x)$ is defined as [34]

$$f_G(x) = \frac{1}{\beta_G}\,\exp\left(\frac{\mu_G - x}{\beta_B}\right)\,\exp\left(-\exp\left(\frac{\mu_G - x}{\beta_B}\right)\right), \tag{6.12a}$$

with the coefficients

$$\beta_G = \sigma_S\,\frac{\sqrt{6}}{\pi}, \tag{6.12b}$$

and

$$\begin{aligned}\mu_G &= \mu_S - \beta_b \cdot \textit{Euler-Mascheroni Constant}\\ &\simeq \mu_S - \beta_G \cdot 0.5772156\end{aligned} \tag{6.12c}$$

where μ_S, σ_S are the mean and the standard deviation of the probability distribution and can be estimated from the simulations.

Fig. 6.15 (a)-(c) represent the statistic results of maximal curvatures estimated from merely 1000 simulations. Under such a 'small' number of simulations it is difficult to

tell that to which analytic distribution is the system response more similar. Contrarily a better match of the Gumbel-distribution with the nonlinear system response can be concluded by Fig. 6.15 (d)-(f), which are resulted from 10,000 simulations. At the region of higher curvatures apparent probabilities can also be determined under such enormous simulations, as a result it is possible to make a reasonable prognosis about the failure probability of structure systems according to particular criteria.

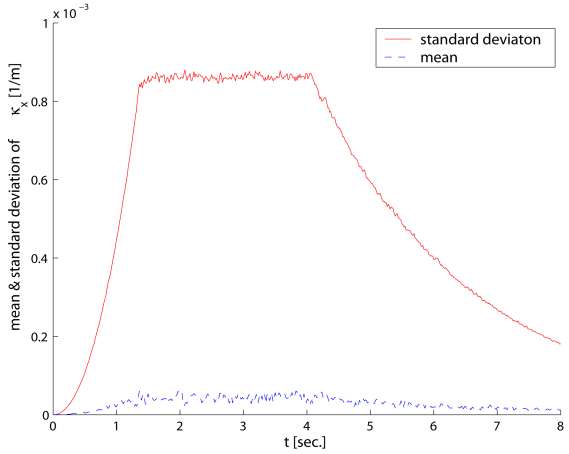

(a) statistic results of κ_x

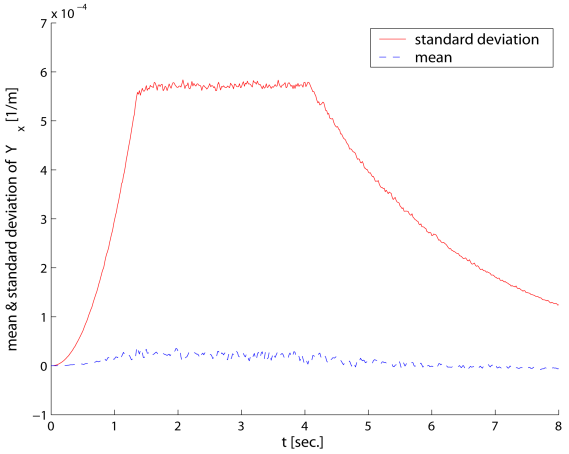

(d) statistic results of Y_x

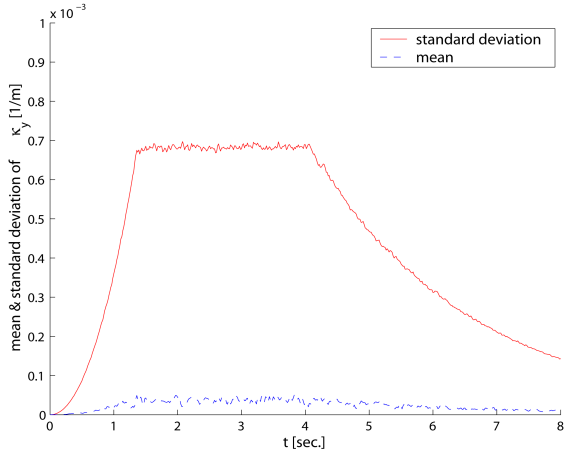

(b) statistic results of κ_y

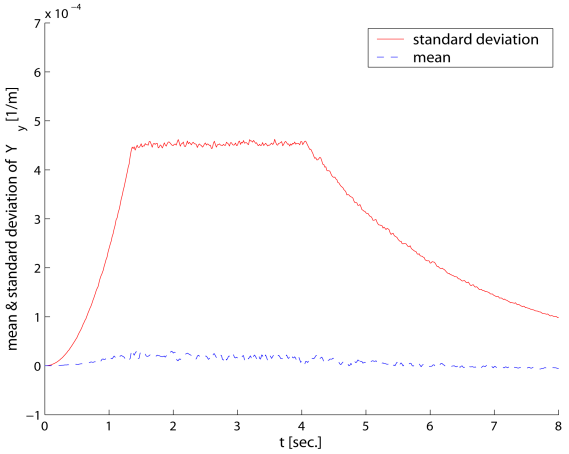

(e) statistic results of Y_y

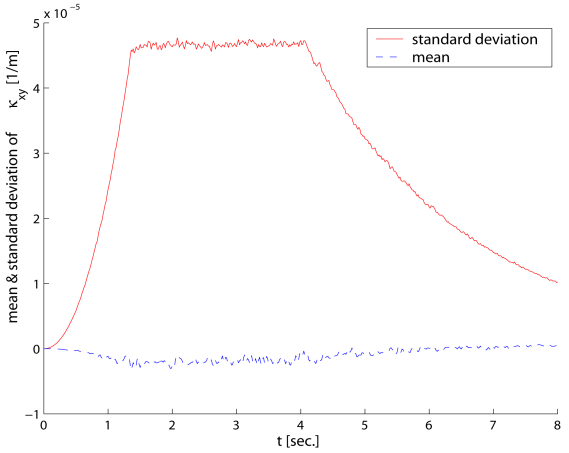

(c) statistic results of κ_{xy}

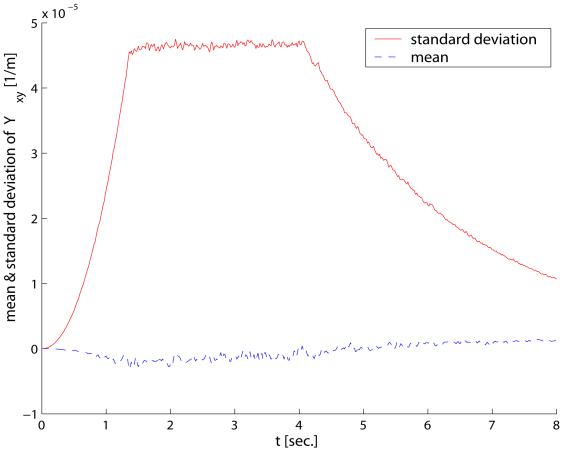

(f) statistic results of Y_{xy}

Figure 6.14: (a)-(c) Mean and Standard Deviation of Curvatures, (d)-(f) Mean and Standard Deviation of Y-Variables, Resulted from 10,000 Realizations

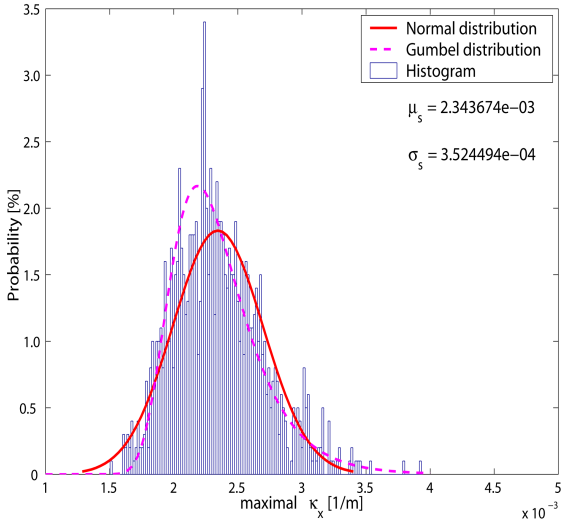

(a) statistic results of max. κ_x

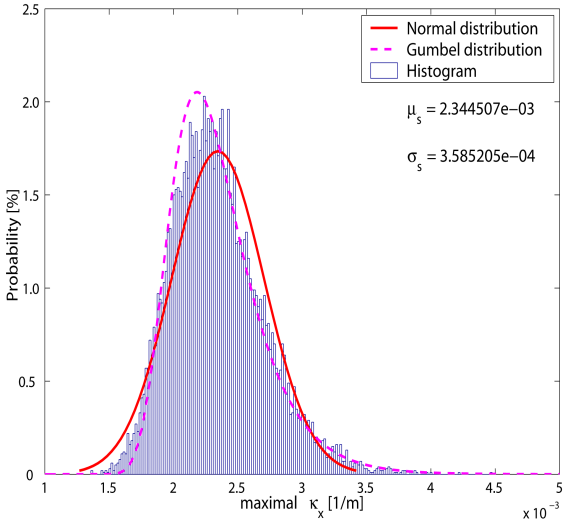

(d) statistic results of max. κ_x

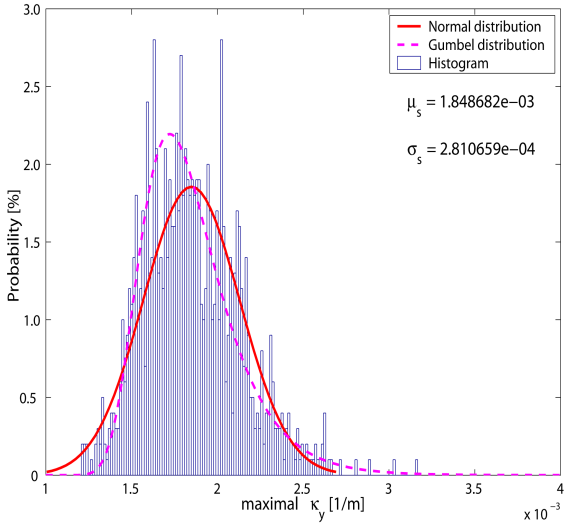

(b) statistic results of max. κ_y

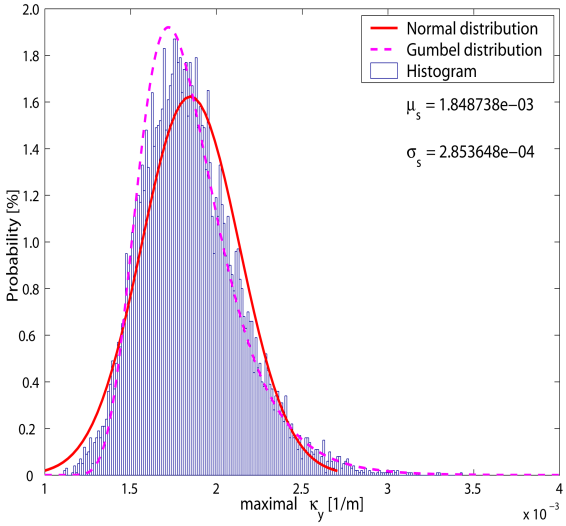

(e) statistic results of max. κ_y

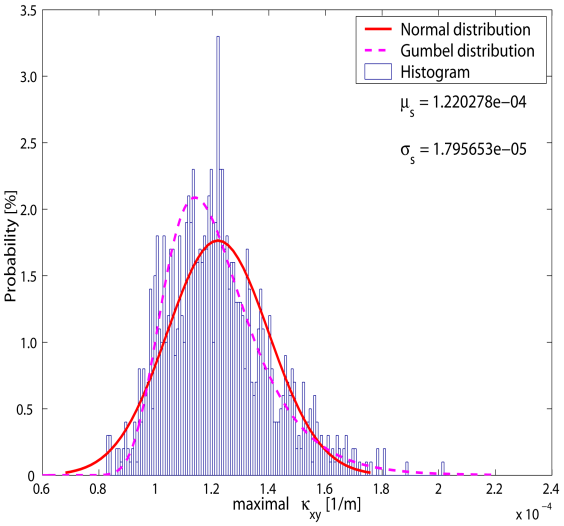

(c) statistic results of max. κ_{xy}

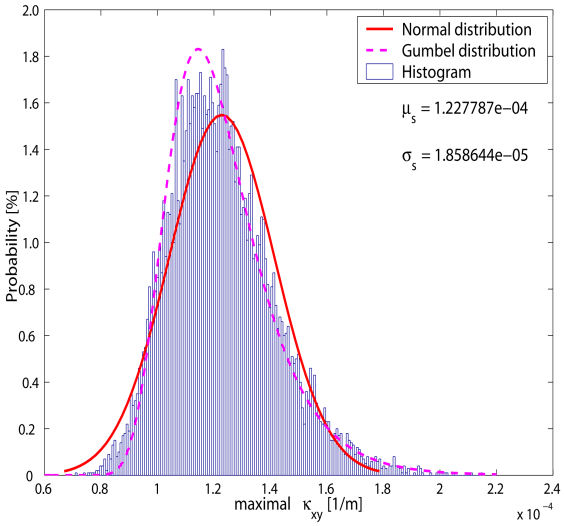

(f) statistic results of max. κ_{xy}

Figure 6.15: (a)-(c) Histogram, Estimated Normal and Gumbel Density of Maximal Curvatures from 1000 Simulations, (d)-(f) Histogram, Estimated Normal and Gumbel Density of Maximal Curvatures from 10,000 Simulations

Chapter 7

Summary and Conclusions

Achievements

In the present work the procedure of reducing the DOF of flat plate systems for nonlinear dynamic analyses through the application of *Plastic Shape Functions* is established. With this method it is possible to solve the stochastic nonlinear dynamic problems of large scale plate structures through the *direct Monte Carlo Simulation* even on a *commercial PC*. The kernel of this procedure, i.e., the Plastic Shape Function, is developed systematically basing on the common *Finite Element Method* and can be easily adopted in the numerical FE-programs.

As the theoretical constituents of this work the following subjects are handled:

- Hysteretic material model – Relying on the original Bouc-Wen model and its extensions, especially the works of Park (1986) and Simulescu (1989), a two-dimensional hysteretic model in the principal stress plane (2D-HMiPSP) is derived. To verify the validity of this model, it is compared with the von Mises yielding criteria and the Ziegler's hardening model through numerical examples with a good agreement. In order to be implanted in the FE formulation the 2D-HMiPSP is analytically translated to the Cartesian coordinate system and numerically proofed. Further the translated hysteretic model relying on the stress-strain level is turned into a hysteretic moment-curvature relation by proposing the Y-variables, which are then compared with results of the nonlinear fiber model.
- Curvature related stiffness matrix – By establishing the FE model according to the *Principle of Virtual Work* a nonlinear part of internal virtual works is introduced by using Y-variables, which have the same unit as curvatures. Additional interpolation functions, which have to be compatible with second derivatives of the bi-cubic deformation shape functions of the selected 4-nodes Schäfer plate element, are derived for the Y-variables, so that the consistency of the virtual works is ensured. Based on these compatible interpolation functions, the so-called *curvature related stiffness matrices* corresponding to the hysteretic Y-variables

are established. These curvature-based stiffness matrices are also the foundation of the development of plastic shape functions.

- Reduction of nonlinear equations – Usually the yielding occurs only on small regions or particular nodes in a discretized system. Therefore not all the nodes and elements have to be considered as yielding related. To reduce the number of the auxiliary nonlinear equations, which can dominate the entire computing time upon a certain proportion, the *Patch* and *Split Method* are proposed in the global differential equation system.

- Development of Plastic Shape Function – Using the column vectors of curvature related stiffness matrices as global loadings and together with applying the FEM based static analyses, the systematic development process of plastic shape functions is established. The plastic shape function approximates directly the nonlinear system response, which is the linear superposition of numerous eigenmodes in the classical way. Only a few low frequency modes are retained to simulate the elastic deformations, while all other eigenmodes are replaced by some particular plastic shape functions. As a result the system DOF, independent of its original size, are dramatically reduced to a feasible small number for the direct Monte Carlo Simulation.

With all the theoretical preparations this procedure is first realized on a rectangular steel plate with a small number of DOF, so that the validity of this procedure is controlled by comparing it with the reference solutions (or the 'exact' solutions within the maximal accuracy bounds of the FE discretization), which are resulted from the utilization of the entire modal DOF. Then this procedure is further applied on a large scale RC flat slab, which is excited by vertical seismic accelerations, to perform $10,000$ times Monte Carlo simulations. In between the 'nonlinear column support effects' are verified on a additional independent system to sustain the RC slab example with the lack of reference solutions.

Accuracy

The basic assumption - which is also the approaching target - of the plastic shape function is the existence of the particular, locally concentrated, discontinuous curvature distribution parts which resulted from the yielding (or called as plastic parts of curvatures). Consequently the plastic shape function has these yielding specific curvature distributions in nature, although with the first sight it is merely a modal vector of static deformations, and its accuracy arrives the level of curvatures with the help of the compatible interpolation functions of Y-variables.

As represented in examples of various yielding conditions, the reference solutions can be very well approximated by the solutions resulted from the reduced modal bases which extended by the plastic shape functions. The curvature error ratios between the reference and the plastic shape function applied solutions is about 3% to 5%. These errors come from two major parts: (1) The simulation of elastic system responses through

the few low frequency modes. (2) The interactions of plastic shape functions, which produce locally undesired redundant curvatures. The former effect can be recognized by the almost unchanged error ratios of elastic regions between solutions with or without applying plastic shape functions. The error part (2) can be realized through the local analyses of the yielding related elements and it can be found that the error ratios are lower on the yielding nodes than on the nodes around them.

The accuracy of the plastic shape function is certified again through the study case of nonlinear column support effects. In this example it is even found that the nonlinear plate behaviors at the corners of the single column support will be critically miscalculated if only a few eigenmodes, as in the elastic dynamics, are considered.

Efficiency

The efficiency of this procedure is directly dependent on the proportion of the number of plastic shape functions to the system DOF. The smaller this proportion is, the more efficient is this procedure, since a huge part of the modal DOF, needed for describing the nonlinear deformations, can be replaced by plastic shape functions. An other influence factor is the number of the auxiliary nonlinear equations attached to the global differential equation system. When the number of these nonlinear equations is over a certain amount, the computing time required for them, which is almost independent of the size of the reduced modal space, can dominate the entire calculation costs and lessen the efficiency achieved by the plastic shape functions.

Fortunately, in the engineering practices the proportion of the yielding zones to the system scale will be limited under the critical state with the reason of structure safety. And it is demonstrated in this work that for a system with about $30,000$ DOF and with a yielding ratio of $1/600$, this procedure is capable of performing $10,000$ Monte Carlo Simulations for probability analyses directly on the commercial PC.

Flexibility

The major components of this work, i.e., the nonlinear material model, the curvature related stiffness matrices and the plastic shape functions are independent from each other according to their individual concepts. Therefore it is possible to replace the material model with another one or to use different plate element in the FE formulation for various study cases. But the principles of deriving the curvature related stiffness matrices and developing the plastic shape functions will keep unchanged.

Besides the nonlinear material model, this procedure is built on the basis of FEM, therefore it is absolutely compatible with the commercial FE programs. For example, in the MSC-Nastran® the method of *modal augmentation* [36], which extends the reduced modal bases with static shape vectors, has been suggested to increase the ac-

curacy of modal analysis.

Another flexibility comes from the element-wise development of the plastic shape function. According to the boundary, material and support conditions the plastic shape functions of one, or maximal of four yielding related elements can be arbitrarily combined together to simulate all kinds of curvature distributions as illustrated in the examples. Through the combination of plastic shape functions of adjacent elements the reduced DOF can be condensed again.

Limitation and Prospect

The applicability of plastic shape functions is basically limited to the non-punctiform, uniformly distributed loading with frequencies locating in a certain range, which are the same limitations of linear modal analyses, since the plastic shape function is merely developed to simulate the curvature discontinuity resulted from yielding. But it is believed that with the elemental curvature figure of the plastic shape function, discontinuous curvature distribution of other reasons can also be simulated, just like the 'M-Moden' developed in [42] for the single moment load on a beam.

Another limitation of this procedure is the time consuming of solving the hysteretic equations. In the example of Monte Carlo Simulation one single calculation process costs about 2 minutes, if this computing time raises to 10 times because of the *Size Effect*, e.g., proportional increasing of system DOF and number of yielding nodes, a Monte Carlo Simulation might be no more feasible for the commercial PC even though the modal DOF remain small against the total system DOF. For such problems the development of more efficient nonlinear material models, numerical computing processes (such as the advanced MCS) or mechanical treatment of yielding zones will be necessary.

This work is just a small contribution of the development of plastic shape functions. Much more work needs to be done: Further condensation of plastic shape functions for large yielding zones, development of plastic shape functions for shell structures, for 3D volumes, for combination constructions, or extension of this concept to geometrical nonlinearity are all themes of the next step.

Appendix A

Introduction of the Classical Plasticity Theory

As a branch of continuum mechanics, the origin of plasticity can be dated back to a series of papers from 1864 to 1872, in which the first yield condition was proposed by Tresca. That was based on his experimental results on extrusion of metals and is regarded as maximum shear stress yielding [41] [16]. Since then, tremendous progresses has been made by many researchers, such as Saint-Venant, Levy, von Mises, Prandtl, Prager, Drucker. . . , etc, who have established the cornerstones for the plasticity theory.

The theory of plasticity, which is phenomenological in nature, deals with the stress-strain or load-deflection relationships for a plastically deforming material or structure. Therefore the mathematical formulation of these relationships should follow the experimental observations, from which it can be concluded that plastic deformation has the following features: [41]:

- Associating with the dissipation of energy, the plastic deformation is irreversible.
- Plastic deformation is history or path dependent due to its dissipation feature.
- The constitutive equations for plastic deformation are assumed to be invariant with respect to the time scale, which means that the plastic deformation is rate insensitive.

In other words, the plastic deformations are determined by nonlinear, time independent constitutive equations in increment or rate form. With this consideration the constitutive theory of plastic deformation should contain the following components

1. The initial yield stress σ_Y^0 or the initial yield surface (cf. Section A.1) should be known. The general formulation of the yield surface in three-dimensional cases can be represented through the yield function as

$$F(\boldsymbol{\sigma}, \sigma_Y^0) = 0 \ , \tag{A.1}$$

where $\boldsymbol{\sigma}$ is the stress state tensor.

2. The criterion for loading or unloading should be specified (cf. Section A.1). Because of the dependence on the stress history and state, the plastic behaviors under the conditions of the elastic loading, of the plastic loading and of the unloading, are different from each other. This is also the main distinction between the nonlinear elasticity theory and the plasticity theory.

3. The constitutive equation for plastic deformation should be formulated. This process is the center of the plasticity theory (cf. Section A.2, A.3).

4. Except for perfectly plastic material, or in the small region of plastic flow of mild steel, the growth of subsequent yield surface should be known. The subsequent yield surface defines the boundary of the current elastic region (cf. Section A.3).

A.1 Yielding Criteria

For the three-dimensional cases in general, the six independent stress components serve as independent coordinate axes and establish a six-dimensional stress space, in which a point specifies a stress state. All the possible stress states that cause yielding can be imagined to constitute a closed hypersurface, which is called the *yield surface*.

The yield surface is the boundary between the elastic and the plastic deformation and divides the stress space into to domains. In order to know if the stress state locates in the elastic or the plastic deformation domain, in which the stress-strain relationship is different from each other, it is necessary to determine the shape and position of the yield surface in the stress space.

If the material is isotropic, which is the assumption of the present work, the yielding depends only on the magnitudes of the principal stresses but not its orientation. The yielding function can be represented therefore in the three-dimensional principal stress space. Further, with the experimental evidence exposed by Bridgeman in 1952 [10], it can be assumed that the hydrostatic pressure has no effect on plastic yielding for metallic material. Accordingly the plastic yielding depends only on the deviatoric stress tensor $\mathbf{S}$ and the yield function for isotropic metallic material can be written as

$$F(J_2', J_3') = 0 \ , \tag{A.2}$$

in which J_2' and J_3' are the second and the third invariants of the deviatoric stress tensor. It is to note that equation (A.2) represents geometrically a cylinder with a general shape of the surface in the principal stress space, whose center line is the hydrostatic pressure axis ($\sigma_1 = \sigma_2 = \sigma_3$). The projection of yield surface on the deviatoric plane, which is perpendicular to hydrostatic pressure axis, will be illustrated according to the yield criterion in the following.

Tresca Criterion

In 1864 Tresca proposed that the plastic yielding will occur when the maxium shear stress reaches the critical value k, which is a material constant. This criterion can be written in terms of principal stress as [41]

$$\max\left[\, \tfrac{1}{2}|\sigma_1 - \sigma_2|, \tfrac{1}{2}|\sigma_2 - \sigma_3|, \tfrac{1}{2}|\sigma_3 - \sigma_1| \,\right] = k \ . \tag{A.3}$$

From the uniaxial test or alternatively from the pure shear test this critical value can be determined as

$$k = \frac{\sigma_Y}{2} = \tau_Y \ , \tag{A.4}$$

where σ_Y and τ_Y are yield stress under uniaxial tension and pure shear respectively.

von Mises Criterion

Later in 1913 von Mises suggested that the plastic yielding will occur only when the second invariant J_2' of the deviatoric stress tensor $\mathbf{S}$ reaches a critical value k^2. The von Mises yield criterion can be represented as

$$F(\sigma_{ij}) = J_2' - k^2 \begin{cases} = 0 & \text{for yielding or plastic deformation} \\ < 0 & \text{for elastic deformation} \end{cases} \tag{A.5}$$

or it can be rewritten in terms of principal stress components for the yielding as

$$J_2' = \tfrac{1}{6}\left[(\sigma_1 - \sigma_2)^2 + (\sigma_2 - \sigma_3)^2 + (\sigma_3 - \sigma_1)^2\right] = k^2 \ . \tag{A.6}$$

The material property k in equation (A.6) can be estimated by a simple tension test or a pure shear test and results

$$k = \frac{\sigma_Y}{\sqrt{3}} = \tau_Y \ , \tag{A.7}$$

which is different from the critical value of Tresca's in equation (A.4).

In the principal stress space the equation (A.3) from Tresca draws a regular hexagon on the deviatoric plane, which has discontinuity at the corner, while equation (A.6) from von Mises represents a smooth circular locus on it (s. Fig. A.1(a)). Under the condition of plane stress ($\sigma_3 = 0$), equation (A.6) can be reduced to

$$\sigma_1^2 - \sigma_1\sigma_2 + \sigma_2^2 = 3k^2 \ . \tag{A.8}$$

This equation represents the von Mises ellipse in the $\sigma_1 - \sigma_2$ plane (s. Fig. A.1(b)).

With the experimental investigations from, e.g., Lode (1925), Taylor & Quinney (1932) and Lianis & Ford (1957), it can be concluded that the von Mises criterion is better for predicting yielding of metals than the Tresca criterion.

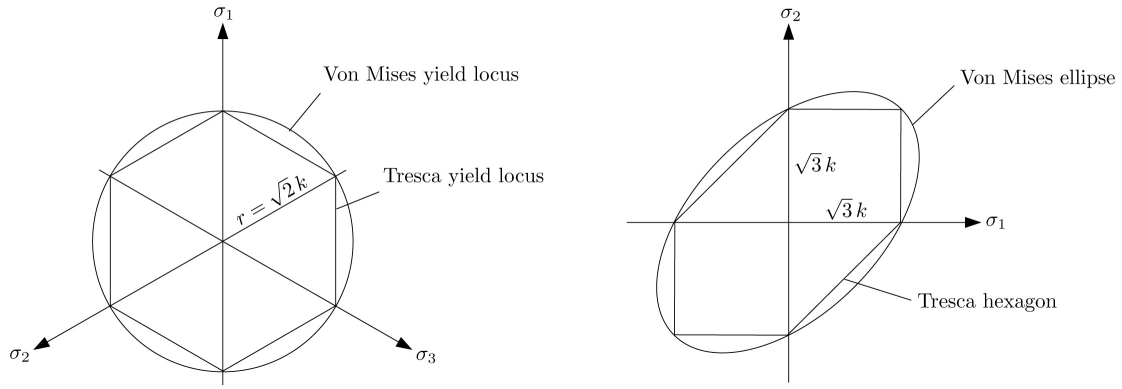

(a) Deviatoric Stress Plane (b) Principal Stress Plane

Figure A.1: Tresca and von Mises Yield Function

Loading and Unloading

As mentioned before the indication of loading or unloading is one of the bases of the plasticity theory. It identifies whether the deformation is elastic or plastic. Rewriting the general yield function as $F(\boldsymbol{\sigma}) = f(\boldsymbol{\sigma}) - k_0 = 0$, the loading and unloading criteria for work-hardening materials can be written as [41]

$$\begin{aligned}
&F(\boldsymbol{\sigma}) < 0, \quad \text{(elastic deformation)} \\
&F(\boldsymbol{\sigma}) = 0, \quad dF = f(\boldsymbol{\sigma} + d\boldsymbol{\sigma}) - f(\boldsymbol{\sigma}) = \frac{\partial f}{\partial \boldsymbol{\sigma}} : d\boldsymbol{\sigma} > 0 \quad \text{(loading)} \\
&F(\boldsymbol{\sigma}) = 0, \quad dF = f(\boldsymbol{\sigma} + d\boldsymbol{\sigma}) - f(\boldsymbol{\sigma}) = \frac{\partial f}{\partial \boldsymbol{\sigma}} : d\boldsymbol{\sigma} = 0 \quad \text{(neutral loading)} \\
&F(\boldsymbol{\sigma}) = 0, \quad dF = f(\boldsymbol{\sigma} + d\boldsymbol{\sigma}) - f(\boldsymbol{\sigma}) = \frac{\partial f}{\partial \boldsymbol{\sigma}} : d\boldsymbol{\sigma} < 0 \quad \text{(unloading)}
\end{aligned} \tag{A.9}$$

In the stress space the vector $\partial f / \partial \boldsymbol{\sigma}$ is the outer normal $\mathbf{n}$ to the yield surface. After these criteria only the loading case can result in plastic deformation for the work-hardening materials, i.e., only when $d\boldsymbol{\sigma}$ is directed outward to the yield surface. Obviously by unloading, which $d\boldsymbol{\sigma}$ points inward from the yield surface, the deformation is purely elastic. The reason why there is no plastic deformation during the neutral loading - while $d\boldsymbol{\sigma}$ is tangential to the yield surface - is that the continuity in the stress-strain relations should be satisfied.

It is to note that for the perfectly plastic material the initial yield surface keeps unchanged during the plastic deformation. Therefore, by further loadings beyond yielding, the stress point has to be on the yield surface and remain there, i.e., the stress increment $d\boldsymbol{\sigma}$ can only be tangential to the yield surface. Consequently, for the perfectly plastic material the only loading case means $dF = \partial f / \partial \boldsymbol{\sigma} : d\boldsymbol{\sigma} = 0$ mathematically.

A.2 Constitutive Equation of Perfectly Plastic Materials

After pointing out the onset of plastic behaviors with the yield criteria, the next step of establishing the plasticity theory is to formulate the stress-strain relationship under yielding. First the constitutive equation for the perfectly plastic material will be introduced in this section.

It is to emphasize that the following constitutive equations, because of the nature of perfectly plastic materials, are one-way valid. That means, for a defined current stress state σ_{ij} with a given strain increment $d\epsilon_{ij}$ the corresponding stress increment $d\sigma_{ij}$ can be uniquely determined. But the magnitude of the strain increment cannot be uniquely determined by the given current strass σ_{ij} and the stress increment $d\sigma_{ij}$ from the coming constitutive equations.

Levy-Mises Equation

Levy(1870,1871) and von Mises(1913) proposed independently a generalized constitutive equation for three-dimensional plastic deformations by extending the work of Saint-Venant(1870). With the following assumptions:

1. The elastic strain $\boldsymbol{\epsilon}^e$ is small and can be neglected. So the total strain $\boldsymbol{\epsilon}$ is equal to the plastic strain $\boldsymbol{\epsilon}^p$.
2. The increment of strain $d\epsilon$ or $\dot{\boldsymbol{\epsilon}}$ is coaxial with the deviatoric stress $\mathbf{S}$.

the Levy-Mises constitutive equation can be formulated as

$$\dot{\boldsymbol{\epsilon}} = \dot{\lambda}\mathbf{S} \tag{A.10a}$$

or in terms of tensor components as

$$\dot{\epsilon_{ij}} = \dot{\lambda} S_{ij} \ . \tag{A.10b}$$

In equation (A.10) $\dot{\lambda}$ is a proportionality parameter, which can be determined from the yield criterion.

With the assumption of perfectly plastic material, i.e. σ_Y is constant, and with use of von Mises criterion (A.5), in which $J_2' = \frac{1}{2} S_{ij} S_{ij}$ is applied, the parameter $\dot{\lambda}$ can be calculated by squaring equation (A.10b) as

$$\dot{\lambda} = \sqrt{\frac{3\dot{\epsilon}_{ij}\dot{\epsilon}_{ij}/2}{\sigma_Y^2}} = \frac{3}{2}\frac{\dot{\epsilon_e}}{\sigma_Y} \ , \tag{A.11}$$

where $\dot{\epsilon_e}$ is the equivalent of effective strain rate and is defined by

$$\dot{\epsilon_e} = \frac{\sqrt{2}}{3}\Big[(\dot{\epsilon}_1 - \dot{\epsilon}_2)^2 + (\dot{\epsilon}_2 - \dot{\epsilon}_3)^2 + (\dot{\epsilon}_3 - \dot{\epsilon}_1)^2\Big]^{1/2} = \sqrt{\frac{2}{3}\,\dot{\epsilon}_{ij}\dot{\epsilon}_{ij}} \tag{A.12}$$

The Levy-Mises Equation (A.10) is usually called as *flow rule of plasticity.*

Prandtl-Ruess Equation

When the elastic strain ϵ^e is comparable to the plastic strain ϵ^p, the negligence of ϵ^e will result in a significant error. Considering this, Prandtl(1927) and Reuss(1930) proposed a constitutive equation for the plastic strain rate similar to Levy-Mises equation as

$$\dot{\epsilon}^{\,p}_{ij} = \dot{\lambda} S_{ij} \ , \tag{A.13}$$

where $\dot{\lambda}$ is a parameter and can be determined by using the yield criterion. It is assumed that, plastic deformations don't result in volume changes, which means

$$\epsilon^p_{kk} = \epsilon^p_{xx} + \epsilon^p_{yy} + \epsilon^p_{zz} = \epsilon^p_1 + \epsilon^p_2 + \epsilon^p_3 = 0 \ , \tag{A.14}$$

thus the plastic strain rate $\dot{\boldsymbol{\epsilon}}^{\,p}$ in equation (A.13) is deviatoric in nature.

The shape change caused by the elastic deformation can be represented by the deviatoric elastic strain $\epsilon'^e_{ij} = S_{ij}/2G$, where G is the shear modulus, according to the elasticity theory [30] . Differentiating the deviatoric elastic strain with respect to time results it's rate form, which is

$$\dot{\epsilon}'^e_{ij} = \frac{1}{2G}\,\dot{S}_{ij} \ . \tag{A.15}$$

The total rate of shape change, i.e. the total deviatoric strain rate, can be obtained by adding equations (A.13) and (A.15) as

$$\dot{\epsilon}'_{ij} = \frac{1}{2G}\,\dot{S}_{ij} + \dot{\lambda} S_{ij} \tag{A.16}$$

Similar to the derivation of equation (A.11) the parameter $\dot{\lambda}$ of Prandtl-Reuss equation (A.13) can be expressed as

$$\dot{\lambda} = \frac{3\,\dot{\epsilon}^p_e}{2\,\sigma_Y} \ , \tag{A.17}$$

where $\dot{\epsilon}^p_e$ is the equivalent or effective rate of the plastic strain and is defined by

$$\dot{\epsilon}^p_e = \frac{\sqrt{2}}{3}\Big[(\dot{\epsilon}^p_1 - \dot{\epsilon}^p_2)^2 + (\dot{\epsilon}^p_2 - \dot{\epsilon}^p_3)^2 + (\dot{\epsilon}^p_3 - \dot{\epsilon}^p_1)^2\Big]^{1/2} = \sqrt{\frac{2}{3}\,\dot{\epsilon}^p_{ij}\dot{\epsilon}^p_{ij}} \ . \tag{A.18}$$

It is to note that the application of Levy-Mises or Prandtl-Reuss equation is not limited to perfectly plastic materials. For example, instead of a constant, the yield strength σ_Y can be considered as a function of a certain hardening parameter(s) to generalize these constitutive equations. For the hardening materials the determination of the parameter $\dot{\lambda}$ will be different from the equation (A.11) or (A.17) . It is to remind that not only the strains mentioned above, but also the strains resulted from the hydrostatic stresses still have to be considered to build the total strains.

Plastic Potential Theory

In contrast with the empirical postulations, which base on experimental observations, von Mises proposed in 1928 a general mathematical treatment of the constitutive equation for the plastic deformation or flow.

According to the method of potential energy in the elasticity theory the strain can be determined as [67]

$$\epsilon_{ij} = \frac{\partial U_c}{\partial \sigma_{ij}} \ , \tag{A.19}$$

where U_c is the complementary strain energy. Applying this idea to plasticity theory, von Mises proposed that the plastic strain rate $\dot{\epsilon}^p_{ij}$ could be related to the stress σ_{ij} through a plastic potential function $Q(\sigma_{ij})$ and derived as

$$\dot{\epsilon}^p_{ij} = \dot{\lambda}\frac{\partial Q(\sigma_{ij})}{\partial \sigma_{ij}} \ , \tag{A.20}$$

where $\dot{\lambda}$ is a proportional positive scalar factor and can be determined by yield criterion.

The key point of using the plastic potential theory is to determine the effective form of the plastic potential function $Q(\sigma_{ij})$. A common approach in plasticity theory is to assume that the plastic potential function $Q(\sigma_{ij})$ is the same as the yield function $F(\sigma_{ij})$. Then equation (A.20) can be rewritten as

$$\dot{\epsilon}^p_{ij} = \dot{\lambda}\frac{\partial F(\sigma_{ij})}{\partial \sigma_{ij}} \tag{A.21}$$

It can be seen from equation (A.21) that the plastic strain $\dot{\epsilon}^p_{ij}$ relates to the yield function and is normal to the yield surface. Therefore it is called *associated flow rule*. If $Q \neq F$, the flow rule is then called nonassociated. For metallic or nonporous material the association of Q with F can be well verified from experiments. On the other hand, it can be mathematically proved that if the material is stable according to Drucker's stability postulate, then the flow rule must be associated.

The Drucker's postulate declares, if a material is stable, the following inequality must hold [41]:

$$W = \int_{C_\sigma} \Delta\boldsymbol{\sigma} : d\boldsymbol{\epsilon} \geq 0 \ , \tag{A.22}$$

where W is the work done over a closed stress cycle C_σ . This fairly strong condition (A.22) can only be satisfied by hardening materials. The Drucker's stability postulate leads to two general conclusions:

1. The yield surface is convex.
2. The plastic strain rate or increment is normal to the yield surface.

By applying the von Mises yield criterion (A.5) in the equation (A.21) it becomes

$$\dot{\boldsymbol{\epsilon}}^p = \dot{\lambda}\frac{\partial F}{\partial \boldsymbol{\sigma}} = \dot{\lambda}\frac{\partial J_2'}{\partial \boldsymbol{\sigma}} = \dot{\lambda} S \ , \tag{A.23}$$

which is the Prandtl-Reuss equation (A.13).

A.3 General Constitutive Equation with Hardening Rule

If the material has hardening behavior, i.e., the strength of material will increase even though the initial yield stress is reached, then the subsequent yield point/surface, which depends on the specific hardening parameter(s), has to be determined. The hardening parameters indicate the extension (isotropic hardening), translation (kinematic hardening), or distortion of the yield surface for each time step. Generally the yield function with consideration of hardening character can be written as

$$F(\boldsymbol{\sigma}, \alpha_i^h) = 0 \qquad (i = 1, 2, \ldots, n) \ , \tag{A.24}$$

where α_i^h are all possible hardening parameters, which can be scalars, vectors, or tensors.

For the use of the present work only the kinematic hardening model, which can describe the Bauschinger effect observed on the mild steel, will be explained in detail. Descriptions of the other hardening models, e.g., isotropic, mixed, or nonuniform hardening, can be found in the publications [41], [16], or [45].

Kinematic Hardening Rule

In order to describe the Bauschinger effect, in which the isotropic hardening model fails, Prager introduced the kinematic hardening model. This model assumes that the yield surface keeps its shape and size but translates in the stress space during the process of plastic deformation [16]. The subsequent yield surface due to the kinematic hardening can be formulated as

$$F(\boldsymbol{\sigma}, \boldsymbol{\alpha}^h) = f(\boldsymbol{\sigma} - \boldsymbol{\alpha}^h) - k = 0 \ , \tag{A.25}$$

where $\boldsymbol{\alpha}^h$ is a tensorial hardening parameter, which is usually called the *back stress*, and k is a material constant. $\boldsymbol{\alpha}^h$ and k in equation (A.25) represent geometrically the center and the size of the yield surface respectively.

The main subject of the hardening model is to specify the evolution of $\boldsymbol{\alpha}^h$. According to the history-dependent nature of plastic deformation, it can be expected that $\boldsymbol{\alpha}^h$ will be formulated in incremental form as a function of $d\boldsymbol{\epsilon}^p$, $\boldsymbol{\sigma}$, or $\boldsymbol{\alpha}^h$ itself. Based on the

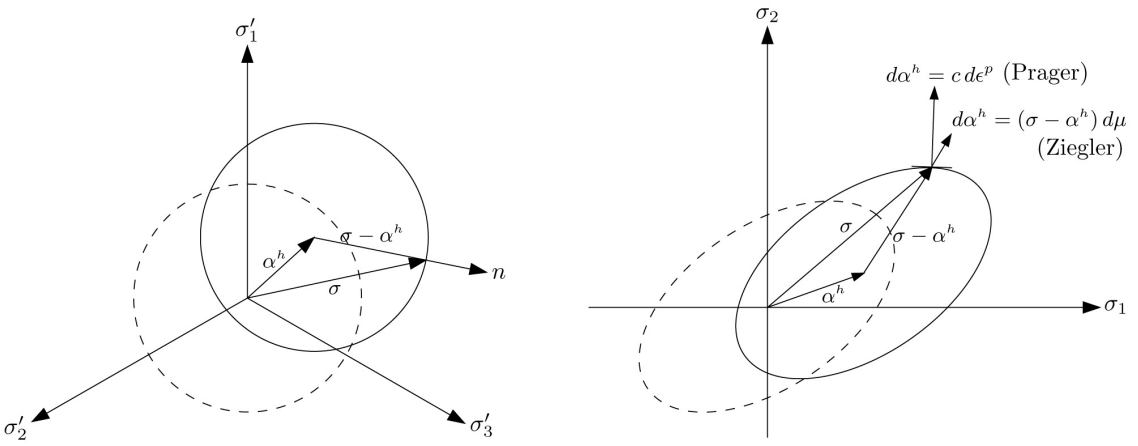

(a) Deviatoric Stress Plane (b) Principal Stress Plane

Figure A.2: Prager and Ziegler Kinematic Hardening Model

experimental investigations, Prager(1955) proposed a linear constitutive equation for the back stress $\boldsymbol{\alpha}^h$ as

$$d\boldsymbol{\alpha}^h = c\, d\boldsymbol{\epsilon}^p \ , \tag{A.26a}$$

where c is a material constant. By using associated flow rule (A.21), the Prager's model (A.26a) can be rewritten as

$$d\boldsymbol{\alpha}^h = c\, d\lambda \frac{\partial F}{\partial \boldsymbol{\sigma}} \ . \tag{A.26b}$$

According to this model the yield surface is assumed to move in the direction of the plastic strain increment, which is normal to the yield surface at the loading point (s. Fig. A.2). Prager's linear kinematic model is inconsistent for three- and two-dimensional cases and has a transverse softening or hardening effect. Using Prager's model the yield surface will not only translate but also change its shape, which dose not really represent a kinematic hardening rule as described earlier.

To overcome the deficiency of Prager's linear kinematic model, Ziegler(1959) proposed the following modified model:

$$d\boldsymbol{\alpha}^h = (\boldsymbol{\sigma} - \boldsymbol{\alpha}^h) d\mu \ , \tag{A.27}$$

where $d\mu$ is a proportional scalar constant determined by the yield criterion. It can be seen that under the Ziegler's model the moving direction of yield surface is assumed to be parallel to the vector $\boldsymbol{\sigma} - \boldsymbol{\alpha}^h$. It should be noted that by using the von Mises criterion the moving direction of Prager's model is the same as the one of Ziegler's model in three-dimensional cases (s. Fig. A.2(a)), but different in two-dimensional cases (s. Fig. A.2(b)).

Plastic Stress-Strain Relations

Using the plastic potential theory with the associated flow rule, the plastic strain for hardening materials can be expressed as equation (A.21), in which the yield function

is replaced by equation (A.25). To determine the hardening parameter $\boldsymbol{\alpha}^h$, the consistency assumption proposed by Prager can be used, which is [41]

$$dF = \frac{\partial F}{\partial \boldsymbol{\sigma}} : d\boldsymbol{\sigma} + \frac{\partial F}{\partial \boldsymbol{\alpha}^h} : d\boldsymbol{\alpha}^h = 0 \ . \tag{A.28}$$

For Ziegler's hardening model setting equation (A.25) and (A.27) in equation (A.28) it follows:

$$\frac{\partial f}{\partial \boldsymbol{\sigma}} : d\boldsymbol{\sigma} + \frac{\partial f}{\partial \boldsymbol{\alpha}^h} : (\boldsymbol{\sigma} - \boldsymbol{\alpha}^h) d\mu = 0 \ . \tag{A.29}$$

And according to the equation (A.25) is $\partial f/\partial \boldsymbol{\sigma} = -\partial f/\partial \boldsymbol{\alpha}^h$, so that the proportional scalar $d\mu$ can be determined by

$$d\mu = \frac{\partial f/\partial \boldsymbol{\sigma} : d\boldsymbol{\sigma}}{\partial f/\partial \boldsymbol{\sigma} : (\boldsymbol{\sigma} - \boldsymbol{\alpha}^h)} \tag{A.30a}$$

and consequentially is

$$d\boldsymbol{\alpha}^h = \frac{(\boldsymbol{\sigma} - \boldsymbol{\alpha}^h)}{\partial f/\partial \boldsymbol{\sigma} : (\boldsymbol{\sigma} - \boldsymbol{\alpha}^h)} \, l \ , \tag{A.30b}$$

where

$$l = \frac{\partial f}{\partial \boldsymbol{\sigma}} : d\boldsymbol{\sigma} \ .$$

In order to determine the plastic strain rate $\dot{\boldsymbol{\epsilon}}^p$, i.e., the proportional positive scalar factor $\dot{\lambda}$, the normality condition of associated flow rule is used, so that the component of $d\boldsymbol{\sigma}$ in the normal direction to the yield surface is parallel to $d\boldsymbol{\epsilon}^p$. Mathematically it can be formulated as

$$d\boldsymbol{\epsilon}^p = \frac{1}{K^P} \left(\mathbf{n} : d\boldsymbol{\sigma} \right) \mathbf{n} = \frac{1}{K^P} \frac{l}{\partial f/\partial \boldsymbol{\sigma} : \partial f/\partial \boldsymbol{\sigma}} \frac{\partial f}{\partial \boldsymbol{\sigma}} \ . \tag{A.31}$$

where $\mathbf{n}$ is the normal vector of yield surface and $K^P > 0$ is a proportional factor. Comparing this with equation (A.21) it follows

$$d\lambda = \frac{1}{K^P} \frac{l}{\partial f/\partial \boldsymbol{\sigma} : \partial f/\partial \boldsymbol{\sigma}} \ . \tag{A.32}$$

With use of von Mises yield criterion the parameter K^P can be calculated under uniaxial tension as [41]

$$\frac{1}{K^P} = \frac{3}{2} \left(\frac{1}{E^t} - \frac{1}{E} \right) \ , \tag{A.33}$$

where E is the Young's modulus and E^t is the tangential stiffness, i.e., the post-yielding strength for linear hardening. And K^P is considered as plastic modulus.

It should be mentioned that the classical isotropic hardening and Prager's or Ziegler's kinematic hardening models can give a reasonable description of the elasto-plastic behavior merely for monotonic loading cases, but not for the cyclic loading, in which the material responses are more complex and have the features such as smooth elastic-plastic transition, cyclic creep effect and stabilization of the isotropic hardening [20]. For cyclic loading cases further models were proposed [41], e.g. Mroz's multi-surface model, nonlinear kinematic hardening model or endochronic theory ..., etc..

Appendix B

Hysteretic Model and its Developments

For the engineering uses, the hysteresis of cyclic loading can be formulated through the simple bilinear model [37] or through the smoothly distributed Ramberg-Osgood model [38]. Both of them are case-distinguishing for loading or unloading, therefore a discretization of the loading history is necessary. The analysis of the system response with these models can be accomplished by means of a step-by-step numerical integration, but these models are difficult to put in mathematically convenient forms for analytical solution.

Another method to formulate the hysteretic material behavior is the differential equation models, which are generally given in mathematically explicit form; consequently an analytical solution of the response may be obtained. In this method additional state variables were introduced and the force-displacement relationship is formulated through nonlinear differential equations.

Considering a nearly elasto-plastic system with a linear pre-yielding restoring force and a post-yielding stiffness, the total restoring force Q can be separated into an elastic part Q_{el} and a hysteretic part Q_H by introducing a state variable z as following

$$\begin{aligned} Q(x, \dot{x}, t) &= Q_{el} + Q_H \\ &= \alpha\, k\, x + (1 - \alpha)\, k\, z \ , \end{aligned} \tag{B.1}$$

where x is the instantaneous displacement, k is the pre-yielding stiffness, α is the ratio of post-yielding to pre-yielding stiffness and z characterizes the hysteretic component, which is a function of the time history of x [101].

Two familiar models of the nonlinear differential equation of the hysteretic variable z will be introduced in the following.

B.1 Bilinear Model

With use of Heaviside function $H(.)$, which is the mathematical expression of case distinction, Suzuki and Minai [92] proposed a one-dimensional distributed bilinear model for the hysteretic variable z in the equation (B.1), which satisfies

$$\dot{z} = \dot{x}\,[\,1 - H(\dot{x})H(z - x_L) - H(-\dot{x})H(-z - x_L)]\ , \tag{B.2}$$

where x_L is the yielding limit of x.

Comparing this model with the classical plasticity theory, the multiplication of the two Heaviside functions in equation (B.2) controls at the same time two criteria of determining the yielding, namely the yielding criterion through $H(z-1)$ and the loading-unloading criterion through $H(\dot{x})$. The second multiplication of Heaviside functions with the minus sign serves for the determination of yielding under compression.

The equation (B.2) alone describes the elastic perfectly-plastic material behavior. Together with the elastic part as formulated in (B.1) the bi-linear hysteretic Model of Suzuki-Minai is illustrated in Fig. B.1.

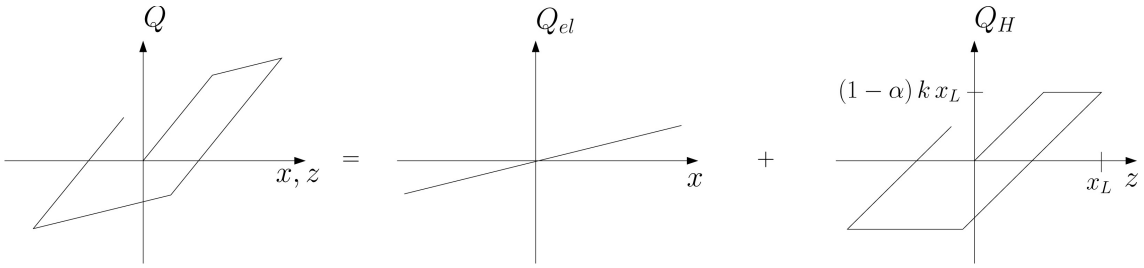

Figure B.1: Bilinear Hysteretic Model from Suzuki-Minai

B.2 Bouc-Wen Hysteretic Model

A smooth hysteretic material model, which can better indicate the features of material response under cyclic loading, was first proposed by Bouc [9]. In his model the hysteretic parameter z is formulated as

$$\dot{z} = A\,\dot{x} - \beta\,|\dot{x}|\,z - \gamma\,\dot{x}\,|z|\ , \tag{B.3}$$

where A, β and γ are material constants.

Further, in [99] Wen generalized the Bouc's model with an additional parameter n as the power index and suggested that

$$\dot{z} = \begin{cases} A\,\dot{x} - \beta\,|\dot{x}|\,z^n - \gamma\,\dot{x}\,|z^n| & \text{for } n \text{ is odd} \\ A\,\dot{x} - \beta\,|\dot{x}|\,|z|\,z^{n-1} - \gamma\,\dot{x}\,z^n & \text{for } n \text{ is even.} \end{cases} \tag{B.4}$$

This nonlinear equation is usually called as the *Bouc-Wen model*.

The scale or the bound of the hysteretic loop is controlled by the parameter A, while β and γ govern the shape or the volume of the hysteretic loop. The smoothness of the elastic-plastic transition is then decided by n – as n increases the transition will be sharper and by the limiting case $n = \infty$ it is identical to an elastic perfectly-plastic model. Usually these parameters are determined directly from the experiments of materials. Owing to this flexibility various hardening systems, even softening systems, can be represented easily by modifying these parameters. Further parameter studies can be found in references [98], [26] and [33]. In Fig. B.2 the schema of Bouc-Wen's model with material constants $A = 1$, $\beta = \gamma = 0.5$ and $n = 2$ is shown.

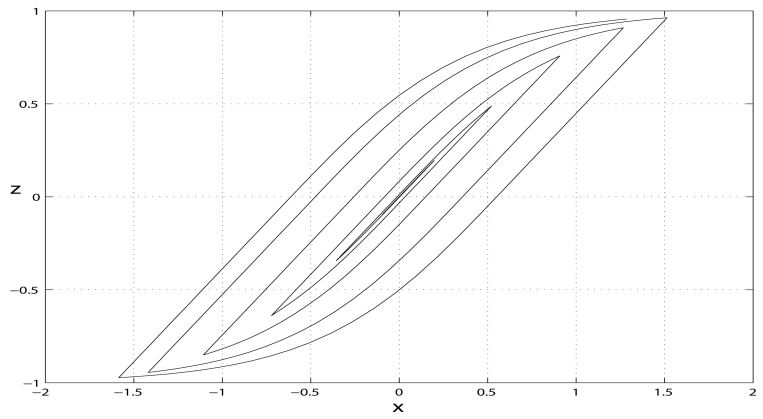

Figure B.2: Smooth Hysteresis of Bouc-Wen Model ($A = 1$, $\beta = \gamma = 0.5$, $n = 2$)

It was pointed out by Wen [101] and also by Casciati [12] that the Bouc-Wen model (B.4) doesn't obey the *Drucker's stability postulate* [41] when the displacement doesn't change its sign during the cyclic loading. This problem can be corrected by increasing the power n in the governing equation, which will aggravate the numerical computing work, or by adding a second hysteretic item [12]. But when the system is under random excitations this deficiency is no more significant [101].

Although the disobeying of Drucker's postulate under some cases, this model is widely extended and applied in many fields because of its flexibility and variability. It was extended by Baber and Wen in [6] for multi-degree-of-freedom (MDOF) systems with degradation. In [5] Baber modified this model to consider the pre-damage of systems. The further extensions of Bouc-Wen model for 2-D structures under biaxial excitations, for 3-D frames and for biaxial plus torsional excitations, can be found in [53], [13] and in [102] respectively. A tensorial expression of the smooth hysteretic model for the application to the continua was also accomplished in [88], [12]. Pradlwarter, Schuëller and Schenk proposed a hysteretic model, which combines the Suzuki-Minai's model with Bouc-Wen's, so that it has a linear-elastic region with clear defined limits of elasticity and plasticity [61]. About the detailed developments of Bouc-Wen model and its

applications in various fields, the references [101] and [98] can be read.

With another aspect the smooth transition feature can also be explained by the limit analysis of cross-section. Considering a rectangular cross-section under bending the moment-curvature relation $M - \kappa$ in elastic region can be expressed non-dimensionally as

$$\frac{\kappa}{\tilde{\kappa}_y} = \frac{M}{\tilde{M}_y} \qquad (0 \leq M \leq \tilde{M}_y) \ , \tag{B.5}$$

where $\tilde{M}_y$ and $\tilde{\kappa}_y$ are the elastic limit of moment and curvature respectively, by which the maximum stress in cross-section just reaches the yield stress σ_Y. Beyond the elastic limit $\tilde{M}_y$ part of the rectangular cross-section is loaded with σ_Y, as the other still behaves elastically. The $M - \kappa$ relation is then nonlinear and the transition from elastic- to plastic-limit is characterized by [28]

$$\frac{\kappa}{\tilde{\kappa}_y} = \frac{1}{\sqrt{3 - 2\,M/\tilde{M}_y}} \qquad (\tilde{M}_y \leq M \leq \tilde{M}_p) \ , \tag{B.6}$$

where $\tilde{M}_p$ is the plastic limit of moment (the whole cross-section is under the yield stress σ_Y). This smooth elastic-plastic transition is plotted in Fig. B.3, to which the Bouc-Wen model is very similar.

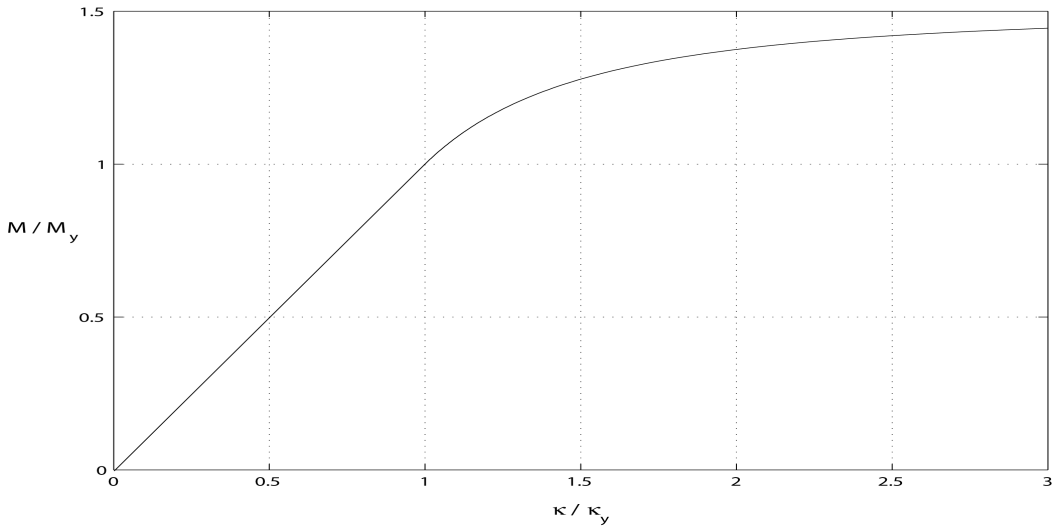

Figure B.3: Elastic-plastic $M - \kappa$ Diagram for Rectangular Cross Section

B.3 Multi-variable Hysteretic Model

The first multi-variable hysteretic model was proposed by Park et al. [53] to describe the biaxial hysteretic restoring forces of columns under stochastic two-dimensional earthquake excitations. The hysteretic components are modeled by two coupled nonlinear

differential equations as

$$\begin{aligned} \dot{z}_x &= A\,\dot{u}_x - \beta\,|\dot{u}_x\,z_x|\,z_x - \gamma\,\dot{u}_x\,z_x^2 - \beta\,|\dot{u}_y\,z_y|\,z_x - \gamma\,\dot{u}_y\,z_x\,z_y \\ \dot{z}_y &= A\,\dot{u}_y - \beta\,|\dot{u}_y\,z_y|\,z_y - \gamma\,\dot{u}_y\,z_y^2 - \beta\,|\dot{u}_x\,z_x|\,z_y - \gamma\,\dot{u}_x\,z_x\,z_y\ , \end{aligned} \tag{B.7}$$

where u_x, u_y are the displacements and A, β, γ are material constants. The total restoring forces can be expressed similar to equation (B.1) in matrix form as

$$[Q] = \alpha\,[K]\,[u] + (1-\alpha)\,[K]\,[z]\ , \tag{B.8}$$

where $[K]$ is the initial stiffness matrix and $[Q]$, $[u]$ and $[z]$ are vectors.

It was also shown in [53] that the equation (B.7) can be drawn back to the one-dimensional equation (B.4) with $n = 2$, when u_x/u_y is a constant. Consequently, the equation (B.4) can be used to find the relation between the yield strength and the material constants A, β and γ. By yielding is $\dot{z} = 0$ and z reaches its limit z_L, which is the corresponding elastic deformation of the yield strength. According to equation (B.4) with $n = 2$ it gives

$$z_L = \sqrt{A/(\beta+\gamma)}\ . \tag{B.9a}$$

If $A = 1$ and $\beta = \gamma$ is assumed, then it follows

$$\beta = \frac{1}{2}\,(\frac{1}{z_L})^2\ . \tag{B.9b}$$

Later Simulescu et al. [88] developed a hysteretic model for three-dimensional continua in a tensorial notation as follows

$$\sigma_{ij} = \lambda\left[\,\alpha^*\,\epsilon_{kk} + (1-\alpha^*)\,\xi_{kk}\right]\delta_{ij} + 2\,\mu\left[\,\alpha_{ij}\,\epsilon_{ij} + (1-\alpha_{ij})\,\xi_{ij}\right]\ . \tag{B.10}$$

In this equation λ and μ are the Lamé's constants, δ_{ij} is the Kronecker's delta and the term α_{ij} is a symmetric tensor with the definition of $\alpha^* = \alpha_{11} = \alpha_{22} = \alpha_{33}$. The Einstein summation convention is applied in this equation. If $\alpha_{ij} = 1$, then equation (B.10) reduces to the constitutive equation of elastic material behaviors. The hysteretic variable ξ is suggested as

$$\dot{\xi}_{ij} = -b_{ij}\,\dot{\epsilon}_{ij} - c_{ij}|\dot{\epsilon}_{ij}|\,|\xi_{ij}|^{n_{ij}-1}\,\xi_{ij} - d_{ij}\,\dot{\epsilon}_{ij}\,|\xi_{ij}|^{n_{ij}}\ , \tag{B.11}$$

where b_{ij}, c_{ij}, d_{ij} and $n_{ij} \geq 1$ are material constants. Under the plane stress condition ($\sigma_{33} = 0$) the equation (B.10) can be rewritten with the principal stresses as

$$\begin{aligned} \sigma_1 &= \alpha\,\frac{E}{1-\nu^2}\,(\epsilon_1 + \nu\,\epsilon_2) + (1-\alpha)\,\frac{E}{1-\nu^2}\,(\xi_1 + \nu\,\xi_2) \\ \sigma_2 &= \alpha\,\frac{E}{1-\nu^2}\,(\nu\,\epsilon_1 + \epsilon_2) + (1-\alpha)\,\frac{E}{1-\nu^2}\,(\nu\,\xi_1 + \xi_2)\ , \end{aligned} \tag{B.12}$$

This hysteretic stress-strain relation (B.11) and (B.12) is similar to the Park's biaxial model (B.7) and (B.8), which is a hysteretic force-displacement relation and doesn't

include all the terms of tensor product suggested in Simulescu's model.

Another hysteretic model expressed in a tensorial notation is proposed by Casciati in [12]. It was derived from the von Mises yielding criterion (A.6) with adoption of Prager's hardening rule (A.26) and can be formulated with deviatoric variables as

$$\dot{\boldsymbol{\xi}}' = A\,\dot{\boldsymbol{\epsilon}}' - \beta\,|\dot{\boldsymbol{\epsilon}}' : \boldsymbol{\xi}'|\,\|\boldsymbol{\xi}'\|^{n-2}\,\boldsymbol{\xi}' - \gamma\,(\dot{\boldsymbol{\epsilon}}' : \boldsymbol{\xi}')\,\|\boldsymbol{\xi}'\|^{n-2}\,\boldsymbol{\xi}'\ , \tag{B.13}$$

where $\boldsymbol{\epsilon}'$ is the deviatoric strain tensor and the hysteretic parameter $\boldsymbol{\xi}'$ is defined as the deviatoric stress minus the Prager's hardening parameter $\xi'_{ij} = S_{ij} - \alpha^h_{ij}$. In this model the hardening character is directly included.

Appendix C

Schäfer Plate Element

C.1 Deformation Shape Functions

The normalized deformation shape functions of the Schäfer plate element expressed through the natural coordinates $\eta = x/a$ and $\zeta = y/b$, where a and b are the side lengths of the plate element, are

$$
\begin{aligned}
N_1(\eta,\zeta) &= 1 - 3\,\eta^2 - 3\,\zeta^2 + 2\,\eta^3 + 2\,\zeta^3 + 9\,\eta^2\zeta^2 - 6\,\eta^3\zeta^2 - 6\,\eta^2\zeta^3 + 4\,\eta^3\zeta^3 \\
N_2(\eta,\zeta) &= a\big(-\eta + 2\,\eta^2 - \eta^3 + 3\,\eta\zeta^2 - 6\,\eta^2\zeta^2 - 2\,\eta\zeta^3 + 3\,\eta^3\zeta^2 + 4\,\eta^2\zeta^3 - 2\,\eta^3\zeta^3\big) \\
N_3(\eta,\zeta) &= b\big(-\zeta + 2\,\zeta^2 + 3\,\eta^2\zeta - \zeta^3 - 2\,\eta^3\zeta - 6\,\eta^2\zeta^2 + 4\,\eta^3\zeta^2 + 3\,\eta^2\zeta^3 - 2\,\eta^3\zeta^3\big) \\
N_4(\eta,\zeta) &= a\,b\big(-\eta\zeta + 2\,\eta^2\zeta + 2\,\eta\zeta^2 - \eta^3\zeta - 4\,\eta^2\zeta^2 - \eta\zeta^3 + 2\,\eta^3\zeta^2 + 2\,\eta^2\zeta^3 - \eta^3\zeta^3\big) \\
N_5(\eta,\zeta) &= 3\,\eta^2 - 2\,\eta^3 - 9\,\eta^2\zeta^2 + 6\,\eta^3\zeta^2 + 6\eta^2\zeta^3 - 4\,\eta^3\zeta^3 \\
N_6(\eta,\zeta) &= a\big(\eta^2 - \eta^3 - 3\,\eta^2\zeta^2 + 3\,\eta^3\zeta^2 + 2\,\eta^2\zeta^3 - 2\,\eta^3\zeta^3\big) \\
N_7(\eta,\zeta) &= b\big(-3\,\eta^2\zeta + 2\,\eta^3\zeta + 6\,\eta^2\zeta^2 - 4\,\eta^3\zeta^2 - 3\,\eta^2\zeta^3 + 2\,\eta^3\zeta^3\big) \\
N_8(\eta,\zeta) &= a\,b\big(\eta^2\zeta - \eta^3\zeta - 2\,\eta^2\zeta^2 + 2\,\eta^3\zeta^2 + \eta^2\zeta^3 - \eta^3\zeta^3\big) \\
N_9(\eta,\zeta) &= 9\,\eta^2\zeta^2 - 6\,\eta^3\zeta^2 - 6\,\eta^2\zeta^3 + 4\,\eta^3\zeta^3 \\
N_{10}(\eta,\zeta) &= a\big(3\,\eta^2\zeta^2 - 3\,\eta^3\zeta^2 - 2\,\eta^2\zeta^3 + 2\,\eta^3\zeta^3\big) \\
N_{11}(\eta,\zeta) &= b\big(3\,\eta^2\zeta^2 - 2\,\eta^3\zeta^2 - 3\,\eta^2\zeta^3 + 2\,\eta^3\zeta^3\big) \\
N_{12}(\eta,\zeta) &= a\,b\big(-\eta^2\zeta^2 + \eta^3\zeta^2 + \eta^2\zeta^3 - \eta^3\zeta^3\big) \\
N_{13}(\eta,\zeta) &= 3\,\zeta^2 - 2\,\zeta^3 - 9\,\eta^2\zeta^2 + 6\,\eta^3\zeta^2 + 6\,\eta^2\zeta^3 - 4\,\eta^3\zeta^3 \\
N_{14}(\eta,\zeta) &= a\big(-3\,\eta\zeta^2 + 6\,\eta^2\zeta^2 + 2\,\eta\zeta^3 - 3\,\eta^3\zeta^2 - 4\,\eta^2\zeta^3 + 2\,\eta^3\zeta^3\big) \\
N_{15}(\eta,\zeta) &= b\big(\zeta^2 - \zeta^3 - 3\,\eta^2\zeta^2 + 2\,\eta^3\zeta^2 + 3\,\eta^2\zeta^3 - 2\,\eta^3\zeta^3\big) \\
N_{16}(\eta,\zeta) &= a\,b\big(\eta\zeta^2 - 2\,\eta^2\zeta^2 - \eta\zeta^3 + \eta^3\zeta^2 + 2\,\eta^2\zeta^3 - \eta^3\zeta^3\big)\ .
\end{aligned}
\tag{C.1}
$$

For the curvature κ_x the corresponding second derivations of the shape function N, i.e. $B_{x,i} = \partial^2 N_i / \partial x^2$ are

$$
\begin{aligned}
B_{x,1} &= \frac{1}{a^2}(-6+12\,\eta)(1-3\,\zeta^2+2\,\zeta^3) & B_{x,9} &= \frac{1}{a^2}(6-12\,\eta)(3\,\zeta^2-2\,\zeta^3)\\
B_{x,2} &= \frac{1}{a}(4-6\,\eta)(1-3\,\zeta^2+2\,\zeta^3) & B_{x,10} &= \frac{1}{a}(2-6\,\eta)(3\,\zeta^2-2\,\zeta^3)\\
B_{x,3} &= \frac{b}{a^2}(6-12\,\eta)(\zeta-2\,\zeta^2+\zeta^3) & B_{x,11} &= \frac{b}{a^2}(6-12\,\eta)(\zeta^2-\zeta^3)\\
B_{x,4} &= \frac{b}{a}(4-6\,\eta)(\zeta-2\,\zeta^2+\zeta^3) & B_{x,12} &= \frac{b}{a}(-2+6\,\eta)(\zeta^2-\zeta^3)\\
B_{x,5} &= \frac{1}{a^2}(6-12\,\eta)(1-3\,\zeta^2+2\,\zeta^3) & B_{x,13} &= \frac{1}{a^2}(-6+12\,\eta)(3\,\zeta^2-2\,\zeta^3)\\
B_{x,6} &= \frac{1}{a}(2-6\,\eta)(1-3\,\zeta^2+2\,\zeta^3) & B_{x,14} &= \frac{1}{a}(4-6\,\eta)(3\,\zeta^2-2\,\zeta^3)\\
B_{x,7} &= \frac{b}{a^2}(-6+12\,\eta)(\zeta-2\,\zeta^2+\zeta^3) & B_{x,15} &= \frac{b}{a^2}(-6+12\,\eta)(\zeta^2-\zeta^3)\\
B_{x,8} &= \frac{b}{a}(2-6\,\eta)(\zeta-2\,\zeta^2+\zeta^3) & B_{x,16} &= \frac{b}{a}(-4+6\,\eta)(\zeta^2-\zeta^3)\ .
\end{aligned}
\tag{C.2a}
$$

The second derivations $B_{y,i} = \partial^2 N_i / \partial y^2$ for the curvature κ_y are

$$
\begin{aligned}
B_{y,1} &= \frac{1}{b^2}(1-3\,\eta^2+2\,\eta^3)(-6+12\,\zeta) & B_{y,9} &= \frac{1}{b^2}(3\,\eta^2-2\,\eta^3)(6-12\,\zeta)\\
B_{y,2} &= \frac{a}{b^2}(\eta-2\,\eta^2+\eta^3)(6-12\,\zeta) & B_{y,10} &= \frac{a}{b^2}(\eta^2-\eta^3)(6-12\,\zeta)\\
B_{y,3} &= \frac{1}{b}(1-3\,\eta^2+2\,\eta^3)(4-6\,\zeta) & B_{y,11} &= \frac{1}{b}(3\,\eta^2-2\,\eta^3)(2-6\,\zeta)\\
B_{y,4} &= \frac{a}{b}(\eta-2\,\eta^2+\eta^3)(4-6\,\zeta) & B_{y,12} &= \frac{a}{b}(\eta^2-\eta^3)(-2+6\,\zeta)\\
B_{y,5} &= \frac{1}{b^2}(3\,\eta^2-2\,\eta^3)(-6+12\,\zeta) & B_{y,13} &= \frac{1}{b^2}(1-3\,\eta^2+2\,\eta^3)(6-12\,\zeta)\\
B_{y,6} &= \frac{a}{b^2}(\eta^2-\eta^3)(-6+12\,\zeta) & B_{y,14} &= \frac{a}{b^2}(\eta-2\,\eta^2+\eta^3)(-6+12\,\zeta)\\
B_{y,7} &= \frac{1}{b}(3\,\eta^2-2\,\eta^3)(4-6\,\zeta) & B_{y,15} &= \frac{1}{b}(1-3\,\eta^2+2\,\eta^3)(2-6\,\zeta)\\
B_{y,8} &= \frac{a}{b}(\eta^2-\eta^3)(-4+6\,\zeta) & B_{y,16} &= \frac{a}{b}(\eta-2\,\eta^2+\eta^3)(2-6\,\zeta)\ .
\end{aligned}
\tag{C.2b}
$$

And the second derivations $B_{xy,i} = \partial^2 N_i / \partial x \partial y$ for the curvature κ_{xy} are

$$
\begin{aligned}
B_{xy,1} &= \frac{1}{a\,b}(6\,\eta - 6\,\eta^2)(6\,\zeta - 6\,\zeta^2) & B_{xy,9} &= \frac{1}{a\,b}(6\,\eta - 6\,\eta^2)(6\,\zeta - 6\,\zeta^2)\\
B_{xy,2} &= \frac{1}{b}(1 - 4\,\eta + 3\,\eta^2)(6\,\zeta - 6\,\zeta^2) & B_{xy,10} &= \frac{1}{b}(2\,\eta - 3\,\eta^2)(6\,\zeta - 6\,\zeta^2)\\
B_{xy,3} &= \frac{1}{a}(6\,\eta - 6\,\eta^2)(1 - 4\,\zeta + 3\,\zeta^2) & B_{xy,11} &= \frac{1}{a}(6\,\eta - 6\,\eta^2)(2\,\zeta - 3\,\zeta^2)\\
B_{xy,4} &= (-1 + 4\,\eta - 3\,\eta^2)(1 - 4\,\zeta + 3\,\zeta^2) & B_{xy,12} &= (2\,\eta - 3\,\eta^2)(-2\,\zeta + 3\,\zeta^2)\\
B_{xy,5} &= \frac{1}{a\,b}(-6\,\eta + 6\,\eta^2)(6\,\zeta - 6\,\zeta^2) & B_{xy,13} &= \frac{1}{a\,b}(6\,\eta - 6\,\eta^2)(-6\,\zeta + 6\,\zeta^2)\\
B_{xy,6} &= \frac{1}{b}(-2\,\eta + 3\,\eta^2)(6\,\zeta - 6\,\zeta^2) & B_{xy,14} &= \frac{1}{b}(1 - 4\,\eta + 3\,\eta^2)(-6\,\zeta + 6\,\zeta^2)\\
B_{xy,7} &= \frac{1}{a}(-6\,\eta + 6\,\eta^2)(1 - 4\,\zeta + 3\,\zeta^2) & B_{xy,15} &= \frac{1}{a}(6\,\eta - 6\,\eta^2)(-2\,\zeta + 3\,\zeta^2)\\
B_{xy,8} &= (2\,\eta - 3\,\eta^2)(1 - 4\,\zeta + 3\,\zeta^2) & B_{xy,16} &= (1 - 4\,\eta + 3\,\eta^2)(2\,\zeta - 3\,\zeta^2)
\end{aligned}
\tag{C.2c}
$$

C.2 Compatible Interpolation Functions of Curvatures

The following interpolation functions $\tilde{N}^*_x$, $\tilde{N}^*_y$ and $\tilde{N}^*_{xy}$ are compatible with the shape functions of curvatures – B_x, B_y and B_{xy}, respectively, which are the second derivatives of the deformation shape function N under the use of the bi-cubic deflection approach.

The compatible interpolation functions corresponding to $\kappa_x(\eta, \zeta)$ are

$$
\begin{aligned}
\tilde{N}^*_{x,1} &= (1 - \eta)(1 - 5.5\,\zeta + 9\,\zeta^2 - 4.5\,\zeta^3)\\
\tilde{N}^*_{x,2} &= \eta\,(1 - 5.5\,\zeta + 9\,\zeta^2 - 4.5\,\zeta^3)\\
\tilde{N}^*_{x,3} &= \eta\,(\zeta - 4.5\,\zeta^2 + 4.5\,\zeta^3)\\
\tilde{N}^*_{x,4} &= (1 - \eta)(\zeta - 4.5\,\zeta^2 + 4.5\,\zeta^3)\\
\tilde{N}^*_{x,5} &= (1 - \eta)(-4.5\,\zeta + 18\,\zeta^2 - 13.5\,\zeta^3)\\
\tilde{N}^*_{x,6} &= (1 - \eta)(9\,\zeta - 22.5\,\zeta^2 + 13.5\,\zeta^3)\\
\tilde{N}^*_{x,7} &= \eta\,(9\,\zeta - 22.5\,\zeta^2 + 13.5\,\zeta^3)\\
\tilde{N}^*_{x,8} &= \eta\,(-4.5\,\zeta + 18\,\zeta^2 - 13.5\,\zeta^3)
\end{aligned}
\tag{C.3a}
$$

The compatible interpolation functions corresponding to $\kappa_y(\eta,\zeta)$ are

$$\begin{aligned}
\tilde{N}^*_{y,1} &= (1-5.5\,\eta+9\,\eta^2-4.5\,\eta^3)(1-\zeta)\\
\tilde{N}^*_{y,2} &= (9\,\eta-22.5\,\eta^2+13.5\,\eta^3)(1-\zeta)\\
\tilde{N}^*_{y,3} &= (-4.5\,\eta+18\,\eta^2-13.5\,\eta^3)(1-\zeta)\\
\tilde{N}^*_{y,4} &= (\eta-4.5\,\eta^2+4.5\,\eta^3)(1-\zeta)\\
\tilde{N}^*_{y,5} &= (\eta-4.5\,\eta^2+4.5\,\eta^3)\,\zeta\\
\tilde{N}^*_{y,6} &= (-4.5\,\eta+18\,\eta^2-13.5\,\eta^3)\,\zeta\\
\tilde{N}^*_{y,7} &= (9\,\eta-22.5\,\eta^2+13.5\,\eta^3)\,\zeta\\
\tilde{N}^*_{y,8} &= (1-5.5\,\eta+9\,\eta^2-4.5\,\eta^3)\,\zeta
\end{aligned} \tag{C.3b}$$

And the compatible interpolation functions corresponding to $\kappa_{xy}(\eta,\zeta)$ are

$$\begin{aligned}
\tilde{N}^*_{xy,1} &= (1-3\,\eta+2\,\eta^2)(1-3\,\zeta+2\,\zeta^2)\\
\tilde{N}^*_{xy,2} &= (4\,\eta-4\,\eta^2)(1-3\,\zeta+2\,\zeta^2)\\
\tilde{N}^*_{xy,3} &= (-\eta+2\,\eta^2)(1-3\,\zeta+2\,\zeta^2)\\
\tilde{N}^*_{xy,4} &= (-\eta+2\,\eta^2)(4\,\zeta-4\,\zeta^2)\\
\tilde{N}^*_{xy,5} &= (-\eta+2\,\eta^2)(-\zeta+2\,\zeta^2)\\
\tilde{N}^*_{xy,6} &= (4\,\eta-4\,\eta^2)(-\zeta+2\,\zeta^2)\\
\tilde{N}^*_{xy,7} &= (1-3\,\eta+2\,\eta^2)(-\zeta+2\,\zeta^2)\\
\tilde{N}^*_{xy,8} &= (1-3\,\eta+2\,\eta^2)(4\,\zeta-4\,\zeta^2)\\
\tilde{N}^*_{xy,9} &= (4\,\eta-4\,\eta^2)(4\,\zeta-4\,\zeta^2)
\end{aligned} \tag{C.3c}$$

According to (3.51) $\tilde{N}^*_{x,i}(\eta,\zeta)$ will be expanded to $\tilde{N}_{x,i}(\eta,\zeta)$ in regard to the interpolation nodes defined in Fig. 3.10 as

$$\begin{aligned}
\tilde{N}_{x,1} &= (1-\eta)(0.5-2.75\,\zeta+4.5\,\zeta^2-2.25\,\zeta^3)\\
\tilde{N}_{x,2} &= \eta\,(0.5-2.75\,\zeta+4.5\,\zeta^2-2.25\,\zeta^3)\\
\tilde{N}_{x,3} &= \eta\,(0.5\,\zeta-2.25\,\zeta^2+2.25\,\zeta^3)\\
\tilde{N}_{x,4} &= (1-\eta)(0.5\,\zeta-2.25\,\zeta^2+2.25\,\zeta^3)\\
\tilde{N}_{x,5} &= (2-3\,\eta)(0.5-2.75\,\zeta+4.5\,\zeta^2-2.25\,\zeta^3)\\
\tilde{N}_{x,6} &= (-1+3\,\eta)(0.5-2.75\,\zeta+4.5\,\zeta^2-2.25\,\zeta^3)\\
\tilde{N}_{x,7} &= \eta\,(4.5\,\zeta-11.25\,\zeta^2+6.75\,\zeta^3)\\
\tilde{N}_{x,8} &= \eta\,(-2.25\,\zeta+9\,\zeta^2-6.75\,\zeta^3)
\end{aligned}$$

$$
\begin{aligned}
\tilde{N}_{x,9} &= (-1+3\,\eta)(0.5\,\zeta - 2.25\,\zeta^2 + 2.25\,\zeta^3)\\
\tilde{N}_{x,10} &= (2-3\,\eta)(0.5\,\zeta - 2.25\,\zeta^2 + 2.25\,\zeta^3)\\
\tilde{N}_{x,11} &= (1-\eta)(-2.25\,\zeta + 9\,\zeta^2 - 6.75\,\zeta^3)\\
\tilde{N}_{x,12} &= (1-\eta)(4.5\,\zeta - 11.25\,\zeta^2 + 6.75\,\zeta^3)\\
\tilde{N}_{x,13} &= (2-3\,\eta)(4.5\,\zeta - 11.25\,\zeta^2 + 6.75\,\zeta^3)\\
\tilde{N}_{x,14} &= (-1+3\,\eta)(4.5\,\zeta - 11.25\,\zeta^2 + 6.75\,\zeta^3)\\
\tilde{N}_{x,15} &= (-1+3\,\eta)(-2.25\,\zeta + 9\,\zeta^2 - 6.75\,\zeta^3)\\
\tilde{N}_{x,16} &= (2-3\,\eta)(-2.25\,\zeta + 9\,\zeta^2 - 6.75\,\zeta^3)
\end{aligned}
\tag{C.4}
$$

Similarly will $\tilde{N}^*_{y,i}(\eta,\zeta)$, which regards to Fig. 3.9 (b), be expanded to $\tilde{N}_{y,i}(\eta,\zeta)$, which regards to Fig. 3.10, as following

$$
\begin{aligned}
\tilde{N}_{y,1} &= (0.5 - 2.75\,\eta + 4.5\,\eta^2 - 2.25\,\eta^3)(1-\zeta)\\
\tilde{N}_{y,2} &= (0.5\,\eta - 2.25\,\eta^2 + 2.25\,\eta^3)(1-\zeta)\\
\tilde{N}_{y,3} &= (0.5\,\eta - 2.25\,\eta^2 + 2.25\,\eta^3)\,\zeta\\
\tilde{N}_{y,4} &= (0.5 - 2.75\,\eta + 4.5\,\eta^2 - 2.25\,\eta^3)\,\zeta\\
\tilde{N}_{y,5} &= (4.5\,\eta - 11.25\,\eta^2 + 6.75\,\eta^3)(1-\zeta)\\
\tilde{N}_{y,6} &= (-2.25\,\eta + 9\,\eta^2 - 6.75\,\eta^3)(1-\zeta)\\
\tilde{N}_{y,7} &= (0.5\,\eta - 2.25\,\eta^2 + 2.25\,\eta^3)(2-3\,\zeta)\\
\tilde{N}_{y,8} &= (0.5\,\eta - 2.25\,\eta^2 + 2.25\,\eta^3)(-1+3\,\zeta)\\
\tilde{N}_{y,9} &= (-2.25\,\eta + 9\,\eta^2 - 6.75\,\eta^3)\,\zeta\\
\tilde{N}_{y,10} &= (4.5\,\eta - 11.25\,\eta^2 + 6.75\,\eta^3)\,\zeta\\
\tilde{N}_{y,11} &= (0.5 - 2.75\,\eta + 4.5\,\eta^2 - 2.25\,\eta^3)(-1+3\,\zeta)\\
\tilde{N}_{y,12} &= (0.5 - 2.75\,\eta + 4.5\,\eta^2 - 2.25\,\eta^3)(2-3\,\zeta)\\
\tilde{N}_{y,13} &= (4.5\,\eta - 11.25\,\eta^2 + 6.75\,\eta^3)(2-3\,\zeta)\\
\tilde{N}_{y,14} &= (-2.25\,\eta + 9\,\eta^2 - 6.75\,\eta^3)(2-3\,\zeta)\\
\tilde{N}_{y,15} &= (-2.25\,\eta + 9\,\eta^2 - 6.75\,\eta^3)(-1+3\,\zeta)\\
\tilde{N}_{y,16} &= (4.5\,\eta - 11.25\,\eta^2 + 6.75\,\eta^3)(-1+3\,\zeta)
\end{aligned}
\tag{C.5}
$$

For the expansion of $\tilde{N}^*_{xy,i}(\eta,\zeta)$ considering first a general quadratic function in x-direction

$$f(\eta) = a_1 + a_2\,\eta + a_3\,\eta^2\ ,$$

which can be interpolated for example through the polynomials of η in the first parentheses of $\tilde{N}^*_{xy,1}(\eta,\zeta)$, $\tilde{N}^*_{xy,2}(\eta,\zeta)$ and $\tilde{N}^*_{xy,3}(\eta,\zeta)$ as

$$
\begin{aligned}
f(\eta) &= a_1 + a_2\,\eta + a_3\,\eta^2\\
&= f(0)(1 - 3\,\eta + 2\,\eta^2) + f(1/2)(4\,\eta - 4\,\eta^2) + f(1)(-\eta + 2\,\eta^2)\ .
\end{aligned}
$$

Because the node Nr.2 in Fig. 3.9 (c) will be replaced by two nodes, i.e. Nr.5 and Nr.6

in Fig. 3.10, the following relations are used

$$f(1/3) = \frac{2}{9}f(0) + \frac{8}{9}f(1/2) - \frac{1}{9}f(1)$$
$$f(2/3) = -\frac{1}{9}f(0) + \frac{8}{9}f(1/2) + \frac{2}{9}f(1) \ ,$$

which lead to

$$f(1/2) = \frac{9}{8}f(1/3) - \frac{1}{4}f(0) + \frac{1}{8}f(1) \quad \text{and}$$
$$f(1/2) = \frac{9}{8}f(2/3) + \frac{1}{8}f(0) - \frac{1}{4}f(1) \ .$$

Therefore the quadratic function can be decomposed for example as

$$\begin{aligned} f(\eta) &= f(0)(1-3\eta+2\eta^2) + 0.5f(\frac{1}{2})(4\eta-4\eta^2) + 0.5f(\frac{1}{2})(4\eta-4\eta^2) + f(1)(-\eta+2\eta^2) \\ &= f(0)(1-3\eta+2\eta^2) + (\frac{9}{16}f(\frac{1}{3}) - \frac{1}{8}f(0) + \frac{1}{16}f(1))(4\eta-4\eta^2) \\ &\quad + (\frac{9}{16}f(\frac{2}{3}) + \frac{1}{16}f(0) - \frac{1}{8}f(1))(4\eta-4\eta^2) + f(1)(-\eta+2\eta^2) \\ &= f(0)(1-3.25\,\eta+2.25\,\eta^2) + f(\frac{1}{3})(2.25\,\eta-2.25\,\eta^2) \\ &\quad + f(\frac{2}{3})(2.25\,\eta-2.25\,\eta^2) + f(1)(-1.25\,\eta+2.25\,\eta^2) \ . \end{aligned}$$

Similarly for the y-direction the quadratic function can be interpolated with four nodes as

$$\begin{aligned} f(\eta) &= a_1 + a_2\,\eta + a_3\,\eta^2 \\ &= f(0)(1-3.25\,\eta+2.25\,\eta^2) + f(\frac{1}{3})(2.25\,\eta-2.25\,\eta^2) \\ &\quad + f(\frac{2}{3})(2.25\,\eta-2.25\,\eta^2) + f(1)(-1.25\,\eta+2.25\,\eta^2) \ . \end{aligned}$$

Therefore the 16 interpolation functions according to Fig. 3.10 are

$$\begin{aligned} \tilde{N}_{xy,1} &= (1-3.25\,\eta+2.25\,\eta^2)(1-3.25\,\zeta+2.25\,\zeta^2) \\ \tilde{N}_{xy,2} &= (-1.25\,\eta+2.25\,\eta^2)(1-3.25\,\zeta+2.25\,\zeta^2) \\ \tilde{N}_{xy,3} &= (-1.25\,\eta+2.25\,\eta^2)(-1.25\,\zeta+2.25\,\zeta^2) \\ \tilde{N}_{xy,4} &= (1-3.25\,\eta+2.25\,\eta^2)(-1.25\,\zeta+2.25\,\zeta^2) \\ \tilde{N}_{xy,5} &= (2.25\,\eta-2.25\,\eta^2)(1-3.25\,\zeta+2.25\,\zeta^2) \\ \tilde{N}_{xy,6} &= (2.25\,\eta-2.25\,\eta^2)(1-3.25\,\zeta+2.25\,\zeta^2) \\ \tilde{N}_{xy,7} &= (-1.25\,\eta+2.25\,\eta^2)(2.25\,\zeta-2.25\,\zeta^2) \\ \tilde{N}_{xy,8} &= (-1.25\,\eta+2.25\,\eta^2)(2.25\,\zeta-2.25\,\zeta^2) \end{aligned}$$

$$
\begin{aligned}
\tilde{N}_{xy,9} &= (2.25\,\eta - 2.25\,\eta^2)(-1.25\,\zeta + 2.25\,\zeta^2) \\
\tilde{N}_{xy,10} &= (2.25\,\eta - 2.25\,\eta^2)(-1.25\,\zeta + 2.25\,\zeta^2) \\
\tilde{N}_{xy,11} &= (1 - 3.25\,\eta + 2.25\,\eta^2)(2.25\,\zeta - 2.25\,\zeta^2) \\
\tilde{N}_{xy,12} &= (1 - 3.25\,\eta + 2.25\,\eta^2)(2.25\,\zeta - 2.25\,\zeta^2) \\
\tilde{N}_{xy,13} &= (2.25\,\eta - 2.25\,\eta^2)(2.25\,\zeta - 2.25\,\zeta^2) \\
\tilde{N}_{xy,14} &= (2.25\,\eta - 2.25\,\eta^2)(2.25\,\zeta - 2.25\,\zeta^2) \\
\tilde{N}_{xy,15} &= (2.25\,\eta - 2.25\,\eta^2)(2.25\,\zeta - 2.25\,\zeta^2) \\
\tilde{N}_{xy,16} &= (2.25\,\eta - 2.25\,\eta^2)(2.25\,\zeta - 2.25\,\zeta^2)
\end{aligned}
\tag{C.6}
$$

Appendix D

Beam Element

D.1 Hermite's Interpolation Function

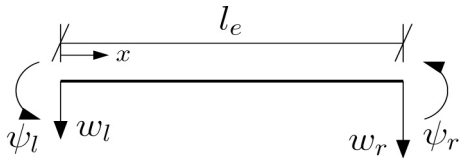

Figure D.1: Beam Element

The deflection of the beam element by using the Hermite's interpolation function can be formulated as

$$w(x) = N_1(x)\, w_l + N_2(x)\, \psi_l + N_3(x)\, w_r + N_4(x)\, \psi_r \ , \tag{D.1a}$$

with

$$\begin{aligned} N_1(x) &= 1 - 3(x/l_e)^2 + 2(x/l_e)^3 \\ N_2(x) &= -l_e\big((x/l_e) - 2(x/l_e)^2 + (x/l_e)^3\big) \\ N_3(x) &= 3(x/l_e)^2 - 2(x/l_e)^3 \\ N_4(x) &= l_e\big((x/l_e)^2 - (x/l_e)^3\big) \ . \end{aligned} \tag{D.1b}$$

The curvature can be calculated as

$$\kappa_x(x) = \frac{\partial^2 w(x)}{\partial x^2} = \mathbf{B}\, \mathbf{w}_e \ , \tag{D.2a}$$

where $\mathbf{w}_e^T = [\, w_l \ \psi_l \ w_r \ \psi_r]$ and

$$\begin{aligned} \mathbf{B} &= \left[\begin{array}{cccc} \partial^2 N_1/\partial x^2 & \partial^2 N_2/\partial x^2 & \partial^2 N_3/\partial x^2 & \partial^2 N_4/\partial x^2 \end{array} \right] \\ &= \frac{1}{{l_e}^2} \left[\begin{array}{cccc} -6 + 12\dfrac{x}{l_e} & l_e(4 - 6\dfrac{x}{l_e}) & 6 - 12\dfrac{x}{l_e} & l_e(2 - 6\dfrac{x}{l_e}) \end{array} \right] \end{aligned} \tag{D.2b}$$

Consequently, the deformation stiffness matrix is

$$\mathbf{K}_e = \int \mathbf{B}^T (EI) \mathbf{B}\, dx = \frac{EI}{{l_e}^3} \left[\begin{array}{cccc} 12 & -6\, l_e & -12 & -6\, l_e \\ -6\, l_e & 4\, {l_e}^2 & 6\, l_e & 2\, {l_e}^2 \\ -12 & 6\, l_e & 12 & 6\, l_e \\ -6\, l_e & 2\, {l_e}^2 & 6\, l_e & 4\, {l_e}^2 \end{array} \right] . \tag{D.3}$$

Appendix E

Stochastic Processes

E.1 Definition of Stochastic Processes

In the field of the civil engineering the uncertainties involved in the system characteristics are small and are not the major issue in comparison with the external excitations, such as the wind blasts, the earthquakes, the water waves, etc. Therefore the primary incentive for the adaptation of probabilistic methods in structural dynamic analyses are the random excitations.

To describe the time variance of the excitation in the dynamic analysis, the loading will be formulated as a stochastic process, which is defined as [43]

> *A random process is a parametered family of random variables with the parameter (or parameters) belonging to an indexing set (or sets).*

In other words: the stochastic loading process is a sequence (family) of random variables $\tilde{p}(t_1)$, $\tilde{p}(t_2)$ ..., in which $\tilde{p}(t_i)$ indicates the random input at time t_i, and the entire sequence is simply denoted by $\tilde{p}(t)$. In context with finite element systems the single stochastic process can be generally extended to a multi-dimensional vector of stochastic processes $\tilde{\mathbf{p}}(t)$, whose components $\tilde{p}_N(t)$ correspond to each degree of freedom. Since the input, i.e., the loading, is a random process, it is to expect that the interested output, i.e., the system response, will also be a random process.

The mathematical foundation of stochastic processes in terms of the application in the stochastic dynamics can be found for example in [44] and [89] respectively. In view of numerical treatment a comprehensive survey of the stochastic processes modeling and probabilistic methods is given in [72].

E.2 Representation of Stochastic Processes

By researching the system responses under random excitations, the first step is to establish the representation of the stochastic loading process. The requirement on such mathematical model is the accurate reproduction of the probabilistic characteristics residing in the process, which are known from various measurement and investigations in the past. The most common representations for stochastic processes are the followings [70].

Spectral representation

Samples of the random process will be generated with specified spectral density information according to this procedure, which appears to be widely utilized in the literature, e.g., [80], [86]. The simplest case, to which this representation applies, is the White Gaussian Noise (WGN), which is a stationary ergodic process. In such case the loading process is formulated as the sum of various independent random processes, whose amplitude is resulted from the spectral density function and multiplied further with a random phase angle, which has the unit probability density function from 0 to 2π. The resulted process will approach Gaussian under the consideration of the *central limit theorem.*

Further advances are made for the generation of two- and three-dimensional homogeneous Gaussian stochastic fields using the fast Fourier transform technique, which improves the computational efficiency (e.g., [81], [82], [83], [84], [85]). For the non-stationary case this method can be extended to generate the stochastic waves [19] and to comprise non-Gaussian stochastic fields [105] through a memoryless nonlinear transformation together with an iterative procedure to meet the target spectral density. By weighting of the constant spectral densities the shot noise can be generated.

Karhunen-Loève Representation

With this method the stochastic process will be formulated as the infinite series of deterministic orthogonal functions multiplied by random coefficients. The determination of the stochastic process becomes then an incentive to solve the eigenvalue problem of the covariance matrix of the process. For two reasons is this procedure quite often utilized in stochastic mechanics. One of the reason is, the random coefficients of the Karhunen-Loève expansion are uncorrelated for Gaussian stochastic processes. The other reason is, the mean-square error resulting from a finite representation of a stochastic process is minimized under applying the eigenfunctions of the Karhunen-Loève expansion [70]. A generalization of the Karhunen-Loève expansion, which is denoted as polynomial chaos expansion, for non-Gaussian process can be found in [29], [97] and [21].

Wavelets Representation

In comparison with the spectral representation by Fourier analysis is the wavelets representation more suitable to describe the local feature of multi-dimensional inhomogeneous random fields [70]. For lots of stochastic problems, the wavelet representation can be regarded as an approximate Karhunen-Loève expansion, and it is shown that the wavelet analysis may be an advantageous approach for system identification and damage detection purposes. Recently this method has been applied in stochastic mechanics to represent, e.g., random sea motion [95] and random fields [106].

E.3 Generation of White Gaussian Noise Process

Considering a stochastic loading process $\tilde{p}(t)$, whose Fourier transformation are defined as

$$\begin{aligned} \tilde{P}(\omega) &= \int_{-\infty}^{\infty} \tilde{p}(t)\, e^{-i\omega t}\, dt \ , \quad \text{with} \quad i = \sqrt{-1} \\ \tilde{p}(t) &= \frac{1}{2\pi} \int_{-\infty}^{\infty} \tilde{P}(\omega)\, e^{i\omega t}\, d\omega \ . \end{aligned} \tag{E.1}$$

Through the autocorrelation function $R_{xx}(\omega)$, the Fourier transformed $\tilde{P}(\omega)$, which is also a random process, is associated with the power spectral density $S_{xx}(\omega)$ as showed in the equations (E.2) to (E.6). For the stationary process, e.g., the Gaussian process, the relations between $R_{xx}(\tau)$ and $S_{xx}(\omega)$ are formulated according to the *Wiener-Khintchine theorem* [43] as

$$\begin{aligned} S_{xx}(\omega) &= \frac{1}{2\pi} \int_{-\infty}^{\infty} R_{xx}(\tau)\, e^{-i\omega\tau}\, d\tau \\ R_{xx}(\tau) &= \int_{-\infty}^{\infty} S_{xx}(\omega)\, e^{i\omega\tau}\, d\omega \ . \end{aligned} \tag{E.2}$$

Besides, instead of using the definition $R_{xx}(\tau) = E\big[\, \tilde{p}(t)\, \tilde{p}(t+\tau) \big]$ via the ensemble average, the autocorrelation function can be obtained with the assumption of an ergodic process as [17]

$$R_{xx}(\tau) = \lim_{z\to\infty} \frac{1}{z} \int_{-z/2}^{z/2} \tilde{p}(t)\, \tilde{p}(t+\tau)\, dt = \langle\, \tilde{p}(t)\, \tilde{p}(t+\tau)\, \rangle \ , \tag{E.3}$$

which is the time average of an arbitrary single realization.

Applying the second equation of (E.1) and its equivalent form

$$\tilde{p}(t) = \frac{1}{2\pi} \int_{-\infty}^{\infty} \tilde{P}^{*}(\omega)\, e^{-i\omega t}\, d\omega \ , \tag{E.4}$$

where $\tilde{P}^*(\omega)$ is the complex conjugate of $\tilde{P}(\omega)$, in (E.3) so that the autocorrelation function can be rewritten as [23]

$$\begin{aligned} R_{xx}(\tau) &= \langle\, \tilde{p}(t)\, \tilde{p}(t+\tau)\, \rangle \\ &= \big\langle (\frac{1}{2\pi} \int_{-\infty}^{\infty} \tilde{P}^*(\omega')\, e^{-i\omega' t}\, d\omega')(\frac{1}{2\pi} \int_{-\infty}^{\infty} \tilde{P}(\omega)\, e^{i\omega(t+\tau)}\, d\omega) \big\rangle \\ &= (\frac{1}{2\pi})^2 \int_{-\infty}^{\infty} \Big(\int_{-\infty}^{\infty} \big\langle \tilde{P}^*(\omega') \tilde{P}(\omega) \big\rangle\, e^{i(\omega-\omega')t}\, d\omega' \Big)\, e^{i\omega\tau}\, d\omega \ , \end{aligned} \tag{E.5a}$$

which should be independent of t for a stationary process. This can be fulfilled, if

$$\big\langle \tilde{P}^*(\omega') \tilde{P}(\omega) \big\rangle = \big\langle \big|\tilde{P}(\omega)\big|^2 \big\rangle\, \delta(\omega - \omega') \tag{E.5b}$$

valid, so that (E.5a) is further modified to

$$R_{xx}(\tau) = \frac{1}{2\pi} \int_{-\infty}^{\infty} \big\langle \big|\tilde{P}(\omega)\big|^2 \big\rangle\, e^{i\omega\tau}\, d\omega \ . \tag{E.5c}$$

Comparing (E.5c) with the expression in (E.2), the relation between $\tilde{P}(\omega)$ and $S_{xx}(\omega)$ can be derived as

$$\big\langle \big|\tilde{P}(\omega)\big| \big\rangle = \sqrt{2\pi\, S_{xx}(\omega)} \ , \tag{E.6}$$

where $\big\langle \big|\tilde{P}(\omega)\big| \big\rangle$ means the *time average of the spectral amplitude magnitude* of the loading process.

For the digital treatment the frequency will be discretized as $\omega_m = m\,\Delta\omega$ with $m = 0, 1, 2 \cdots$, which leads to the periodization of the loading $\tilde{p}_{per}(t)$ with a period $T_p = 2\pi/\Delta\omega$. And the periodic loading process can be represented through the Fourier series as

$$\tilde{p}_{per}(t) = \sum_{m=-\infty}^{\infty} P_m\, e^{i\omega_m t} \quad \text{with} \quad P_m = \frac{1}{T_p} \int_{-T_p/2}^{T_p/2} \tilde{p}_{per}(t)\, e^{-i\omega_m t}\, dt \ . \tag{E.7}$$

As shown in Fig. E.1, if the non-periodic process $\tilde{p}(t)$ is bounded and the frequency sampling $\Delta\omega$ is fine enough, such that the repeated partial signals in $\tilde{p}_{per}(t)$ wouldn't overlap, the following relation can be found

$$\tilde{P}(\omega_m) = \int_{-T_p/2}^{T_p/2} \tilde{p}_{per}(t)\, e^{-i\omega_m t}\, dt = T_p\, P_m \ . \tag{E.8}$$

The discretization of frequency also causes the periodization of the autocorrelation function, which is expressed as

$$\tilde{R}_{per}(\tau) = \sum_{m=-\infty}^{\infty} S_m\, e^{i\omega_m \tau} \quad \text{with} \quad S_m = \frac{1}{T_p} \int_{-T_p/2}^{T_p/2} \tilde{R}_{per}(\tau)\, e^{-i\omega_m \tau}\, d\tau \ , \tag{E.9a}$$

and similarly it can be derived that

$$S_{xx}(\omega_m) = T_p\, S_m \ . \tag{E.9b}$$

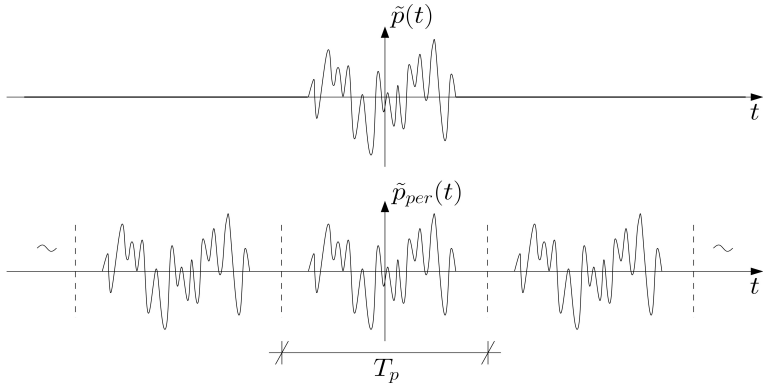

Figure E.1: Non-periodic / Periodic Loading processes

Setting (E.8) and (E.9b) in (E.6) the following formulation of the discrete spectral amplitude magnitude in time average, which is generally adopted in the literature, e.g., [82], [98], can be achieved

$$\langle \left| \tilde{P}_m \right| \rangle = \sqrt{2\pi \, S_m / \, T_p} = \sqrt{S_m \, \Delta\omega} \; . \tag{E.10}$$

For the general white noise signals is the power spectral density $S_{xx}(\omega_m)$, i.e., S_m, a constant.

With (E.10) the spectral coefficients P_m of the random process $\tilde{p}_{per}(t)$ can be written as

$$P_m = \langle \left| \tilde{P}_m \right| \rangle \, e^{i\theta_m} \; , \tag{E.11}$$

where θ_m is the equally distributed random phase angle between $[0..2\pi]$.

Finally, the random process can be rebuilt through the discrete inverse Fourier transformation as

$$\tilde{p}_{per}(t) = \sum_{m=-\infty}^{\infty} \sqrt{S_m \, \Delta\omega} \, e^{i(\omega_m t + \theta_m)} \; . \tag{E.12}$$

Bibliography

[1] *DIN V ENV 1993-1: Eurocode 3: Bemessung und Konstruktion von Stahlbauten*. Beuth-Verlag, Berlin, 1993.

[2] *DIN V ENV 1992-1-1: Eurocode 2 Teil 1-1: Grundlagen und Anwendungsregeln für den Hochbau*. Beuth-Verlag, Berlin, Mai 1992.

[3] R. Adrezin and H. Benaroya. Non-linear stochastic dynamics of tension leg platforms. *Journal of Sound and Vibration*, 220(1):27–65, 1999.

[4] T.S. Atalik and S. Utku. Stochastic linearization of multidegree of freedom nonlinear systems. *Earthquake Engineering and Structural Dynamics*, 4:411–420, 1976.

[5] T.T. Baber and M.N. Noori. Random vibration of pinching, hysteretic systems. *Engineering Mechanics Division, ASCE*, 110(7):1036–1049, 1984.

[6] T.T. Baber and Y.K. Wen. Random vibration of hysteretic degrading systems. *Engineering Mechanics, ASCE*, 107:1069–1087, 1981.

[7] Klaus-Jürgen Bathe. *Finite-Elemente-Methoden*. Springer-Verlag, 1986.

[8] F.K. Bogner, R.L. Fox, and L.A. Schmit. The Generation of Inter-Element Compatible Stiffness and Mass Matrices by the Use of Interpolation Formulas. In *Proc. Conf. Matrix Methods in Struct. Mech.*, pages 397–444, Air Force Inst. of Tech., Wright-Patterson AFB, Ohio, 1966.

[9] R. Bouc. Forced Vibration of a Mechanical System with Hysteresis (abstract). In *Proceedings of the* 4^{th} *Conference on Nonlinear Oscillations*, Prag, Czechoslovakia, 1967.

[10] P.W. Bridgeman. *Studies in large plastic flow and fracture. Metallurgy and Metallurgical Engineering Series.* McGraw-Hill, 1952.

[11] B. Carcia-Archilla, J. Novo, and E.S. Titi. Postprocessing the galerkin method: A novel approach to approximate inertial manifolds. *Siam Journal of Numerical Analysis*, 35(3):941–972, 1998.

[12] F. Casciati. Stochastic dynamics of hysteretic media. *Structural Safety*, 6:259–269, 1989.

[13] F. Casciati and L. Faravelli. Stochastic equivalent linearization for 3-d frames. *Engineering Mechanics, ASCE*, 114(10):1760–1771, 1988.

[14] T.K. Caughey. Random excitation of a system with bilinear hysteresis. *Transactions of the ASME, Journal of Applied Mechanics*, 27:649–652, 1960.

[15] T.K. Caughey. Equivalent linearization techniques. *Journal of the Acoustical Society of America*, 35(11):1706–1711, 1963.

[16] W.F. Chen and D.J. Han. *Plasticity for Structural Engineers*. Springer-Verlag, 1988.

[17] R.W. Clough and J. Penzien. *Dynamics of Structures*. McGraw-Hill Book Co., Singapore, 1993.

[18] M.C. Comerio. *Disaster Hits Home- New Policy for Urban Housing Recovery*. Berkeley: University of California press., 1998.

[19] G. Deodatis and M. Shinozuka. Simulation of seismic ground motion using stochastic waves. *Journal of Engineering Mechanics*, 115(12):2723–2737, 1989.

[20] D.C. Drucker and L. Palgen. On stress-strain relations suitable for cyclic and other loadings. *Appl. Mech.*, 48:479, 1981.

[21] J.R. Field and M. Grigoriu. On the accuracy of the polynomial chaos approximation. *Probabilistic Engineering Mechanics*, 19(1-2):65–80, 2004.

[22] G.S. Fishman. *Monte Carlo: concepts, algorithms, and applications*. Springer, Springer Series in operations research. New York, 1995.

[23] Reif Frederick. *Statistische Physik und Theorie der Wärme*. Walter de Gruyter, New York, 1987.

[24] A.M. Freudenthal. Introductory remarks. *Structural Safety and Reliability*, pages 5–9, 1972.

[25] P.L. Gatti and V. Ferrari. *Applied Structural and Mechanical Vibrations - Theory, Methods and Measuring Instrumentation*. E & FN Spon, Berlin Heidelberg, 1999.

[26] M. Geisenhofer. *Statistische Linearisierung für große Mehrfreiheitsgradsysteme in reduzierter Basis aus elastischen und plastischen Ansatzmoden*. Dissertation, Lehrstuhl für Baumechanik, Technische Universität München, München, Germany, 2002. Berichte aus dem Konstruktiven Ingenieurbau, 1/2002.

[27] M. Geisenhofer and H. Grundmann. Equivalent Statistical Linearization of Hysteretic Systems using a Reduced Set of Shape Functions. In *Structural safety and reliability - Proceedings of the 8^{th} international conference, ICOSSAR '01*, Newport Beach, CA, USA, 2001.

[28] J.M. Gere and S.P. Timoshenko. *Mechanics of materials*. Thornes, 1999.

[29] R.G. Ghanem and P.D. Spanos. *Stochastic Finite Elements: A Spectral Approach*. Springer-Verlag, 1991.

[30] D. Gross, W. Hauger, W. Schnell, and P. Wriggers. *Technische Mechanik, Band 4*. Springer-Verlag, 1993.

[31] H. Grundmann and M. Geisenhofer. Stochastic Dynamics of Hysteretic Frame Structures - Equivalent Statistical Linearization on a Reduced Base of Shape Functions. In *Structural safety and reliability - Proceedings of the* 8^{th} *international conference, ICOSSAR '01*, Newport Beach, CA, USA, 2001.

[32] J. Guggenberger, H. Grundmann, and Y.-L. Lin. Monte Carlo simulation of the hysteretic response of frame structures using plastification adapted shape functions. In *Proceeding of the* 4^{th} *international conference of computational stochastic mechanics*, pages 249–258, Corfu, Greece, 2002.

[33] J.M. Guggenberger. *Stochastische Dynamik von Rahmentragwerken mit hysteretischem Materialverhalten - Untersuchungen in reduzierter orthogonaler Basis*. Dissertation, Lehrstuhl für Baumechanik, Technische Universität München, München, Germany, 2004. Berichte aus dem Konstruktiven Ingenieurbau, 5/2004.

[34] E.J. Gumbel. *Statistics of Extremes*. Columbia University Press, New York, 1967.

[35] H. Haken. *Synergetics, An Introduction*. Springer-Verlag, 1983.

[36] S. Huttner. Using Residual Vectors (Modal Augmentation) in MSC Nastran to Improve Quality and Accuracy of Modal Analysis. In *Proceedings of the Nafems Conference on Validation of FEM Analyses - Models and Results*, Wiesbaden, Germany, 2002.

[37] W.D. Iwan. Application of nonlinear analysis techniques. In *Proceeding of applied mechanics in earthquake engineering, Winter Annual Meeting of ASME*, pages 135–161, New York, 1974.

[38] P.C. Jennings. Periodic response of a general yielding structure. *Engineernig Mechanics Division, ASCE*, 90:131–165, 1964.

[39] K. Kanai. Semi-empirical formula for the seismic characteristics of the ground. *Bullitin of the Earthquake Research Institute, University of Tokyo*, 35:309–325, 1957.

[40] I.E. Kazakov. Generalization of the method of statistical linearization to multidimensional systems. *Automation and Remote control*, 26:1201–1206, 1965.

[41] Akhtar S. Khan and Sujian Huang. *Continuum Theory of Plasticity*. John Wiley & Sons, INC., 1995.

[42] Y.-L. Lin. Entwicklung von Formfunktionen zur Simulation vom elastoplastischen Materialverhalten mit modaler Superposition. Diplomarbeit, Technische Universität München, München, Germany, 2001. Lehrstuhl für Baumechanik, Nr.127.

[43] Y.K. Lin. *Probabilistic Theory of Structural Dynamics*. McGraw-Hill, Toronto, 1967.

[44] Y.K. Lin and G.Q. Cai. *Probabilistic Structural Dynamics. Advanced Theory and Applications*. McGraw-Hill, New York, 1995.

[45] Herbert Mang and Günter Hofstetter. *Festigkeitslehre*. Springer-Verlag, 2004.

[46] H.G. Matthies and M. Mayer. Nonlinear Galerkin Methods for the Model Reduction of Nonlinear Dynamical Systems. Technical report, Institut für wissenschaftliche Rechenmethoden, Technische Universität Braunschweig, 2002.

[47] M. Mayer. *Die Sicherheit der Bauwerke*. J. Springer Verlag, Berlin, 1926.

[48] G. Mehlhorn. *Der Ingenieurbau - Tragwerkszuverlässigkeit - Einwirkungen*. Ernst und Sohn, Berlin, 1996.

[49] Z.C. Moh, R.N. Hwang, T.S. Ueng, and M.L. Lin. 1999 Chi Chi Earthquake of Taiwan. In *17th Australasian Conf. on the Mechanics of Structures and Materials*, Gold Coast, Australia, 2002.

[50] Hans G. Natke. *Einführung in Theorie und Praxis der Zeitreihen- und Modalanalyse*. Friedr. Vieweg & Sohn, Braunschweig/Wiesbaden, 1983.

[51] H. Nyquist. Certain topics in telegraph transmission theory. *Trans. AIEE*, 47:617–644, Apr. 1928.

[52] Y.J. Park and A.H.-S. Ang. Seismic damage analysis of r/c nuclear structures. In *Proceedings of the* 9^{th} *SMiRT Conference*, pages 229–236, Lausanne, Switzerland, 1987.

[53] Y.J. Park, Y.K. Wen, and A.H.-S. Ang. Random vibration of hysteretic systems under bi-directional ground motions. *Earthquake Engineering and Structural Dynamics*, 14:543–557, 1986.

[54] C. Petersen. *Dynamik der Baukonstruktionen*. Vieweg & Sohn, Braunschweig/ Wiesbaden, 2000.

[55] F. Poirion. Response of an airplane to non-gaussian atmospheric turbulence. *Journal of Aircraft*, 28(9):579–583, 1991.

[56] H.J. Pradlwarter. Selective MC Simulation Technique for Nonlinear Structural Reliability. In *Proceedings of ASCE Specialty Conference*, pages 69–72, Denver, Colorado, 1992.

[57] H.J. Pradlwarter and G.I. Schëller. On advanced monte carlo simulation procedures in stochastic structural dynamics. *International Journalof Non-linear mechanics*, 32(4):735–744, 1997.

[58] H.J. Pradlwarter and G.I. Schëller. Assessment of low probability events of dynamical systems by controlled monte carlo simulation. *Probabilistic Engineering Mechanics*, 14(3):213–227, 1999.

[59] H.J. Pradlwarter and G.I. Schuëller. Equivalent linearization - a suitable tool for analyzing mdof-systems. *Probabilistic Engineering Mechanics*, 8:115–126, 1992.

[60] H.J. Pradlwarter, G.I. Schuëller, and P.G. Melnik-Melnikov. Reliability of mdof-systems. *Probabilistic Engineering Mechanics*, 9:235–243, 1994.

[61] H.J. Pradlwarter, G.I. Schuëller, and C.A. Schenk. A computational procedure to estimate the stochastic dynamic response of large non-linear FE-models. *Computer methods in applied mechanics and engineering*, 192(7-8):777–801, 2003.

[62] H.J. Pradlwarter, G.I. Schuëller, and G.S. Szekely. Random eigenvalue problems for large systems. *Computers & Structures*, 80:2415–2424, 2002.

[63] C. Proppe, H.J. Pradlwarter, and G.I. Schuëller. Equivalent linearization and monte carlo simulation in stochastic dynamics. *Probabilistic Engineering Mechanics*, 18:1–15, 2003.

[64] K.-A. Reckling. *Plastizitätstheorie und ihre Anwendung auf Festigkeitsprobleme*. Springer-Verlag, 1967.

[65] J.B. Roberts and P.D. Spanos. *Random Vibration and Statistical Linearization*. John Wiley & Sons, New York, 1990.

[66] R.Y. Rubinstein. *Simulation and the Monte Carlo method*. John Wiley & Sons, New York, 1981.

[67] Adel S. Saada. *Elasticity: Theory and Applications*. Pergamon Press Inc., 1974.

[68] A. Sawczuk and T. Jaeger. *Grenztragfähigkeits-Theorie der Platten*. Springer-Verlag, 1963.

[69] C.A. Schenk. *Computational Procedures for Uncertainty Assessment of Large Non-Linear Finite Element Systems*. Dissertation, Leopold-Franzens Universität Innsbruck, Fakultät für Bauingenieurwesen und Architektur, Innsbruck, Austria, 2003.

[70] C.A. Schenk and G.I. Schuëller. *Uncertainty Assessment of Large Finite Element Systems*. Springer-Verlag, Berlin Heidelberg, 2005.

[71] G.I. Schuëller. Engineering Applications of Stochastic Mechanics - Achievements and Prospectives. In *Proceedings of the IUTAM-Symposium on Advances in Nonlinear Stochastic Mechanics*, Trondheim, 1995.

[72] G.I. Schuëller. A state-of-the-art report on computational stochastic mechanics. *Probabilistic Engineering Mechanics*, 4:197–321, 1997.

[73] G.I. Schuëller and H.J. Pradlwarter. The role of Stochastic Dynamics in Risk and Reliability Assessment of Structures and Mechanical Systems. In *Nonlinear Dynamics and Stochastic Mechanics, editors, W. Kliemann and Sri Namachchivaya*, pages 383–410, 1995.

[74] G.I. Schuëller, H.J. Pradlwarter, and C.A. Schenk. Non-stationary response of large linear FE models under stochastic loading. *Computers and Structures*, 81:937–947, 2003.

[75] G.I. Schuëller, H.J. Pradlwarter, M. Vasta, and N. Harpornchai. Benchmark study on non-linear stochastic structural dynamics. In *Proceedings of the* 7^{th} *International Conference on Structural Safety and Reliability, editors, N. Shiraishi, M. Shinozuka and Y.K. Wen*, Rotterdam: Balkema, 1998.

[76] U. Sellgren. Component Mode Synthesis - A method for efficient dynamic simulation of complex technical systems. Technical report, Department of Machine Design, The Royal Institute of Technology (KTH) Stockholm, Sweden, 2003.

[77] L.F. Shampine and M.W. Reichelt. The matlab ode suite. *SIAM Journal on Scienfific Computing*, 18:1–22, 1997.

[78] L.F. Shampine, M.W. Reichelt, and J.A. Kierzenka. Solving index-1 daes in Matlab and Simulink. *SIAM Review*, 41:538–552, 1999.

[79] C.E. Shannon. Communication in the presence of noise. In *Proc. Institute of Radio Engineers*, pages 10–21, 1949.

[80] M. Shinozuka. Monte carlo solution of structural dynamics. *Computers and Structures*, 2(5+6):855–874, 1972.

[81] M Shinozuka. Digital simulation of random processes in engineering mechanics with the aid of FFT technique. In *Stochastic Problems in Mechanics, editors, S.T. Ariaratnam and H.H.E. Leipholz, Waterloo*, pages 277–286, 1974.

[82] M Shinozuka. Stochastic fields and their digital simulation. In *Stochastic Methods in Structural Dynamics, editors, G.I. Schuëller and M. Shinozuka, Martinus Nijhoff Publishers*, pages 93–133, 1987.

[83] M. Shinozuka and G. Deodatis. Response variability of stochastic finite element systems. *Journal of Engineering Mechanics*, 114(3):499–519, 1988.

[84] M. Shinozuka and G. Deodatis. Simulation of stochastic processes by spectral representation. *Applied Mechanics Reviews*, 44(4):191–204, 1991.

[85] M. Shinozuka and G. Deodatis. Simulation of multi-dimensional gaussian stochastic fields by spectral representation. *Applied Mechanics Reviews*, 49(1):29–53, 1996.

[86] M. Shinozuka and C. Jan. Digital simulation of random processes and its application. *Journal of Sound and Vibration*, 25(1):111–128, 1972.

[87] M. Shinozuka and Y-K. Wen. Monte carlo solution of nonlinear vibrations. *AIAA J*, 10(1):37–40, 1972.

[88] I. Simulescu, T. Mochio, and M. Shinozuka. Equivalent linearization method in nonlinear FEM. *Engineering Mechanics, ASCE*, 115(3):475–492, 1989.

[89] K. Sobzyk. *Stochastic Differential Equations with Application to Physics and Engineering*. Kluwer Academic Publishers, Dordrecht Boston London, 1991.

[90] L. Socha and T.T. Soong. Linearization in analysis of nonlinear stochastic systems. *Applied Mechanics Reviews*, 44(10):399–422, 1991.

[91] Y. Suzuki and R. Minai. Seismic Reliability Analysis of Hysteretic Structures Based on Stochastic Differential Equations. In *Proceeding of the* 4^{th} *ICOSSAR*, pages 177–186, Kobe, Japan, 1985.

[92] Y. Suzuki and R. Minai. Application of stochastic differential equations to seismic reliability analysis of hysteretic structures. *Probabilistic Engineering Mechanics*, 3(1):43–52, 1988.

[93] R. Szilard. *Theroy and Analysis of Plates - Classical and Numerical Methods*. PRENTICE-HALL, INC., Englewood Cliffs, New Jersey, 1974.

[94] H. Tajimi. A statistical method of determining the maximum response of a building during earthquake. In *Proceedings of the* 2^{th} *World Conference on Earthquake Engineering*, Tokyo, Japan, 1960.

[95] M. Vannucci, A. Moro, and P.D. Spanos. Wavelets in random processes representation. In *Probabilistic Mechanics and Structural Releability, editors, D.M. Frangopol and M.D. Grigoriu*, pages 672–675, 1996.

[96] C.-H. Wang and Y.K. Wen. Evaluation of pre-northridge low-rise steel buildings. i: Moedling. *Journal of Structural Engineering*, 126(10):1160–1168, 2000.

[97] H. Waubke. *Dynamische Berechnungen für den Halbraum mit streuenden Parametern mittels orthogonaler Polynome*. Dissertation, Lehrstuhl für Baumechanik, Technische Universität München, München, Germany, 1996. Berichte aus dem Konstruktiven Ingenieurbau, 2/1996.

[98] H. Waubke. *Moment-Closure Technik zur Abschätzung der elasto-plastischen Reaktion von Stockwerksrahmen auf zufällige Belastungen aus Windereignissen*. Habilitation, Lehrstuhl für Baumechanik, Technische Universität München, München, Germany, 1999. Berichte aus dem Konstruktiven Ingenieurbau, 1/1999.

[99] Y.K. Wen. Methods for random vibration of hysteretic systems. *Engineering Mechanics Division, ASCE*, 102(EM2):249–263, 1976.

[100] Y.K. Wen. Equivalent linearization for hysteretic systems under random excitation. *Transactions of the ASME, Journal of Applied Mechanics*, 47(3):150–154, 1980.

[101] Y.K. Wen. Methods of random vibration for inelastic structures. *Applied Mechanics Reviews*, 42(2):39–52, February 1989.

[102] Y.K Wen and C.-H. Yeh. Bi-axial and trosional response of inelastic structures under random excitation. In *Proceeding of the Symposium on Stochastic Structural Dynamics*, University of Illinois, Illinois, USA, 1988.

[103] Horst Werkle. *Finite Elemente in der Baustatik*. Vieweg & Sohn, Braunschweig/ Wiesbaden, 2001.

[104] Wikipedia. List of natural disasters by death toll — Wikipedia, the free encyclopedia, 2006. [Online; accessed 4-July-2006].

[105] F. Yamazaki and M. Shinozuka. digital generation of non-gaussian stochastic fields. *Journal of Engineering Mechanics*, 114(7):1183–1197, 1988.

[106] B.A. Zeldin and P.D. Spanos. Random field simulation using wavelet bases. *Probabilistic Engineering Mechanics*, 63(4):946–952, 1996.

[107] K. Zilch and G. Zehetmaier. *Bemessung im konstruktiven Betonbau*. Springer, 2006.